2D kinematic characterization of a representative sample of local (U)LIRGs. A 'kinemetry' analysis based on VIMOS/VLT Integral Field Spectroscopy.

A thesis presented for the degree of Doctor of Philosophy

Enrica Bellocchi

CENTRO DE ASTROBIOLOGÍA
ASOCIADO AL NASA ASTROBIOLOGY INSTITUTE
CSIC
Consejo Superior de Investigaciones Científicas
INTA

UAM
UNIVERSIDAD AUTONOMA
DE MADRID

Consejo Superior de Investigaciones Científicas
Centro de Astrobiología
Departamento de Astrofísica

Universidad Autónoma de Madrid
Facultad de Ciencias
Departamento de Física Teórica

SUPERVISOR:
Dr. Santiago Arribas Mocoroa
CO-SUPERVISOR:
Dr. Luis Colina Robledo

TUTOR:
Dra. Ángeles Isabel Díaz Beltrán

Madrid, April 7, 2014

Contents

Abstract

Luminous and ultraluminous infrared galaxies (i.e., LIRGs, L_{IR} = [8-1000 μm] = 10^{11} - 10^{12} $L_{\odot}$, and ULIRGs, $L_{IR} > 10^{12}$ $L_{\odot}$, respectively) host the most extreme star-forming events in the present universe. Although they are rare in the local universe, they are much more numerous at high-z and are relevant contributors to the whole past star formation beyond z $\sim$ 1. Local (U)LIRGs were initially assumed to be the local counterpart of high-z (U)LIRGs similar to those discovered by *Spitzer* and the more luminous sub-mm galaxies (SMGs). More recently, several authors have found that in the local universe (U)LIRGs cover a similar star formation rate (SFR) range than high-z normal star-forming galaxies (SFGs). Therefore, low-z (U)LIRGs offer a unique opportunity to study, at high linear resolution and signal-to-noise ratio (S/N), extreme SF events and compare them with those observed at high-z. Furthermore, their analysis would allow the methods and techniques applied to high-z galaxies to be tested. One particular relevant and interesting topic is the kinematics characterization of high-z galaxies in order to better understand how galaxies assembled and evolved at early epochs. In the context of the proposed evolutionary scenarios, there is a strong interest in kinematically characterizing galaxies as *disks* and *mergers*, as their relative fraction is a key observational input to constrain different evolutionary scenarios.

This thesis is focused on the 2D kinematics characterization of a unique sample observed with VIMOS/VLT integral field unit (IFU) consisting of 38 local (U)LIRG systems (51 individual galaxies). This sample significantly enlarges previous samples both in number and characteristics, showing a large variety of dynamical phases: from mostly isolated disks for low-luminosity LIRGs to a majority of merger remnants for ULIRGs. It shows the first attempt to obtain a statistically significant study of the 2D kinematic properties of these systems as a function of the infrared luminosity, morphology (i.e., interaction phase) and dynamical status. The majority of the sources (i.e., 31/38) covers the less studied LIRG luminosity range: this is relevant because they fill the gap between the extreme cases and the general population of local SFGs, complementing previous studies which are mainly focused on ULIRGs. Then, the luminosity range covered by the sample is particu-

larly relevant for the high-z comparison since local (U)LIRGs cover a SFR range similar to that of high-z normal SFGs. In order to expand the luminosity range we have also included a subsample formed by ULIRGs (i.e., 25 objects) observed with INTEGRAL/WHT. The main findings and conclusions are summarized as follows:

Spatially resolved kinematics in (U)LIRGs

We kinematically characterize the status of the sample deriving the 2D kinematic properties of two distinct kinematic components (i.e., *narrow* and *broad*). The 'systemic'/'narrow' component is found over the whole line-emitting region of the system while the 'broad' one is generally found in the inner (spatially resolved) regions of most of the LIRGs and ULIRGs, likely tracing nuclear outflows. The systemic component traces the overall velocity field and shows a large variety of kinematic 2D structures: most of the objects (76%) are dominated by rotation. We find that rotation anti-correlates with the infrared luminosity, with a higher fraction of objects with complex kinematics among ULIRGs than in LIRGs.

A clear correlation between the different phases of the merging process and the mean kinematic properties inferred from the velocity maps is found. In particular, isolated disks, interacting galaxies, and merging systems define a sequence of increasing mean velocity dispersion and decreasing velocity field amplitude, which is characterized by intrinsic average dynamical ratios (v^*/σ) of 4.7, 3.0, and 1.8, respectively. In terms of the observed dynamical support (v/σ), the sample covers the gap between local spirals and E/SOs. The LIRGs classified as isolated disks partially overlap with the values of local spirals but show larger turbulence and thicker disks. Interacting systems and mergers have values closer to those of low-velocity dispersion E/SOs, though with higher velocity amplitudes. Our dynamical mass estimates indicate that ULIRGs are more massive than LIRGs by, on average, a factor of about 2. The subclass of (U)LIRGs classified as mergers and the Lyman break analogs (LBAs) share similar kinematic properties, although the dynamical mass of LBAs is a factor 5 smaller, on average. This is a clear indication that, independent of the mass of the system and of whether it is dusty or dust-free, starburst winds and tidally induced forces produce dynamically hot systems characterized by $\sigma \sim$ 70-80 km s^{-1} and $v/\sigma \sim$ 1-2.

Distinguishing *disks* from *mergers*: tracing the kinematic asymmetries in local (U)LIRGs using *kinemetry*-based criteria

In order to quantify the relative importance of the kinematic asymmetries with respect to rotation in (U)LIRG systems, we have used the *kinemetry* method (developed by Kra-

jnović et al. 2006) along with the kinematic criteria proposed by Shapiro et al. (2008). From the analysis of a sub-sample of 4 LIRGs for which the morphology is clearly defined, we develop a new optimized criterium (i.e.,'weighted', Bellocchi et al. 2012) in order to better distinguish between 'disks' from 'post-coalescence mergers'. We then apply both criteria (i.e., Shapiro's and *weighted*) to the whole (U)LIRG sample, then studying its robustness against angular resolution effects (distance) on the basis of simulated observations of these objects at z=3 with the *NIRSpec/JWST* angular resolution.

The kinematic properties of (U)LIRGs derived using the *kinemetry* method are in general consistent with their morphology (i.e., isolated disks have low kinematic asymmetries in their kinematic maps while post-coalescence and ongoing-mergers show higher kinematic asymmetries). However, some discrepancies between the morphological and kinematical classifications exist, making the analysis subjected to relatively large uncertainties when objects have a total kinematic asymmetry (K_{tot}) in the range 0.19 (0.15) $<$ K_{tot} $<$ 0.9 (0.6) in the weighted and (unweighted) plane. Outside this range, regular disks and complex mergers are well identified. This behavior is found for both the unweighted and weighted methods, which give similar results when the whole sample is considered.

From this analysis, we can conclude that in some cases it is uncertain to classify systems as *disk/merger* using *kinemetry*-based criteria, and this clearly depends on the definition of a *disk* (*merger*). The asymmetry limit suggested by our data to separate *disks* from *mergers* is significantly lower than the one proposed by Shapiro et al. (2008). In fact, according to Shapiro's limit only a fraction of ongoing and post-coalescence mergers are classified as such, overestimating the fraction of disks, thus lowering the value of the fraction of merger/disk systems.

Furthermore, a linear trend is found between the K_{tot} and the infrared luminosity L_{IR} with the most luminous objects (ULIRGs) showing the highest total kinematic asymmetries. A linear (inverse) trend is derived between the K_{tot} and the intrinsic dynamical ratio v^*/σ: morphologically classified *disks* show higher dynamical ratio and lower total kinematic asymmetry K_{tot}. The opposite is found for the *mergers*. An interesting trend is also found between the total kinematic asymmetry K_{tot} and the projected nuclear separation along the merger process. Initially, the smaller the nuclear separation the larger the K_{tot}, which reaches its maximum value during the 'ongoing merger phase' (nuclear separations $\sim$ 2-5 kpc) and then decreases during the post-coalescence mergers phase, although with a relatively large dispersion.

Finally, we also include some preliminary works which will be developed in detail in the near future. First, the spectral energy distribution (SED) analysis, in order to derive the stellar masses in our systems. Their comparison with the dynamical mass estimates

allows to estimate the gas fraction in our local systems. Furthermore, our local kinematic results are compared with those derived for high-z SFGs in previous IFS-based works, in order to study the similarities (or discrepancies) in the kinematics and dynamics between low-z (U)LIRGs and high-z SFGs.

Resumen

Las galaxias luminosas y ultraluminosas infrarrojas (LIRGs, L_{IR} = [8-1000 μm] = 10^{11} - 10^{12} $L_{\odot}$, y ULIRGs, $L_{IR} > 10^{12}$ $L_{\odot}$, respectivamente) alojan los eventos más extremos de formación estelar encontrados en el universo local. Aunque estos objetos no son comunes localmente, son más numerosos a alto *redshift (z)* y contribuyen de forma importante a la densidad de tasa de formación estelar del universo mas allá de $z \sim 1$. Inicialmente, se pensaba que las (U)LIRGs locales eran el equivalente local a las (U)LIRGs a alto *z*, como las descubiertas por *Spitzer* y las más luminosas galaxias sub-milimétricas (SMGs). Recientemente, varios autores han encontrado que las (U)LIRGs locales tienen tasas de formación estelar (SFR) similares a las galaxias normales dominadas por formación estelar (SFGs) a alto *z*. Por lo tanto, las (U)LIRGs locales ofrecen una oportunidad única para estudiar, con alta resolución espacial y buena relación señal-ruido, eventos de formación estelar extremos y compararlos con los que se observan en el universo lejano. Además, su análisis permite evaluar los métodos y las técnicas generalmente aplicadas a alto *z*. La caracterización cinemática de galaxias a alto *z* es particularmente relevante e interesante para entender mejor como las galaxias se han formado y evolucionado durante las primeras épocas del universo. La caracterización cinemática de las galaxias en *discos* y *mergers* es esencial dado que su fracción relativa contribuye a acotar de forma importante los diferentes escenarios evolutivos.

Esta tesis está enfocada a la caracterización cinemática 2D de una muestra de 38 sistemas de (U)LIRG locales (51 galaxias individuales) observadas con la unidad de espectroscopía de campo integral del instrumento VIMOS/VLT. Esta muestra extiende significativamente otras muestras previas en número y en características, presentando una gran variedad de fases dinámicas: desde los discos más aislados en el caso de LIRGs de baja luminosidad a galaxias que han sufrido un *major merger* (ULIRGs). De la misma manera, esta muestra es el primer intento para obtener un estudio estadísticamente significativo de las propiedades cinemáticas 2D de estos sistemas en función de la luminosidad infrarroja, la morfología (fase de interacción) y el estado dinámico. La mayoría de las

fuentes (31/38) cubren el rango de baja luminosidad (LIRG) poco estudiado hasta ahora: esto es importante porque estas galaxias tienen propiedades cinemáticas intermedias entre las que caracterizan los casos extremos (ULIRGs) y las poblaciones de galaxias locales dominadas por formación estelar. De esta forma se complementan los estudios previos principalmente centrados en el rango de alta luminosidad (ULIRG). Por lo tanto, el rango de luminosidad cubierto por nuestra muestra tiene particular relevancia para la comparación con muestras a alto z, dado que las (U)LIRGs locales tienen tasas de formación estelar parecidas a las que caracterizan las SFGs a alto z. Por otro lado, para extender el rango de luminosidad hemos incluido una sub-muestra formada por 25 ULIRGs observadas con INTEGRAL/WHT. Los principales resultados y conclusiones de esta tesis son los siguientes:

Cinemática espacialmente resuelta en las (U)LIRGs

Caracterizamos el estado cinemático de la muestra derivando las propiedades 2D de dos componentes cinemáticas distintas ('estrecha' y 'ancha'). La componente 'sistémica/estrecha' se encuentra en todo el campo de emisión del sistema mientras la componente 'ancha', en general, está localizada en las regiones centrales (resueltas espacialmente) de la mayoría de las LIRGs y ULIRGs, y probablemente traza *outflows*. La componente sistémica traza el campo de velocidad global y muestra una gran variedad de estructuras cinemáticas en 2D: la mayoría de los objetos (76%) están dominados por rotación. Se encuentra una anti-correlación entre la rotación y la luminosidad infrarroja: la fracción de objetos con cinemática compleja es mayor entre las ULIRGs que entre las LIRGs.

Se ha encontrado una clara correlación entre las diferentes fases en el proceso de fusión y las propiedades cinemáticas promedio inferidas a partir de los mapas de velocidad. En particular, discos aislados, galaxias en interacción y sistemas en fase de fusión definen una secuencia caracterizada por una dispersión de velocidad promedio creciente y una amplitud del campo de velocidad decreciente, los cuales están caracterizados por un cociente intrínseco dinámico promedio (v^*/σ) de 4.7, 3.0, y 1.8, respectivamente. En términos de soporte dinámico observado (v/σ), la muestra abarca el rango entre las espirales locales y las E/S0s. Los valores de las LIRGs clasificadas como discos aislados se superponen parcialmente con los valores de las espirales locales, con la diferencia de que las LIRGs presentan turbulencias más elevadas y discos más gruesos. Sistemas en interacción y en fase de fusión tienen valores más cercanos a los que se derivan para las galaxias E/S0 con baja dispersión de velocidad, aunque presentan amplitudes de velocidad mas altas. Nuestras estimaciones de las masas dinámicas indican que ULIRGs son más masívas que

las LIRGs en un factor 2 en promedio. La subclase de (U)LIRGs clasificadas como *mergers* y las *Lyman break analogs* (LBAs) comparten ciertas propiedades cinemáticas similares, aunque la masa dinámica de las LBA es 5 veces más pequeña en promedio. Este resultado indica claramente que, independiente de la masa de un sistema y de su cantidad de polvo, los vientos generados por eventos de formación estelar y fuerzas de marea inducidas producen sistemas dinámicos calientes caracterizados por $\sigma \sim$ 70-80 km s^{-1} y v/$\sigma \sim$ 1-2.

Diferenciando los *discos* de los *mergers*: asimetrías cinemáticas en (U)LIRGs locales usando criterios basados en en método *kinemetry*

Con el fin de cuantificar la importancia relativa de las asimetrías cinemáticas con respecto a la rotación en los sistemas (U)LIRGs, nuestro análisis se ha basado en el uso del método *kinemetry* (desarrollado por Krajnović et al. 2006) junto a los criterios cinemáticos propuestos por Shapiro et al. 2008. Con el análisis de una sub-muestra de 4 LIRGs con la morfología claramente definida, hemos desarrollado un nuevo criterio optimizado (i.e.,'ponderado', Bellocchi et al. 2012) para diferenciar mejor las galaxias de tipo 'disco' de aquellas en la fase de 'post'-coalescencia. Asimismo aplicamos ambos criterios (el de Shapiro y el *ponderado*) a la muestra completa de (U)LIRGs, estudiando así su robustez frente a los efectos de resolución angular (distancia) basados en observaciones simuladas de estos objetos a z=3 con la resolución angular de *NIRSpec/JWST*.

Las propiedades cinemáticas de las (U)LIRGs derivadas usando el método de *kinemetry* son, en general, consistentes con sus morfologías (discos aislados muestran mapas cinemáticos caracterizados por asimetrías cinemáticas bajas mientras que las galaxias en fase de coalescencia y post-coalescencia tienen asimetrías cinemáticas mas altas). Sin embargo, se han encontrado discrepancias entre la clasificación morfológica y cinemática, lo que hace que el análisis esté sujeto a incertidumbres relativamente grandes cuando los objetos tienen una asimetría cinemática global (K_{tot}) entre $0.19 < K_{tot} < 0.9$. Fuera de este rango, discos regulares y galaxias en fase de fusión muy complejas son fácilmente identificables. Este comportamiento se encuentra cuando se aplican los dos métodos, los cuales dan resultados parecidos cuando se considera la muestra entera.

De este análisis se puede concluir que en unos casos clasificar los sistemas como discos/'mergers' con criterios basados en *kinemetry* tiene sus incertidumbres, y que el resultado claramente depende de la definición de disco y 'merger'. El límite de asimetría para separar discos y 'mergers' sugerido por nuestros datos es significativamente inferior al que Shapiro y colaboradores proponen. De hecho, con el criterio de Shapiro sólo algunas de las galaxias en fase de fusión o post-fusión se clasifican como tales, a la vez que se sobrestima la fracción de discos, y por lo tanto disminuye el cociente entre el número de

sistemas 'merger' y disco.

Además, encontramos una relación lineal entre el K_{tot} y la luminosidad infrarroja L_{IR} con los objetos mas luminosos (ULIRGs) caracterizados por una asimmetría cinemática global más alta. También derivamos una relación lineal inversa entre el K_{tot} y el cociente intrínseco dinámico v^*/σ: galaxias clasificadas morfológicamente como discos muestran un cociente dinámico más alto y asimetría cinemática global K_{tot} más baja. Lo contrario sucede con los 'mergers'. Una tendencia interesante se encuentra también entre la asimmetría cinemática global K_{tot} y la separación nuclear proyectada a lo largo del proceso de fusión. Inicialmente, cuanto menor es la separación nuclear, mayor es su K_{tot}, que alcanza su valor máximo durante la fase de fusión (separaciones nucleares $\sim$ 2-5 kpc) para después disminuir durante la fase de post-fusión, aunque con una dispersión relativamente grande.

Finalmente, se incluyen también unos trabajos preliminares que serán desarrollados en detalle en un futuro próximo. Primero, el análisis de la distribución espectral de energía (SED) para inferir los valores de las masas estelares en nuestros sistemas. Su comparación con las estimaciones de las masas dinámicas permite determinar la fracción de gas en nuestras galaxias. Además de esto, se comparan nuestros resultados cinemáticos con los que se han derivado para galaxias con alta formación estelar a alto z en trabajos precedentes basados en el análisis de espectroscopía de campo integral. Esto es útil para estudiar las similitudes (o discrepancias) en la cinemática así como en la dinámica entre las (U)LIRGs locales y las SFGs en el universo lejano.

Chapter 1

Infrared Bright Galaxies

In this chapter we present a summary of the properties of local infrared bright galaxies, such as the luminous and ultraluminous infrared galaxies (i.e., LIRGs, L_{IR} = [8-1000 μm] = 10^{11} - 10^{12} $L_{\odot}$, and ULIRGs, L_{IR} = 10^{12} - 10^{13} $L_{\odot}$, respectively). The morphology and nuclear activity of this class of galaxies are discussed. Then, the properties of their high-redshift counterparts are outlined. Furthermore, we emphasize the role of the kinematics in understanding the galaxy evolution along with the importance of study such a local population in order to compare the results with those derived at high-z. We finally describe the structure and main goals of this thesis work.

1.1 Discovery and classification

The importance of infrared (IR) bright galaxies has been recognized since their discovery more than 40 years ago by Rieke & Low (1972) using ground-base IR observations at 1-25 μm. IR bright galaxies emit most of their bolometric luminosity in the infrared band (i.e., $L_{Bol} \approx L_{IR[8-1000\mu m]}$). In 1983 a large amount of infrared sources ($\sim$ 250000; Helou & Walker 1988), too faint to be detected in the optical, have been revealed by the *Infrared Astronomical Satellite* (IRAS; Neugebauer et al. 1984). IRAS carried out the first all-sky survey at far-infrared wavelengths, observing in four IR bands centered at 12, 25, 60, and 100 μm.

According to their IR luminosity (L_{IR}) they were classified as luminous, ultra-luminous, and hyper-luminous infrared galaxies (i.e., LIRG, L_{IR} = 10^{11} - 10^{12} $L_{\odot}$, and ULIRG, L_{IR} = 10^{12} - 10^{13} $L_{\odot}$ and HyLIRG $L_{IR} > 10^{13}$ $L_{\odot}$, respectively; see Tab. 1.1). They are important populations to study galaxy evolution since provide a unique opportunity to investigate in detail the extreme star forming events generally found at high-z. Depending on the total infrared luminosity L_{IR}, the shape of their spectral energy distributions (SEDs) changes

(i.e., Sanders & Mirabel 1996, see Fig. 1.1). Specifically, the higher the L_{IR}, the higher the S_{60}/S_{100} and the lower the S_{12}/S_{25}. According to the IRAS colors (Sanders et al. 1988), the flux ratio S_{25}/S_{60} is considered in order to classify the sources as:

- Cold (U)LIRGs: system with $S_{25}/S_{60} < 0.3$. They are at early mergers stages, showing a nuclear spectral type of HII or Low Ionization Nuclear Emission-line Region (LINER). This group comprises about 75% of ULIRGs;
- Warm (U)LIRGs: system with $S_{25}/S_{60} > 0.3$. Most of these galaxies show Seyfert-like spectra (Sanders et al. 1988). About 25% of ULIRGs fall into this group.

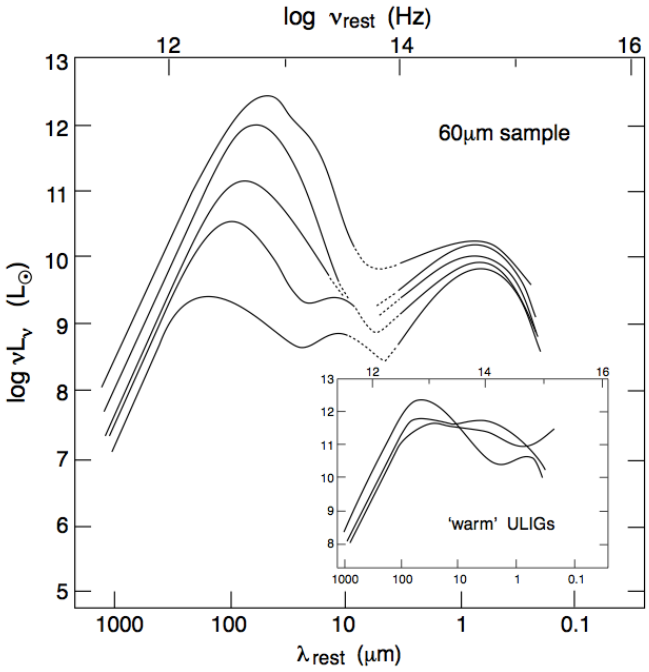

Figure 1.1: Variation of the mean SEDs (from sub-millimetre to UV wavelengths) with increasing L_{IR} for the 60 μm sample of infrared galaxies. (Insert) Examples of the subset ($\sim$ 15% for the current sample) of ULIRGs with *warm* infrared colors (Sanders & Mirabel 1996).

1.2 Power source in (U)LIRGs

From the very early investigations, a large fraction of studies tried to determine what powers (U)LIRG systems. Both Active Galactic Nuclei (AGN) ad star forming activity (i.e., Sanders & Mirabel 1996; Veilleux et al. 1999a; Risaliti et al. 2006; Valiante et al. 2009; Alonso-Herrero et al. 2012) can co-exist in these systems, although the fraction of galaxies dominated by the presence of an AGN increases with L_{IR}, while lower luminosity

Table 1.1: Abbreviations and Definitions adopted for IRAS Galaxies

F_{FIR}	1.26×10^{-14} {2.58 S_{60} + S_{100}} [W m^{-2}]
L_{FIR}	L(40-500 μm) = $4\pi D_L^2$ C F_{FIR} [$L_\odot$]
F_{IR}	1.8×10^{-14} {13.48 S_{12} + 5.16 S_{25} + 2.58 S_{60} + S_{100}} [W m^{-2}]
L_{IR}	L(8 - 1000 μm) = $4\pi D_L^2$ C F_{FIR} [$L_\odot$]
LIRG	Luminous Infrared Galaxy, L_{IR} = 10^{11}-10^{12} $L_\odot$
ULIRG	Ultra-luminous Infrared Galaxy, L_{IR} = 10^{12}-10^{13} $L_\odot$
HyLIRG	Hyper-luminous Infrared Galaxy, $L_{IR} > 10^{13}$ $L_\odot$

Notes. The quantities S_{12}, S_{25}, S_{60}, and S_{100} are the IRAS flux densities in Jy at 12, 25, 60, and 100 μm. C is a scaling factor in the range 1.4-1.8 to account for the extrapolated flux long-ward the 100 μm IRAS filter. D_L is the luminosity distance. $L_\odot = 3.84 \times 10^{26}$ W = 3.84×10^{33} erg s^{-1}. Table adapted from Sanders & Mirabel (1996).

LIRGs are mainly powered by star-formation (i.e., Rieke & Lebofsky 1979; Telesco & Harper 1980; Scoville et al. 2000; Alonso-Herrero et al. 2006; Kartaltepe et al. 2010; U et al. 2012).

Thus, the observed mid- and far-IR emission in the IR bright galaxies was interpreted as due to the ultraviolet (UV) photons, coming from early-type stars (or AGN), which are absorbed by the dust are then re-emitted at longer wavelengths, typically in the infrared, approximately with the spectrum of a blackbody at the temperature of the dust ($\sim$ 20-80 K). In order to properly describe their SEDs various models (e.g., Helou 1986; Rowan-Robinson 1986) of the infrared emission suggested that the secondary peak in the mid-IR is due to the emission from small dust grains near hot stars, while the stronger peak (i.e., $\lambda \geq$ 100-200 μm) is due to the dust emission from infrared cirrus ($T_D \leq$ 20 K) heated by the older stellar population (i.e., Sanders & Mirabel 1996). A 'starburst' component emerges at $\lambda \sim$ 60 μm in more infrared luminous galaxies, while in Seyfert galaxies an even warmer component peaking at $\lambda \sim$ 25 μm represents warm dust directly heated by the AGN. Specifically, there has been controversy over the extent to which LIRGs and ULIRGs in the local universe are powered by intense star formation as opposed to AGN (i.e., Sanders & Mirabel 1996 review).

1.2.1 Results from infrared spectroscopy

(U)LIRG systems are characterized by large amount of dust and gas which cause the extinction to vary, on average, from A_V = 2-6 mag for the LIRGs (e.g., Alonso-Herrero et al. 2006) up to $A_V >$ 40 mag in ULIRGs (e.g., Genzel et al. 1998). The advent of IR space telescopes such as the *Infrared Space Telescope* (ISO; Kessler et al. 1996), *Spitzer Space Telescope* (Werner et al. 2004) and, more recently, *Herschel Space Observatory*

(Pilbratt et al. 2010) made possible the mid- and far-IR spectroscopy of (U)LIRGs, even though the IR observations are generally characterized by a worse resolution than in the optical[1].

Up to date, most of the studies have been based on the analysis of large samples of (U)LIRGs observed using long-slit spectroscopy (e.g., Duc et al. 1997; Goldader et al. 1997a,b). Indeed, with the advent of *Spitzer*, large samples of ULIRGs have been observed by Lutz et al. (1999); Veilleux et al. (1999b); Farrah et al. (2007); Nardini et al. (2008, 2010) and Veilleux et al. (2009) using this technique: these studies confirmed that most of the luminosity of ULIRGs is produced by star-formation. For instance, Farrah et al. (2007) studied a sample of 53 local ULIRGs showing that the AGN dominates the IR emission only in 20% of the ULIRGs. Alonso-Herrero et al. (2011) decomposed the *Spitzer* mid-IR of a sample of 53 LIRGs into AGN and starburst components using star-forming galaxy templates and clumpy torus models, finding that the energy output of the local LIRGs is mainly due to massive starbursts with a small AGN contribution, while the AGN contribution increases with L_{IR} (e.g., Nardini et al. 2010; Alonso-Herrero et al. 2011; see Fig. 1.2).

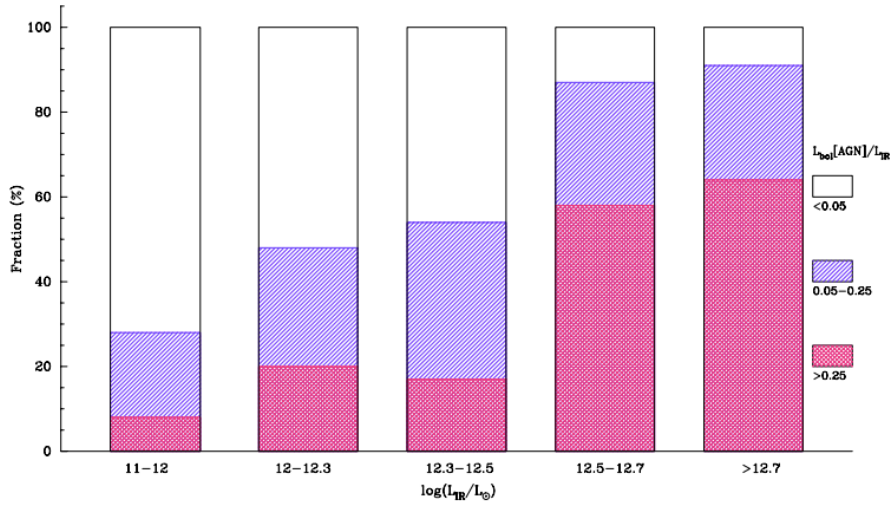

Figure 1.2: Fractional AGN bolometric contribution to the IR luminosity for a local sample of LIRGs and ULIRGs. The AGN bolometric contributions are from Nardini et al. (2010). Figure from Alonso-Herrero et al. (2011).

Thanks to the relatively high spatial resolution (provided by a 3.5 m mirror) and sensitivity of the *PACS* and *SPIRE* instruments on board the *Herschel* telescope, we can study the origin and nature of the cosmic infrared background through, e.g., the examination of their SEDs. In particular Sajina et al. (2012), combining *Spitzer* and

[1]While *IRS/Spitzer* can reach a spectral resolution R $\sim$ 600, *PACS* on *Herschel* is characterized by higher spectral resolution, R $\sim$ 1000-5500, showing values more similar than those reached in the optical.

Herschel data to study the infrared SEDs of a sample of 191 24 μm-selected sources in the redshift range 0.3-2.8, found that $\sim$ 30% of the sources are starbursts (predominantly at lower redshifts, where an AGN contributes $<$ 20% of L_{IR}), $\sim$ 23% are AGNs (i.e., where the AGN contributes $>$ 50% of L_{IR}), while the majority of them ($\sim$ 47%) are composites, showing both significant AGN and starburst activity.

1.2.2 Studies based on optical spectroscopy

Although (U)LIRGs are objects affected by the presence of dust, optical spectroscopy is a valuable tool to classify the excitation mechanism that dominates the galaxy. As in the IR range, most of the optical surveys have been carried out using long-slit spectroscopy, as the works of Veilleux et al. (1999a); Kewley et al. (2001); Corbett et al. (2003); Rodríguez Zaurín et al. (2009); Soto & Martin (2012).

Several optical diagnostic diagrams have been proposed to discriminate the ionization mechanisms present in emission-line objects, as those by Kauffmann et al. (2003); Kewley et al. (2006). These diagnostics classify the source according to the physical processes responsible for the gas excitation into three big groups:

(a) HII-like ionization, that indicates photoionization by O and B stars;
(b) Seyfert-like ionization, that identifies the presence of an AGN;
(c) LINER-like activity, which can be produced by a variety of processes (i.e., the presence of a low-luminosity AGN, the trigger of starbursts, and large scale fast shocks).

Kim (1995) analyzed the nuclear ionization state of a complete sample of ULIRGs (the 1 Jy sample) using long-slit spectroscopy and, according to this classification, they found that the fraction of ULIRGs dominated by Seyfert activity increases in galaxies with luminosities above $L_{IR} \approx 10^{12.3}$ $L_{\odot}$. In contrast, the proportion of HII galaxies dominated by photo-ionization by hot stars seems to decrease with luminosity. The LINER-like galaxies show a constant proportion throughout the IR luminosity range. The nuclear activity derived from optical spectroscopy shows that the lower luminosity LIRGs are mainly powered by star-formation, and that the number of AGN-dominated galaxies increases with the increasing of the L_{IR}. The presence and importance of an AGN, highly obscured by dust, is still under debate, although it appears to be more relevant in warm galaxies with high luminosity (see Veilleux et al. 1999a).

More recently, Yuan et al. (2010) investigated the nuclear activity of $\sim$ 500 IR-selected galaxies. As shown in Fig. 1.3, they classified the nuclear activity of (U)LIRGs as HII (star-forming) galaxies, Seyferts, LINERs including a combination of starburst and AGN activity (hereafter, 'starburst-AGN' composite), finding that most of the sources are starburst-AGN

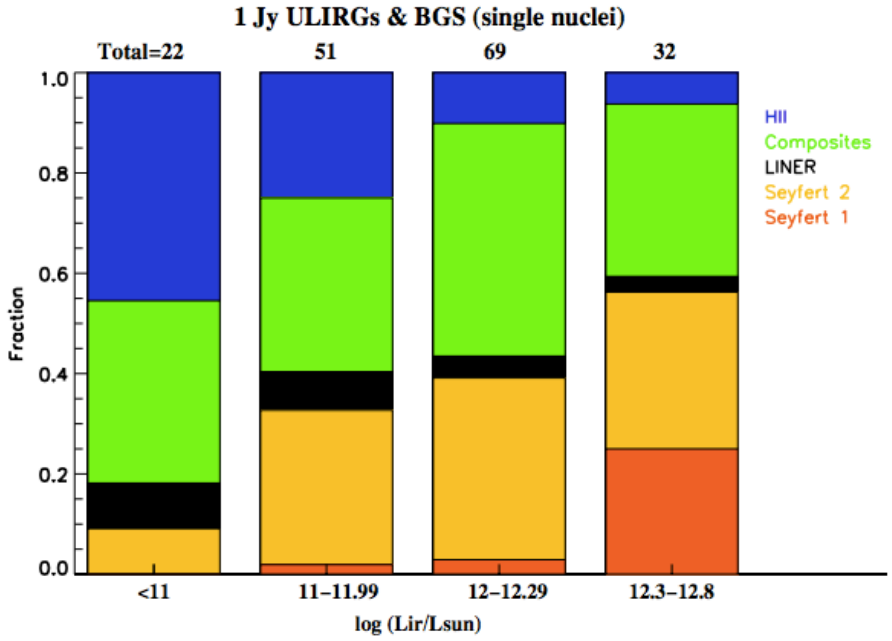

Figure 1.3: Nuclear activity from optical spectroscopy as function of the L_{IR} for the 1Jy ULIRG sample Figure from Veilleux et al. (1999a) and the LIRGs in the BRG sample (Veilleux et al. 1995). Figure from Yuan et al. (2010).

composites and Seyfert galaxies (i.e., $\sim$ 45% each) while less than 5% are LINERs. In ULIRGs, starburst-AGN composite galaxies dominate at early-intermediate stages of the merger, while AGN galaxies dominate during the final merger stages. They also found that the relative strength of the AGN versus starburst activity shows a significant increase at high L_{IR}. In the Bright Galaxy Sample[2] (BRGs), which covers lower L_{IR} than the 1 Jy ULIRG sample, a larger portion of star-forming galaxies has been found ($\sim$ 26%) while the fraction of composite galaxies is 42% and that of Seyfert galaxies is 25%.

1.3 Interaction phase and morphology in (U)LIRGs

1.3.1 The relation between the interaction phase and the L_{IR}

Already 40 years ago, the interaction process among galaxies was considered key to explain the nuclear activity and the starbursts. Toomre & Toomre (1972) showed that the morphological features as tidal tails and bridges observed in close pairs of galaxies can be explained considering the collision of two spiral galaxies. On the other hand, Larson & Tinsley (1978) suggested that the interaction may trigger the star-formation activity.

[2]The BGS is similar to the RBGS but compiled using earlier versions of the IRAS catalogs.

The importance of merger in this type of galaxies was confirmed by Gehrz et al. (1983) with the study of the interacting system Arp 299 (i.e., IC 694 and NGC 3690).

Sanders & Mirabel (1996) summarized the results from using observations of a complete sample of LIRGs draw from the IRAS Bright Galaxy Survey (BGS, Mirabel & Sanders 1989) supplemented by data for a subsample of less luminous BGS objects and data for a larger sample of ULIRGs from the survey of Kim et al. (1995). The majority of the infrared galaxies at $L < 10^{11}$ $L_{\odot}$ appear to be single, gas-rich spirals whose infrared emission can be accounted for star-formation. In the LIRG luminosity range the number of interacting systems strongly increases while at $L_{IR} > 10^{12}$ $L_{\odot}$ the galaxies contain large concentration of molecular gas and, due to their heavy dust obscuration, it becomes hard to distinguish the relative role of starburst and AGN activity. In this luminosity range most of the systems are mergers.

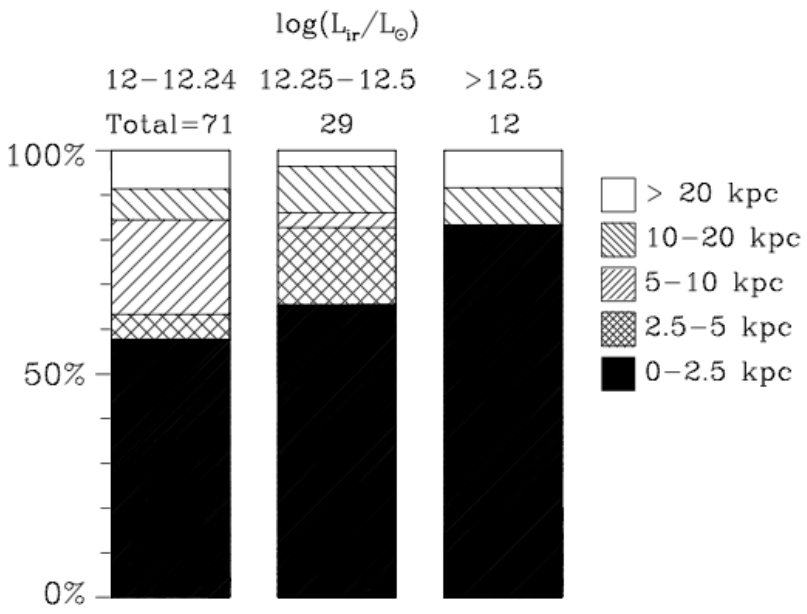

Figure 1.4: Apparent nuclear separation as function of the L_{IR}. Figure from Veilleux et al. (2002).

It has been proposed that ULIRGs are systems that transform gas-rich disk galaxies into moderate-mass ellipticals through merger events (i.e., Sanders & Mirabel 1996; Genzel et al. 2001; Tacconi et al. 2002), with some, but not all, evolving to quasars (QSOs; Colina et al. 2001; Sanders et al. 2003). These objects exhibit a large variety of morphologies, which suggest different dynamical phases: from mostly isolated disks for low-luminosity LIRGs to a majority of interacting systems and merger remnants for ULIRGs (e.g., Borne et al. 2000; Farrah et al. 2001; Bushouse et al. 2002; Veilleux et al. 2002; Arribas et al. 2004).

In Fig. 1.4, drawn from Veilleux et al. (2002), is shown the relation between the fraction of interacting systems with respect to their L_{IR} range. More than 90% of the ULIRGs are interacting systems at different merger phases (e.g., Murphy et al. 1996; Veilleux et al. 2002) while LIRGs are generally spirals which show a morphology much less disturbed than that shown in ULIRGs when in the early phases of the interaction. This trend has been further confirmed by the recent optical and IR spectroscopic studies (i.e., Yuan et al. 2010; Sajina et al. 2012).

Haan et al. (2011) analyzed a sample of $\sim$ 70 LIRGs observed with *HST* in the redshift range $0.01 < z < 0.05$, showing evidence of a large fraction of galaxies with double or triple nuclei. They found that the projected nuclear separation is significantly smaller for ULIRGs (median value of 1.2 kpc) than for LIRGs (median value of 6.7 kpc), suggesting that the LIRG phase appears earlier in mergers than the ULIRG phase.

As shown in Fig 1.5 by Kartaltepe et al. (2010), the fraction of galaxies classified as spirals (blue solid line) drops dramatically with L_{IR} while the fraction of major mergers (green solid line) increases. Lower luminosity LIRGs are a mix of mergers and single isolated disk galaxies while the ULIRG population is clearly dominated by major mergers.

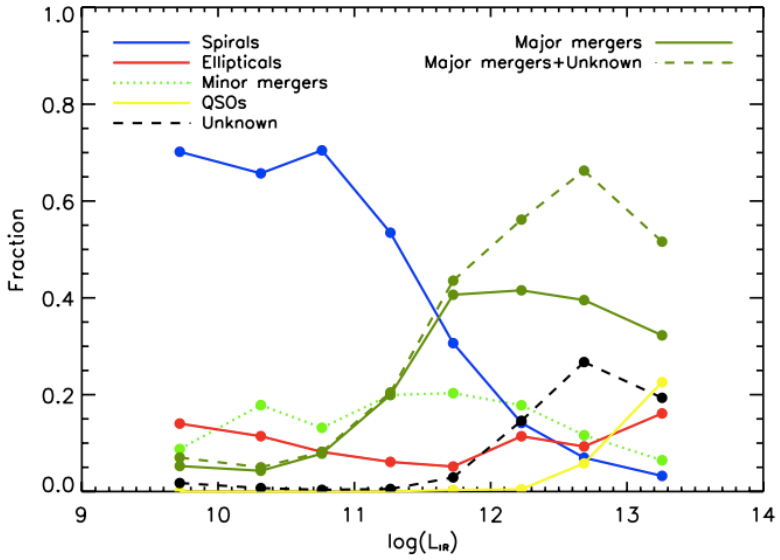

Figure 1.5: Fraction of 70 μm sources that are morphologically classified as spirals (blue solid line), ellipticals (red solid line), minor mergers (green dotted line), major mergers (dark green solid line), QSOs (yellow solid line), unknown (black dashed line), or major mergers+unknown (green dashed line) as a function of L_{IR}. Note that the fraction of galaxies classified as spirals drops dramatically with L_{IR} while the fraction of major mergers increases. There is also a larger fraction of galaxies classified as unknown at high L_{IR}, which corresponds to high redshift. Figure from Kartaltepe et al. (2010).

1.3.2 Predicting the morphology of the merger remnant

Theoretical models predict that the mass ratio of the interacting galaxies affects the properties of the merger remnant. As derived in Cox et al. (2006) the result of a *major* merger (mass ratio 1:1) between two disk galaxies effectively destroys the disks leaving a spheroidal-looking object (see Fig. 1.6; i.e., Heyl et al. 1994; Mihos & Hernquist 1996; Naab et al. 1999; Naab & Burkert 2003).

In contrast to this scenario, Lotz et al. (2008) found that, when considering *major* (i.e., equal-mass) gas-rich disc mergers, the majority of merger remnants appear disk-like and dusty in g-band light, due to the presence of a low-mass star-forming disc. All their remnants even show a large bulge component as well.

On the other hand, Bournaud et al. (2004) confirm the fact that *minor* mergers (i.e., mass ratios in the range 4:1 - 10:1) results in disturbed spiral galaxies. They investigated the less studied range of mass ratios 4:1 - 10:1 using N-body simulations, finding that such mergers can result in very peculiar systems. The remnant actually shows the morphology of a disk galaxy with exponential profile, but whose kinematics is closer to that of elliptical systems. In Fig. 1.7 the results of a specific mass ratio (7:1) merger simulation are shown.

Furthermore, Bournaud et al. (2007) studied multiple, subsequent, minor galaxy mergers using various mass ratios, ranging from 4:1 to 50:1. They showed that, as well as a major merger event, several 'minor' mergers of disk galaxies can lead to the formation of elliptical-like galaxies with global morphological and kinematical properties similar to that observed in real elliptical galaxies. In Fig. 1.8 a schematic description of the nature of the binary and multiple merger remnants as a function of the number of mergers and its mass ratio is shown. In particular, at higher redshift, minor mergers can be more frequent than major mergers, and probably have formed some elliptical galaxies seen today. Minor mergers could partially explain the high boxiness of massive ellipticals, and some fundamental relations observed in ellipticals. In addition, these results indicate that spiral galaxies cannot have grown only by a succession of minor mergers because repeated minor mergers, even at high mass ratios, destroy disks into spheroids.

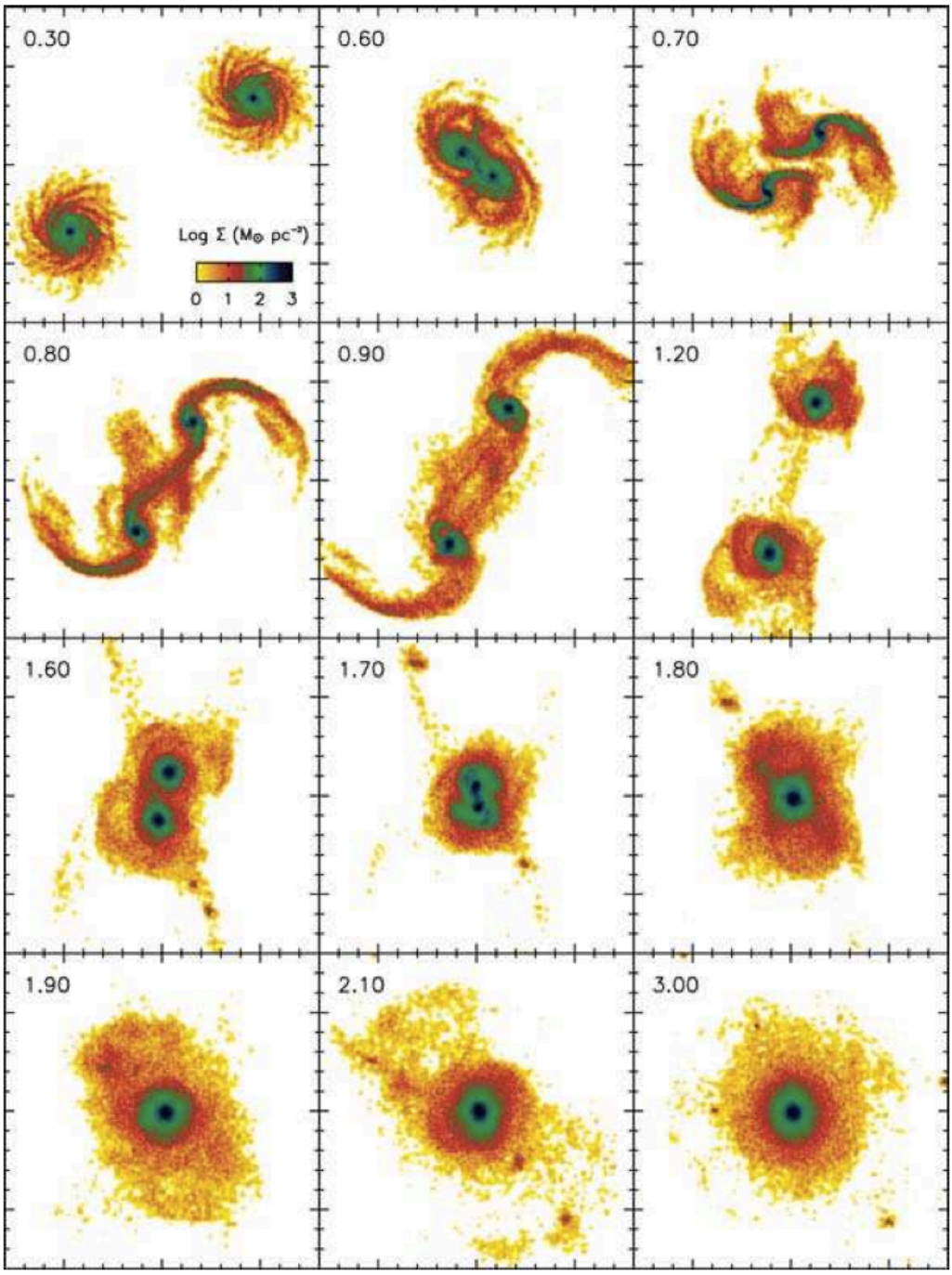

Figure 1.6: Projected stellar (disc plus bulge) density during a *major* merger. Each panel measures 160 kpc on a side, and the number in the upper left-hand side of each frame is the simulation time measured in Gyr. The disc galaxy initially on the lower left-hand side is coplanar with the orbital plane while the upper right-hand disc is tilted by 30°. Figure from Cox et al. (2006).

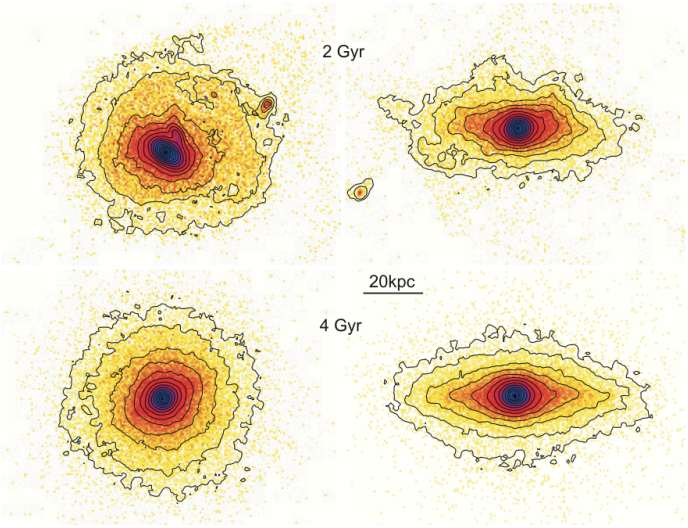

Figure 1.7: Snapshots of the 7:1 merger simulation (left: face-on - right: edge-on), at different epochs. *Top:* 2 Gyr after the beginning of the simulation, the system can be regarded as an advanced merger remnant. The nuclei of the two galaxies have merged 400 Myr ago, but strong asymmetries and tidal debris are still visible. *Bottom:* 2 Gyr later, the system is fully relaxed. Its vertical light distribution resembles that of early-type spirals or S0 galaxies. Figure from Bournaud et al. (2004).

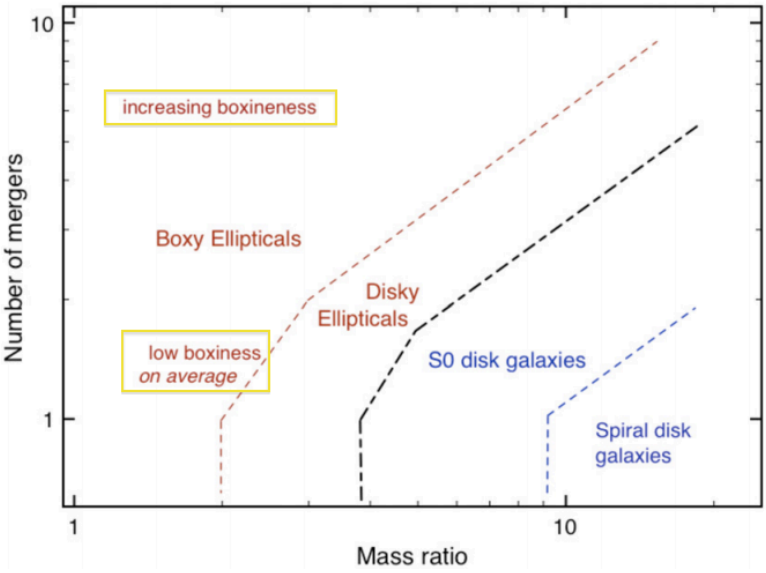

Figure 1.8: Schematic description of the nature of the binary and multiple merger remnants, as a function of the number of mergers and the mass ratio. This scheme gives a representative estimate of the number of mergers required to transform a disk galaxy (Sp or S0) into an elliptical-like system. For instance, the ellipticals formed by 1:1 mergers or 5 $\times$ 7:1 sequences are generally boxy on average (they appear disky as well under some projections), and their boxiness is moderate. An increasing degree of boxiness can be obtained with an increasing number of mergers. Figure from Bournaud et al. (2007).

1.4 High-redshift (U)LIRGs

1.4.1 (U)LIRG contribution to the total IR luminosity density ($\rho_{\rm LIR}$)

In recent years with the advent of the new generation of IR satellites, there has been considerable effort devoted to understanding the properties of distant IR-selected galaxies. Although the IR bright sources comprise the dominant population of extragalactic objects at $L_{\rm Bol} > 10^{11}$ $L_{\odot}$, they are not common in the local universe (e.g., Lagache et al. 2005). In particular, follow-up observations with *ISO* and *Spitzer* have shown that (U)LIRGs are much more numerous at high-z and are relevant contributors to the whole past star formation beyond z $\sim$ 1 (e.g., Elbaz et al. 2002; Le Floc'h et al. 2005; Pérez-González et al. 2005; Bridge et al. 2007; Caputi et al. 2007; Pérez-González et al. 2008; Magnelli et al. 2009). While at z $\sim$ 1 LIRGs and ULIRGs represent 70% of the star formation activity (i.e., Le Floc'h et al. 2005), in the local universe these galaxies represent $\sim$ 6% of the IR emission (i.e., Soifer & Neugebauer 1991). Indeed, LIRGs and ULIRGs account for, respectively, $\sim$ 5% and $<$ 1% of the local IR background (Lagache et al. 2005) being the local density of LIRGs is 2 orders of magnitude higher than that of ULIRGs (e.g., Soifer et al. 1987).

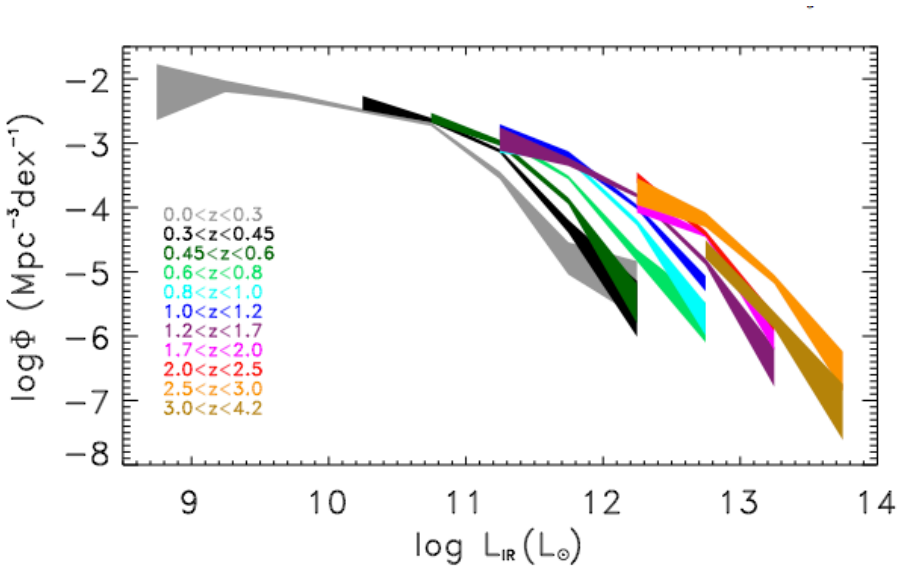

Figure 1.9: Total IR Luminosity Function estimated by combining the *Herschel* data plotted in all the different redshift intervals, from z $\sim$ 0 up to z $\sim$ 4. Figure from Gruppioni et al. (2013).

Gruppioni et al. (2013) using *PEP/HerMES Herschel* data were able to derive the total IR luminosity function (LF, Φ) up to z $\leq$ 4 (see Fig. 1.9). The total IR LF allows

a direct estimate of the total comoving IR luminosity density ($\rho_{\rm LIR}$) as a function of z. More recent results from Magnelli et al. (2013) argued that the ρ_{LIR} of LIRGs and ULIRGs significantly evolves with redshift as confirmed by previous works (e.g., Pérez-González et al. 2005; Caputi et al. 2007); in particular, a factor of $\sim$ 130 and $\sim$ 40 between z = 0 and z $\sim$ 1 has to be applied to these respective classes. Their results are consistent with that found by Murphy et al. (2011). Samples of galaxies selected at 24 μm have been used to investigate the population of IR bright galaxies at high-z. These studies used SED fitting methods to estimate the $L_{\rm IR}$ of these galaxies. They showed that the typical infrared luminosity has decreased by an order of magnitude from z $\sim$ 2 to the present (i.e., Pérez-González et al. 2005).

Assuming that $\rho_{\rm LIR}$ is totally produced by star formation it can be converted to SFR density ($\rho_{\rm SFR}$) using the Kennicutt (1998) relation. LIRGs are significant contributors to the ρ_{SFR} at $0.5 < z < 2$. The cosmological evolution of the global ρ_{SFR} is a fundamental element for understanding galaxy evolution from high to low redshift, since the growth of galaxies is closely traced by star formation. Numerous authors (i.e., Lilly et al. 1995; Madau et al. 1996; Steidel et al. 1999; Brinchmann et al. 2004; Bouwens et al. 2006; Hopkins & Beacom 2006) derived the value of its peak to be $\sim 10^{-1}$ $M_\odot$ yr^{-1} Mpc^{-3} in the redshift range z = 1 - 3. The galaxy evolutionary models support the hypothesis that this peak can be associated with the increased rate of galaxy mergers and interactions in that redshift range, inducing high SFRs, considering the merger process the main mechanism able to form massive galaxies (i.e., Di Matteo et al. 2005; Guyon et al. 2006; Sijacki et al. 2011).

Furthermore, local (U)LIRGs were initially assumed to be the local counterpart of high-z (U)LIRGs similar to those discovered by *Spitzer* and the more luminous sub-mm galaxies (SMGs; e.g. Blain et al. 2002; Tacconi et al. 2006). Indeed, the SMGs, detected by deep sub-mm (i.e., SCUBA; Holland et al. 1999) and radio surveys, represent a population of IR bright galaxies mainly located at z $\sim$ 2. They are powered by intense starbursts (from 100 up to 1000 $M_\odot$ yr^{-1}, i.e., 10 times more than ULIRGs) or Compton-thick, dust enshrouded AGN associated with the formation of super-massive black holes (Blain et al. 2002, Ivison 2002). According to their morphology (Chapman et al. 2003), their luminosity and SED (Frayer et al. 2003; Egami et al. 2004) they seem to be the high-z counterparts of the low-z LIRG and ULIRG galaxies (Blain et al. 2002; Chapman et al. 2005; Vieira et al. 2013). Recently, Arribas et al. (2012) found that, when using Hα as a tracer for both local and high-z samples, the size distributions for local (U)LIRGs and distant massive SFGs cover a similar range of values, although a higher frequency of compact objects is found locally. The differences are smaller than those reported using a variety of other

tracers as derived in Rujopakarn et al. (2011), who suggested that star-forming regions of local ULIRGs are significantly smaller (sub-kpc scale) than those found in their high-z counterparts, indicating that ULIRGs found locally are a different population from the high-z ULIRGs and SMGs (e.g., Muzzin et al. 2010).

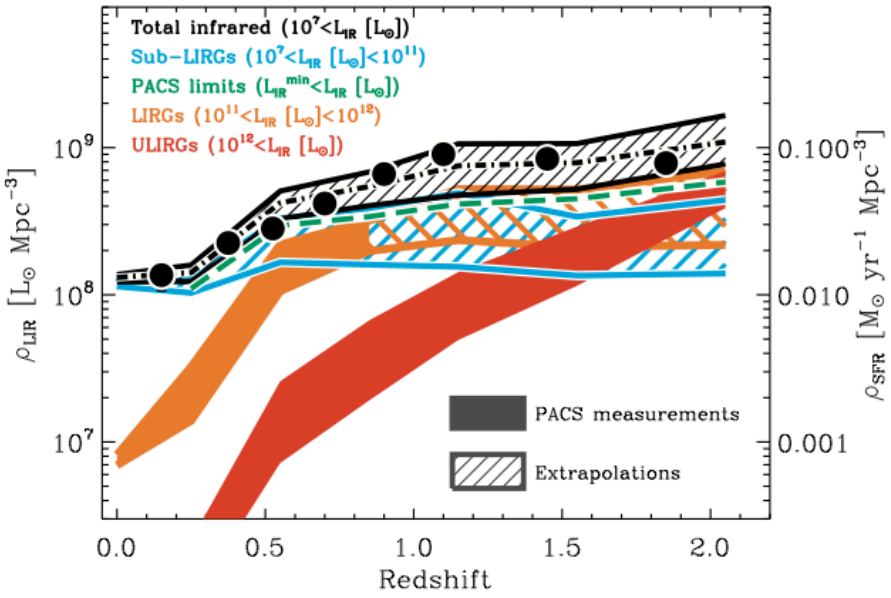

Figure 1.10: Evolution of the total comoving IR energy density (black area) and the relative contribution of the'fain' galaxies (light blue area), LIRGs (orange area) and ULIRGs (red area). The black dot-dashed line shows the best fit of the total comoving IR energy density, i.e., defined by integrating the IR LFs best-fitting our data points. The green dashed line shows the best fit of the comoving IR energy density of galaxies which are above the PACS detection limit of our ultradeep sub-sample (i.e., $> L_{IR}^{min}$). Black circles represent the total comoving IR energy density inferred by Gruppioni et al. (2013). The right axis of the panel shows the evolution of the obscured SFR density assuming that SFR [$M_\odot$ yr^{-1}] = 10^{-10} × L_{IR} [$L_\odot$] for a Chabrier (2003) IMF. Figure from Magnelli et al. (2013).

1.4.2 The *Main Sequence*

A different point of view has emerged recently, according to which the peak of the cosmic SFR density, ρ_{SFR}, is expected to follow the evolution of the cosmic gas inflow rate (i.e., Kereš et al. 2005; Genel et al. 2008; Conselice et al. 2013). This is suggested by the existence of a tight correlation between the stellar mass ($M_\star$) and star formation rate (SFR) in star-forming galaxies (SFGs; see Fig. 1.11), which define a main sequence (MS) that has been recognized in the local universe (Brinchmann et al. 2004; Salim et al. 2007; Peng et al. 2010), as well as at intermediate redshifts $0.5 < z < 3$ (i.e., Noeske et al. 2007; Elbaz et al. 2007; Daddi et al. 2007; Pannella et al. 2009; Rodighiero et al. 2010;

Karim et al. 2011), and beyond (i.e., Daddi et al. 2009; González et al. 2010).

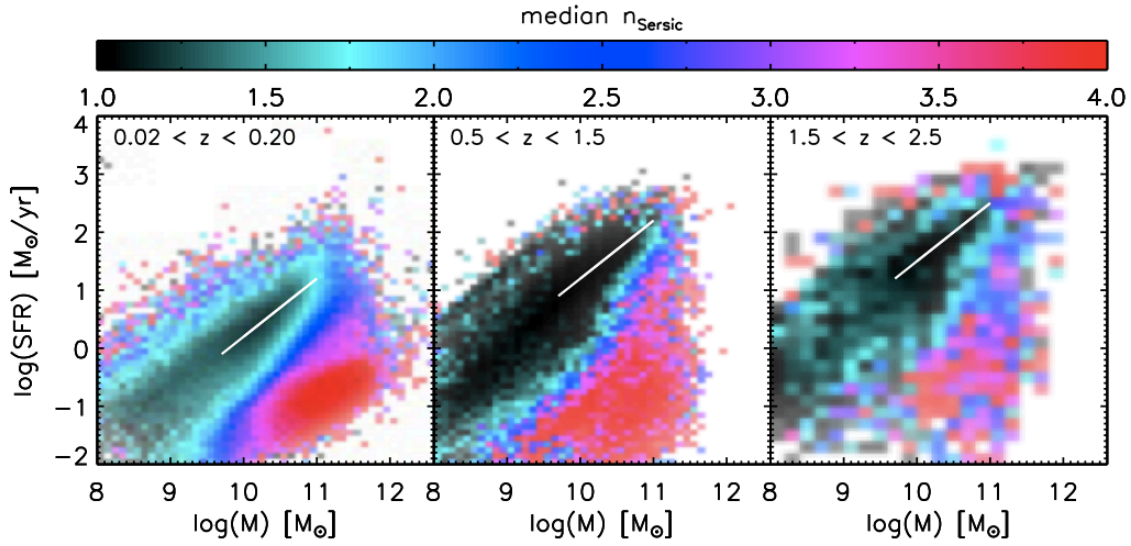

Figure 1.11: Surface brightness profile shape in the SFR-mass diagram. A 'structural main sequence' is clearly present at all observed epochs, and well approximated by a constant slope of 1 and a zero point that increases with lookback time (white line). While SFGs on the MS are well characterized by exponential disks, quiescent galaxies at all epochs are better described by de Vaucouleurs profiles. Those galaxies that occupy the tip and upper envelope of the MS also have cuspier light profiles, intermediate between MS galaxies and red and dead systems. Figure from Wuyts et al. (2011).

Among the SFGs, 'outliers' are known to exist, with very high specific SFR (sSFR = SFR/$M_\star$) compared to normal MS galaxies, such as local ULIRGs (e.g., Sanders & Mirabel 1996; Elbaz et al. 2007) and, at least, some of the SMGs at $1 < z < 4$ (e.g., Tacconi et al. 2008; Daddi et al. 2007, 2009; Takagi et al. 2008). They are galaxies in which the sSFR has been boosted by some event, possibly a (gas-rich) major merger (e.g., Mihos & Hernquist 1996; Di Matteo et al. 2008; Martig & Bournaud 2010; Bournaud et al. 2011), as suggested by local ULIRGs and SMGs (e.g., Dasyra et al. 2006a; Daddi et al. 2010; Genzel et al. 2010): we refer to them as *above*-MS galaxies. This tight correlation has thus invoked two distinct modes of star formation: the *normal star-forming mode* which describes galaxies lying on the SFR-$M_\star$ relation (i.e., MS galaxies) which evolve through secular processes such as gas accretion (e.g., Dekel et al. 2009a; Davé et al. 2010), while the *starburst mode* describes galaxies falling well above the MS (i.e., *above*-MS galaxies) which are likely driven by major mergers, representing a star-bursting period with respect to the galaxies on the MS[3] (Rodighiero et al. 2011; Wuyts et al. 2011).

Cold, filamentary streams of gas have been proposed on the basis of cosmological simulations as an efficient mechanism to penetrate the galaxies surrounding halos, and

[3]At $z \sim 2$ red and dead (passive) galaxies exist at these cosmic epochs and form a separate sequence below the MS of SFGs.

deposit new (or recycled) fuel for star formation (i.e., Kereš et al. 2005, 2009; Dekel & Birnboim 2006; Dekel et al. 2009a). Evidence from kinematics strongly supports such a continuous (i.e., non-major merger) triggering and maintenance of star formation for the bulk of SFGs (i.e., Genzel et al. 2008; Shapiro et al. 2008; Förster Schreiber et al. 2009, 2011). It is worth mentioning that this mechanism may play a significant role at $z \geq 2$ but might be less usual at $z < 1$ (i.e., Dekel et al. 2009a; Kereš et al. 2009).

While SFGs on the MS are well characterized by exponential disks, quiescent galaxies at all epochs are better described by de Vaucouleurs profiles which form a separate sequence below the MS of star-forming galaxies (see Wuyts et al. 2011). On the one hand, the *above*-MS galaxies show light profiles intermediate between MS galaxies and red and dead systems. As shown in Fig. 1.12, Gruppioni et al. (2013) derived the contribution of MS and *above*-MS galaxies to the total IR LF, Φ, in three different redshift bins. This indicates that the bright-end of the total IR LF is dominated by *above*-MS sources (yellow area). In the local universe (U)LIRGs are *above*-MS galaxies, but cover a similar SFR range with MS galaxies found at high-z.

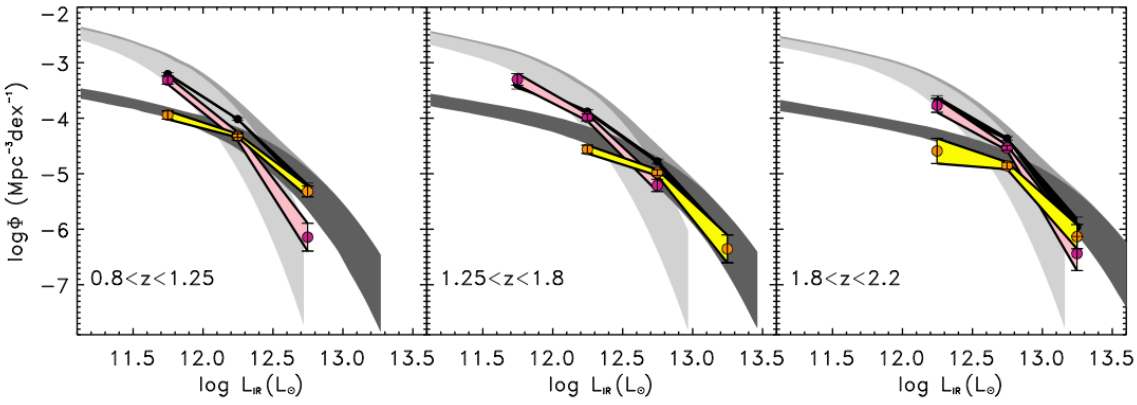

Figure 1.12: Contribution of MS ($\pm 1\sigma$ uncertainty region: pink shaded area) and *above*-MS ($\pm 1\sigma$ uncertainty region: yellow shaded area) galaxies to the total IR LF (black filled dots and area) in three different redshift bins. For comparison, the recent estimates of Sargent et al. (2012) in similar z-bins are shown as grey (total LF, in background), light grey (MS LF) and dark grey (above-MS LF) filled regions. Figure from Gruppioni et al. (2013).

1.5 Galaxy kinematics as a tool for constraining the galaxy evolution

1.5.1 Mergers vs. Cold accretion flows evolutionary scenarios

In the standard model of hierarchical galaxy assembly (or *standard hot model*) mergers are the dominant source of mass accretion and growth in massive high-redshift galaxies (i.e., Somerville et al. 2001; Cole et al. 2000). In this scenario, galaxies are assumed to form at the center of the dark matter halos as the baryonic gas cools (e.g., Baugh 2006), and their subsequent evolution is controlled by the merging histories of the halos containing them (e.g., Cole et al. 1994).

As derived from the observations, major merging is undoubtedly taking place at high-z (e.g., Tacconi et al. 2006, 2008): more recently, Kartaltepe et al. (2012), studying a sample of ULIRGs at z $\sim$ 2, found that the majority of the sources show signs of major mergers. These mechanisms support the hypothesis that gas-rich late-type galaxies can transform into gas-poor early-type E/S0 galaxies, as predicted using detailed simulations (Mihos & Hernquist 1996; Combes 2004; Conselice 2006). As a result of this framework, we expect to find galaxies characterized by complex and disturbed kinematics, such as distorted and asymmetric velocity field, as a proof of a strong ongoing interaction.

In the last few years many works found that most of the high-z galaxies show as a disk-like rotating velocity field pattern, although they appear to be turbulent (i.e., Lehnert et al. 2009; Burkert et al. 2010) as given by their high velocity dispersion (i.e., σ = 30-100 km s^{-1}) and low dynamical ratio (v/σ $<$ 1; Genzel et al. 2008; Förster Schreiber et al. 2009; Wisnioski et al. 2011). In order to explain their kinematic patterns in new models of disk formation at high-z, recent theoretical works (i.e., Kereš et al. 2005; Davé 2008; Genel et al. 2008; Dekel et al. 2009a; Ceverino et al. 2010), based on semi-analytical approaches and hydrodynamical simulations, have invoked a rapid but more continuous gas accretion via *cold flows* and/or minor mergers, which likely play an important role in driving the mass growth of massive star forming galaxy at high-z (e.g., Daddi et al. 2007; Elbaz et al. 2007; Noeske et al. 2007), able to supply gas directly to the center of the galaxies (i.e., Kereš et al. 2005; Ocvirk et al. 2008; Dekel et al. 2009a).

In particular, Ceverino et al. (2010) modeled cold and hot flows with a disk galaxy forming in the center. In Fig 1.13 the most 'unstable' case of simulated galaxy at z=2.3 is considered, with high gas fraction and low rotational velocity. They followed the formation and evolution of individual clumps in the disk gas, showing how the accretion quickly makes an unstable gas disk, which forms giant clumps that migrate to the center.

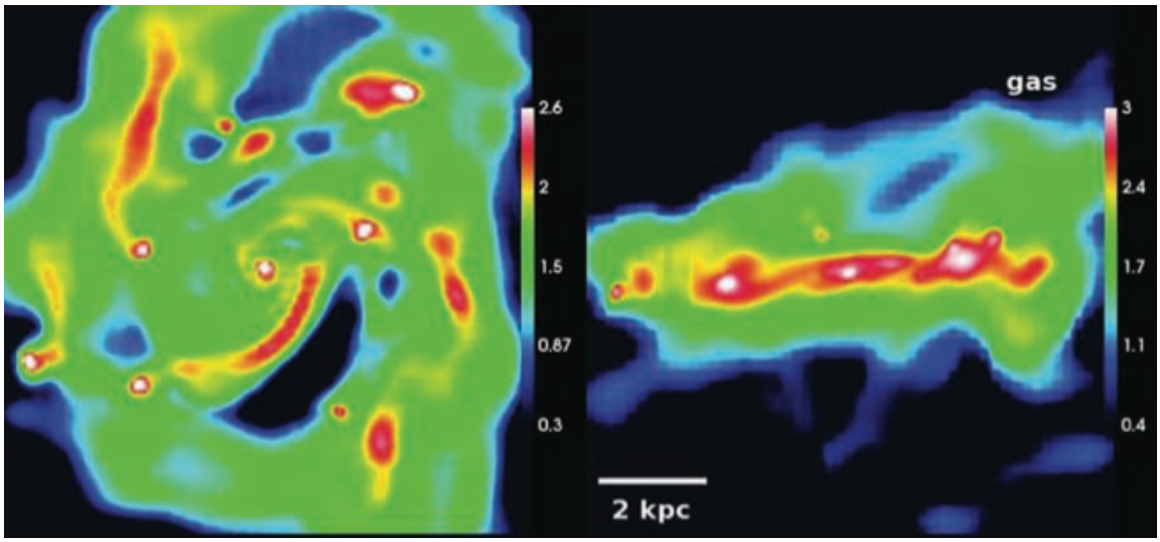

Figure 1.13: Gas surface density maps of galaxy A at z = 2.3. The side of each panel is 10 kpc. Shown are face-on views (left-hand panel) and edge-on views (right-hand panel). The disc is fragmented to elongated features and round dense clumps. Stars form at a high rate in the clumps and at the centre of the bulge. Most of the clumps are in situ to the disc and are not associated with dark-matter concentrations. The colour code was chosen to emphasize the clumps at the expense of saturating the highest densities. Figure from Ceverino et al. (2010).

One of the first evidences of the 'clumpy disk' picture came from the work of Förster Schreiber et al. (2006), observing the Hα emission of a sample of 14 BM/BX galaxies. They confirmed the presence of a significant fraction of galaxies with rotation fields characteristic of disks, large enough to be resolved in 0.5 arcsec seeing. Then, a large portion of the strongly SFGs at z = 1 - 3 does not show the disturbed kinematics expected according to the hierarchical model but is characterized by regularly rotating disks (e.g., Cresci et al. 2009; Epinat et al. 2009; Förster Schreiber et al. 2009; Gnerucci et al. 2011). This result has suggested that even stronger star formation may be fueled by the accretion of pristine gas from the halo and by dynamical instabilities within the massive gaseous disks (Genel et al. 2008; Dekel et al. 2009b; Bouché et al. 2010; Cresci et al. 2010).

Another evidence of this smooth accretion is provided by the 'inverse' metallicity gradient observed in rotationally-supported star-forming galaxies at z $\sim$ 3 (e.g., Cresci et al. 2010, see Fig. 1.14) as the central gas has been diluted by the accretion of primordial gas, as predicted by 'cold flow' models. The cold gas is essentially primordial such that it has a very low abundance of elements heavier than helium (metallicity). As it is funneled to the centre of a galaxy, it will lead the central gas having an overall lower metallicity than gas further from the centre, due to the fact that the gas further out has been enriched by supernovae and stellar winds, and not diluted by the primordial gas. Thus, the central star forming regions show a lower metallicity than less active ones, opposite to

what is seen in local galaxies. A more general relation supporting this scenario has been found between stellar mass $M_\star$, the gas-phase metallicity and SFR (i.e., the so-called Fundamental Metallicity Relation, FMR): this is a tight relation for SFGs that connects the three quantities and which does not evolve with redshift up to $z \sim 3$ (e.g., Mannucci et al. 2010).

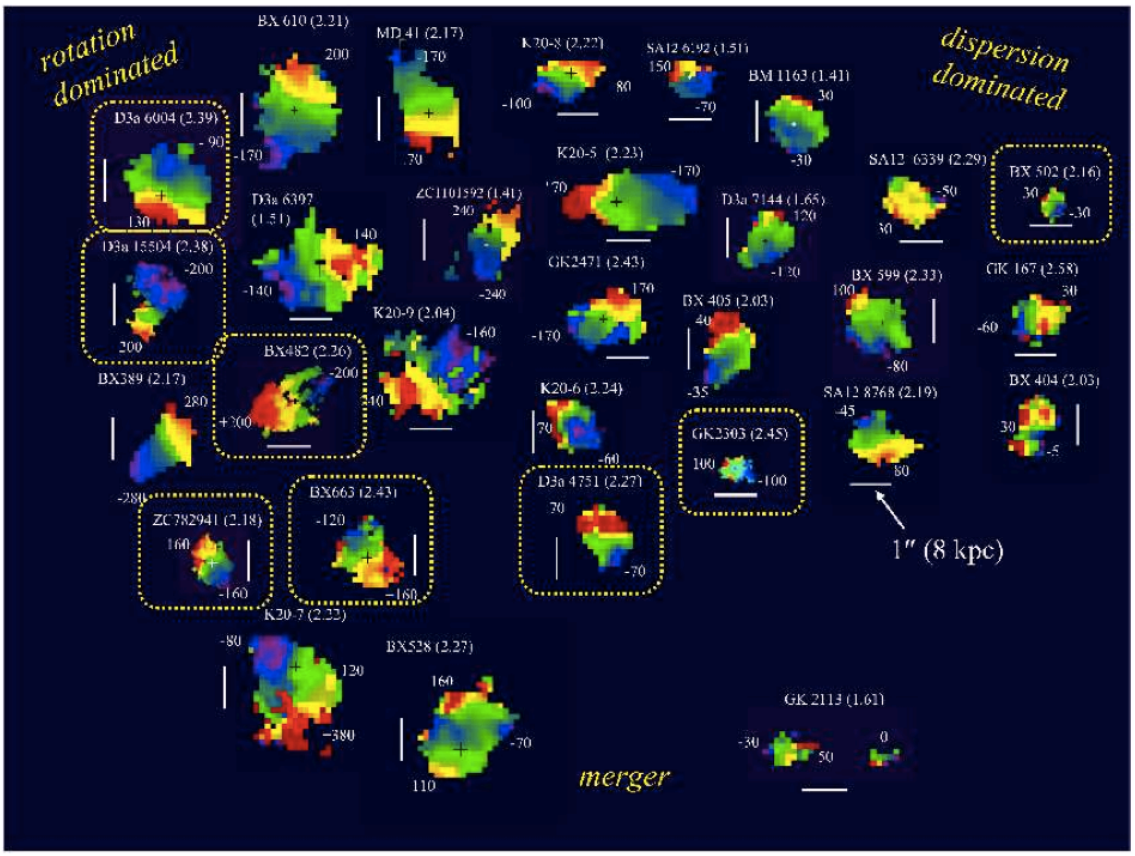

Figure 1.14: Velocity fields for 30 of the 62 galaxies of the SINS Hα sample. The color coding is such that blue to red colors correspond to the blueshifted to redshifted line emission with respect to the systemic velocity. The minimum and maximum relative velocities are labeled for each galaxy (in km s^{-1}). All sources are shown on the same angular scale; the white bars correspond to 1″, or about 8 kpc at $z = 2$. The galaxies are approximately sorted from left to right according to whether their kinematics are rotation-dominated or dispersion-dominated, and from top to bottom according to whether they are disk-like or merger-like as quantified by our *kinemetry* (Shapiro et al. 2008). Galaxies observed with the aid of adaptive optics (both at the 50 and 125 mas $pixel^{-1}$ scales) are indicated by the yellow rounded rectangles. Figure from Förster Schreiber et al. (2009).

A new scenario able to explain the formation of massive spheroidal galaxies has been proposed by Naab et al. (2009) using a high-resolution hydrodynamical cosmological simulation. In particular, for a more complete scenario, they combined the hierarchical cosmological models with continuos gas accretion with the merging of small stellar systems (minor mergers). Once these processes are taken into account the hierarchical models

favor a 'two-phase formation' process. In their simulation, a first phase (i.e., $2 < z < 6$) is dominated by *in situ* star formation from inowing cold gas (e.g., Dekel et al. 2009b) which produces a massive and dense stellar system with compact size (i.e., $r_{1/2} \leq 1$ kpc). This phase, characterized by the formation of the cores of ellipticals, is followed by a second one (i.e., $0 < z < 3$) with little *in situ* star formation but significant accretion of stellar material. This material can be stripped at larger radii and increases the size of the system with time.

The discrepancies between morphological and kinematical results have increased the importance of kinematic studies, since objects photometrically irregular in broad-band *HST* images show 'regular' kinematic maps (i.e., Bournaud et al. 2008; van Starkenburg et al. 2008; Puech 2010; Jones et al. 2010; Förster Schreiber et al. 2011; Genzel et al. 2011). Along with morphological and physical studies, the kinematic analysis of a system is the fundamental tool that allows a more complete understanding of the galaxy evolutionary scenarios.

1.5.2 The role of the IFS-based kinematics

The aforementioned results emphasize the crucial role of spatially- and spectrally-resolved investigations of galaxies at different redshifts, such as those based on integral field spectroscopy (IFS), in order to map their morphology and kinematics. They allow to reveal the kinematical status and internal processes at work within galaxies and more clearly understand the role of the dominant mechanisms involved at early epochs of galaxy formation. Indeed, one of the goal of high-z IFS surveys is the kinematical characterization of the different systems in order to distinguish and constrain modes of star-formation in high-z galaxies, such as the 'major merger' vs. 'steady cool gas accretion' scenarios, which are still under discussion (e.g. Genzel et al. 2001; Tacconi et al. 2008; Dekel et al. 2009b; Förster Schreiber et al. 2009; Lemoine-Busserolle & Lamareille 2010; Lemoine-Busserolle et al. 2010; Bournaud et al. 2011; Epinat 2011).

In particular, the 2D kinematic characterization of galaxies provides a powerful diagnostic:

i) to infer the main source of dynamical support (e.g., Puech et al. 2007; Epinat et al. 2009);
ii) to distinguish between relaxed virialized systems and merger events (e.g., Flores et al. 2006; Shapiro et al. 2008; Bellocchi et al. 2012, Arribas et al. 2014 submitted);
iii) to detect and characterize radial motions associated with feedback mechanisms, like outflows (e.g., Shapiro et al. 2009; Rupke & Veilleux 2013; Bellocchi et al. 2013;

Förster Schreiber et al. 2013);

iv) to infer fundamental galaxy quantities like dynamical masses (e.g., Colina et al. 2005; Bellocchi et al. 2012, 2013) among other topics.

1.5.3 Understanding the discrepancies in the *disk-merger* classifications: the importance of low-z (U)LIRGs observed with IFS

According to the *standard hot model* and *cold flows* scenarios of galaxy formation, *mergers* and *disk*-like galaxies are, respectively, the expected types of galaxies supposed to dominate in each scenario. A useful way to figure out which is the dominant scenario that drives the galaxy evolution at different cosmic epochs is to estimate the number ratio of *(rotating) disks* to *mergers* (i.e., disk/merger fraction). Some discrepancies can raise in classifying several kinds of galaxies in *disks/mergers* when applying different techniques. The first and most widely used technique was the visual morphological classification (e.g., Dasyra et al. 2008; Kartaltepe et al. 2010; Zamojski et al. 2011); then other classification methods, as the estimate of the asymmetry and clumpiness parameters (e.g., Conselice et al. 2003) and the use of the Gini-M_{20} plane (e.g., Lotz et al. 2008), have been considered as well. In the last decade, measures of galaxy kinematics (e.g., Genzel et al. 2008; Förster Schreiber et al. 2006, 2009) have increased their importance: in order to kinematically classify the systems, a visual (kinematic) classification has been applied by Flores et al. (2006) and Yang et al. (2008) to investigate the properties of the velocity fields of galaxies observed with IFS at intermediate redshift (i.e., $0.4 \leq z \leq 0.7$).

More recently, several authors (e.g., Shapiro et al. 2008; Gonçalves et al. 2010; Bellocchi et al. 2012; Swinbank et al. 2012) used the *kinemetry* methodology (Krajnović et al. 2006; see Fig. 1.15) which allows to quantify the kinematic asymmetries of several galaxy samples located at different redshifts from analyzing their velocity fields and velocity dispersion maps in order to distinguish and characterize *merging* and *non-merging (disk)* systems. Taking advantage of this methodology, Jesseit et al. (2007) and Kronberger et al. (2007) investigated the distortions in the velocity fields of simulated interacting *disk-merger* galaxies at different redshifts, between $z = 0$ - 1. Jesseit et al. (2007) tried to understand the possible formation of ellipticals by merger of disks. They found that disk merger remnant generated by equal mass (1:1) merger are rounder than 1:3 remnant. Then, the non-rotating subset of the representative SAURON sample (i.e., Emsellem et al. 2004) of local galaxies agrees with 1:1 merger simulation, while the rotating subset can be reproduced by the 3:1 merger remnant. On the other hand, Kronberger et al. (2007)

investigated resolution effects simulating distorted velocity fields at high-z: they found that distortions are still visible at intermediate redshift for large (Milky Way type) galaxies while for small (disc scale length $\sim$ 2 kpc) galaxies strong distortions are not visible in the velocity fields.

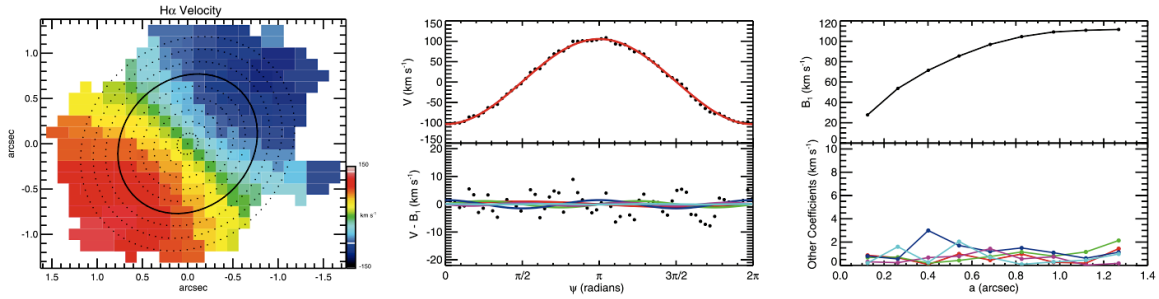

Figure 1.15: *Left:* Velocity field of a toy disk model with kinemetry ellipses overlaid. *Middle: Kinemetry* expansion as a function of angle along the solid ellipse. The top panel shows the measured velocities (black points) and the fit with the B1 coefficient (red line); the bottom panel shows the residuals from this fit (black points) and the higher order coefficients measured as a function of (A1, A2, B2, A3 and B3). *Right: Kinemetry* expansion from the middle panel, now shown for all ellipses as a function of semi-major axis length *a*. The top panel shows B1 as a function of a; this is the rotation curve. The bottom panel shows the strength of the higher order coefficients (same colors as above), all of which are negligible, as would be expected in an ideal disk. In this toy model, deviations from zero in these coefficients reflect the noise in the velocity field. Figure from Shapiro et al. (2008).

All of these different methods for identifying *disks* and *mergers* make difficult the comparison of the results, where a disagreement between the morphological and kinematical classifications cannot be ruled out. The study of the structure and kinematics of samples of local galaxies is necessary to understand the physical processes (e.g., SF, AGN, tidal torques, outflows) that these galaxies undergo, and their implications for understanding similar types of galaxies at high-z. Indeed, IFS data of local galaxies with SFR comparable to existing high-z samples could clarify the interpretation of high-z galaxy data. A sample of low-z galaxies would allow to test the methods applied to high-z galaxies on data with higher signal-to-noise-ratio and higher resolution (e.g., testing for mergers with *kinemetry* as in Shapiro et al. 2008; Bellocchi et al. 2012, Bellocchi et al. in prep.), and on artificially redshifted data. Until recently, IFS study of local galaxies has not been widely available, as historical work has relied on long-slit spectroscopy. However, the more recently surveys based on IFS such as ATLAS3D (Cappellari et al. 2011), GHASP (Epinat et al. 2010), CALIFA (Sánchez et al. 2012) and DISKMASS (Bershady et al. 2010) have now provided IFS of well-resolved, large, local galaxies but none of these samples includes galaxies with SFRs comparable to z $\sim$ 2 objects. Similar works based on IFS data (i.e., OSIRIS/Keck, Basu-Zych et al. 2009; Gonçalves et al. 2010) have focused on nearby objects (i.e., supercompact UV-luminous galaxies (ScUVLGs) and Lyman break analogs

(LBAs) at z $\sim$ 0.2). The morphology and kinematics of LBAs projected at high-z are similar to those of compact and dispersion-dominated z $\sim$ 2 galaxies (i.e., Basu-Zych et al. 2009). This suggests that galaxy interactions and/or mergers might also drive the dynamics of dispersion-dominated z $\sim$ 2 galaxies.

Despite their relevance, the number of spatially resolved kinematic studies based on low-z (U)LIRGs is rather limited. Most of the local IFS studies in the optical and near-IR bands have been focused on individual objects (e.g., Colina et al. 1999; Tecza et al. 2000; Arribas et al. 2001; García-Marín et al. 2006; Bedregal et al. 2009) or small samples (e.g., Monreal-Ibero et al. 2006; García-Marín et al. 2007, 2009), generally at the highest luminosity (i.e., ULIRGs). Other works with larger samples of (U)LIRGs have been focused on the excitation conditions of the extended ionized gas (i.e., Monreal-Ibero et al. 2010) and on establishing the structure of the ionized nebula as traced by the Hα line (i.e., Rodríguez-Zaurín et al. 2011). Colina et al. 2005 discussed IFS-based Hα velocity maps for 11 ULIRGs, finding that in general their kinematics is dominated by motions associated with tidal forces, rather than by an ordered rotation. Recently Westmoquette et al. (2012) have expanded this census by presenting optical (Hα) IFS of 18 ULIRGs observed with VIMOS at the Very Large Telescope (VLT), finding that a large fraction of objects is dominated by rotation.

The lack of 2D kinematical analysis applied to a large and local sample of galaxies with SFR comparable to those existing at high-z strengthen the relevance of this work which is aimed at kinematically characterizing the largest sample of local ($<$z$>$ = 0.022) (U)LIRGs analyzed so far, where the majority of the systems are in the less studied low-luminosity domain (i.e., LIRGs).

1.6 Thesis Project

In this introduction we have shown the relevance in studying local (U)LIRGs as they host the most extreme star-forming events in the present universe, commonly found at high-z. Although (U)LIRGs are rare in the local universe (e.g., Lagache et al. 2005), they are much more numerous at high-z and are relevant contributors to the whole past star formation beyond z $\sim$ 1 (e.g., Le Floc'h et al. 2005; Pérez-González et al. 2005, 2008). Local (U)LIRGs were initially assumed to be the local counterparts of high-z (U)LIRGs similar to those discovered by *Spitzer* and the luminous sub-mm galaxies (SMGs; e.g., Blain et al. 2002; Tacconi et al. 2006). More recently, several authors have suggested that high-z (U)LIRGs are scaled-up versions of lower luminosity low-z (U)LIRGs (e.g., Pope et al. 2006; Papovich et al. 2007; Elbaz et al. 2010, 2011; Nordon et al. 2010; Takagi et al. 2010), finding that in the local universe (U)LIRGs cover a similar SFR range than normal high-z SFGs (i.e., Wuyts et al. 2011).

Therefore, low-z (U)LIRGs offer a unique opportunity to study, at high linear resolution and signal-to-noise ratio (S/N), extreme SF events and compare them with those observed at high-z. Furthermore, their analysis would allow the methods and techniques applied to high-z galaxies to be tested. One relevant and interesting topic is the 2D kinematic characterization of high-z galaxies in order to better understand how galaxies assembled and evolved at early epochs. In particular, in the context of the proposed evolutionary scenarios, there is a strong interest in kinematically characterizing galaxies as *disks* and *mergers*, as their relative fraction is a key observational input to constrain different evolutionary scenarios, as we have seen in Sect. 1.5.

In this context I have developed the present project pursing the following goals:

(i) to obtain an atlas of ionized gas velocity fields and velocity dispersion maps which allow to characterize the 2D kinematic properties of this important galaxy population;

(ii) to obtain and discuss basic fundamental properties like dynamical support, dynamical masses, velocity amplitude, mean velocity dispersion as well as those related to the outflows, looking for dependencies with other galaxy properties, like L_{IR} and dynamical phase;

(iii) to compare and discuss these properties with those of other relevant low-z samples, either of similar (e.g., LBAs) or lower SFR (e.g., spirals and/or E/S0);

(iv) to study criteria that permit to characterize the evolutionary status of these systems by kinematically distinguishing between *disk* and *merger* systems and

(v) to perform simulated observations at high-z to anticipate the potential of the *NIRSpec* instrument on board of the *JWST* in this particular field.

To obtain our goals we will analyze a unique sample of local (U)LIRGs observed with VIMOS/VLT integral field unit (IFU) consisting of 38 local (U)LIRG systems (51 individual galaxies). This sample significantly enlarges previous samples both in number and characteristics. It shows a large variety of morphologies, which suggest different dynamical phases: from mostly isolated disks for low-luminosity LIRGs to a majority of merger remnants for ULIRGs. A large fraction (i.e., 31/38) of sources covers the less studied LIRG luminosity range and this is relevant for two main reasons. On the one hand, it complements previous studies focused on ULIRGs, filling the gap between the extreme cases and the general population of local star-forming galaxies (SFGs). On the other hand, as several authors suggested, high-z (U)LIRGs are scaled-up versions of low-z (U)LIRGs and many have similar SFRs (e.g., Pope et al. 2006; Papovich et al. 2007; Elbaz et al. 2010, 2011; Nordon et al. 2010; Takagi et al. 2010). Though the LIRG range represents the *core* sample, for parts of the analysis, we have also included a subsample formed by ULIRGs (i.e., 25 objects in total) observed with INTEGRAL/WHT (i.e., Colina et al. 2005; García-Marín et al. 2007, 2009) to expand the luminosity range. Then, our sample is ideal for pursuing our goals.

The chapter structure is as follows:

- **Sample selection, Observations and Data Treatment (Chapter 2):** In this chapter we introduce the VIMOS sample and how it has been selected. As mentioned above it encompasses a wide variety of morphological types, suggesting different dynamical phases (isolated spirals, interacting galaxies, ongoing- and post-mergers), nuclear excitations (HII, Seyfert and LINER) and luminosities (i.e., LIRGs and ULIRGs). Up to now, this is the largest sample for which a detailed 2D kinematic analysis is performed.

  We also briefly describe the instrumental set up used and the details of the observations. In *Data treatment* we explain the data reduction procedures and the specific analyses applied, such as the line fitting techniques and the 2D kinematic maps creation.

- **Spatially resolved kinematics in (U)LIRGs (Chapter 3):** We present the 2D kinematical characterization of the galaxy sample as traced by the Hα emission line. We obtain the 2D kinematic properties of distinct kinematic components (i.e., *narrow* and *broad*), deriving the basic kinematic properties (e.g., v^*/σ) able to characterize the kinematic status of the sample. The dynamical masses and the mass ratio in pairs have been determined and discussed as well, which allow to understand the dynamical state of the galaxies.

  A comparison with local samples of spirals, ellipticals and Lyman break analogs (LBAs) is also performed. This chapter has been published as Bellocchi et al. (2013) in A&A.

- **Distinguishing *disks* from *mergers* in local (U)LIRGs using *kinemetry*-based criteria (Chapter 4):**

  We focus on the *kinemetry* method (developed by Krajnović et al. 2006) along with the kinematic criteria proposed by Shapiro et al. (2008) as a way to quantify the relative importance of rotation with respect to the kinematic asymmetries in (U)LIRG systems. We then develop a new optimized criterium (i.e.,'weighted' method) in order to better distinguish between 'disks' and 'post-coalescence mergers'. We apply this new approach to our local sample of (U)LIRGs then studying its robustness against angular resolution effects (distance) on the basis of simulated observations of these objects at z=3 with the angular resolution of *NIRSpec/JWST*. This is important for the kinematical classification of high-z galaxies. Other, less studied, *kinemetry*-based criteria are proposed and discussed in App. C.

  The first part of this chapter has been published as Bellocchi et al. (2012) in A&A while the second one (i.e., the application of these methods to the whole sample) is in preparation (Bellocchi et al. 2014 in prep.).

- **Future work (Chapter 5):** In this chapter we present some preliminary analyses and results of topics that will be developed in more detail in the future. First, the spectral energy distribution (SED) analysis applied to a subsample of galaxies which allows to derive the stellar masses ($M_\star$) of these objects. These estimates enable a direct comparison with the dynamical mass values derived in this thesis and also the estimate of the gas mass in our local systems. This work has been carried out in collaboration with Prof. Stephane Charlot and Dr. Camilla Pacifici at the IAP (Paris) using the MAGPHYS tool (i.e., da Cunha et al. 2008).

We also present preliminary results based on the comparison between our local kinematic results and those derived for high-z SFGs in previous IFS-based works. This helps us to highlight the similarities (or discrepancies) in the kinematics between low-z (U)LIRGs and high-z SFGs.

- In the **Conclusions (Chapter 6)** we summarize the main results derived in this thesis.

  A series of appendices are presented at the end of these chapters in order to complement the analyses previously described. In App. A the kinematic maps of the whole sample are shown along with a detailed description of the peculiarities of each source; in App. B the near-infrared effective radius determination is discussed; in App. C other *kinemetry*-based criteria are described; then, in App. D the dynamical mass of the ULIRGs sample observed with INTEGRAL/WHT are derived using our approach.

Chapter 2

Sample Selection, Observations and Data Treatment

In this chapter we introduce the VIMOS sample and how it has been selected. It consists of 38 local ($z < 0.1$) LIRG and ULIRG systems (51 individual sources), which cover a large infrared luminosity range, although mainly focused on LIRGs. It encompasses a wide variety of morphological types, suggesting different dynamical phases (isolated spirals, interacting galaxies, ongoing- and post-mergers) and nuclear excitations (HII, Seyfert and LINER). Up to now, this is the largest sample for which a detail kinematic results are derived. In addiction, we also present the properties of an extended sample observed with INTEGRAL/WHT, which mainly covers the ULIRG range.

Furthermore, we briefly describe the instrumental set up used and the details of the observations. In Data Treatment we explain the data reduction procedures and the specific analyses applied, such as the line fitting techniques and the 2D kinematic maps creation.

2.1 The sample

The sample analyzed in this work is part of a large program aimed at characterizing the properties of local LIRGs and ULIRGs on the basis of optical and infrared integral field spectroscopic facilities both in the southern (VIMOS at Very Large Telescope (VLT), Le Fèvre et al. 2003), and northern hemisphere (INTEGRAL at William Herschel Telescope (WHT), Arribas et al. 1998; and PMAS at Calar Alto Observatory (CAHA), Roth et al. 2005). The complete survey contains about 70 galaxies covering the entire LIRG and ULIRG range, and representing the different morphologies (spirals, early interactions, advanced mergers, and post-mergers) observed in this class of objects. The VIMOS sample contains a total of 38 (U)LIRGs systems (51 individual galaxies) of the southern hemi-

sphere drawn from the Revised Bright Galaxy Sample (RBGS, Sanders et al. 2003). Of these systems 31 are LIRGs (i.e., $<L_{IR}> = 2.9 \times 10^{11}$ $L_{\odot}$) with a mean redshift of 0.024 (corresponding to D $\sim$ 100 Mpc), and the remaining seven are ULIRGs (i.e., $<L_{IR}> = 1.6 \times 10^{12}$ $L_{\odot}$) with a mean redshift of 0.069 (D $\sim$ 300 Mpc; see Table 2.1). Therefore, this sample includes a good representation of the relatively less studied LIRG luminosity range. It encompasses a wide variety of morphological types, suggesting different dynamical phases (isolated spirals, interacting galaxies, and ongoing- and post-mergers), and nuclear excitations (HII, Seyfert, and LINER). Some objects have evidence in their optical spectra of hosting an AGN, showing high [NII]/Hα values and/or broad Hα emission lines (e.g., IRAS F05189-2524, IRAS F21453-3511; Monreal-Ibero et al. 2010, Arribas et al. 2012). The sample is not complete either in luminosity or in distance. However, it covers well the relevant luminosity range and is representative of the different morphologies within the (U)LIRG phenomenon.

2.1.1 The morphological classification

The morphology class was derived using ground-based images (i.e., Digital Sky Survey (DSS) and additional archival Hubble Space Telescope (HST) images when available). The sources have been morphologically classified following a simplified version of the scheme proposed by Veilleux et al. (2002), with three main classes instead of five (see Arribas et al. 2008; Rodríguez-Zaurín et al. 2011 for further details, also see Fig. 2.1). Briefly, the three morphological classes are defined as follows:

- Class 0: objects that appear to be single isolated galaxies, with a relatively symmetric disk morphology and without evidence for strong past or ongoing interaction (hereafter *disk*).
- Class 1: objects in a pre-coalescence phase with two well-differentiated nuclei separated a projected distance $>$ 1.5 kpc. For these objects, it is still possible to identify the individual merging galaxies and their corresponding tidal structures due to the interaction (hereafter *interacting*).
- Class 2: objects with two nuclei separated a projected distance $\leq$ 1.5 kpc or a single nucleus with a relatively asymmetric morphology suggesting a post-coalescence merging phase (hereafter *merger*).

In Table 2.1 we present the main properties of the sample. In some cases the properties of individual galaxies in multiple systems could be inferred separately and were therefore treated individually.

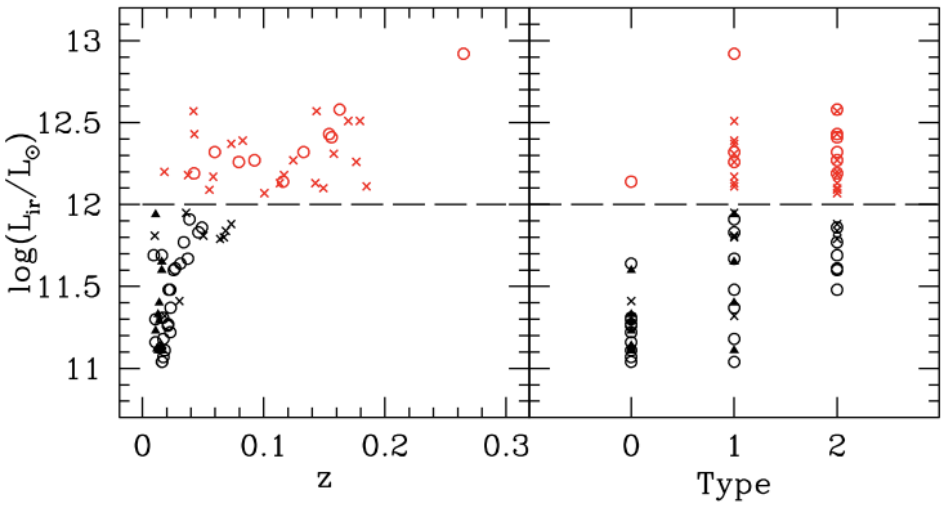

Figure 2.1: Distribution of the objects of the sample in the luminosity - redshift (left) and luminosity - morphological/merging type (right) planes, where 0 indicates a single isolated object, 1 interacting pairs in a pre-coalescence phase, and 2 a single system with evidence of having suffered a merger (i.e. post-coalescence phase). Circles correspond to the current VIMOS sample, whereas crosses and filled triangles are the INTEGRAL and PMAS samples, respectively (see text). The dashed line divides the sample in LIRGs (black symbols) and ULIRGs (red symbols) (see Arribas et al. 2008).

As part of the analysis, additional galaxies with available IFS data have been included to increase the number of systems in the ULIRG luminosity range. These data (Colina et al. 2005; García-Marín et al. 2007, 2009) correspond to our own observations taken with INTEGRAL/WHT. The main properties of this ULIRG sample are listed in Tab. 2.1.1.

Table 2.1: General properties of the (U)LIRG sample.

ID1 IRAS (1)	ID2 Other (2)	z (3)	D (Mpc) (4)	scale (pc/″) (5)	log L_{IR} ($L_\odot$) (6)	Class (7)	seeing (″) (8)	Notes (9)
F01159-4443	ESO 244-G012	0.022903	99.8	462	11.48 (N)	1	1.0	a,d
F01341-3735	ESO 297-G011	0.017305	75.1	352	11.18 (G11:10.99)	1	1.0	a,d
F01341-3735	ESO 297-G012	0.017305	75.1	352	11.18 (G12:10.72)	1	0.8	a,d
F04315-0840	NGC 1614	0.015983	69.1	325	11.69	2	1.2	
F05189-2524		0.042563	188.2	839	12.19	2	1.6	
F06035-7102		0.079465	360.7	1501	12.26	1	1.0	
F06076-2139		0.037446	165	743	11.67 (N)	1	1.2	a,d
F06206-6315		0.092441	423.3	1720	12.27	1	0.6	
F06259-4780	ESO 255-IG007	0.038790	171.1	769	11.91(N)	1	0.9	b,d
F06295-1735	ESO 557-G002	0.021298	92.7	431	11.27	0	1.6	
F06592-6313		0.022956	100	464	11.22	0	1.1	
F07027-6011	AM 0702-601	0.031322	137.4	626	11.64 (N:11.04)	0	1.1	a,d
F07027-6011	AM 0702-601	0.031322	137.4	626	11.64 (S:11.51)	0	1.1	a,d
F07160-6215	NGC 2369	0.010807	46.7	221	11.16	0	0.6	
08355-4944		0.025898	113.1	521	11.60	2	1.1	
08424-3130	ESO 432-IG006	0.016165	70.1	329	11.04 (S)	1	2.1	a,d
F08520-6850	ESO 60-IG016	0.046315	205.4	909	11.83	1	0.9	
09022-3615		0.059641	267	1153	12.32	2	2.0	
F09437+0317	IC-563 / 564	0.020467	89	415	11.21 (N:10.99)	1 (0)	0.7	a,c,d
F09437+0317	IC-563 / 564	0.020467	89	415	11.21 (S:10.82)	1 (0)	0.8	a,c,d
F10015-0614	NGC 3110	0.016858	73.1	343	11.31	0	1.1	
F10038-3338	ESO 374-IG032	0.034100	149.9	679	11.77	2	0.9	
F10257-4339	NGC 3256	0.009354	40.4	192	11.69	2	1.0	
F10409-4556	ESO 264-G036	0.021011	91.4	425	11.26	0	1.1	
F10567-4310	ESO 264-G057	0.017199	74.6	350	11.07	0	0.9	
F11255-4120	ESO 319-G022	0.016351	70.9	333	11.04	0	0.8	
F11506-3851	ESO 320-G030	0.010781	46.6	221	11.30	0	0.8	
F12043-3140	ESO 440-IG058	0.023203	101.1	468	11.37 (S)	1	1.0	a,d
F12115-4656	ESO 267-G030	0.018489	80.3	375	11.11	0	1.4	
12116-5615		0.027102	118.5	545	11.61	2 (0)	1.2	
F12596-1529	MCG-02-33-098	0.015921	69.0	324	11.07	1	0.8	
F13001-2339	ESO 507-G070	0.021702	94.5	439	11.48	2 (0/1)	1.2	
F13229-2934	NGC 5135	0.013693	59.3	280	11.29	0	0.9	
F14544-4255	IC 4518	0.015728	68.2	320	11.11 (E:10.80)	1	0.7	a,d
F14544-4255	IC 4518	0.015728	68.2	320	11.11 (W:10.80)	1	0.9	a,d
F17138-1017		0.017335	75.2	352	11.41	2 (0)	0.5	
F18093-5744	IC 4687/4686/4689	0.017345	75.3	353	11.57 (N:11.47)	1	0.8	b,d
F18093-5744	IC 4687/4686/4689	0.017345	75.3	353	11.57 (C:10.87)	1	2.1	b,d
F21130-4446		0.092554	423.9	1722	12.09	2	0.7	
F21453-3511	NGC 7130	0.016151	70.0	329	11.41	2	0.6	
F22132-3705	IC 5179	0.011415	49.3	234	11.22	0	1.3	
F22491-1808		0.077760	352.5	1471	12.17	1	1.1	
F23128-5919	AM 2312-591	0.044601	197.5	878	12.06	1	1.8	

Continues on next page

Continued from previous page.

Col (1): Object designation in the Infrared Astronomical Satellite (IRAS) Faint Source Catalog (FSC). Col (2): Other identification. Col (3): Redshift from the NASA Extragalactic Database (NED). Col (4): Luminosity distance assuming a ΛDCM cosmology with $H_0 = 70$ km s^{-1} Mpc^{-1}, $\Omega_M = 0.3$, and $\Omega_\Lambda = 0.7$, using the E. L. Wright Cosmology calculator, which is based on the prescription given by Wright (2006). Col (5): Scale. Col (6): Infrared luminosity (L_{IR}= L(8-1000) μm) in units of solar bolometric luminosity, calculated using the fluxes in the four IRAS bands as given in Sanders et al. (2003) when available. Otherwise, the standard prescription given in Sanders & Mirabel (1996) with the values in the IRAS Point and Faint Source catalogs was used. Col (7): Morphological class defined as follows: 0 identifies *isolated* objects, 1 *pre-coalescence* systems, and 2 stands for *merger* objects. For those objects for which the morphological classification is uncertain, the various possible classes are shown in the table with the preferred morphological classification indicated in the first place and the alternative classification within brackets (see text for further details). Col (8): Average seeing during the observations. Col (9): Notes with the following code: (a) System composed of two galaxies. (b) System composed of three galaxies. (c) There are two VIMOS pointings for the northern source. (d) Interacting system (i.e., see notes *a* and *b*) for which the total infrared luminosity L_{IR} could be approximately assigned among the members of the system according to the MIPS/*Spitzer* photometry*. (The estimations for the individual sources are shown in parentheses in Col. (6)). When the whole infrared luminosity contribution is assigned only to one of the sources of the system, either *Spitzer* data at 24 μm are not available or the limited angular resolution does not allow the different galaxies to be separated. Each source is identified according to its position in the VIMOS FoV according to N,S,C E and W which stand for the northern, southern, central, eastern, and western object, respectively. *MIPS/*Spitzer* data are available at the NASA/IPAC Infrared Science Archive (http://irsa.ipac.caltech.edu).

Table 2.2: Main properties of the INTEGRAL/WHT ULIRG sample.

ID1 IRAS (1)	z (2)	D (Mpc) (3)	scale (pc/″) (4)	log L_{IR} ($L_\odot$) (5)	Notes (6)
06268+3509	0.17	813	2895	12.51	
06487+2208	0.144	682	2522	12.57	
F08572+3015 NW	0.05835	259	1130	12.15*	b
F08572+3015 SE	0.05835	259	1130	12.15*	b
11087+5351	0.143	677		12.13	
12112+0305 NE	0.07332	330	1395	12.35*	b
12112+0305 SW	0.07332	330	1395	12.35*	b
12490-1009	0.101	465	1854	12.07	
13156+0435	0.113	525	2058	12.13	
14060+2919	0.117	545	2113	12.18	
14348-1447 NE	0.08273	378	1556	12.37*	b
14348-1447 SW	0.08273	378	1556	12.37*	b
15206+3342	0.12441	580	2232	12.25	a
15250+3609	0.05516	245	1072	12.07	a
16007+3743	0.185	898	3100	12.11	
17208-0014	0.04281	190	844	12.41	a
18580+6527	0.176	850	2986	12.26	
Arp 220	0.01813	78	368	12.17	c
Arp 299	0.010	43	205	11.81	
Mrk 231	0.04217	186	832	12.55	a
Mrk 273	0.03778	167	749	12.16	c
Mrk 463	0.05	222	9984	11.81	

Col (1): object designation in the Infrared Astronomical Satellite (IRAS) Faint Source Catalog (FSC). Col (2): redshift taken from the NASA Extragalactic Database (NED). Col (3): luminosity distance assuming a ΛDCM cosmology with $H_0 = 70$ km s^{-1} Mpc^{-1}, $\Omega_M = 0.3$, and $\Omega_\Lambda = 0.7$, using the E. L. Wright Cosmology calculator, which is based on the prescription given by Wright (2006). Col (4): scale. Col (5): infrared luminosity (L_{IR} = L(8-1000) μm) in units of solar bolometric luminosity, calculated using the standard prescription given in Sanders & Mirabel (1996). Col (6): notes with the following code (see Colina et al. 2005 for further details): (a) single nucleus. (b) interacting pair with angular separation larger than 1″. (c) double nucleus with angular separation less than 1″.
*The infrared luminosity refers to the whole system.

2.2 Observing Techniques

The general term 3D-spectroscopy refers to those techniques that allow to obtain spatially-resolved spectra over a two dimensional field. In an extragalactic context, each point of the galaxy (α, δ) has an associated spectrum (λ) and all the information are stored in a two dimensional detector. Mainly, three kinds of 3D spectroscopy methods are used, as the *long-slit scanning*, *Fabry-Pèrot interferometry* and *integral field spectroscopy (IFS)*. The transition from long-slit to IFS techniques (also known as 3D spectroscopy) allowed to avoids the loss of light, generally affecting the narrow slit geometry, and to require less observing time then that needed by long slit spectroscopy.

The main idea for IFS is to divide the telescope focal plane into a number of elements, which can be achieved using lenslets, fibers, slicers or combination of them and to create a pseudo-slit to disperse the light and which is recorded on a two dimensional detector. Figure 2.2 shows an illustration of the integral field spectroscopy techniques from of Allington-Smith 2007. The main objective of IFS is to simultaneously produce a spectrum of every spatial element (referred to as 'spaxel') in a field of view (FoV), with the spatial sampling and size of FoV determined by the instrument. The output for the data reduction process is a data cube with 2-dimensional spatial information and spectral information as a third axis. These 3D-techniques are thus a good compromise between resolution, exposure time and homogeneity of the data.

We briefly mention the four most important techniques to resample a telescope focal plane to be arranged onto the detector, giving examples of some current facilities working with them:

- **Lenslet Array:** SAURON/WHT (Spectroscopic Areal Unit for Research on Optical Nebulae) is one of the current instrument working with this technique, with a large FoV and a design similar to that of TIGER/CFHT (or OASIS/CFHT).

- **Fiber Array:** INTEGRAL/WHT and PPAK/CAHA both use this configuration.

- **Lenslets + Fiber:** The most popular instruments that today make use of this technique are PMAS/CAHA, VIMOS/VLT and FLAMES/VLT, and GMOS. While a normal long-slit spectrograph on a 4-meter class telescope could produce a few tens of spectra per night of observation, today a spectrograph like VIMOS can obtain several thousands of spectra per night.

- **Image Slicer:** SINFONI/VLT and MUSE/VLT are based on this design (i.e., Eisenhauer et al. 2003).

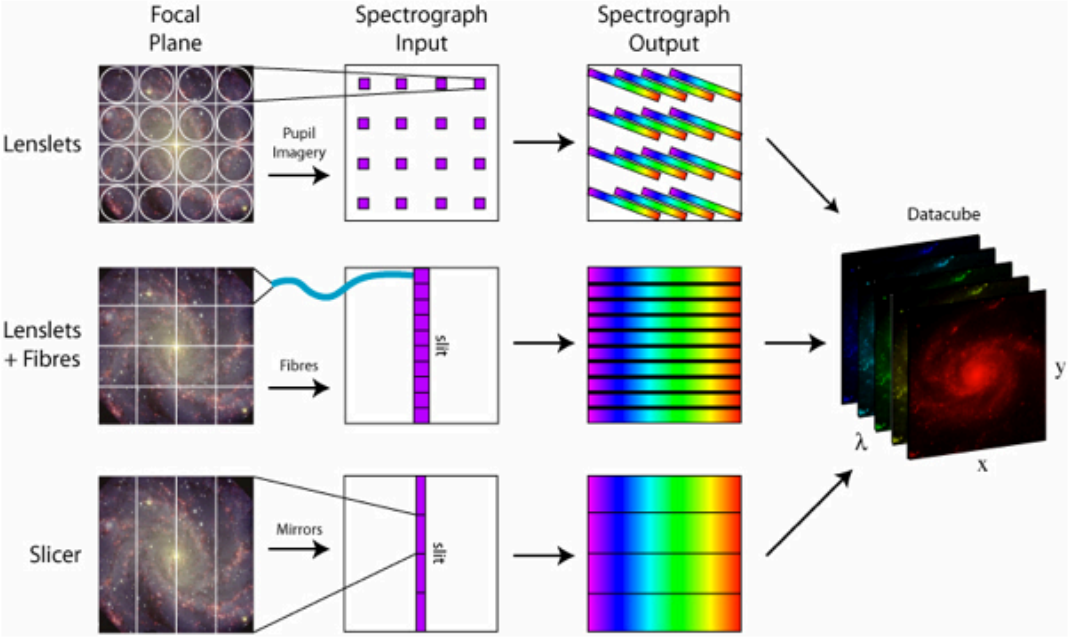

Figure 2.2: The main integral field spectroscopy techniques. Credit: M. Westmoquette, adapted from Allington-Smith 2007.

In the present day, larger IFS surveys are being carried out as the Calar Alto Legacy Integral Field Area (CALIFA) survey 5 (Sánchez et al. 2012) and the ATLAS3D survey 6 (Cappellari et al. 2011), both aiming at characterizing the local galaxy population in great detail with a total of 600 (CALIFA) and 260 (ATLAS3D) targeted galaxies.

A more detailed discussion of the IFU techniques can be found in Ren & Allington-Smith (2002) and reference therein. In the next section we will focus on the VIMOS instrument configuration.

2.3 VIMOS at Very Large Telescope

The **V**isible **M**ulti-**O**bject **S**pectrograph (VIMOS) instrument on the 8.2-m VLT is a visible (0.36 - 1.0 μm) wide field imager and multi-object spectrograph mounted on the Nasmyth focus B of UT3 Melipal. It is made of 4 quadrants of 7′ x 8′ each separated by a gap of $\sim$ 2′ with a 0.205″ pixel size. A schematic opto-mechanic layout is shown in Fig. 2.3.

VIMOS operates in three different modes, allowing imaging and multi-object or IFS from low to high resolution regimes (i.e., R $\sim$ 200 - 2500). This work has been done using IFS in high resolution mode such that we will focus on this mode giving some more details. In particular, the integral field unit consists of 6400 (80 $\times$ 80) fibers coupled to

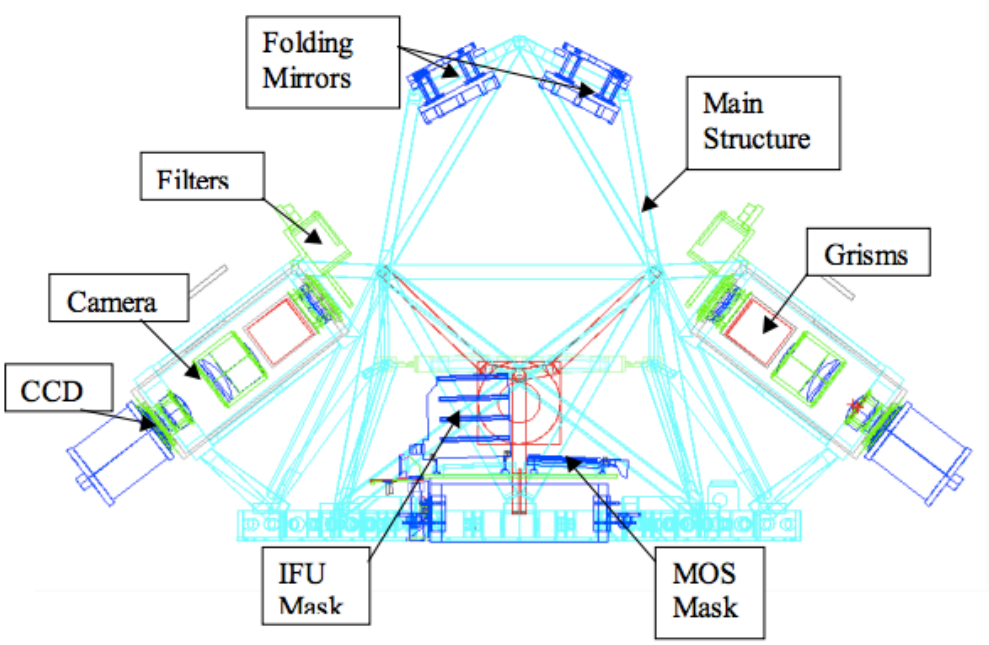

Figure 2.3: VIMOS Opto-Mechanical layout, top view.

microlenses, with a choice of two spatial samplings (or magnifications; i.e., 0.67″ or 0.33″ per fiber), able to do observations in low (R $\sim$ 200, i.e., LR) or high (R $\sim$ 2500, i.e., MR or HR) resolution modes. A masking-shutter allows to select only the central region of the IFU FoV (i.e., quadrants #2 in Fig. 2.4, delimited by the yellow lines, each of them composed by 20 $\times$ 20 fibers), such that higher spatial resolution translates to a smaller FoV. Thus, the sky area accessible to an IFU with VIMOS observation is a function of the chosen spectral and spatial samplings (i.e., Zanichelli et al. 2005): at low spectral resolution (i.e., shutter OFF, 80$\times$80 fibers) the FoV is 54″$\times$54″ with a spatial sampling of 0.67″/fibre, while a FoV of 27″$\times$27″ is reached with a spatial sampling of 0.33″/fibre (see Fig. 2.4). In Tab. 2.3 the FoV, the spectral resolution along with other spectral characteristics of the different combination of grisms/filters for the IFU mode for a pixel scale of 0.67″ are listed.

2.3.1 The observations

In this work the observations of the (U)LIRG sample (see Sect. 2.1) were carried out in service mode during three periods (i.e., P76, P78 and P81). They cover the spectral range 5250-7400 Å with the high-resolution grating GG435 ('HR-orange' mode) with a mean spectral resolution of 3470 (dispersion of 0.62 Å pix^{-1}) and a mean seeing of 1.05″ (see

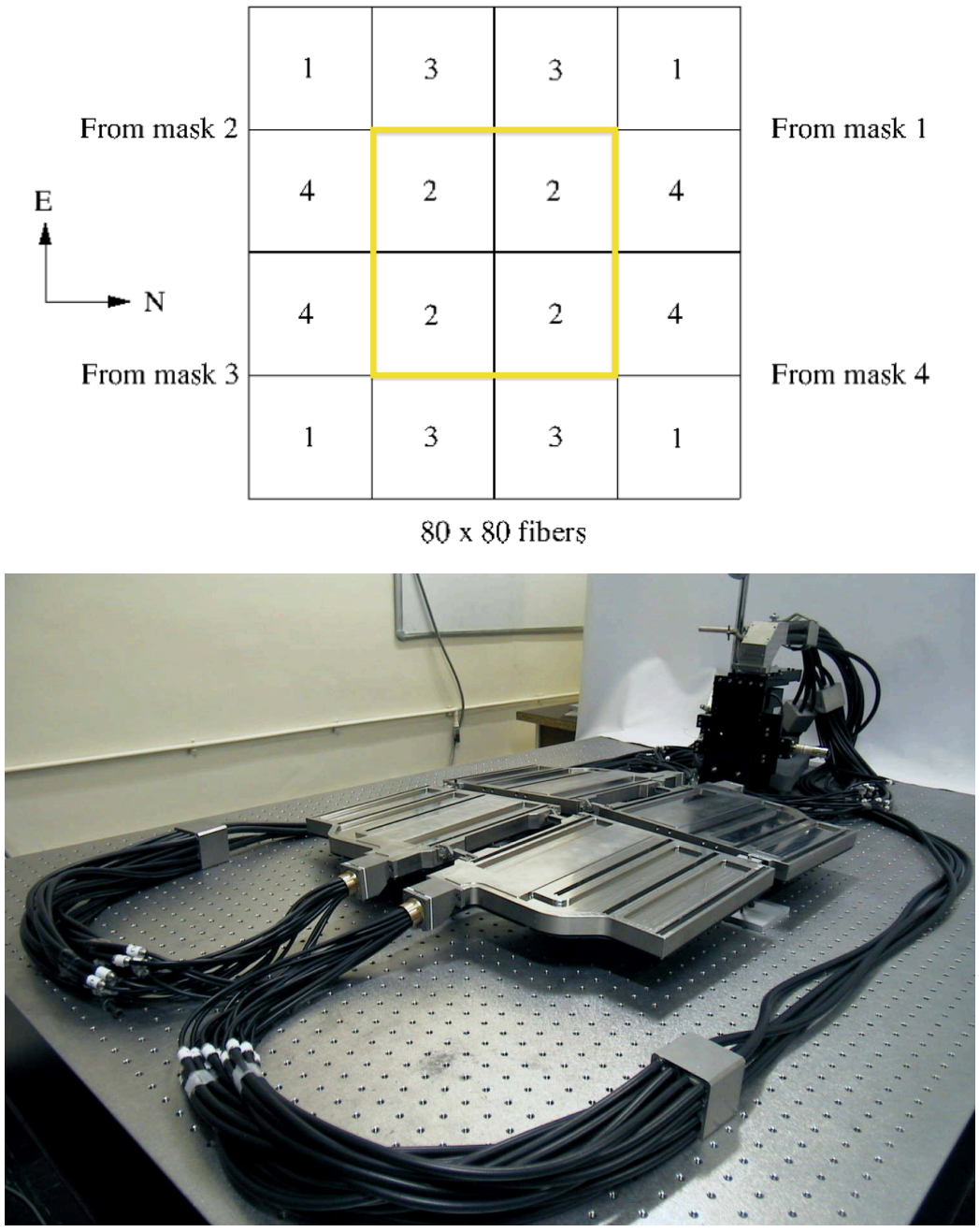

Figure 2.4: *Top:* IFU head with details of the fiber modules. Each quadrant (or mask) is made of four pseudo-slits, which are identified by the number # 1, 2, 3, 4. Each pseudo-slit is composed by 20 $\times$ 20 fibers. The IFU head is then composed by 80$\times$80 fibers. North is to the right, East to the top. *Bottom:* Integral field unit of VIMOS. The four quadrants are shown along with the four pseudo-slit for each quadrant. This image has been taken from *www.oamp.fr/virmos* web page.

Table 2.3: Spectral characteristics for the IFU mode for a pixel scale of 0.67″.

Grism	Filter	Wavelength range (Å)	FoV	Shutter	Spec. Res. $R = \lambda/\Delta\lambda$	Dispersion (Å pix^{-1})
LR blue	OS-blue	4000 - 6700	54″ × 54″	OFF	220	5.3
LR red	OS-red	5900 - 9150	54″ × 54″	OFF	260	7.3
MR	GG475	4900 - 10150	27″ × 27″	ON	720	2.5
HR blue	-	3700 - 5350	27″ × 27″	ON	1440	0.71
HR orange	GG435	5250 - 7400	27″ × 27″	ON	2650	0.6
HR red	GG475	6450 - 8600	27″ × 27″	ON	3100	0.6

Tab. 2.1). The FoV in this configuration is 27″×27″, having a *spaxel* scale of 0.67″ per fiber (i.e., 1600 spectra are obtained simultaneously from a 40×40 fiber array). A square 4 pointing dithering pattern was used. With a relative offset of 2.7″ (i.e., 4 spaxels), this pattern provides an effective FoV of 29.5″×29.5″. The exposure time per pointing ranges from 720 to 850 seconds, so that, the total integration time per galaxy is between 2880 and 3400 seconds.

2.4 Data reduction

In this section we describe the data reduction steps along with the procedures used to reduce the data. The data reduction of the two-dimensional fiber spectra has been performed using a combination of the pipeline provided by ESO (version 2.0.2) via `EsoRex` (version 3.5.1) and a set of customized `IRAF` and IDL scripts (i.e., some details are given in Arribas et al. 2008). In a first step the pipeline is used to perform the basic reduction steps to the individual quadrants (i.e., bias subtraction, spectra tracing and extraction, correction of fiber and pixel transmission, and relative flux calibration; Sect. 2.4.1). Then, once the individual quadrants are partially reduced, they are combined together into a single data-cube (Sect. 2.4.2). In what follows, these steps are discussed and described in detail.

2.4.1 Basic reduction steps

A sketch of a pseudo-slit (i.e., corresponding to one of the pseudo-slits #2 in Fig. 2.4) formed by the fibers at the spectrograph entrance and a raw image as those obtained at the telescope are shown in Fig. 2.5. The x-axis represents the dispersion direction, whereas the y-axis represents the spatial one: a 2D detector is able to store 3D information, where each spectrum comes from a different region of the observed galaxy.

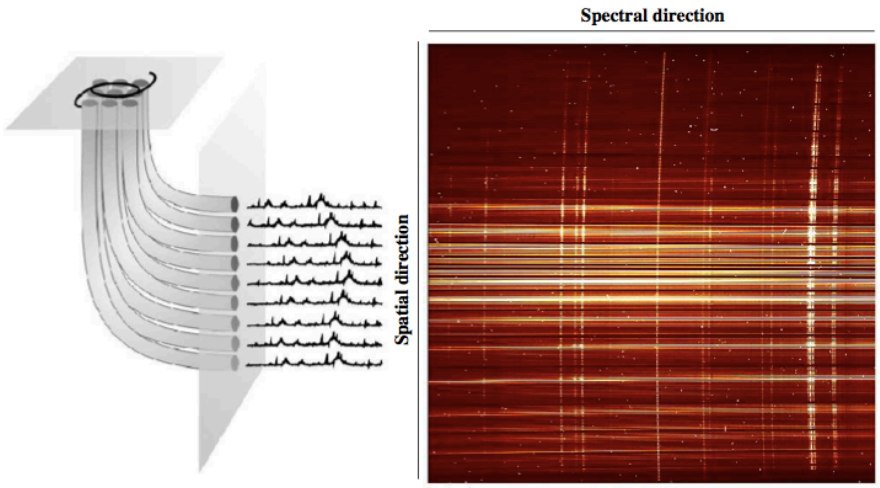

Figure 2.5: **Left:** The galaxy light is collected in the focal plane by the fiber bundle; the fibers are reordered forming a pseudo-slit and then dispersed by the spectrometer. **Right:** Raw image as obtained at the telescope. The spectral and spatial directions are indicated.

1. **The Bias (subtraction)**

   The *bias* is an image obtained from a CCD with no actual exposure time: its current is not zero and this is just an off-set due to the electronics. It has to be subtracted in the reduction of all the images (i.e., flat-field, arc lamp, standard star and scientific exposures) and can be subtracted in two different ways:

   - subtracting the mean of the overscan section (i.e., a region of the CCD not exposed to the light);
   - averaging zero exposure time frames and subtracting the entire image to the data frames. The differences in the values are due to the electronic structure present in the *bias*, which is not constant over all the CCD. To eliminate those local artifacts the combined image generated by using the `IRAF vmbias` recipe was used for the *bias* correction. This method is useful when the bias have some structures.

2. **Spectra tracing and extraction**

   The calibration files have to be created once all the frames (i.e., flat-field, arc lamp, standard star and scientific exposures) have been bias-subtracted. Since the light coming from the astronomical source is collected by the fibers and dispersed onto the CCD, the information coming from each fiber has to be individually identified and traced in order to preserve the full spatial and spectral information provided by

IFS. By fiber identification we mean the correct association to a fiber position on the IFU mask to a corresponding position on the CCD. The VIMOS pipeline recipe used in this step is called `vmifucalib`. With this routine the input flat-field image is processed to determine the spatial extraction mask (i.e., `ifu_trace.fits`) and the fiber-to-fiber relative transmission correction (i.e., `ifu_transmission.fits`). The flat-field spectra are obtained using a lamp with a continuos spectrum (or sky emission). The wavelength calibration file (i.e., `ifu_idu.fits`) is derived using the arc lamp exposures, characterized by a rich spectrum of narrow emission lines with well known wavelengths (see Fig. 2.6).

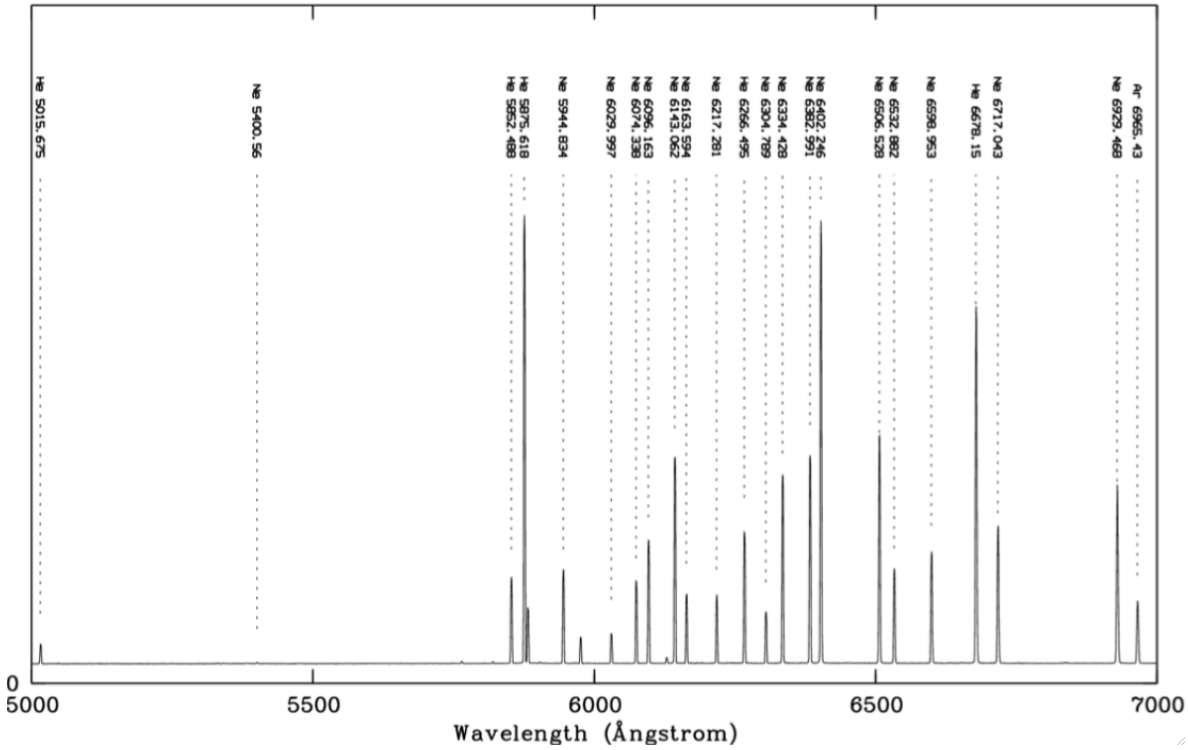

Figure 2.6: HR-orange arc line spectrum from 5000 to 7000 Å. The lines used for calibration are indicated (He + Ne + Ar).

3. **Flat-field correction**

Under a uniform illumination the signal response on the CCD will never be uniform, since the pixels present sensitivity variations, and the fibers different transmission. This is mainly due to two reasons:

(a) the light source, reaching the telescope focal plane, has to go across the fibers (having different transmissions);

(b) this light (outgoing of these fibers) will be dispersed through the spectrograph.

The spectral extraction procedure is applied to the flat field exposure itself. Due to the high signal-to-noise ratio over the entire wavelength range, flat-field spectra are used to trace and identify the fibers. The position of each fiber center is traced along the CCD using a 4th degree polynomial and the 'path' followed by the light is saved into a file. Thus, the polynomials obtained for the flat can be used in all the scientific images observed during the same night.

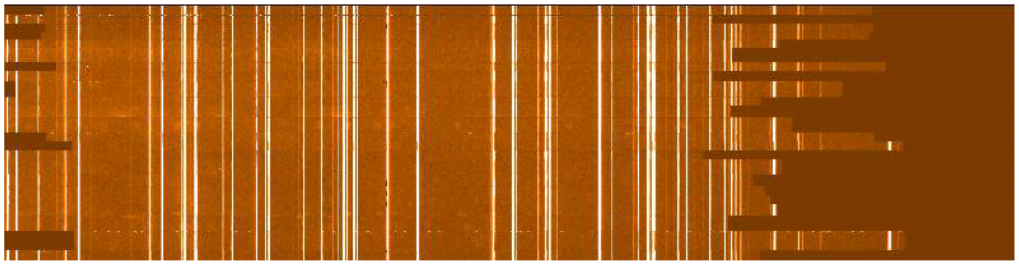

Figure 2.7: Example of good result of an extracted and wavelength calibrated arc spectrum.

4. **Wavelength and Flux calibrations**

   The wavelength calibration transforms the dispersion axis from pixel into wavelength units using a well characterized arc-lamp image (e.g., He + Ne + Ar lamp, see Fig. 2.7). The lamp corrects even for the fact that the lines do not fall exactly at the same pixel along the dispersion axis for the different fibers (see the aligned spectra in Fig. 2.7).

   Then, the image counts have to be transformed into flux units and corrected for the instrumental response, using the information of a well characterized spectrophotometric standard star. The VIMOS pipeline recipe `vmifustandard` is used. This routine is used to extract the IFU spectra of a spectro-photometric standard star applying the input extraction mask, after aligning it to the brightest spectra. With the calibration file and the atmospheric extinction data, the sensitivity function of the system is derived. Thus, the signal of any given galaxy can be transformed from counts to flux density (erg s^{-1} cm^{-2} $Å^{-1}$).

5. **Spectra extraction**

   Finally, the `IRAF` recipe `vmifuscience` is used to extract IFU scientific spectra applying the input extraction mask, after aligning it to the brightest spectra detected on the input exposure. The extracted spectra are then resampled at a constant wavelength step, after aligning the input wavelength calibration to the positions of a set of identified sky lines. The extracted spectra are eventually corrected for the relative differences in transmission from fiber to fiber.

2.4.2 Post-data reduction

In this section we explain how the derived flux calibrated spectra for each quadrant are combined together to get the final data-cube.

- **Cube creation from the individual pointings:** for each pointing a data-cube is created and then placed in their respective quadrant. In Fig. 2.8 the FoV covered by the four different VIMOS pointings are shown.

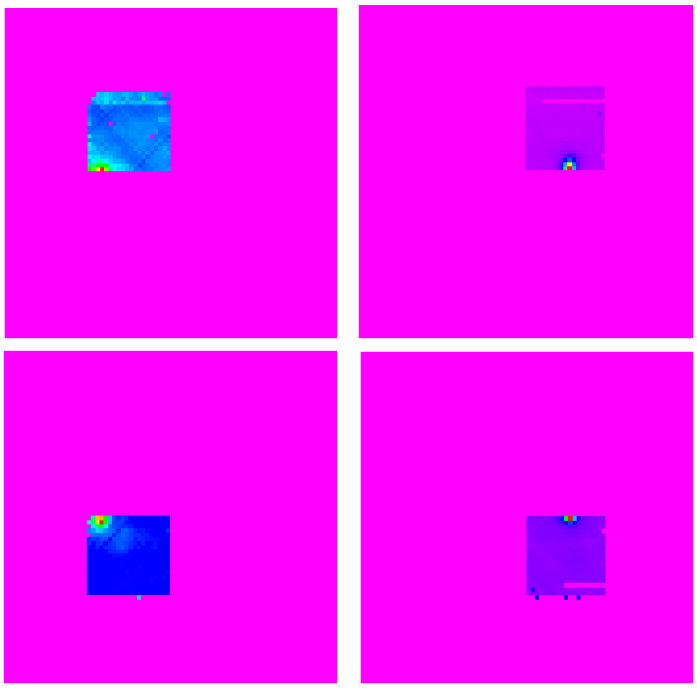

Figure 2.8: Different FoV covered by the four quadrants (i.e., #2) in high-resolution mode for the galaxy IRAS F01159-4443. North is on the right and East is at the top.

- **Flat-field correction:** as explained in point 3 of Sect. 2.4.1, the signal response on the CCD of a sky line at 6300 Å should be the same for all the spaxels of each quadrant and among the four quadrants, but it is not since the pixels present sensitivity variations and the fibers different transmissions. The line width σ (Å), the central wavelength and the flux intensity distributions of this sky line for all the spaxels of each quadrant (see Fig. 2.9) can be derived using an IDL routine. From these plots an estimation of the quality of the wavelength and flux calibrations can be derived, as well as the homogeneity of the instrumental profile. In Fig. 2.9 the results obtained for one of the four quadrants is considered: the histograms represent the distributions of, respectively, the line width (FWHM, in red), the central wavelength (in green) and flux emission (in blue) of the sky line for all the

spaxels. On the top, the flux distribution clearly highlights the fact that the spaxels have different flux values. On the bottom, the corrected sky line flux distribution is shown, in which the flux is the same for all the spaxels. In the last step the flux has to be the same for the four quadrants.

- **Masking 'bad' fibers:** a mask is created in order to remove fibers with low transmission and not well traced.

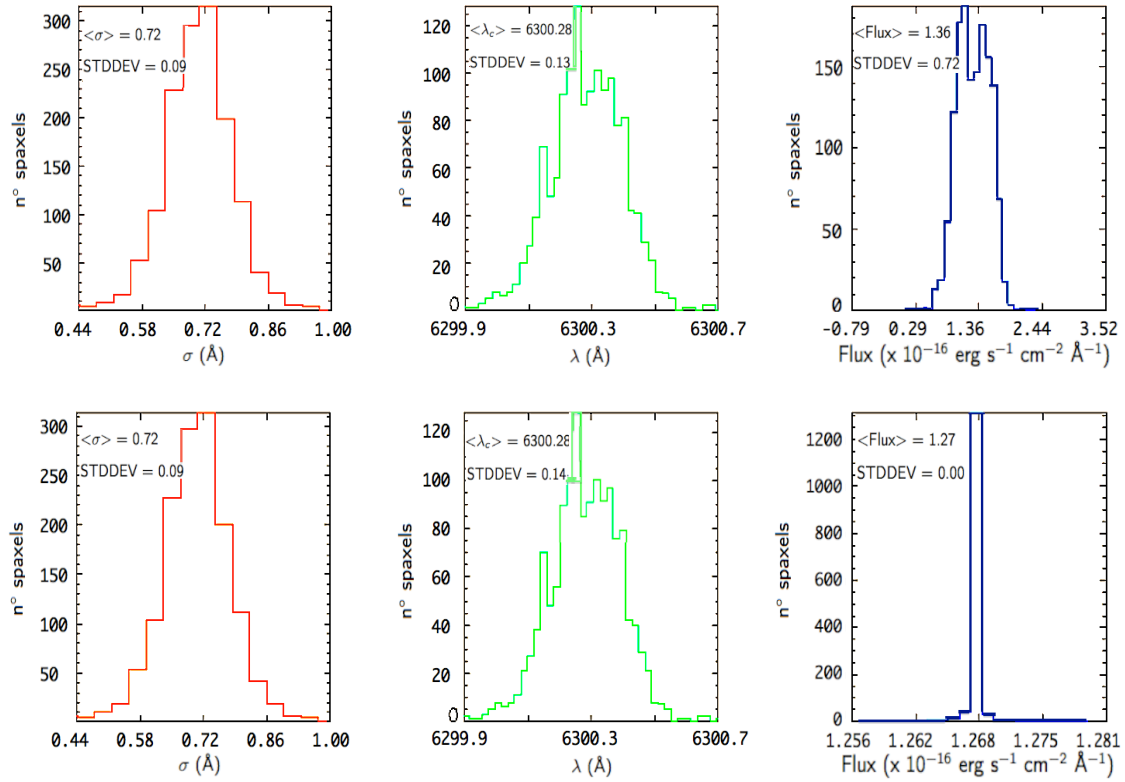

Figure 2.9: The sky line distributions of the line width (FWHM), central wavelength and flux for all the spaxels. **Top panel:** the flux distribution of the sky line shows the range of flux values for all the spaxels. **Bottom panel:** The same distribution after the flat-field correction. Now the measured flux has the same value for all the spaxels in the quadrant.

- **Combining the four cubes:** using the `IRAF` recipe `imcombine` the four cubes corresponding to each pointing are combined together taking into account the relative offsets among them. Indeed, a square four-pointing dithering pattern is applied with a relative offset of 2.7″ (i.e., four spaxels). In this configuration the final FoV is 29.5″ × 29.5″, slightly larger than than obtained without dithering (i.e., 27″ × 27″). The four cubes (i.e., 40 × 40 spaxels) are shown in Fig. 2.10. Combing them together we end up with the final data cube (i.e., 44 × 44 spaxels).

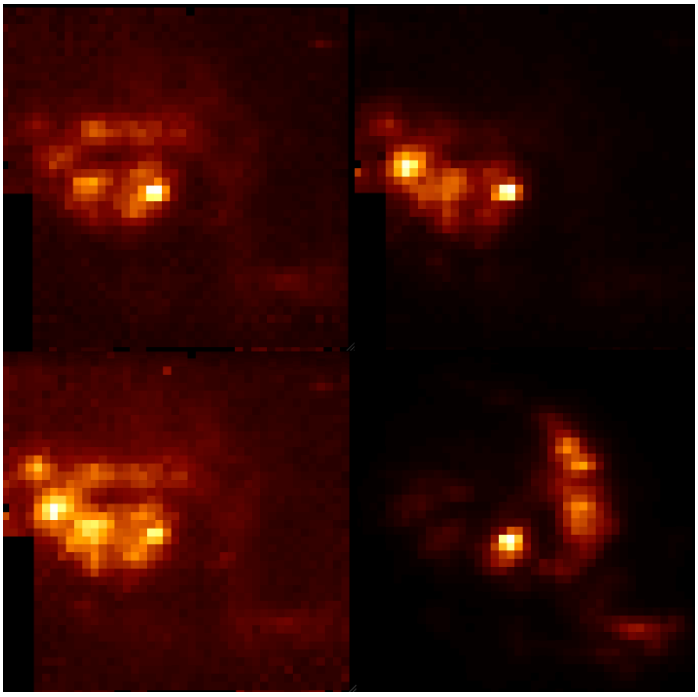

Figure 2.10: One of the pointings of the source IRAS F10257-4339 taken at different wavelengths. North in on the top and East on at the left.

- **Sky emission subtraction:** The measurements of the sky are taken simultaneously and under the same conditions as when the galaxy under study was observed, using a region composed by 20-30 spaxels where no galaxy emission is present.

  The importance of the sky subtraction depends on the individual galaxies. It is relevant if an emission line of interest is adjacent to (or coincides with) a sky line, particularly in the low surface brightness regions where the relative importance of the sky emission is critical. In the nuclear region (high surface brightness) the residuals of the sky subtraction are generally irrelevant, whereas then become more important in the most external/low surface brightness areas since they could be at the same count level than detections than the weakest emission lines.

  The sky spectrum is obtained by median combining spaxels in the offset sky exposures and then subtracted. It is created using the `IRAF` routine `create_sky.cl` and then removed from the data cube using the `IRAF` routine `remove_sky.cl`. In the peculiar case in which the object of interest completely fills the FoV, a separate field dedicated to sampling the sky background may be required. This can sometimes be observed simultaneously with the science data, or may need to be a separate observation (depending on the instrument capabilities). The sky field should sample blank sky as close as possible to the object field.

- **Cosmic Rays rejection:** a set of dither exposures are taken in order to cope with dead spaxels and to remove cosmic rays. This is done using the `IRAF` task `imcombine` which allows the improvement of the S/N of the image and the rejection of the cosmic rays.

2.5 Data analysis

In this section the line fitting method applied to Hα - [NII] emission lines is discussed. Furthermore, the flux intensity, velocity field, and velocity dispersion maps are generated along with a VIMOS continuum image for the whole sample. The panels in Appendix A show the Hα maps of the relative galaxies. When HST images are available (i.e., acquired by NICMOS F160W (H-band) and ACS F814W (I band)), they are also shown in the panels.

2.5.1 Line fitting

The observed Hα and [NII]$\lambda\lambda$6548, 6583 Å emission lines of the individual spectra are fitted to Gaussian profiles using an IDL routine (i.e., MPFITEXPR, implemented by C. B. Markwardt). This algorithm derives the best set of lines that match the available data. In case of adjusting multiple lines, the line flux ratios and wavelengths of the different lines are fixed according to the atomic physics. The widths are constrained to be equal for all the lines and greater than the instrumental contribution (σ_{INS}). We select spaxels where Hα lines are detected with S/N $>$ 4, fitting automatically all the lines to single Gaussian profiles (i.e., 1 component (1c) fit), which gave good results for the majority of the spectra. However, for certain regions of the galaxies, a multicomponent fit (e.g., 2 components (2c) per line) was required in order to adequately fit the data. Looking at the Hα line profile and the residuals of the fit, we decided to apply 1c or 2c fitting. Where the presence of one or two components was dubious the percentage of spectra was generally small (i.e., typically a few percent) since it was clear that one or two components were preferred for a large majority. There are a few cases where decomposition introduces some uncertainties, and these are commented on Appendix A. Two components are considered when the 2c fits give a significantly lower χ^2 value than that derived when using 1c fits (i.e., χ^2_{2c} / $\chi^2_{1c} < 0.5$). We check all the spectra by visual inspection.

A couple of examples showing two different kinds of fittings, 1c and 2c, are shown in Fig. 2.12. Only a few systems do not show clear signs of broad components (e.g., IRAS F06259-4780 S, IRAS F09437+0317 S, IRAS F12043-3140 N, and IRAS F22132-3705).

For each emission line/component, we end up with the following information: line

flux, central wavelength (λ_c), and intrinsic width ($\sigma_{line} = \sqrt{\sigma^2_{obs} - \sigma^2_{INS}}$)[1], together with their corresponding fitting errors. However, a better estimate of the actual uncertainties associated with the kinematic parameters is obtained by combining in quadrature fitting and calibration errors (see Sect. 2.3). For high S/N spectra fitting errors are small (typically, $\Delta\lambda < 0.1$ Å; $\Delta\sigma < 0.1$ Å) and calibration errors can be considered the main source of uncertainty (and vice versa for spectra with S/N < 5).

When 2c fitting is applied we can identify systemic (or *narrow*) and secondary (or *broad*) components, according to their widths. These components usually have different central velocities, confirming that they are two kinematically distinct components. The lines associated with different components were fitted simultaneously, maintaining for each component the assumptions mentioned before. The narrow component usually extends over the whole galaxy line-emitting region, while the broad component covers a smaller area corresponding to the nuclear regions of the galaxies (see Fig. 2.11 as an example).

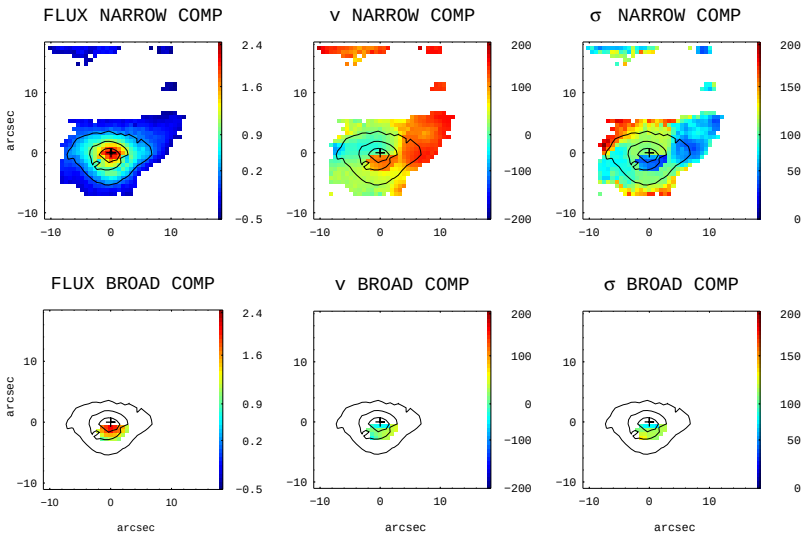

Figure 2.11: The flux intensity, velocity field, and velocity dispersion maps for the narrow (green line in Fig. 2.12) and broad (light blue line in Fig. 2.12) components as derived from the line fitting for the galaxy IRAS F18093-5744 C are shown. In App. A the complete panel is shown.

We note that due to the different resolving power of the original spectra, authors use a different number of line components to fit the observed profiles. For instance, Colina et al. (2005) consider only one component for most of their sample due to the relatively low spectral resolution of their INTEGRAL/WHT data (i.e., R = 1500), while Westmoquette et al. (2012) use two or three components thanks to the higher spectral resolution of the VIMOS/VLT data (i.e., R = 3100). When considering only one component, v and σ are in general similar to those of the narrow component in a 2-Gaussian fit. Further details on the line fitting will be given in Sect. 3.1 in Chapter 3.

[1]An average value of the σ_{INS} of (37 $\pm$ 2) km s^{-1} is used (see Tab. 4.3).

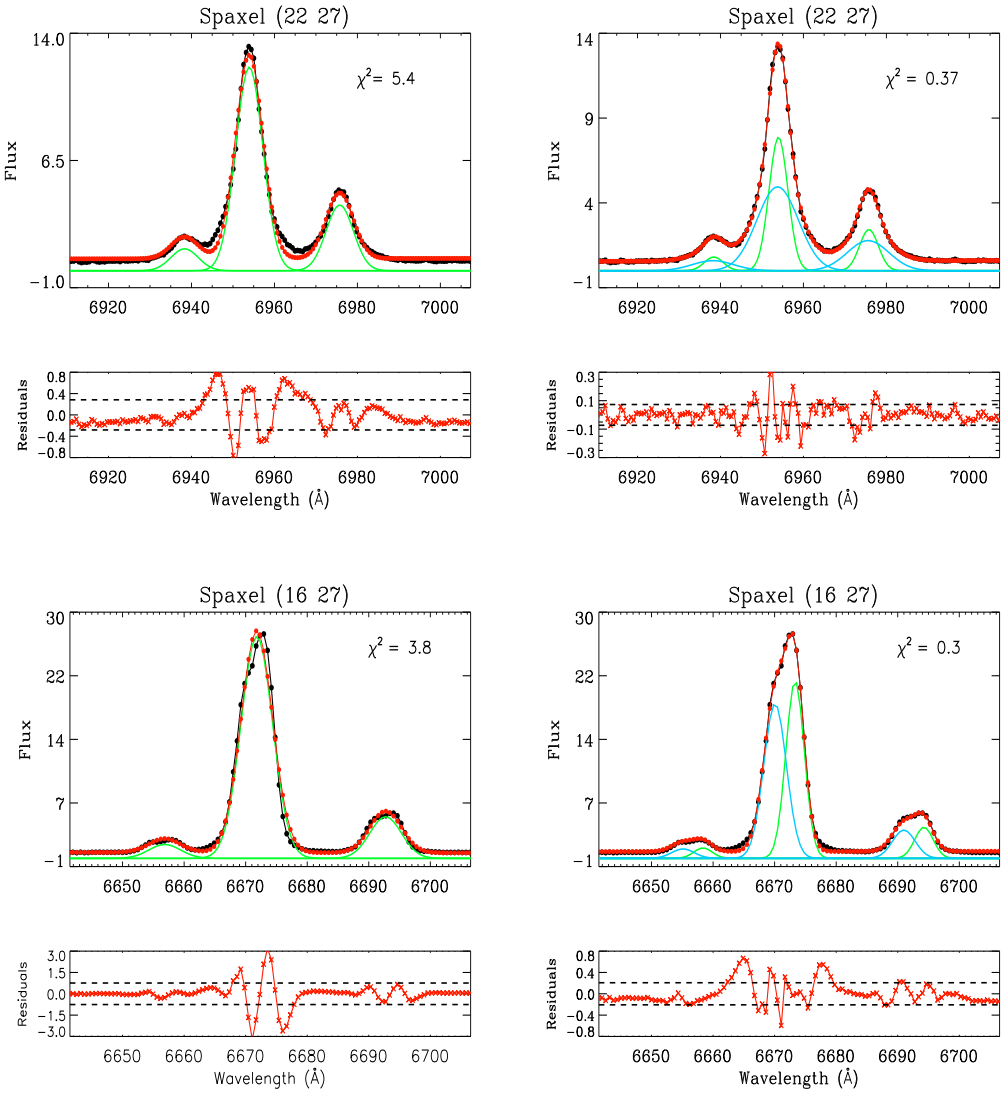

Figure 2.12: Examples of one (1c, on the left) and two (2c, on the right) component Gaussian fits to the Hα + [NII] profiles in two different spaxels in IRAS F09022-3615 (top) and IRAS F18093-5744 C (bottom). The χ^2 for all the Gaussian fittings is shown for a direct comparison. The systemic (narrow) component is shown in green, while the broad one is shown in light blue. The red curve shows the total contribution coming from the Hα + [NII] Gaussian fit. Below, the residuals (i.e., data - model) are presented: they clearly show when two components are needed to properly fit asymmetric line profiles. The standard deviation value of the residuals (i.e., $\pm$ 1σ) is shown using dashed lines.

2.5.2 Map generation

In this section we briefly describe how the Hα maps are derived for all the sources of our sample. In particular, the flux intensity, velocity field, and velocity dispersion maps for the narrow and broad components are obtained using IDL procedures (i.e, *jmaplot*, Maíz-Apellániz 2004) after applying the line fitting, as shown in Fig. 2.11. The kinematic maps for all the systems are shown and discussed in detail in App. A. As a reference, we also include the continuum image generated from the VIMOS-IFU data cube. When HST imaging is available, it is also shown.

In one case, i.e., the northern galaxy in IRAS F09437+0317 (IC 564), we have applied a different treatment combing two different pointings. Indeed, as shown in Fig. 2.13, North-East and North-West pointings have been needed in order to observe most of the emission coming from this source. For each pointing we generate the same kinematic maps created for the whole sample, centered using the continuum peak, as shown in Fig. 2.14. Since they partially overlap, we combine them into a single pointing ending up with a final FoV of $\sim 50 \times 40$ arcsec^2 (see Fig. 2.15, and also App. A). In order to do that, we take advantage of both the features in the continuum and velocity field maps in the two pointings, along with some respective structures shown in the Hα flux maps, since during the reduction processes the astrometry information in the final data cube has not been conserved.

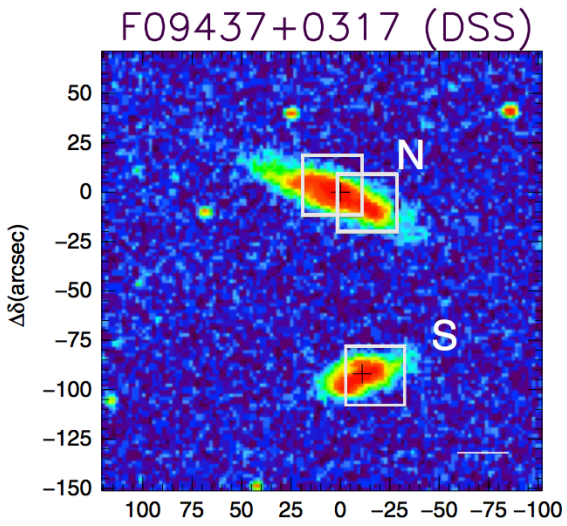

Figure 2.13: DSS image of the interacting system IRAS F09437+0317 taken from Rodríguez-Zaurín et al. (2011).

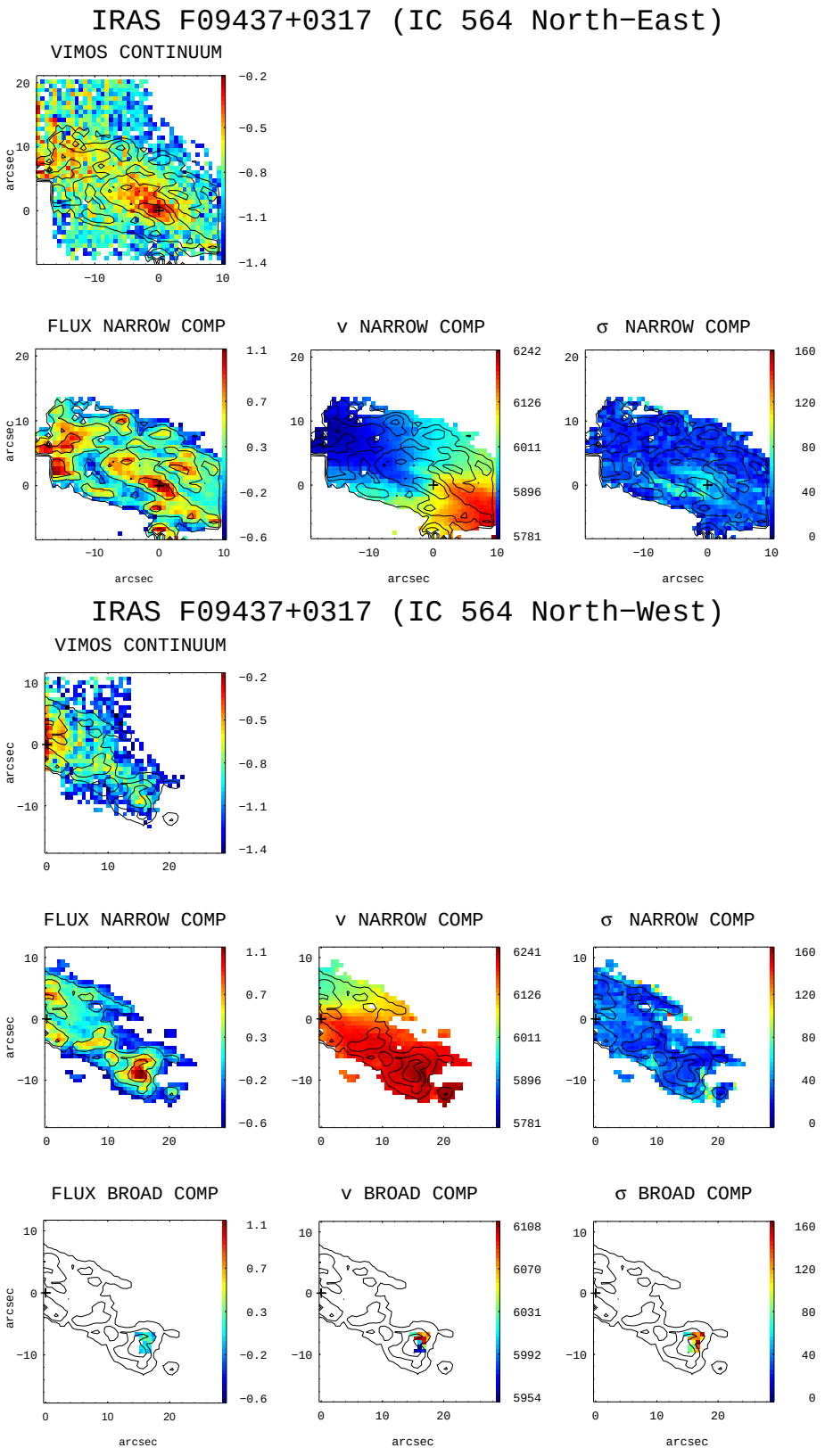

Figure 2.14: North-East and North-West pointings of the northern galaxy IRAS F09437+0317.

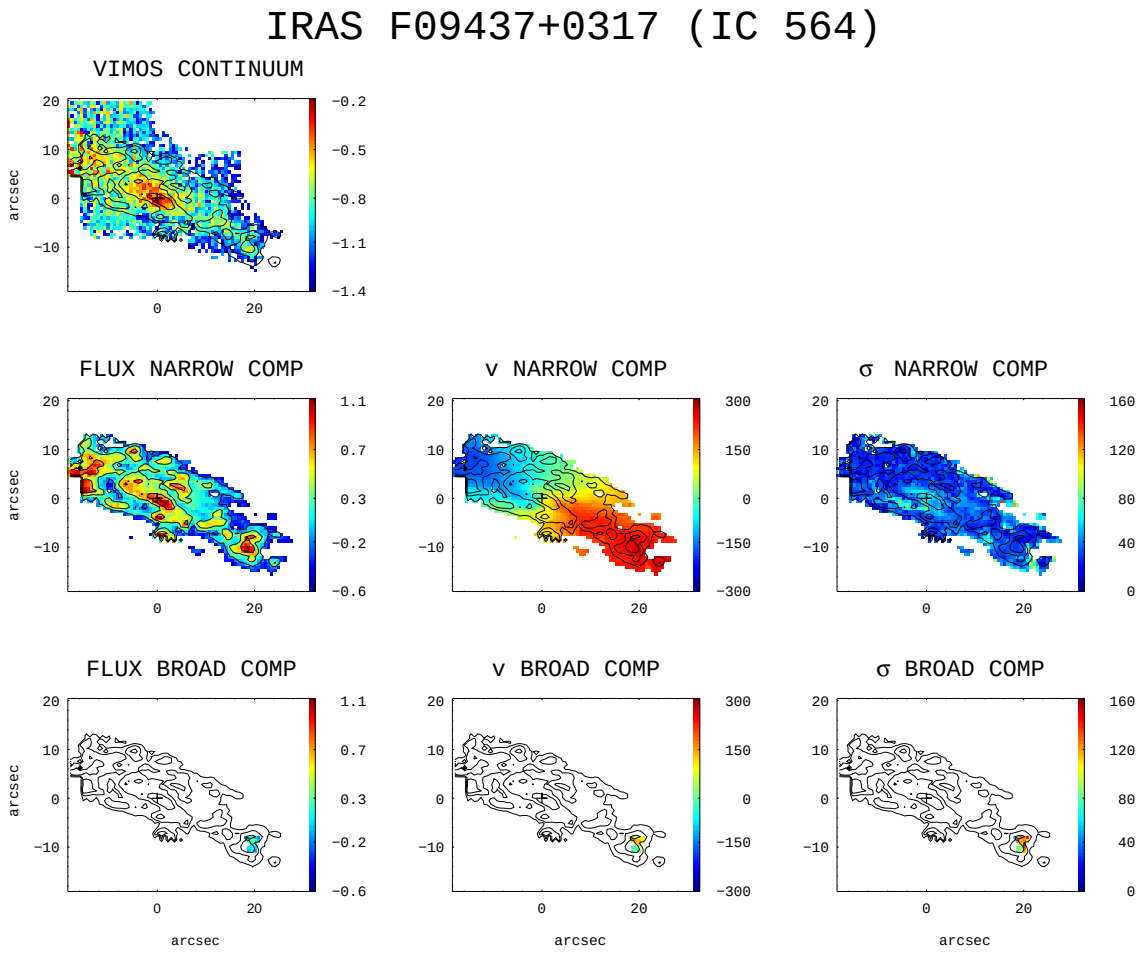

Figure 2.15: Final combined maps of the northern galaxy IRAS F09437+0317.

Chapter 3

Spatially resolved kinematics in (U)LIRGs

In this chapter the 2D kinematics of the ionized gas, as traced by Hα, of 38 local ($z < 0.1$) LIRGs and ULIRGs (51 individual sources) presented in Chapter 2 is investigated. It shows the first attempt to obtain statistically significant results of the 2D kinematic properties of these systems as a function of the infrared luminosity, morphology and dynamical status.

From the Hα emission line fitting two kinematically distinct components can be identified in the systems. The 2D and global kinematic properties are discussed and the role of rotation is then analyzed. We find a clear trend between the the different phases of the merging process and the mean kinematic properties inferred from the IFS kinematic maps (i.e., the more isolated objects are the more rotation dominated objects). The inferred kinematics properties for (U)LIRGs are then compared with those of other local samples (i.e., E/S0, Spirals, Lyman Break Analogs).

The dynamical mass estimates for the present (U)LIRG sample are also determined. They cover a wide range of values (i.e., 0.04 - 1.4 $m_\star$), with ULIRGs more massive (i.e., $\sim 0.5 \pm 0.2$ $m_\star$) than LIRGs by, on average, a factor of about 2. We also infer the mass ratio in galaxy-pairs, confirming that most (U)LIRG mergers involve sub-$m_\star$ galaxies of similar mass.

3.1 Introduction

As largely discussed in Chapter 1, the 2D kinematic characterization of galaxies is a key element to study the physical processes that govern their formation and evolution. Up to date, the number of spatially resolved kinematic studies of low-z (U)LIRGs is rather limited despite their relevance, where most of the works have focused on individual objects

or small samples, generally at the highest luminosity (i.e., ULIRGs). For this reason, we significantly expand previous samples (in number and characteristics) considering a local sample of 38 (U)LIRG systems observed with the VIMOS/VLT with IFS, where a large fraction (i.e., 31/38) of sources cover the less studied LIRG luminosity range.

In this chapter we discuss the 2D kinematic properties of the two kinematically distinct components identified in these systems from analyzing their Hα emission lines. The comparison of such properties with those of other relevant low-z samples is considered as well, even determining such a fundamental parameter as the dynamical mass, useful to understand the dynamical state of our galaxies. We then present the atlas of ionized gas velocity fields and velocity dispersion maps in App. A. Finally, in Sect. 3.4 we summarize the most relevant findings and conclusions.

3.2 Results from the line fitting

As discussed in Sect. 2.5.2, the products of the line fitting applied to the Hα lines are the flux intensity, velocity field, and velocity dispersion maps for the narrow and broad components, obtained using IDL procedures. All of these maps are shown and discussed in detail in App. A for the whole sample.

3.2.1 Narrow (systemic) component properties

The narrow component covers the whole Hα line-emitting region of these galaxies and generally contains most of the Hα flux. Therefore, it is morphologically similar to the total flux (i.e., narrow + broad) Hα maps presented by Rodríguez-Zaurín et al. (2011). The spatial extension of this component (10 - 350 kpc^2; see Tab. 3.3) is similar to that of the continuum emission, though in some cases there are significant structural differences (e.g., F01341-3735 (S, N); see also Rodríguez-Zaurín et al. 2011). Its spatial distribution and kinematic properties represent those of the entire galaxy, and it is therefore identified as the systemic component.

This narrow (systemic) component shows a large variety of 2D kinematic properties. The kinematic maps of some sources show very regular patterns, with a spider-like velocity field and a centrally peaked velocity dispersion distribution, as expected for pure rotating disk (e.g., IRAS F11506-3851, IRAS F12115-4656). However, most of the objects have some kind of irregularities and distortions in their velocity maps, despite a large rotation component in many cases. These departures from a regular rotation pattern include: i) kinematic axes that are poorly defined (e.g., IRAS F13229-2934), non-perpendicular

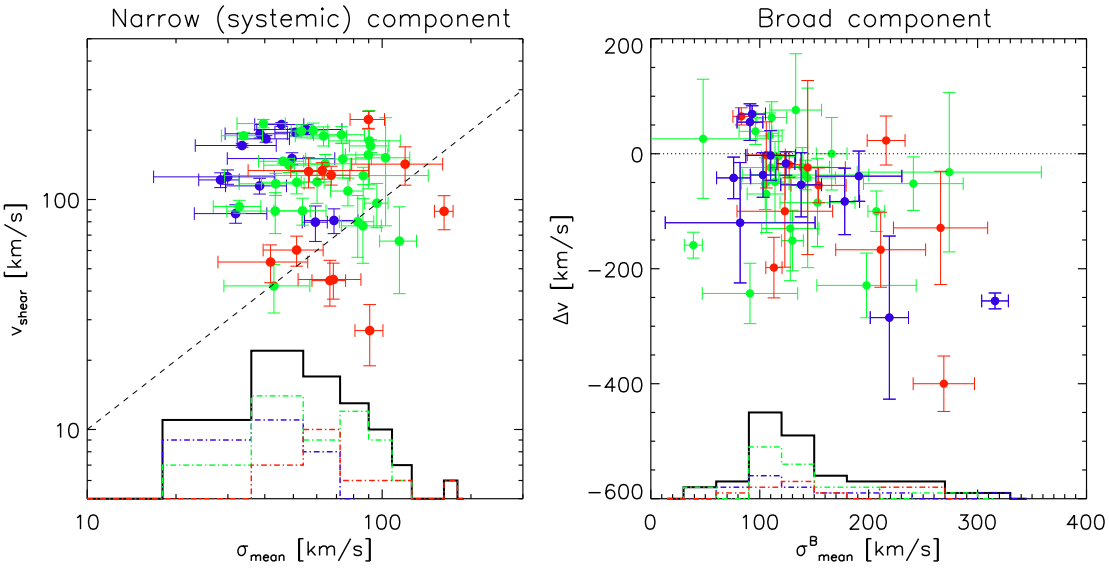

Figure 3.1: **Left panel:** Velocity shear, v_{shear}, versus the mean velocity dispersion, σ_{mean}, for the narrow (systemic) component. Blue, green, and red dots distinguish, respectively, morphological classes 0 (isolated disks), 1 (interacting), and 2 (mergers). The distribution of σ_{mean} values is also shown, with the contribution of the different morphological classes. The 1:1 dot line is shown as reference to highlight the fact that most of the sources have $v_{shear} > \sigma_{mean}$. **Right panel:** Velocity shift, Δv, between the broad and narrow components versus the mean velocity dispersion of the broad component, σ^{B}_{mean}. The horizontal dot line indicates the zero velocity shift. Most of the objects have a blueshifted broad component.

each to another (e.g., IRAS F11255-4120), and/or shifted with respect to the photometric axes (e.g., IRAS F10038-3338), ii) asymmetry between the approaching and receding regions (e.g., IRAS F13229-2934), and iii) off-nuclear kinematic center (e.g., IRAS F12596-1529). In addition, the velocity dispersion maps generally show an asymmetric structure. Although the highest velocity dispersion is usually coincident with the optical nucleus and therefore seems to trace the mass, there are cases where the absolute peak is associated with (tidal) structures located at large galactocentric distances (e.g., in IRAS F04315-0840 at 3.6 kpc; in IRAS F10015-0614 at 4 kpc; in F12043-3140 S at 3.4 kpc). Interestingly, a significant number of systems have ring-like structures of high velocity dispersion (i.e., $\sigma \sim$ 150 - 200 km s^{-1}) in their outer regions (e.g., IRAS F07027-6011S, IRAS 09022-3615, IRAS F12116-5615). These are regions of relatively low Hα emission, which are likely ionized by shocks (Monreal-Ibero et al. 2010 and references therein).

We have used our IFS-based velocity maps to infer some global kinematic properties associated with this component (see Tab. 3.3). Fig. 3.1 shows the observed (i.e., uncorrected for inclination) velocity shear, v_{shear}[1], and the spatially resolved uniformly

[1] v_{shear} is defined as half of the difference between the median value of the 5 percentile at each end of the velocity distribution (i.e., $v_{shear} = \frac{1}{2}$ ($v^{5\%}_{max}$ - $v^{5\%}_{min}$)), following previous works (e.g., Gonçalves et al.

weighted mean velocity dispersion, σ_{mean}, of the narrow (systemic) component over the whole line-emitting region. These two properties have a relatively large range of values ($30 < v_{shear} < 220$ km s^{-1}; $30 < \sigma_{mean} < 160$ km s^{-1}). However, the scatter in the figure is dominated not by errors associated with the observations and/or the analysis but by errors associated with different intrinsic properties among the objects. This reflects that the selected (U)LIRGs represent a kinematically diverse sample. In fact, the figure shows a clear dependence on the mean v_{shear} and σ_{mean} values with the morphological class, with isolated disks having relatively lower values than systems in a more evolved dynamical phase (interacting and merging systems; see Tab. 3.3). In Sect. 3.2, we discuss in more detail the mean kinematic properties of (U)LIRGs as a function of their morphology/dynamical status.

3.2.2 Broad component

The broad component is generally restricted to the central regions, though in some cases it is found at very large galactocentric distances (up to $\sim$ 7 kpc in IRAS F23128-5919). Although in most of the cases, the (projected) area covered by the broad component is smaller than 3 kpc^2, there is a significant fraction (12/46) of objects with an extension larger than 5 kpc^2 (see Tab. 3.4). In a few cases, the broad component can be dominant in terms of flux in the innermost spaxels (e.g., IRAS F05189-2524, IRAS F08355- 4944). In some cases the broad emission is offset with respect to the photometric nucleus, thus defining an asymmetric structure (e.g., IRAS F12043-3140 S, IRAS F18093-5744 N). At some locations the broad component can be due to the line-of-sight overlapping of two physically distinct structures (e.g., IRAS F06076-2139, where the emission from the northern galaxy overlaps with the ring of the southern source; see also Arribas et al. 2008).

Due to sampling limitations, compactness, and low-surface brightness constraints, the detailed study of the 2D kinematic structure of this component is sometimes difficult. However, in several sources it is clearly resolved, and the kinematic axes can be well defined. For instance, in IRAS F04315-0840 (NGC 1614) the kinematic axes associated with the broad component are nearly perpendicular to those of the narrow component, which is a clear feature of outflows perpendicular to the disk (Heckman et al. 1990; Bellocchi et al. 2012). The velocity dispersion maps of several objects do not have a radial symmetry and/or have an off-nuclear kinematic center of symmetry (e.g., IRAS F04315-0840, IRAS F06035-7102, IRAS F07160-6215, IRAS F10038-3338).

The range of the global kinematic properties of the broad component (right panel of

2010).

Fig. 3.1) in velocity dispersions is significantly larger than that of the narrow component, with values of up to $\sim$ 320 km s^{-1} (i.e., FWHM $\sim$ 750 km s^{-1} for IRAS F07027-6011N). However, a large fraction of sources (i.e., 26/46) are in the range $90 < \sigma^{B}_{mean} < 150$ km s^{-1} (see Tab. 3.4). The mean central velocity of the broad component is blueshifted with respect to that of the narrow component for a majority of sources, reaching values up to Δv = -400 km s^{-1} (i.e., IRAS F05189-2524). There is however, a significant fraction of objects (9/46) with redshifted velocities, which seem to cluster around velocity dispersion values of $\sim$ 100 km s^{-1}.

The presence of AGNs may affect the kinematic properties of this component (e.g., Lípari et al. 2003; Westmoquette et al. 2012, Rupke & Veilleux 2013, Arribas et al. 2014 submitted). One of the two class 0 objects with large FWHM and Δv offset (i.e., IRAS F07027-6011 N) has evidence of hosting an AGN (see Rodríguez-Zaurín et al. 2011; Arribas et al. 2012). Excluding this object, most of the systems with Δv $>$ 100 km s^{-1} and / or $\sigma^{B}_{mean} > 200$ km s^{-1} are class 1 and 2. Among these sources in an advance merging phase, several (i.e., IRAS F05189-2524, IRAS F06206-6315, IRAS F13229-2934, IRAS F14544-4255 W, IRAS F18093-5744 C, IRAS F21453-3511, and IRAS F23128-5919) also have evidence of hosting an AGN according to the optical spectroscopic classification (see Rodríguez-Zaurín et al. 2011) and/or the evidence for a broad Hα line (see Arribas et al. 2012).

As for the spatial extension of the broad component, there is a clear trend with the morphological class. Specifically, the median areas covered by the broad component for classes 0, 1, and 2 are 1.1 kpc^2, 1.5 kpc^2, and 5.2 kpc^2, respectively.

In summary, the present data show that an extended broad component is observed in most of LIRGs and ULIRGs. The mean velocity of most of the objects is blueshifted with respect to the narrow component, with values up to -400 km s^{-1} and FWHM $\sim$ 750 km s^{-1}. The largest extensions and extreme kinematic properties (Δv, FWHM) are observed in interacting and merging systems (classes 1 and 2). The detailed study of the kinematic properties of the broad component will be done elsewhere (Arribas et al in prep.).

3.2.3 Comparison with previous IFS studies

As mentioned above, the detailed comparison of the component properties with previous IFS studies is not straightforward. On the one hand, most of the previous studies are focused on the ULIRG luminosity range (e.g., Colina et al. 2005 and Westmoquette et al. 2012), while a large fraction of the present sources are LIRGs. On the other hand, there is some heterogeneity in the way in which the line fitting and component map construction are performed among the different works. In Colina et al. (2005) only one

single component was in general adjusted to the observed profiles since the relatively low spectral resolution of the INTEGRAL/WHT data does not allow the presence of multiple components in the lines to be reliably distinguished on a spaxel by spaxel basis. However, in general the derived kinematical values of v and σ in a 1-Gaussian fit are similar to those of the narrow component when applying a 2-Gaussian fit. In Westmoquette et al. (2012) multiple components were fitted for most of the sample thanks to the higher spectral resolution of the VIMOS/VLT data. The different components were assigned to the lines mainly using a line intensity criterion (rather than a line width criterion), regardless of the relative velocities of the components. Thus, they do not necessarily represent kinematically distinct components, as in our case. The morphological features seen in our kinematic maps are similar to those reported in these works, which also find asymmetries and departures from rotation for most of their objects. The range of σ found by Colina et al. (2005) (i.e., $50 < \sigma < 150$ km s^{-1}) is similar to the one found here for the narrow component of the present sample. Westmoquette et al. (2012) also found it necessary to adjust multiple components over relatively extended regions. In addiction, they discovered motions associated with outflows for a relatively large fraction of objects in their sample (11/18). However, as we discuss in the next section, we find a larger fraction of rotating systems than in their samples.

3.3 Kinematic characterization of local (U)LIRGs

3.3.1 Kinematic classification

The present sample is formed by a group of morphologically diverse objects, classified on the basis of optical imaging into three groups according to their suggested dynamical status (i.e., isolated relaxed rotating disks: class 0, interacting systems: class 1, and mergers: class 2; see Sect. 2.1.1 for more detailed definitions). In this section we perform a simple kinematic classification of the (U)LIRG sample based on the velocity fields and the velocity dispersion maps of the systemic component. This classification is similar to the one proposed by Flores et al. (2006) and distinguishes three main groups:

1. Rotating disks (RD): both the velocity field and the velocity dispersion maps show the expected pattern for rotation. The major kinematic axis in the velocity field follows the major photometric axis of the continuum map, and the σ-map shows a peak near the galaxy nucleus. Regions of high velocity dispersions associated with the outer faint emission, such as those studied by Monreal-Ibero et al. (2010), are not considered a significant deviation from the global rotation pattern.

2. Perturbed disks (PD): the velocity field shows a general rotation pattern with well-defined approaching and receding regions, but the kinematic axes show some distortions and/or the σ-map has a peak shifted off the center;

3. Complex kinematics (CK): systems with both velocity field and velocity dispersion maps discrepant from the expected normal rotating disks showing the evidence of radial motions and/or disturbed velocity dispersion distribution.

From a total of 51 galaxies in the sample, 49 could be classified according to this scheme[2]. Of these, 14 are undoubtably RD (29%), while for 23 additional ones rotation is likely to be dominant, despite the presence of clear asymmetries (PD, 47%). The remaining 12 show CK (24%). Therefore, for 76% of the galaxies (i.e., 37/49) rotation plays an important role.

3.3.2 The role of rotation in local (U)LIRGs and its dependence on L_{IR}

As for the global properties, objects classified as RD, PD and CK have increasing values of σ_{mean} (i.e., 50 $\pm$ 5, 58 $\pm$ 4, and 91 $\pm$ 8 km s^{-1}, respectively) and decreasing v_{shear} (159 $\pm$ 12, 123 $\pm$ 10, and 112 $\pm$ 15 km s^{-1}, respectively), as shown in Tab. 3.1.

The fraction of rotating systems is considerably larger than those reported previously in ULIRGs by Colina et al. (2005) and Westmoquette et al. (2012). In particular, Colina et al. (2005) found while studying a sample of 11 ULIRGs that the velocity field of the ionized gas is dominated by tidally induced flows and generally does not correspond to rotationally supported systems. Only one system (i.e., IRAS F17208-0014, Arribas & Colina 2003) shows a dominant rotation pattern when fitting the emission lines to a single Gaussian component, and two more (i.e., Arp 220, see Arribas et al. 2001; Colina et al. 2004 and IRAS F08572+3915, see Arribas et al. 2000) could be considered as candidates for rotating systems after a kinematic decomposition similar to the one performed in the present paper. Westmoquette et al. (2012) find a larger fraction of rotating systems (i.e., 8/18) in their sample of ULIRGs. These fractions are significantly smaller than our finding of 37 out of 49 in the present (U)LIRG sample. This may be explained by the fact that the present work includes a large fraction of systems with lower luminosity (i.e., 31/38 LIRGs) than in the mentioned works, which only cover the ULIRG luminosity range.

[2]No kinematic classification has been possible for IRAS F08424-3130 N since it is located on the edge of the VIMOS FoV. For IRAS F12596-1529 the kinematic classification was not possible due to the limited linear resolution.

In fact, we find that the kinematic class clearly correlates with the infrared luminosity L_{IR}. A large fraction (i.e., 6/7) of ULIRGs were classified as CK, while most of the objects with luminosity lower than $10^{11.4}$ $L_{\odot}$ are classified as PD or RD (i.e., PD = 11/21 and RD = 7/21, respectively). Therefore, large deviations from rotation are generally associated with ULIRGs, while the lower end of the luminosity range (i.e., LIRGs) is generally populated by rotation-dominated systems. However, exceptions to this rule exist: there is a ULIRG (i.e., IRAS F06206-6315) with a regular rotation pattern and there are a few LIRGs (e.g., IRAS F13001-2339, IRAS F13229-2934) showing complex kinematics.

It is also worth mentioning that a quantitative analysis of the relative importance of rotation with respect to the kinematic asymmetries, based on the application of *kinemetry* methodology (Krajnović et al. 2006), has been presented in Bellocchi et al. (2012) for four sources (see Sect. 4.4). This methodology will be applied to the whole sample as described in the second part of Chapter 4 (see Sect. 4.8) and then published in a forthcoming work (Bellocchi et al. 2014 in prep.).

3.3.3 Discriminating between disks and mergers in the σ_c/σ_{mean} vs. σ_{mean} plane

The kinematic classification described above shows that rotation is more frequent in systems classified as isolated (class 0) than in those classified as interacting (class 1) and mergers (class 2). The fraction of RD decreases from 46% to 32% for isolated and interacting systems, while none of the mergers are classified as RD. In contrast, only one isolated object presents CK, while the fraction of CK increases to 20% and 55% for interacting systems and mergers, respectively (see Tab. 3.1).

When the central (nuclear) velocity dispersion[3], σ_c, of the systemic component is compared with its spatially resolved mean value, σ_{mean}, a clear segregation between isolated disks and interacting/merging systems is found (Fig. 3.2). Specifically, the derived mean σ_c/σ_{mean} ratios for disks, as well as for interacting and merging systems, are, respectively, (1.8 $\pm$ 0.15), (1.1 $\pm$ 0.05), and (0.97 $\pm$ 0.09). On the one hand, this trend can be explained as a consequence of the tidal effects on the gas velocity dispersion. Isolated relaxed disks (class 0) have relatively low velocity dispersions outside the nuclear region, with a $\sigma_{mean} \approx 44$ km s^{-1} (i.e., a factor of ~ 2 larger than that derived for local spiral galaxies, see Tables 3.1 and 3.2) and, generally, centrally peaked velocity dispersion maps, making the mentioned ratio relatively large. On the other hand, as in principle the

[3]The Hα central velocity dispersion is derived as the mean value of the 4 $\times$ 4 spaxels around the VIMOS continuum flux peak.

Table 3.1: Mean (and median) kinematic properties for the different (U)LIRG samples.

Sample	$< logL_{IR} >$ ($L_\odot$)	SFR ($M_\odot$ yr^{-1})	v_{shear} (km s^{-1})	v^*_{shear} (km s^{-1})	σ_{mean} (km s^{-1})	$v^*_{shear}/\sigma_{mean}$	R^{IR}_{eff} (kpc)	M^{IR}_{dyn} (10^{10} $M_\odot$)	K class* (RD; PD; CK)/T
(1)	(2)	(3)	(4)	(5)	(6)	(7)	(8)	(9)	(10)
ALL	11.4 ± 0.4	88 ± 15 (45)	130 ± 7 (128)	171 ± 9 (177)	63 ± 4 (58)	3.2 ± 0.3 (2.6)	2.5 ± 0.2 (2.4)	4.9 ± 0.6 (3.5)	(14; 23; 12)/49
LIRG	11.3 ± 0.3	44 ± 6 (34)	130 ± 8 (128)	170 ± 9 (167)	59 ± 3 (54)	3.4 ± 0.5 (3.3)	2.5 ± 0.2 (2.4)	4.5 ± 0.5 (3.5)	(14; 22; 6)/42
ULIRG	12.2 ± 0.1	278 ± 20 (272)	130 ± 26 (150)	178 ± 24 (190)	95 ± 12 (90)	2.0 ± 0.4 (1.9)	2.8 ± 0.6 (2.4)	7.1 ± 2.6 (4.8)	(0; 1; 6)/7
(U)LIRG class 0	11.3 ± 0.3	48 ± 18 (32)	150 ± 14 (171)	195 ± 17 (182)	44 ± 4 (46)	4.7 ± 0.5 (4.3)	2.7 ± 0.3 (3.0)	5.1 ± 1.0 (4.9)	(6; 6; 1)/13
(U)LIRG class 1	11.4 ± 0.5	91 ± 25 (41)	135 ± 7 (141)	174 ± 8 (190)	67 ± 3 (63)	3.0 ± 0.3 (2.5)	2.6 ± 0.2 (2.4)	4.8 ± 0.5 (3.5)	(8; 12; 5)/25
(U)LIRG class 2	11.7 ± 0.3	129 ± 32 (86)	98 ± 18 (89)	134 ± 21 (157)	80 ± 11 (67)	1.8 ± 0.3 (1.5)	2.6 ± 0.5 (2.0)	4.7 ± 1.9 (1.7)	(0; 5; 6)/11
(U)LIRG RD	11.4 ± 0.3	65 ± 25 (35)	159 ± 12 (180)	207 ± 16 (207)	50 ± 5 (46)	4.7 ± 0.5 (5.4)	2.7 ± 0.4 (2.5)	5.8 ± 1.0 (5.1)	(14; 0; 0)/49
(U)LIRG PD	11.3 ± 0.4	56 ± 15 (36)	123 ± 10 (119)	160 ± 13 (163)	58 ± 4 (53)	3.1 ± 0.3 (3.1)	2.4 ± 0.2 (2.3)	4.1 ± 0.6 (3.5)	(0; 23; 0)/49
(U)LIRG CK	11.7 ± 0.5	161± 36 (202)	112 ± 15 (127)	155 ± 17 (157)	91 ± 8 (90)	1.7 ± 0.2 (1.7)	2.7 ± 0.5 (2.3)	5.9 ± 1.8 (3.4)	(0; 0; 12)/49

Col (1): Sample: class 0 identifies isolated disks, class 1 denotes pre-coalescence interacting systems, and class 2 stands for mergers (see Sect. 2.1). RD stands for rotation dominated, PD perturbed disks and CK complex kinematic (see Sect. 3.3.1). Col (2): Infrared luminosity. Col (3): Star formation rate derived from the infrared luminosity listed in Col (2) applying the Kennicutt (1998) relation. Col (4): Observed velocity shear as defined in the text. Col (5): Intrinsic velocity shear (i.e., inclination corrected). Col (6): Mean velocity dispersion. Col (7): Dynamical ratio between the intrinsic velocity shear and the mean velocity dispersion. Col (8): Infrared effective radius, derived as explained in Appendix B. Col (9): Dynamical mass derived as explained in the text. Col (10): Number of galaxies classified as RD, PD, CK with respect to the total number of galaxies in the sub-sample.

(*) The total number of galaxies in the present sample is 51, but for the galaxy IRAS 08424-3130 N and IRAS F12596-1529 the kinematical classification was not possible as explained in the text. So, the number of galaxies with kinematical classification is 49.

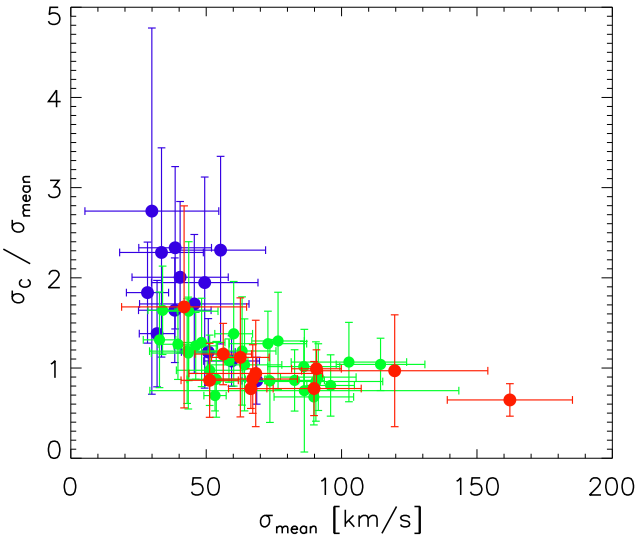

Figure 3.2: Relationship between the central velocity dispersion, σ_c, of the systemic component and its mean velocity dispersion over the observed area, σ_{mean}, for the three different morphological classes. The color code is the same as the one used in Fig. 3.1.

beam smearing of the central velocity gradient in a disk might be significant to enhance the σ_c/σ_{mean} ratio (see Davies et al. 2011), the comparison of samples in this diagram should be done ideally at similar linear resolution. For our particular case, the effects on this ratio are expected to be small (i.e., $\sim$ 10% in the most extreme case), as further discussed in Sect. 3.3.1 In the pre-coalescence (class 1) objects, the velocity dispersion outside the nucleus increases because the main body of the system is perturbed by tidal forces associated with interactions, reducing significantly such a ratio. The largest σ_{mean} values are reached for the ongoing, post-coalescence mergers (class 2). However, though σ_c and, to a lesser degree, σ_{mean} may (slightly) depend on the fitting approach (i.e., to one or two components), the general trend observed in the plot does not depend on the fitting approach[4].

We note that this could be a good kinematic diagnostic diagram for classifying spatially resolved high-z sources, though similar linear resolutions to the ones considered here should be used for a direct comparison. This is the case of several AO-assisted IFS works of high-z SFG samples (e.g., Law et al. 2007; Förster Schreiber et al. 2009; Swinbank et al. 2012), which can reach a sub-kpc scale of the order of those of low-z (U)LIRGs observed under seeing-limited conditions.

In the following section we discuss the dynamical ratio v/σ and its dependence on the

[4]We note that the narrow component of a 2-Gaussian fit has, in general, similar properties compared to those of a single Gaussian fitted line.

kinematical and morphological classes.

3.3.4 Dynamical support in (U)LIRGs: from rotating disks to dispersion-dominated systems

The dynamical ratio between the velocity amplitude and the local velocity dispersion v/σ of a system is a useful parameter to kinematically characterize a system. It allows the distinction between rotation-dominated $v/\sigma > 1$ and random-motion-dominated systems $v/\sigma < 1$ (e.g., Epinat et al. 2012 and references there in). We note that for systems whose kinematic is dominated by tidal forces and/or radial motions (e.g., outflows), v_{shear} may not be tracing rotation. Similarly, in those cases σ_{mean} does not necessary give a measure of velocity dispersion, but it can be the result of integrating several kinematically distinct components. However, since only a small fraction of systems show complex kinematics (see Sect. 3.3.1) and a kinematic decomposition has been applied (Sects. 3.2.1 and 3.2.2.), v_{shear} and σ_{mean} should trace, respectively, rotation and dispersion in most of the cases. In Fig. 3.3 the dynamical ratio v/σ with respect to the mean velocity dispersion is presented. A clear trend is shown among the different morphological classes with *disk* (class 0) galaxies having higher v/σ than objects in a more advanced interaction/merging phase (classes 1, 2; see Tab. 3.1)[5].

Kinematical data of samples of nearby galaxies with available IFS are also included for comparison: elliptical/lenticular galaxies drawn from the SAURON project, studying the stellar kinematics (e.g., Cappellari et al. 2007), local spiral galaxies selected from the Gassendi Hα survey of SPirals (GHASP, Epinat et al. 2010), and Lyman break analogs (LBAs) at redshift ~ 0.2 observed in Hα with OSIRIS/Keck (i.e., Gonçalves et al. 2010)[6]. We note that these works use slightly different definitions for v and σ, but these have no significant impact on the interpretation of the v/σ over σ relationship (see caption of Fig. 3.3).

The (U)LIRGs fill the gap between rotation-dominated spirals and dispersion-dominated ellipticals in the v/σ-σ plane. In particular, there is a clear transition among (U)LIRGs, with isolated (class 0), interacting (class 1), and merging (class 2) sources tending to increase their mean velocity dispersion while decreasing the velocity amplitude, therefore moving from high-σ and low-v/σ spirals to low-σ and high-v/σ ellipticals. Moreover, systems classified as class 0 (LIRGs in all cases) have mean velocities $v_{shear} = (150 \pm$

[5]Although there are two class 0 objects with relatively low v/σ (high σ), we note that one (IRAS F13229-2934, $v/\sigma \sim 1.4$) is known to be affected by the presence of an AGN (Arribas et al. 2012).

[6]While the LBAs have star formation rates (SFRs) similar to our local LIRGs, the spiral and E/S0 samples have considerably smaller rates (see Tab. 3.2).

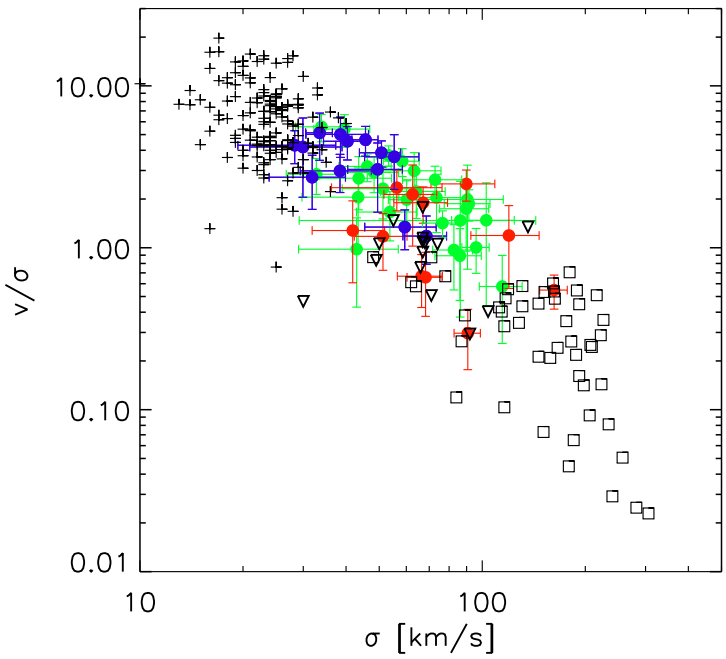

Figure 3.3: Relationship between the observed dynamical ratio v/σ, taking here the v_{shear}/σ_{mean} (see text) and the mean velocity dispersion. Color code is the same as the one adopted in previous figures. The plus signs represent spiral GHASP galaxies (i.e., Epinat et al. 2010), empty squares E/SO objects (i.e., Cappellari et al. 2007), and top-down empty triangles LBAs (i.e., Gonçalves et al. 2010). For the spirals the v parameter is defined as the maximum amplitude of the rotational curve within the extent of the velocity field along the major axis, and σ is the average of the velocity dispersion map. For E/S0, v and σ are luminosity-weighted square quantities derived, respectively, from the velocity field and velocity dispersion maps (see details in Cappellari et al. 2007). For the LBAs, the velocity shear v_{shear} has been defined as in this work, while the velocity dispersion is the flux-weighted mean value.

14) km s^{-1} similar to those of spirals (mean velocity amplitude of $\sim$ 160 km s^{-1}) but with much higher velocity dispersion σ_{mean} (i.e., 44 $\pm$ 4 km s^{-1}, while 24 km s^{-1} for spirals, see Tab. 3.2). This suggests that class 0 LIRGs are rotating disks, more turbulent and thicker than those of normal spirals. Therefore, the main difference between the global kinematic properties of these two samples, rather than the rotational amplitude, is the mean velocity dispersion, which is higher for LIRG disks. On the other hand, interacting (class 1) and merging systems (class 2) have lower dynamical ratios, with kinematical values closer to those obtained for the ellipticals. The trend observed in this plot is consistent with the idea that the process of merging in (U)LIRGs possibly transforms spiral galaxies into intermediate-mass ellipticals (e.g., Genzel et al. 2001; Tacconi et al. 2002; Dasyra et al. 2006b). These class 1 and 2 systems even share similar kinematical properties with the LBAs (see Tables 3.1 and 3.2), discussed in detail in Sect. 3.3.6.

When the number of resolution elements that characterizes a galaxy is small (i.e.,

Table 3.2: Mean (and median) observed kinematic properties for low-z comparison samples from the literature.

Sample	SFR $[M_\odot\ yr^{-1}]$	v (km s^{-1})	σ (km s^{-1})	v/ σ	R_{eff} (kpc)	M_{dyn} (10^{10} $M_\odot$)
(1)	(2)	(3)	(4)	(5)	(6)	(7)
Spiral	1.8 ± 0.4 (0.7)	162 ± 7 (143)	24 ± 0.5 (24)	7.0 ± 0.3 (6.3)	5.5 ± 0.3 (4.8)	11.5 ± 1.5 (4.9)
E/S0	0.12 ± 0.04 (0.08)	47 ± 4 (44)	162 ± 9 (163)	0.34 ± 0.03 (0.34)	2.9 ± 0.3 (2.4)	13.8 ± 3.2 (6.9)
LBA	26.7 ± 7.1 (17.0)	67 ± 11 (63)	71 ± 6 (67)	0.95 ± 0.11(1.1)	1.4 ± 0.1 (1.5)	1.0 ± 0.2 (1.0)

Col (1): Low-z sample: Spiral sample is drawn from Epinat et al. (2010), E/S0 from Cappellari et al. (2007) and LBAs from Gonçalves et al. (2010). Col (2): Star formation rate (SFR). For spirals, it has been derived using only 50 objects, for which the SFRs have been computed from Hα measurements by James et al. (2004) using Salpeter IMF (Salpeter 1955) and applying the Kennicutt et al. (1994) relation. For E/S0 galaxies we considered the SFR computed in Shapiro et al. (2010) for a subsample of 13 sources using the Spitzer/IRAC data at 8.0 μm. They have calibrated this relation from the Yun et al. (2001) relation between SFR and radio continuum. If the Kennicutt (1998) SFR-Hα conversion is applied to calibrate the 8.0 μm SFR estimator, the SFR would lower by $\sim$ 13% (see Wu et al. 2005). For the LBAs, the star formation rates are measured by Gonçalves et al. (2010) from combined Hα and MIPS 24 μm data using Kroupa (2008) IMF. The resulting SFRs are lower by a factor of $\sim$ 1.5 compared to a Salpeter (1955) IMF. Col (3): Observed velocity amplitude obtained as follows: for spirals, it is the observed maximum rotational velocity; for the E/S0 sample it is the luminosity-weighted squared velocity (i.e., $v = \sqrt{< v^2 >}$) within 1 R_{eff}; for LBAs the velocity amplitude has been defined as the v_{shear} in this work. Col (4): Velocity dispersion derived as follows: for spirals, it is the (uniformly weighted) mean velocity dispersion; for E/S0s it is the luminosity-weighted squared velocity dispersion(i.e., $\sigma = \sqrt{< \sigma^2 >}$) within 1 R_{eff}; for LBAs the velocity dispersion is the average velocity dispersion of each spaxel, weighted by flux. Col (5): Dynamical ratio determined as the ratio between the values shown in column (3) and (4). Col (6): Effective radius for the different samples. For spirals it has been derived as half of the optical radius (R_{opt}) associated with the isophotal level at 25 mag $arcsec^{-2}$ in the B-band, where $R_{opt} = 1.9 \times R_{eff}$ (see Epinat et al. 2009); for E/S0 the half-light radius is measured in the I-band from WFPC2/HST images; for LBAs the effective radius was derived by selecting N spaxels with S/N > 6 such that $R_{eff} = \sqrt{(N/\pi)}$ (see Law et al. 2007). Col (7): Dynamical mass determined as follows: for spirals we compute the total mass using the formula employed in their paper for rotation-dominated objects; we compute the dynamical masses for E/S0 using the formula $K\sigma^2$ R_{eff} /G as explained in Cappellari et al. (2006); finally, the dynamical masses of LBAs have been derived in Gonçalves et al. (2010) using the formula 5 σ^2 R_{eff}/G.

galaxy size $\sim$ PSF), the determination of the σ_{mean} values may be affected by the smearing of the velocity field and may lead to artificial peaks in the σ-map (see Davies et al. 2011). Due to the linear resolution limitations, this effect becomes common at higher redshift, as discussed in previous works (e.g., Förster Schreiber et al. 2009; Epinat et al. 2010). However, for local samples, which are observed with much higher linear resolution, this effect is generally neglected. Indeed, this correction was not applied for the local comparison samples used here (i.e., spiral and elliptical/lenticular galaxies). Our LIRGs have spatial scales somewhat larger than those characterizing those systems[7], but the smearing effects are still in general very small[8] and corrections for the individual galaxies

[7]The typical linear resolutions (seeing FWHM $\sim 1''$) of GHASP spirals and E/S0 galaxies are, respectively, 0.27 kpc and 0.09 kpc, while for our LIRGs and ULIRGs they are 0.48 kpc and 1.32 kpc, respectively.

[8]To estimate the smearing effects in our data, we have calculated the velocity gradients along the central regions of our systems and derived the typical range in velocities across a spaxel (δv). When

have not been applied.

On the other hand, there could be some bias when directly comparing our results with those of LBAs at z $\sim$ 0.2 (i.e., Gonçalves et al. 2010). They actually compute the mean velocity dispersion using a flux-weighted quantity. As stated in Davies et al. (2011), a flux-weighted mean velocity dispersion is biased towards bright regions, typically closer to the center, where the intrinsic rotation curve has a steeper gradient: the smearing is potentially more important and the mean velocity dispersion derived in Gonçalves et al. (2010) might be therefore considered as an upper limit[9].

3.3.5 (U)LIRG dynamical masses and mass ratios in interacting systems

Dynamical Mass determinations

Dynamical Mass determinations, which include the stellar, gas, and dark matter contributions, are relevant in the context of (U)LIRGs for several reasons. First, these objects have large amounts of gas and, therefore, the stellar mass gives only a partial estimate to their total mass (i.e., Downes & Solomon 1998; Combes et al. 2011). Second, in order to infer the stellar masses, the SED modeling is difficult due to the presence of several stellar populations (Rodríguez Zaurín et al. 2010), large amounts of dust (e.g., da Cunha et al. 2010), and the complex structure of the extinction (García-Marín et al. 2009; Piqueras López et al. 2013). Therefore, stellar mass measurements not only have their own uncertainties, but intrinsically represent a lower limit to the mass of these systems.

Colina et al. 2005 have found that the warm gas kinematics in ULIRGs is in general coupled to that of the stellar component; therefore, it can be used as tracer of the gravitational potential. The kinematic properties of the ionized gas obtained from our IFS velocity maps are used in the following to estimate the dynamical mass, M_{dyn}. As shown in previous sections, our sample contains systems with a wide range of kinematic properties, from regular rotating disk to merging systems. Hence, for deriving dynamical mass estimates we have used different approximations, distinguishing systems dominated by random motions from those with a large rotation component.

For spherical, bound, and dynamically relaxed systems with random motion, the dynamical mass can be estimated via the virial theorem as

quadratically subtracting δv from σ, it was confirmed that the effects of smearing are negligible (a few percent) for most of the systems. In the worst case (i.e., IRAS F06259-4780 S) the effect was $\sim$ 15% (see Tab. 3.3).

[9]The values of the flux-weighted mean velocity dispersion can be a factor of 1.5 - 3 larger than those derived for the uniformly weighted mean velocity dispersion (see Davies et al. 2011).

$$M_{dyn,vir} = \frac{K\ R_{hm}\ \sigma^2}{G} \approx f(R_{eff}), \tag{3.1}$$

where R_{hm} is the half-mass radius, σ is the mean velocity dispersion, the factor K takes into account the effects of structure on dynamics, and G is the gravitational constant (i.e., $4.3{\times}10^{-3}$ pc $M_{\odot}^{-1}$ (km s^{-1})^2). R_{hm} cannot be obtained directly and is estimated by measuring the half-light radius, R_{eff}, which encloses half the luminosity (see App. B for details).

Taylor et al. (2010) have recently studied the differential effects of non-homology in the dynamical mass determinations based on this formula. In particular, they analyzed the dependence of the K factor on the galaxy structure, parametrized by the Sérsic index n, assuming a spherical mass distribution that is dynamically isotropic and non-rotating, and which, in projection, follows a Sérsic (1963, 1968) surface density profile. According to their expression, the K factor ranges between 7.4 (n = 1, exponential profile) and 4.7 (n = 4, de Vaucouleurs) and gives an idea of the differential effects due to non-homology. We have considered a mean value of $K = 6$, which is also close to the one found by other authors[10] (e.g., Cappellari et al. 2006). Since this formula is only valid for nonrotating systems, we have applied it to galaxies with kinematics compatible with slow rotation (i.e., $v^*_{shear}/\sigma < 2$, where the v^*_{shear} corresponds to the v_{shear} value corrected by inclination i) and complex kinematic (CK) similar to those found by Colina et al. (2005) in ULIRGs.

For the rest of the systems showing a significant rotation component, we have derived the dynamical mass from the circular velocity, obtaining the mass enclosed within a given radius. In particular, we consider the total $M_{dyn} = 2\ M_{1/2}$, where $M_{1/2}$ is the dynamical mass within $r_{1/2}$, the radius that contains the three-dimensional half-light volume[11]. Thus, for an oblate spheroid (Williams et al. 2010),

$$M_{1/2} \approx \frac{v_c^2\ R_{eff}}{G}\ , \tag{3.2}$$

where v_c is the circular velocity at $r_{1/2}$. To infer the circular velocity we have considered both the rotation and dispersion motions. In particular, we included the "asymmetric drift" term, which represents an extra component due to the dispersion of the gas around the disk of the galaxy, following the prescriptions by Epinat et al. (2009) and Williams et al. (2010). Assuming a disk scale length, $h = \frac{r_{1/2}}{\sqrt{2ln2}}$ (Epinat et al. 2009):

[10] We note that the value of $K = 6$ corresponds to m=1.4 in Eq. (1) given in Colina et al. (2005), who used m=1.75, and therefore, the masses derived here are $\sim$ 20% lower than those derived with their formula.

[11] This radius is related to the effective radius by the relation $r_{1/2} \approx 1.33 \times R_{eff}$, for a wide range of radial profiles (e.g., Wolf et al. 2010).

$$M_{dyn} \approx \frac{2\, R_{eff}\, (v_{rot}^2 + 1.35\, \sigma^2)}{G}\,, \tag{3.3}$$

where v_{rot} and σ are the rotation and dispersion velocities and are taken here as the inclination-corrected v^*_{shear}, and σ_{mean}, respectively.

Mass determination can be affected by large uncertainties. In addition to those related to the implicit assumptions of the above expressions, the observed parameters R_{eff}, v_{shear}, and σ_{mean} have their own uncertainties. The use of different tracers (e.g., IR-continuum, Hα) may lead to discrepancies (see App. B for further details). Rotation velocities for individual objects can be significantly affected by the inclination correction, which therefore has an important impact on the M_{dyn} determination due to its quadratic dependence on v^*_{shear} in Eq. (3.3). For a relatively small number of objects (i.e., 8/51) we applied an average inclination correction following Law et al. 2009. Those have a relatively large uncertainty in i, but we apply Eq. (3.3) instead of Eq. (3.1) only for four. As for σ_{mean}, the fact that we are considering the values corresponding to the narrow component (Sect. 3.2.1) minimizes possible effects due to radial motions like outflows, which are generally associated with the broad component. We therefore estimate that the present masses should be corrected on average within a factor of ~ 3.

Dynamical Mass in (U)LIRGs

The Dynamical Mass estimates for the whole (U)LIRG sample range from $\sim 5 \times 10^9$ $M_\odot$ to 2×10^{11} $M_\odot$, with a mean (median) value of $(4.8 \pm 0.6) \times 10^{10}$ $M_\odot$ (3.3×10^{10} $M_\odot$), confirming that (U)LIRGs are intermediate mass systems like previously suggested (i.e., Tacconi et al. 2002; Colina et al. 2005; though Rothberg & Fischer 2010 and Rothberg et al. 2013 find that (U)LIRGs masses are consistent with those of the most massive elliptical galaxies). In terms of $m_\star$ (i.e., $m_\star = 1.4 \times 10^{11}$ $M_\odot$; see Cole et al. 2001), these values correspond to a mean value of (0.35 ± 0.04) $m_\star$ and median of 0.24 $m_\star$. The range of mass covered by the present (U)LIRGs overlaps with those of galaxies in the GHASP and SAURON, although these surveys also include galaxies with masses of ~ 7 $m_\star$ (i.e., $\sim 10^{12}$ $M_\odot$), which are not seen in our sample of (U)LIRGs.

The ULIRGs are more massive than LIRGs by, on average, a factor of about 2 (see Tab. 3.1). The present mean value for ULIRGs of (0.51 ± 0.19) $m_\star$ is between those obtained by Colina et al. (2005) (i.e., 0.4 $m_\star$) and Tacconi et al. (2002) (i.e., 0.86 $m_\star$). If the present sample of ULIRGs is combined with those of Colina et al. (2005) and García-Marín et al. (2007) a mean and median mass values of (0.68 ± 0.13) $m_\star$ and 0.5 $m_\star$ are, respectively, derived. These are also in good agreement with those found in Dasyra et al.

(2006b), where ULIRGs show dynamical masses between sub- and $\sim m_\star$.

Furthermore, in order to homogenize our results with those derived for the INTEGRAL/WHT data, in App. D we compute the dynamical masses of the ULIRG sample observed with this instrument using our approach (i.e., following the $v^*/\sigma = 2$ criterium, as explained in Sect. 3.3.5). We notice that the M_{dyn} derived according to our formulas are a factor ~ 2 lower than those derived when applying the Colina et al. (2005) formula. In part, this discrepancy can be explained as due to a different constant K used in Eq. 3.1, as explained in footnote 10.

The different morphological/kinematical classes do not show a clear trend with M_{dyn} (Tab. 3.1). The mean M_{dyn} for classes 0, 1, and 2 define a weak decreasing sequence, with relatively low statistical significance. Under the assumption that class 2 objects are made by the merger of two class 0 (or individuals classified as 1), one should expect masses for the mergers that are larger (by a factor 2) than those of individual pre-coalescence galaxies, contrary to what is found. To analyze this topic further, we selected the individual galaxies of ten pre-coalescence multiple systems (i.e., 19 LIRGs), and derived a mean dynamical mass and the respective mass ratio between each merging galaxy pair[12]. The mean dynamical mass derived for these sources is $(0.33 \pm 0.05)\ m_\star$: it seems too high when compared with the mean mass for the post-coalescence mergers (i.e., $M_{dyn} = 0.34 \pm 0.14\ m_\star$). However, we point out the limited statistical significance of this result, especially taking into account that two objects (i.e., IRAS F09437+0317 N and IRAS F14544-4255 E) deviate about 3 standard deviation from rest. If these are excluded, a typical mass of $(0.28 \pm 0.04)\ m_\star$ is obtained for pre-coalescence galaxies, a value that is still high if compared with that derived for class 2 objects. This can be explained as due to our L_{IR} selection: a low-mass system may exceed a given infrared luminosity threshold only in the most intense starburst phase, while a higher mass system may pass this threshold even in a more quiescent phase. Since we select sources with $L_{IR} > 10^{11}\ L_\odot$, the fraction of large mass systems in the less active phases (e.g., type 0) is expected to be larger than in the most active ones (e.g., type 2).

A large fraction of the pre-coalescence systems (seven out of ten) have a mass ratio $\leq$ 2.4, with a mean value of 2.0 ± 0.4, while the other three have ratios of 3, 4.3, and 20 (i.e., IRAS F06259-4780, IRAS F14544-4255, and IRAS F12043-3140[13], respectively).

[12]For triple systems we consider the ratio between the two more massive sources. The dynamical mass estimation for the northern galaxy of the system F07027-6011 was not possible due to the presence of an AGN.

[13] Although the relatively high dynamical mass ratio derived for the system IRAS F12043-3140 would suggest that the northern source might be considered as a satellite-galaxy of the southern one, the relative stellar distribution (i.e., continuum map) suggests that the northern system is almost face-on and the mass ratio may be smaller.

These results are in good agreement with the findings by Dasyra et al. (2006a), who found that the majority of ULIRGs are triggered by almost equal-mass major mergers of 1.5:1 average ratio, which indicates that ULIRGs are mainly the products of almost equal mass mergers (i.e., sub-$m_\star$ galaxies; e.g., Tacconi et al. 2002; Colina et al. 2005; Dasyra et al. 2006b)

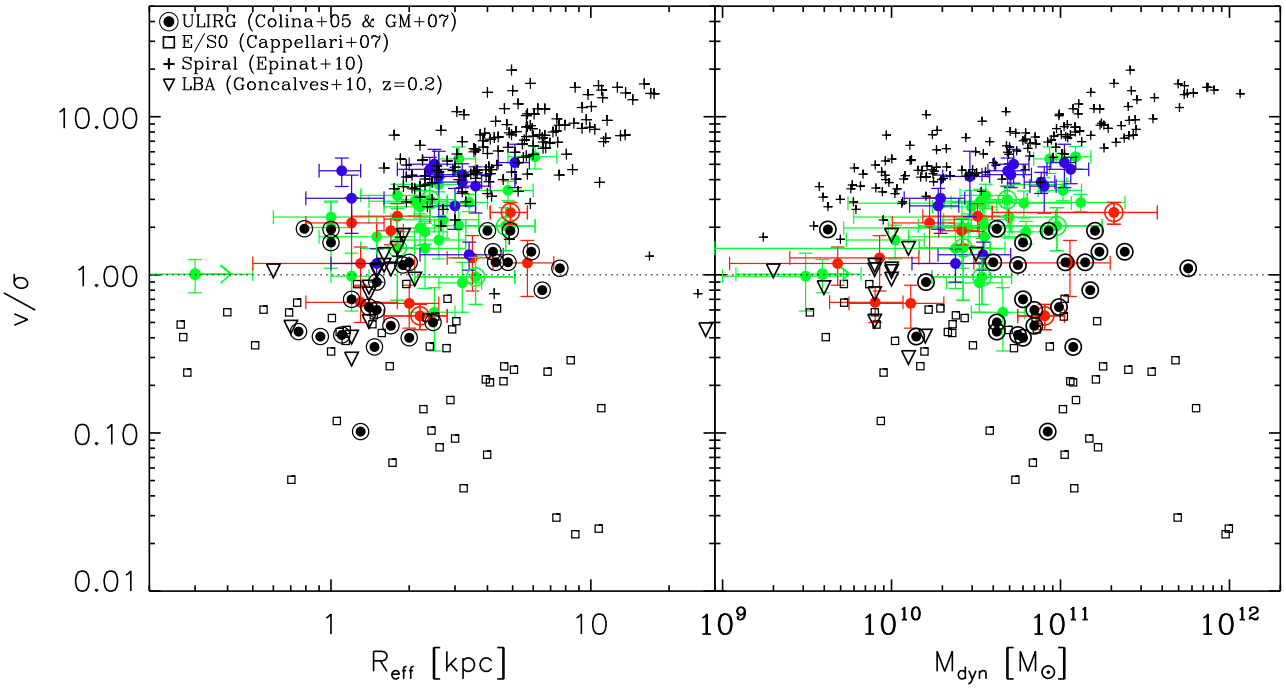

Figure 3.4: Observed (i.e., not inclination corrected) v/σ ratio as a function of the effective radius R_{eff} (left panel) and dynamical mass M_{dyn} (right panel) is shown (see text). The colors used are the same as in the previous figures (i.e., blue for isolated disks, green for interacting galaxies and red for mergers). We identify ULIRGs with a second circle around the dots. The other samples are represented as follows: the nearby isolated spiral galaxies from the GHASP survey (see Epinat et al. 2010) are represented with cross symbols. Local ellipticals and lenticular objects, drawn from Cappellari et al. (2007), are shown with empty squares. LBAs, drawn from Gonçalves et al. 2010, are represented with empty downward triangles, with values derived using the Pa-α line. For these three samples, the effective radii R_{eff}, dynamical ratios v/σ, and dynamical masses M_{dyn} have been derived as explained in the caption of Tab. 3.2. We finally add the ULIRG systems studied in Colina et al. (2005) and those studied in García-Marín et al. (2007) (i.e., empty circle surrounding the black solid dot). In general, Colina et al. (2005) derived their effective radius from the H-band measured using F160W Near Infrared Camera and Multi-Object Spectrometer (NICMOS/HST) images (only for two sources were the F814W WFPC2/HST images used instead). In García-Marín et al. (2007) the effective radius considered is the one derived from the I-band (i.e., F814W) images. For both of the samples, their v/σ ratio is obtained considering the half peak-to-peak velocity difference, and the central velocity dispersion σ_c, applying one Gaussian component fitting to the Hα emission line data. Their dynamical masses are derived using a constant of $K = 7.5$ (see footnote 10 for further details) and the central velocity dispersion σ_c (Colina et al. 2005).

Table 3.3: Kinematic properties of the narrow component for the (U)LIRG sample.

Galaxy ID (IRAS code)	v_{sys} (km s^{-1})	v_{amp} (km s^{-1})	v_{shear} (km s^{-1})	σ_{mean} (km s^{-1})	σ_c (km s^{-1})	$\frac{v^*_{shear}}{\sigma_{mean}}$	i degree	δv (km/s/spx)	K class	M_{dyn} (10^{10} M$_\odot$)	Com
(1)	(2)	(3)	(4)	(5)	(6)	(7)	(8)	(9)	(10)	(11)	(12)
F06295-1735	6373	107 ± 15	87 ± 8	32 ± 9	44 ± 7	3.5 ± 1.1	52 ± 7	4.6	PD	1.9 ± 0.6	vii
F06592-6313	6942	160 ± 11	151± 9	49 ± 20	96 ± 20	3.6 ± 1.5	58 ± 8	12.7	PD	2.0 ± 0.8	v
F07027-6011 S	9270	95 ± 34	81 ± 10	69 ± 14	59 ± 5	2.4 ± 0.7	29 ± 4	12.7	RD	2.4 ± 1.1	v
F07027-6011 N	9582	124 ± 14	115 ± 9	38 ± 9	63 ± 10	3.9 ± 1.0	50 ± 5	10.4	PD	-	iii, v
F07160-6215	3297	237 ± 28	202 ± 10	55 ± 18	128 ± 17	3.8 ± 1.2	75 ± 3	6.2	PD(CK)	8.0 ± 1.4	iv,vii
F10015-0614	5143	218 ± 29	196 ± 7	51 ± 7	60 ± 10	4.3 ± 0.7	63 ± 3	5.3	PD	7.7 ± 1.6	iv,vii
F10409-4556	6241	214 ± 12	193 ± 8	39 ± 9	90 ± 13	5.4 ± 1.3	68 ± 6	7.2	RD	5.3 ± 1.2	iv,v
F10567-4310	5129	149 ± 11	122 ± 9	28 ± 4	52 ± 8	6.4 ± 1.1	42 ± 2	5.9	RD	5.1 ± 1.7	iv,v
F11255-4120	4958	149 ± 13	125 ± 9	30 ± 13	82 ± 25	5.1 ± 2.3	56 ± 2	5.4	PD	2.9 ± 0.9	v
F11506-3851	3114	202 ± 9	184 ± 6	40 ± 8	81 ± 18	7.6 ± 1.6	37 ± 3	13.7	RD	4.9 ± 1.2	v
F12115-4656	5282	221± 29	212 ± 4	46 ± 8	78 ± 20	6.9 ± 1.4	42 ± 3	12.8	RD	11.5 ± 3.2	v
F13229-2934	4059	115 ± 24	80 ± 14	59 ± 6	64 ± 10	2.2 ± 0.5	37 ± 3	5.6	CK	3.5 ± 1.6	vii
F22132-3705	3500	186 ± 5	172 ± 3	33 ± 10	76 ± 15	6.2 ± 1.9	56 ± 4	7.7	RD	10.5 ± 1.8	iv,v
F01159-4443 S	6930	130 ± 17	117 ± 13	46 ± 11	71 ± 16	3.7 ± 1.1	46 ± 8	13.6	PD	3.0 ± 1.2	ii,iv,vii
F01159-4443 N	6792	145 ± 25	119 ± 13	51 ± 12	50 ± 8	6.3 ± 3.0	22 ± 9	16.6	PD	5.0 ± 4.4	ii,vii
F01341/ESO G12	5240	199 ± 59	156 ± 45	90 ± 15	61 ± 18	2.2 ± 0.8	52 ± 10	6.4	PD	6.1 ± 5.5	i,vii
F01341/ESO G11	5200	111 ± 11	93 ± 6	33 ± 6	43 ± 9	7.3 ±3.5	23 ± 11	10.8	PD	3.5 ± 2.3	vii
F06035-7102	23867	184 ± 27	150 ± 26	74 ± 19	63 ± 18	2.6 ± 1.4	52 ± 26	12.9	CK	9.5 ± 8.1	vi
F06076-2139 S	11810	118 ± 38	89 ± 18	43 ± 14	51 ± 11	3.4 ± 1.3	37 ± 3	10.7	PD	3.5 ± 1.5	ii,v
F06076-2139 N	11199	83 ± 52	77 ± 24	86 ± 13	87 ± 11	1.2 ± 0.5	46 ± 11	17.2	PD	3.3 ± 1.2	i, ii, iv, v
F06206-6315	27669	203 ± 21	189 ± 18	64 ± 13	75 ± 23	3.1 ± 0.7	76 ± 10	10.3	PD	4.8 ± 1.5	v
F06259-4780 S	11736	213 ± 19	198 ± 13	53 ± 4	37 ± 6	4.7 ± 0.7	53 ± 9	22.5	RD	7.9 ± 2.9	i,v
F06259-4780 C	11587	104 ± 22	89 ± 12	54 ± 11	47 ± 13	1.9 ± 0.5	62 ± 11	6.6	RD	1.1 ± 0.5	ii, v
F06259-4780 N	11935	229 ± 41	180 ± 64	91 ± 25	77 ± 19	2.3 ± 1.1	58 ± 9	20.7	RD	2.6 ± 1.7	ii, v
08424-3130 S	4914	133 ± 31	119 ± 23	60 ± 7	83 ± 25	2.5 ± 1.2	52 ± 26	11.0	PD	2.8 ± 2.3	ii, iv,vi
08424-3130 N	5029	67 ± 50	66 ± 27	114 ± 16	119 ± 17	0.7 ± 0.5	52 ± 26	-	-	4.6 ± 1.6	ii,iv,vi,viii
F08520-6850 E	13518	123 ± 10	109 ± 15	77 ± 10	100 ± 40	1.6 ± 0.3	62 ± 6	7.9	RD	2.0 ± 0.7	ii, vii
F08520-6850 W	13736	196 ± 12	191 ± 16	73 ± 14	92 ± 20	2.7 ± 0.6	77 ± 4	12.6	PD(RD)	11.3 ± 2.8	ii, vii
F09437+0317 S	5966	236 ± 22	214 ± 9	40 ± 7	50 ± 9	6.1 ± 1.2	63 ± 4	8.0	RD	8.6 ± 1.7	i,v
F09437+0317 N	5983	134 ± 11	189 ± 6	34 ± 5	56 ± 8	6.0 ± 1.0	68 ± 5	4.1	RD	12.3 ± 2.8	iv,v
12043-3140 S	7009	191 ± 35	171 ± 11	101 ± 15	82 ± 21	2.4 ± 0.4	52 ± 2	12.7	PD	6.3 ± 1.6	ii,v
12043-3140 N	7030	54 ± 10	42 ± 10	43 ± 14	51 ± 8	1.2 ± 0.7	52 ± 26	6.5	PD(CK)	0.3 ± 0.2	ii,vi
F12596-1529	4875	163 ± 22	143 ± 14	64 ± 14	66 ± 18	2.3 ± 0.6	75 ± 3	5.9	-	3.5 ± 1.4	iv,vii, viii
F14544-4255 E	4714	220 ± 88	200 ± 15	60 ± 7	63 ± 6	3.5 ± 0.5	78 ± 4	7.6	PD	10.4 ± 3.0	i,vii
F14544-4255 W	4800	146 ± 35	127 ± 11	86 ± 37	82 ± 16	1.7 ± 0.8	59 ± 7	8.7	CK(PD)	2.4 ± 2.3	i,vii
F18093-5744 S	5328	155 ± 7	141 ± 10	48 ± 9	62 ± 13	1.2 ± 0.3	53 ± 6	10.3	RD	3.4 ± 1.3	v
F18093-5744 C	4969	130 ± 25	96 ± 21	96 ± 9	77 ± 25	4.4 ± 0.8	56 ± 4	7.3	CK(PD)	$>$ 0.4 ± 0.3	i,vii
F18093-5744 N	5184	159 ± 9	147 ± 3	46 ± 8	58 ± 7	3.7 ± 0.8	47 ± 3	7.0	RD	3.6 ± 1.1	v
F22491-1808	23283	88 ± 44	80 ± 24	83 ± 11	71 ± 19	1.4 ± 0.5	44 ± 3	10.6	CK(PD)	3.4 ± 1.7	v
F23128-5919	13448	260 ± 62	152 ± 75	103 ± 21	110 ± 23	1.9 ± 1.0	53 ± 8	14.2	CK	2.7 ± 1.2	vii
F04315-0840	4668	162 ± 36	134 ± 11	63 ± 28	70 ± 28	2.5 ± 1.1	58 ± 4	5.6	CK	1.7 ± 0.7	vii
F05189-2524	12808	30 ± 19	27 ± 8	91 ± 10	90 ± 10	0.9 ± 0.5	18 ± 9	6.3	CK	-	iii,vii
08355-4944	7782	73 ± 14	60 ± 9	51 ± 12	44 ± 12	1.5 ± 0.8	52 ± 26	5.0	PD	0.5 ± 0.4	vi
09022-3615	17918	110 ± 36	89 ± 15	162 ± 12	105 ± 12	1.1 ± 0.2	29 ± 2	12.1	CK	8.1 ± 2.5	v
F10038-3338	10287	54 ± 18	45 ± 8	68 ± 16	64 ± 16	0.8 ± 0.4	52 ± 26	5.8	CK	1.3 ± 0.7	vi
F10257-4339	2813	170 ± 34	132 ± 20	56 ± 7	65 ± 7	3.3 ± 0.9	45 ± 10	6.5	PD	3.2 ± 1.7	iv,vii
12116-5615	8163	52 ± 19	44 ± 10	66 ± 9	51 ± 9	0.9 ± 0.2	48 ± 4	7.3	PD	0.8 ± 0.4	v
F13001-2339	6540	169 ± 110	142 ± 27	120 ± 25	116 ± 34	1.3 ± 0.5	65 ± 4	11.9	CK	11.4 ± 8.3	v
F17138-1017	5274	144 ± 21	128 ± 12	67 ± 11	59 ± 11	2.4 ± 0.5	52 ± 8	12.9	PD	2.6 ± 0.7	vii
F21130-4446	28028	228 ± 28	223 ± 19	90 ± 12	69 ± 12	3.2 ± 1.5	52 ± 26	22.1	CK	20.7 ± 16.8	vi
F21453-3511	4816	78 ± 29	53 ± 10	42 ±14	70 ± 14	1.6 ± 0.6	51 ± 2	3.7	PD	0.9 ± 0.6	iv,vii

Notes Derived Hα kinematic quantities for the narrow (systemic) component. Horizontal lines distinguish class 0, 1, and 2 (from top to bottom, respectively). Col (1): IRAS name. Col (2): Systemic velocity calculated as the Hα radial velocity. A mean error of 5-7 km s^{-1} should be added when calibration and fitting errors are considered. Col (3): Hα velocity amplitude defined as the half of the observed 'peak-to-peak' velocity (i.e., half the difference between the maximum and minimum values is considered without applying the inclination correction). Col (4): Hα velocity shear defined as the half of the difference between the median of the 5 percentile at each end of the velocity distribution (i.e., $v^{5\%}_{max}$ and $v^{5\%}_{min}$), as in Gonçalves et al. (2010) (not corrected for the inclination).

Continues on next page

Continued from previous page.

Notes Col (5): Hα mean velocity dispersion. Col (6): Hα central velocity dispersion, derived as the mean of 4 $\times$ 4 spaxels around the VIMOS continuum flux peak. Col (7): Dynamical ratio between the velocity shear (corrected for the inclination) and the mean velocity dispersion values. Col (8): Inclination of the galaxy, defined as $i = \cos^{-1}(b/a)$ (i.e., where a and b are, respectively, the major and minor axes of the object). When possible, it has been inferred directly from the Hα map or continuum images (i.e., DSS, HST and 2MASS). When the morphology of the object was too complex, we assumed a mean inclination of about 52°$\pm$ 26°, equivalent to $< sin\, i > = 0.79 \pm 0.35$ (see appendix in Law et al. 2009). In this case, the uncertainty of the inclination has been computed as the standard deviation of the distribution of the different measures derived when i varies from 0° to 90°, using step of 1°. See details in Col. (12), notes (v, vi, vii). Col (9): Velocity gradient (km s^{-1}) associated with one spaxel derived as explained in the text. Col (10): Kinematical classification inferred from the kinematic maps. RD stands for rotating disk, PD perturbed disk and CK are systems with complex kinematics (see text for details). The galaxy IRAS 08424-3130 N is in the edge of the FoV, and its kinematic classification was not possible. For those objects for which the kinematical classification is controversial, the possible classifications are shown in the table. Col (11): Dynamical masses (see text). Col (12): Comments with the following code: (i) After distributing the total IR luminosity between the individual objects forming the system, this galaxy does not qualify as LIRG as its luminosity is lower 10^{11} $L_{\odot}$. The galaxies IRAS F01341-3735 N and IRAS F09437+0317 N are in the limit to be classified as LIRG (see Col. (6) in Table 2.1). (ii) Systems for which a mask has been applied to the data-cube in order to analyze separately the sources (e.g., N and S stand for northern and southern galaxies). (iii) No R_{eff}^{IR} reliable due to AGN contamination (see Arribas et al. 2012 and App. B for details). (iv) For this galaxy two pointings have been combined to derive the kinematic values. (v) The inclination has been derived using the Hα map. (vi) A mean inclination (i.e., 52° $\pm$ 26°) has been considered. (vii) The inclination has been derived using continuum available images (i.e., HST or DSS or 2MASS). (viii) The kinematic classification was not possible due to the poor linear resolution for IRAS F12596-1529, while the emission of the IRAS 08424-3130 N is only partially included in the FoV.

Table 3.4: Kinematic properties of the broad component for the (U)LIRG sample.

Galaxy ID (IRAS code)	v_{amp} (km s^{-1})	σ_{mean} (km s^{-1})	Area (kpc^2)	v_{amp}/σ_{mean}	Δv offset (km s^{-1})
(1)	(2)	(3)	(4)	(5)	(6)
F06295-1735	90 ± 35	110 ± 23	1.33	0.8 ± 0.4	-3
F06592-6313	217 ± 133	219 ± 18	1.2	1.0 ± 0.6	-285
F07027-6011S	59 ± 10	124 ± 8	6.0	0.5 ± 0.1	-17
F07027-6011N	17 ± 5	316 ± 12	5.1	0.05 ± 0.02	-256
F07160-6215	152 ± 22	91 ± 12	0.3	1.7 ± 0.3	55
F10015-0614	66 ± 32	103 ± 12	1.1	0.6 ± 0.3	-37
F10409-4556	90 ± 97	82 ± 69	0.5	1.1 ± 1.5	-120
F10567-4310	65 ± 47	138 ± 19	1.0	0.5 ± 0.4	-54
F11255-4120	52 ± 49	178 ± 14	0.5	0.3 ± 0.3	-83
F11506-3851	77 ± 30	76 ± 16	0.3	1.0 ± 0.5	-42
F12115-4656	21 ± 20	93 ± 12	1.0	0.2 ± 0.1	69
F13229-2934	143 ± 30	191 ± 40	2.5	0.7 ± 0.2	-39
F22132-3705	-	-	-	-	-
F01159-4443 S	76 ± 10	39 ± 8	1.5	2.0 ± 0.5	-159
F01159-4443 N	84 ± 13	142 ± 58	3.5	0.6 ± 0.3	-37
F01341/ESO G11	71 ± 20	110 ± 28	1.5	0.7 ± 0.3	-24
F01341/ESO G12	142 ± 25	114 ± 10	1.1	1.3 ± 0.3	-49
F06035-7102	19 ± 13	139 ± 25	16.2	0.1 ± 0.1	-28
F06076-2139 S	38 ± 35	91 ± 44	2.5	0.4 ± 0.4	-243
F06076-2139 N	7 ± 11	208 ± 8	1.7	0.03 ± 0.05	-100
F06206-6315	42 ± 38	198 ± 46	6.6	0.2 ± 0.2	-229
F06259-4780 S	-	-	-	-	-
F06259-4780 C	16 ± 15	111 ± 14	2.1	0.14 ± 0.14	63
F06259-4780 N	87 ± 34	133 ± 24	3.5	0.7 ± 0.4	76
08424-3130 S	22 ± 17	109 ± 12	0.5	0.7 ± 0.1	31
08424-3130 N	69 ± 64	128 ± 26	0.3	0.2 ± 0.6	-130
F08520-6850 E	-	-	-	-	-
F08520-6850 W	52 ± 40	130 ± 10	3.7	0.5 ± 0.3	-151
F09437+0317 S	-	-	-	-	-
F09437+0317 N	77 ± 53	106 ± 60	1.3	0.8 ± 0.6	-70
12043-3140 S	203 ± 145	144 ± 26	4.5	1.4 ± 1.0	-42
12043-3140 N	-	-	-	-	-
F12596-1529	145 ± 49	166 ± 14	0.9	0.9 ± 0.3	0
F14544-4255 E	189 ± 89	48 ± 62	0.6	3.9 ± 5.4	26
F14544-4255 W	175 ± 36	241 ± 46	1.5	0.7 ± 0.2	-52
F18093-5744 C	47 ± 24	105 ± 22	1.5	0.5 ± 0.3	-52
F18093-5744 N	34 ± 20	96 ± 15	0.8	0.4 ± 0.2	39
F18093-5744 S	68 ± 66	153 ± 34	0.6	0.4 ± 0.5	-85
F22491-1808	22 ± 22	117 ± 15	9.7	0.2 ± 0.2	-5
F23128-5919	435 ± 63	274 ± 85	54.7	1.6 ± 0.5	-32
F04315-0840	260 ± 54	211 ± 41	8.6	1.2 ± 0.4	-167
F05189-2524	59 ± 40	269 ± 28	14.5	0.2 ± 0.2	-400
08355-4944	63 ± 14	127 ± 10	7.9	0.5 ± 0.1	-19
09022-3615	35 ± 28	216 ± 17	11.9	0.16 ± 0.13	23
F10038-3338	82 ± 89	123 ± 44	2.5	0.7 ± 0.8	-100
F10257-4339	144 ± 38	106 ± 17	5.2	1.4 ± 0.4	-2
12116-5615	50 ± 20	154 ± 25	2.4	0.32 ± 0.14	-55
F13001-2339	137 ± 109	144 ± 38	1.6	1.0 ± 0.8	-24
F17138-1017	4 ± 3	83 ± 8	0.3	0.05 ± 0.04	65
F21130-4446	30 ± 34	113 ± 8	8.0	0.3 ± 0.3	-198
F21453-3511	113 ± 89	266 ± 43	1.3	0.4 ± 0.3	-129

Derived Hα kinematic quantities for the broad component. Horizontal lines distinguish class 0, 1, and 2 (from top to bottom), respectively). Column (1): IRAS name. Column (2): Velocity amplitude. Column (3): Mean velocity dispersion. Column (4): Area covered by the broad component. Column (5): Dynamical ratio between the velocity amplitude (Col. 2) and the mean velocity dispersion (Col. 3). Column (6): Velocity offset, computed as the difference between the mean velocity of the broad and the narrow components. Negative values represent blueshifted values while positive ones are redshifted.

3.3.6 Low-z (U)LIRGs versus LBAs

While low-z (U)LIRGs represent extreme IR-luminous, dusty starbursts in our nearby universe, other type of galaxies, the UV-luminous (i.e., LBA, Heckman et al. 2005), represent the class of (almost) extinction-free starbursts, showing SFRs similar to those of some local LIRGs (see Tab. 3.2). Both low-z IR and UV-bright galaxies are also considered local analogs of SFGs at cosmological distances, SMGs, and LBGs, respectively. So, it is important to establish a direct comparison of the overall kinematics and dynamical mass estimates of both samples based on IFS. Mean kinematic properties and dynamical masses for both samples are given in Tables 3.1 and 3.2), respectively. The corresponding values for local spirals and ellipticals based on IFS are also given for comparison.

On average, IR-luminous galaxies are much more massive than the UV-luminous galaxies with LIRGs and ULIRGs about five and ten times more massive than LBAs, respectively. Differences also clearly exist between (U)LIRGs and LBAs in their kinematics. The observed mean dynamical ratio (v/σ) for all (U)LIRGs is 2.5 larger than for LBAs, indicating that in general IR-luminous galaxies appear to be more rotation-supported than the UV-luminous galaxies. This is particularly true when only (U)LIRGs classified as isolated (class 0) are considered, while interacting (class 1) and merging (class 2) galaxies have, respectively, a ratio of 2.3 $\pm$ 0.2 and 1.3 $\pm$ 0.2, with the latter being much closer to that derived for LBAs (i.e., 0.95 $\pm$ 0.11). Detailed HST imaging of LBAs detected faint tidal features and companions around all LBAs imaged (i.e., Overzier et al. 2008), suggesting that UV-bright starbursts are the product of an interaction or merger. Looking independently at the kinematic tracers (i.e., velocity amplitude and velocity dispersion), there is a clear trend among (U)LIRGs such that the amplitude of the velocity field decreases from isolated to interacting and merging systems while the velocity dispersion increases. The LBAs have a mean velocity dispersion (i.e., 71 $\pm$ 6 km s^{-1}) much higher than that of isolated (U)LIRGs (i.e., 44 $\pm$ 4 km s^{-1}); however they are similar to that of interacting (i.e., 67 $\pm$ 3 km s^{-1}) and mergers (i.e., 80 $\pm$ 11 km s^{-1}). These velocity dispersions are factors of 3 to 4 larger than those of normal spirals (24 $\pm$ 0.5 km s^{-1}, see Epinat et al. 2010), and indicate that the starburst and the interaction/merging process play a dominant role in establishing the kinematic properties of the gas, likely due to combined effect of stellar winds and tidal forces.

So, independent of the overall mass of the system and of whether it is dusty (i.e., class 1 and 2 (U)LIRG) or not (i.e., LBA), the kinematics of low-z starburst galaxies is dominated by the star formation and the tidal forces, and produces dynamically hot systems characterized by an average $\sigma \sim$ 70-80 km s^{-1} and $v/\sigma \sim$ 1-2.

3.4 Summary and conclusions

Using the VIMOS IFS on the VLT, we have obtained spatially resolved kinematics (i.e., velocity fields and velocity dispersion maps) of 38 local (z $<$ 0.1) LIRGS and ULIRGs (51 individual sources). The sample includes sources with different morphological types (i.e., spirals, interacting systems, merger remnants) and is therefore well suited to study the kinematic properties of the (U)LIRG population showing different dynamical phases. A large fraction of the sample galaxies (31/38) covers the relatively less studied LIRG luminosity range, which fills the gap between the ULIRGs and the population of star-forming galaxies at large. This sample has been supplemented by a sample of low-z ULIRGs with their own available IFS (i.e., INTEGRAL/WHT data).

The main results of this chapter can be summarized as follows:

- The Hα emission line profile is well fitted with one or two Gaussians per emission line in most of the spectra, which have allowed us to identify two kinematically distinct components in the systems. One of these components (i.e., 'systemic' or 'narrow' component) is found over the whole line-emitting region of the system is characterized by spatially resolved mean velocity dispersions of $\sigma_{mean} \approx$ 30-160 km s^{-1}. The second component ('broad' component) is found in the inner (spatially resolved) regions of most of LIRGs and ULIRGs. It is characterized by relatively large line widths $\sigma_{mean} \sim$ 320 km s^{-1}, and its central velocity is blueshifted with respect to the systemic component for most of the objects with values up to $\sim$ 400 km s^{-1}. The largest extensions and extreme kinematic properties of the broad component are observed in interacting and merging systems. This component likely traces nuclear outflows.

- The systemic component traces the overall velocity field and shows a large variety of kinematic 2D structures, from very regular velocity patterns typical of pure RD (29%) to kinematically PD (47%), and highly disrupted and CK (24%). Thus, most of the objects (76%) are dominated by rotation. This fraction is larger than previously found in samples of ULIRGs. In fact, we found that the importance of rotation anti-correlates with the infrared luminosity, with a higher fraction of objects with complex kinematics among ULIRGs than in LIRGs (respectively, 6/7 vs. 6/42).

- We find a clear correlation between the different phases of the merging process and the mean kinematic properties inferred from the velocity maps. In particular, isolated disks, interacting galaxies, and merging systems define a sequence of increasing mean velocity dispersion and decreasing velocity field amplitude, which

is characterized by intrinsic average dynamical ratios (v*/σ) of 4.7, 3.0, and 1.8, respectively. We also find that the σ_c/σ_{mean} vs. σ_{mean} plane is an excellent discriminator between disks and interacting/merging systems, with disks showing higher σ_c/σ_{mean} and lower σ_{mean} values by factors of 1.5 to 2, on average.

- In terms of dynamical support (v/σ), the sample covers the gap between local spirals and E/SOs. The LIRGs classified as isolated disks partially overlap with the values of local spirals, with similar velocity amplitudes but larger mean velocity dispersions σ_{mean} (44 vs. 24 km s^{-1}), implying a larger turbulence and thicker disks. Interacting systems and mergers have values closer to those of low-velocity dispersion E/SOs, though with higher velocity amplitudes.

- The dynamical mass estimates for the present (U)LIRG sample range from $\sim$ 0.04 to 1.4 m$_\star$, with ULIRGs ($\sim$ 0.5 $\pm$ 0.2 m$_\star$) more massive than LIRGs by, on average, a factor of about 2. The mass ratio of individual pre-coalescence galaxies is $<$ 2.5 for most of the systems, confirming that most (U)LIRG mergers involve sub-m$_\star$ galaxies of similar mass.

- The subclass of (U)LIRGs classified as mergers and the LBAs share similar kinematic properties, although the dynamical mass of LBAs is a factor 5 smaller, on average. This is a clear indication that, independent of the mass of the system and of whether it is dusty or dust-free, starburst winds and tidally induced forces produce dynamically hot systems characterized by $\sigma \sim$ 70-80 km s^{-1} and v/$\sigma \sim$ 1-2.

Chapter 4

Distinguishing *disks* from *mergers*: tracing the kinematic asymmetries in local (U)LIRGs using *kinemetry*-based criteria

As found in Chapter 3, (U)LIRGs show a large variety of 2D kinematic structures, from very regular velocity patterns to highly disrupted and complex kinematics.

In this chapter, the 'kinemetry' methodology (developed by Krajnovíc and coworkers) is used, as a tool able to quantify kinematic asymmetries in the velocity field and velocity dispersion maps of the systems with respect to those characterizing an ideal rotating disk. This will allow us to develop methods and criteria for distinguishing between disks and mergers using the 2D kinematic maps, which in turn is relevant for constraining different evolutionary galaxy evolutionary models, as we have seen in Chapter 1. To this aim, we first select a small sub-sample of four LIRGs for which the morphology is clearly known (i.e., two isolated disks and two post-coalescence mergers) and located at the same distance to avoid relative resolution effects. The 'kinemetry' method is first applied using the criteria proposed by Shapiro et al. (2008). We also propose a new optimized kinematic criterion in order to differentiate in a more robust way disks and mergers (i.e., Bellocchi et al. 2012), locally and at high-z.

In the second part of this chapter (Sect. 4.3), the methods previously considered are applied to the whole sample, which allow us to draw more general conclusions.

4.1 General context

As pointed out in the Introduction (Chapter 1), the kinematic characterization of different galaxy populations is a key observational input to distinguish between different galaxy evolutionary scenarios, since it helps us to determine the number ratio of rotating disks to mergers at different cosmic epochs. This provides a way of constraining the relative roles of major mergers and steady cool gas accretion in shaping galaxies, which remains a topic of discussion (e.g. Genzel et al. 2001; Tacconi et al. 2008; Dekel et al. 2009b; Förster Schreiber et al. 2009; Lemoine-Busserolle & Lamareille 2010; Lemoine-Busserolle et al. 2010; Bournaud et al. 2011; Epinat 2011).To this aim several authors have already analyzed the velocity fields and velocity dispersion maps of different galaxy samples using the *kinemetry* methodology (Krajnović et al. 2006) with the aim of discerning merging and non-merging systems on the base of their kinematic properties. *Kinemetry* is a tool able to quantify kinematic asymmetries in the velocity field and velocity dispersion maps of the systems with respect to those characterizing an ideal rotating disk.

This chapter is organized as follows: in the first part we select a small subsample of four LIRGs (two disks and two post-coalescence mergers) located at similar distance (to minimize the relative resolution effects). These systems offer the opportunity to explore the potential of the *kinemetry* method when analyzing the velocity fields and velocity dispersion maps in moderately disturbed and partially relaxed systems (Sect. 4.2.1). A new optimized criterion (i.e., weighted, Bellocchi et al. 2012) is also proposed and discussed (Sect. 4.2.8) along with the ones used by Shapiro et al. (2008) for distinguishing between disks and mergers. We then simulate their kinematic maps at high-z (Sect. 4.2.9) at the resolution provided by NIRSpec/JWST, applying the aforementioned *kinemetry*-based criteria to these 'high-z data'.

In Sect. 4.3 the same *kinemetry* analysis is then applied to the whole sample (observed and simulated data) and the results are discussed.

4.2 Studying the kinematic asymmetries of disk and post-coalescence merger LIRGs using a new *kinemetry* criterion

4.2.1 Kinematic properties of the four selected LIRGs

For the present analysis, we select four LIRG galaxies at similar distances ($\sim$ 70 Mpc): two of them (i.e., IRAS F11255-4120, IRAS F10567-4310) had been morphologically classified as *class 0* objects and two (i.e., IRAS F04315-0840, IRAS F21453-3511) as *class 2* objects according to Arribas et al. (2008) and Rodríguez Zaurín et al. (2010). In this classification scheme, *class 0* is defined as an object with a relatively symmetric morphology which appears to be isolated with no evidence of either strong past or ongoing interaction (hereafter, *disks*), while *class 2* is an object with a morphology that is indicative of a post-coalescence merging phase, with a single nucleus or two distinct nuclei at a projected distance D $<$ 1.5 kpc (hereafter, *post-coalescence mergers*). We choose these four systems to be at the same distance as they allow us to discuss their relative kinematic properties avoiding any problems caused by variations in linear resolution. In table 4.1, we present the main properties of the sample, noting that the systems classified as post-coalescence mergers have higher L_{IR} than the disks.

We describe the global kinematic behavior inferred from our IFS maps (i.e, flux intensity, velocity field, and velocity dispersion). We also determine some kinematic parameters (e.g., σ_c, v_c/σ_c, v_{shear}/Σ) that help us to characterize these systems. The ratio of the maximum circular rotation velocity v_c (i.e., the half of the observed peak-to-peak velocity) to the central velocity dispersion σ_c measures the amount of gravitational support of a system in equilibrium. A value of $v_c/\sigma_c \geq 1$ is the signature of a rotation-dominated system, while a lower value (i.e., $v_c/\sigma_c < 1$) means that the object is dispersion-dominated, as in the case of elliptical galaxies, where the galaxy resist to gravitational collapse because of the pressure produced by the random motions of the stars. When analyzing the v_c/σ_c parameter, it is important to realize that the presence of flows, superwinds, or other merger-induced processes are factors that may lead to large v_c or σ_c values. We therefore compute the circular velocity v_c and the central velocity dispersion σ_c using the component of one-Gaussian model fit (i.e., 1c) and the main (i.e., the one defining the systemic behavior) component of the two-Gaussian model fit (i.e., 2c). Since class 0 objects have the characteristics of an *ideal rotating disk*[1] we correct their kinematic values

[1]We refer to an *ideal rotating disk* as a thin disk with gas clouds kinematically characterized by a velocity field that peaks at the galaxy major axis and goes to zero along the minor axis of each orbit,

Table 4.1: General properties of the LIRG sub-sample.

ID1 IRAS (1)	ID2 Other (2)	α (J2000) (3)	δ (J2000) (4)	z (5)	D (Mpc) (6)	scale (pc/″) (7)	log L_{IR} ($L_\odot$) (8)	Class (9)	Ref. (10)
F11255-4120	ESO319-G022	11:27:54.1	-41:36:52	0.016351	70.9	333	11.04	0	1
F10567-4310	ESO264-G057	10:59:01.8	-43:26:26	0.017199	74.6	350	11.07	0	1
F04315-0840	NGC1614	04:33:59.8	-08:34:44	0.015983	69.1	325	11.69	2	1,2
F21453-3511	NGC7130	21:48:19.5	-34:57:05	0.016151	70.0	329	11.41	2	1,2

Col (1): object designation in the IRAS faint source catalogue (FSC). Col (2): other name. Col (3) and (4): right ascension (hours, minutes, and seconds) and declination (degrees, arcminutes, and arcseconds) from the IRAS FSC. Col (5): redshift of the IRAS sources from the NASA Extragalactic Database (NED). Col (6): luminosity distances assuming a ΛDCM cosmology with $H_0 = 70$ km s^{-1} Mpc^{-1}, $\Omega_M = 0.3$ and $\Omega_\Lambda = 0.7$, using the Edward L. Wright Cosmology calculator. Col (7): scale. Col (8): infrared luminosity (L_{IR}= L(8-1000) μm), in units of solar bolometric luminosity, calculated using the fluxes in the four IRAS bands as given in Sanders et al. (2003) when available. Otherwise we use the standard prescription in Sanders & Mirabel (1996) with the values in the IRAS point and faint source catalogues. Col (9): Morphology class. For further information, see Tab. 1 in Rodríguez Zaurín et al. (2010). Col (10): (1) Veilleux et al. (1995); (2) Corbett et al. (2003).

for their respective inclinations; class 2 objects have velocity fields that are distorted such that we derive their kinematic values with and without correcting for the inclination. We derived the ratio of the velocity shear v_{shear} to the global velocity dispersion in the whole galaxy Σ[2], as done in Gonçalves et al. (2010). The v_{shear} (uncorrected for the inclination of the object) was computed as the median of the 5-percentile at each end of the velocity distribution, for the values of v_{max} and v_{min} and then defined as $v_{shear} = \frac{1}{2}(v_{max} - v_{min})$. All these results are shown in Tab. 4.2; their inclinations are drawn from the NED site and are consistent with our own estimates for the Hα distribution.

- IRAS F11255-4120 (ESO 319-G022)

  This is a class 0 object which appears to be a single isolated galaxy with a relatively symmetric morphology according to its DSS image. It is a barred spiral with a ring extending to $\sim$ 4 kpc from the nuclear region that is clearly detected in our Hα image. The orientation of the bar is different in the VIMOS continuum image (P.A. $\sim 110^\circ$) and in the Hα image (P.A. $\sim 150^\circ$).

  For the main component, as shown in the top panel of Fig. 4.1, the velocity dispersion (σ) map has an almost centrally peaked structure with values of 120 km

while the velocity dispersion remains constant along each orbit and decreases between orbits of increasing major axes.

[2]The global velocity dispersion Σ of each object is measured as the mean value over all the spaxels.

s^{-1} (high values also being found in the bar structure) and a lower mean value ($\sim$ 20 km s^{-1}) being found in the ring. The location of this peak does not agree with those of the Hα flux intensity and continuum maps with an offset of about 0.6 kpc (i.e., $\sim$ 2 arcsec). The kinematic center of the velocity field closely agrees with that of the Hα flux peak. The projected orientation of the rotation axis (minor kinematic axis) seems to be different by about 30° from that of the bar in the Hα flux intensity map but is aligned with that of the bar in the continuum. The observed velocity amplitude for the main component at a distance of 4 kpc from the H_α peak is on the order of (300 $\pm$ 8) km s^{-1}.

A small region of about $\sim$ 0.67 kpc x 0.89 kpc in the nuclear region shows traces of a second component which is indicative of non-rotational mechanisms (e.g., outflow/wind). This component is blueshifted by 80 km s^{-1} with respect to the main one and has a large velocity dispersion σ in the range (160 - 220) km s^{-1} and a velocity amplitude on the order of (60 $\pm$ 7) km s^{-1}.

The v_c/σ_c and v_{shear}/Σ have values of 2.3 and 2.7, respectively, supporting the idea that this galaxy is rotationally supported: the kinematic properties of this galaxy seem to be consistent with its morphology (i.e., a rotating disk).

- IRAS F10567-4310 (ESO 264-G057)

  From the DSS image, IRAS F10567-4310 is morphologically classified as a class 0 object (see Rodríguez-Zaurín et al. 2011). The Hα flux map inferred from our IFU data (top panel of Fig. 4.1) shows a ring with a patchy distribution and its peak is in good positional agreement with the center of the galaxy as inferred from the continuum.

  The main component shows a centrally peaked velocity dispersion map with typical values of 60 - 70 km s^{-1}. Its general morphology resembles that of the Hα flux map (i.e., regions with high Hα surface brightness tend to have large velocity dispersions, with a mean value of 40 km s^{-1}). This component has a disk-like regular velocity field with a clear rotation pattern, where the kinematic center in good positional agreement with the Hα flux peak. The observed velocity amplitude is about (300$\pm$6) km s^{-1} when computed at a distance of 4.7 kpc from the kinematic center.

  A secondary kinematically distinct component is identified in the nuclear region over an area of $\sim$ 1.2 kpc x 0.9 kpc; it has a velocity amplitude of (128 $\pm$ 9) km s^{-1} and is blue-shifted by $\sim$ 70 km s^{-1} with respect to the main one; its velocity dispersion is in the range (90 - 180) km s^{-1}.

The v_c/σ_c parameter clearly classifies this object as rotation-dominated with $v_c/\sigma_c \sim 5$ and $v_{shear}/\Sigma \sim 3$. The kinematics of this class 0 object are also consistent with its morphology.

- IRAS F04315-0840 (NGC 1614)

  This is a class 2 object (Fig. 4.1) with a relatively asymmetric morphology: the DSS image shows a tidal tail extending for 13 kpc from the nuclear region. This is a well-studied, post-coalescence late merger, with a bright, spiral structure of a length scale of few kpc (1 - 3 kpc). The spiral structure in the Hα flux map has a different orientation from the continuum.

  The velocity dispersion map of the main component has an irregular structure. Its peak (i.e., 220 km s^{-1}) is found at 2.4 kpc from the nucleus (i.e., Hα flux peak) in the northern arm. The velocity field of the main component is somewhat distorted and chaotic with an amplitude of (325 ± 5) km s^{-1}. The projection of the rotation axis in the outer part (connecting the north-east to south-west part) is not aligned with that of the inner part, which is aligned as north-south direction.

  A broad component is found in the inner region and covers a relatively large area of $\sim$ 2.4 kpc x 2.7 kpc. This component is blue-shifted by 50 km s^{-1} with respect to the main component. Its velocity dispersion is in the range (70 - 400) km s^{-1} with a velocity amplitude of (760 $\pm$ 13) km s^{-1}. The projections of the kinematic major axes of the main and broad component differ by 90° and the blue-shifted region of the velocity field of the broad component has the largest velocity dispersion (i.e., $\sim$ 400 km s^{-1}), supporting the hypothesis of a dusty outflow, where the receding components (which are behind the disk) are obscured, making the whole profile relatively narrow with respect to the approaching component.

  We derive a $v_{shear}/\Sigma \sim 2$ and a $v_c/\sigma_c > 1$ even when the inclination correction is not included (i.e., $v_c/\sigma_c \approx$ 1.4 - 2.4): this illustrates the importance of intrinsic rotation over random motion. Therefore, this parameter implies that we should classify this object as rotation-dominated.

- IRAS F21453-3511 (NGC 7130)

  IRAS F21453-3511 is a peculiar class 2 object, with traces of spiral and asymmetric morphology from the HST and DSS images. The ionized gas, as traced by the Hα emission, is concentrated in the nuclear region and mostly in the northern spiral arm.

The asymmetric velocity dispersion map of the main component clearly has higher values in the northern arm and its central part (i.e., two local maxima can be revealed) with values of 80 km s^{-1}. The velocity field of the same component is asymmetric, and three main regions can be identified: the south-west (SW) part has a mean value of 4900 km s^{-1}, the north-west (NW) one with 4850 km s^{-1} and the eastern (E) part has 4780 km s^{-1}. The NW part could have a different inclination from the remaining observed regions, which can explain this peculiar velocity structure. The kinematic center can be clearly identified with the H_α flux peak, although the rotational axis is not well-defined. The photometric major axis in the NICMOS image seems to be orientated in the NS direction and the ACS image seems to reveal a ring of knots with a major axis orientated along P.A. $\sim 135^\circ$. A small region of about 1.5 kpc x 1.3 kpc in the nuclear part contains a second component. The blue-shifted region of its velocity field has the largest velocity dispersion (i.e., $\sigma \sim 400$ km s^{-1}, see Fig. 4.1). This feature suggests that an outflow is present in the inner part of the galaxy. The amplitude of the velocity dispersion map is about (285 ± 20) km s^{-1}, while the velocity field amplitude is (270 ± 16) km s^{-1}. This component is blue-shifted by 150 km s^{-1} with respect to the main component.

The derived v_c/σ_c and v_{shear}/Σ parameters are respectively closed to 1.3 (when no inclination correction is included) and 1: in this object, the random motions do not seem to dominate, although in its velocity field and velocity dispersion maps there are some anomalies. On the basis of this parameter, we would classify this source as *rotation* dominated.

Table 4.2: Kinematic parameters of the four LIRGs.

Galaxy ID IRAS code	Fit [a]	i [b] degree	v_c [c] (km s^{-1})	σ_c [d] (km s^{-1})	v_c/σ_c	v_{shear} [e] (km s^{-1})	Σ [f] (km s^{-1})	v_{shear}/Σ	R_{eff} (kpc)
F11255-4120	1c	$53^\circ \pm 7^\circ$	187 ± 34	104 ± 7	1.8 ± 0.5				
F11255-4120	2c	$53^\circ \pm 7^\circ$	188 ± 37	83 ± 6	2.3 ± 0.6	125	47	2.7	2.40 ± 0.57
F10567-4310	1c	$36^\circ \pm 4^\circ$	253 ± 32	56 ± 3	4.5 ± 0.8				
F10567-4310	2c	$36^\circ \pm 4^\circ$	255 ± 30	50 ± 2	5.1 ± 0.8	120	41	3	3.20 ± 0.40
F04315-0840	1c	n.c.	157 ± 3	110 ± 11	1.4 ± 0.2				
F04315-0840	2c	n.c.	162 ± 3	69 ± 6	2.4 ± 0.3	132	65	2	0.94 ± 0.14
F04315-0840	1c	$29^\circ \pm 3^\circ$	324 ± 39	110 ± 11	3.0 ± 0.7				
F04315-0840	2c	$29^\circ \pm 3^\circ$	335 ± 40	69 ± 6	4.9 ± 1.0	132	65	2	0.94 ± 0.14
F21453-3511	1c	n.c.	90 ± 6	69 ± 8	1.3 ± 0.2				
F21453-3511	2c	n.c.	78 ± 5	61 ± 4	1.3 ± 0.2	5	51	$\sim$1	2.97 ± 0.82
F21453-3511	1c	$24^\circ \pm 2^\circ$	222 ± 33	69 ± 8	3.2 ± 0.9				
F21453-3511	2c	$24^\circ \pm 2^\circ$	192 ± 28	61 ± 4	3.2 ± 0.7	51	51	$\sim$1	2.97 ± 0.82

[a] One-component fitting (1c) and two-component fitting (2c, referees to the main (systemic) component of the two-Gaussian fit) is consider for the four galaxies. [b]Inclination of the galaxy; n.c. is when no inclination correction is applied. [c]Circular velocity derived as the half of the observed peak-to-peak velocity from the Hα kinematic data. The errors are computed as the root mean square of the sum of the variances computed in an area of 4 $\times$ 4 spaxels around the two peaks (maximum and minimum) of the velocity field map. An additional mean error of 5-7 km s^{-1} can be added when calibration errors are considered (see Tab. 4.3). Corrected and non-corrected values for the inclination are shown. [d]Central velocity dispersion as derived from the $\sigma_{H\alpha}$ maps. These errors are computed as done for the velocity field map. In this case, the calibration errors are on the order of 3-4 km s^{-1}. [e]Velocity shear uncorrected for the inclination of the galaxy. [f]Global velocity dispersion of the whole galaxy.

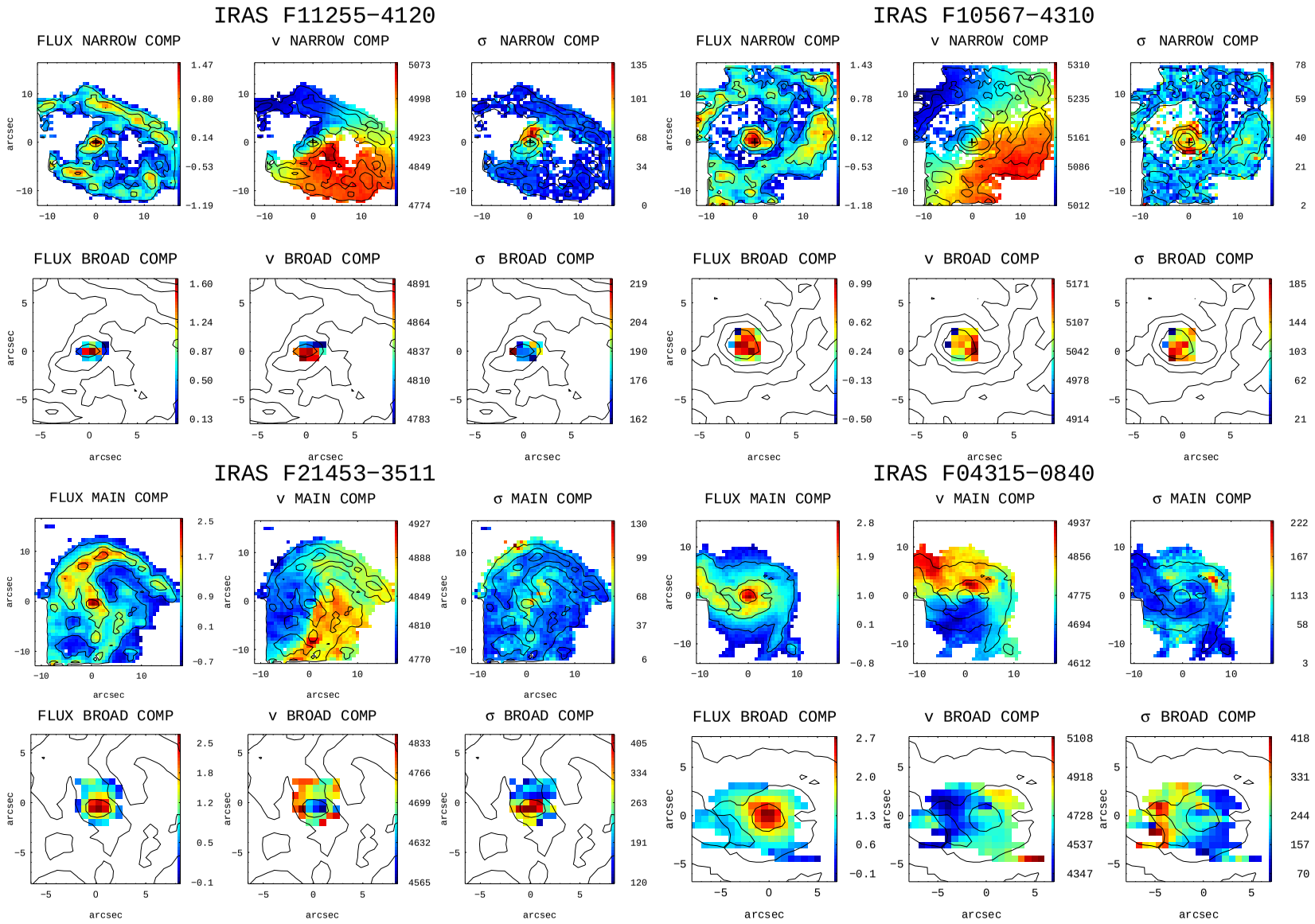

Figure 4.1: Hα kinematic maps for the class 0 objects IRAS F11255-4120 and IRAS F10567-4310 and the class 2 objects IRAS F04315-0840 and IRAS F21453-3511. The flux intensity, velocity field v (km s^{-1}) and velocity dispersion σ (km s^{-1}) maps for the narrow (on the top) and broad (on the bottom) components are shown for each galaxy. Note the different FoV between the narrow and the broad components. The latter has been zoomed in because it covers a small area. All the images are centered using the Hα flux intensity peak and the iso-contours of the Hα flux are overplotted.

4.2.2 The *kinemetry* method

Kinemetry is a generalization of surface photometry to the higher order moments of the line-of-sight velocity distribution of galaxies developed by Krajnović et al. (2006). With the aid of integral field spectroscopic images we are able to generate the velocity and velocity dispersion maps which allow the kinematics of a system to be studied in detail.

This generalization follows the approach of surface photometry by extracting profiles of these maps along ellipses which best fit the predicted profile. The surface brightness and velocity dispersion are even moments which would be expected to have profiles which are consistent with a constant value. On the other hand, the velocity is defined as an odd moment. If it is assumed that the velocity map traces material in a thin disk, inclined at an angle i with respect to the line of sight, then a simple cosine law should well represent the predicted profile:

$$V(r,\psi) = V_{sys} + V_c(r)\, sin(i)\, cos(\psi) \tag{4.1}$$

where r is the semi-major axis length of the ellipse, V_{sys} is the systemic velocity, V_c is the ring circular velocity and ψ is the azimuthal angle measured from the projected major axis. Any deviation from these expected profiles represents a deviation of the data from the idealized model of a thin disk.

The Fourier analysis is the most straightforward way to characterize any periodic phenomenon: the periodicity of a kinematic moment can easily be seen by expressing the moment in polar coordinates where K (x, y) $\rightarrow$ K (r, ψ). The map K(r, ψ) can be expanded as follows to a finite number (N+1) of harmonic terms (frequencies)

$$K(r,\psi) = A_0(r) + \sum_{n=1}^{N} A_n(r)\, sin(n\cdot\psi) + B_n(r)\, cos(n\cdot\psi), \tag{4.2}$$

where ψ is the azimuthal angle in the plane of the galaxy (measured from the major axis) and r is the radius of a generic ellipse. The harmonic series can be presented in a more compact way as

$$K(r,\psi) = A_0(r) + \sum_{n=1}^{N} k_n(r)\cdot cos[n(\psi - \phi_n(r))], \tag{4.3}$$

where the amplitude and the phase coefficients (k_n, ϕ_n) are easily calculated from the A_n, B_n coefficients as $k_n = \sqrt{A_n^2 + B_n^2}$ and $\phi_n = arctan\left(\frac{A_n}{B_n}\right)$. Thus, for an *ideal rotating disk* one would expect the velocity profile to be dominated by the B_1 term, while the velocity dispersion profile dominated by the A_0 term.

In the case of an *odd* moment (μ_{odd}, e.g., velocity field), the sampling ellipse parameters are determined by requiring that the profile along the ellipse is well-described by:

$$\mu_{odd}(\psi, r) \approx B_1(r) \cdot cos(\psi) \tag{4.4}$$

since the velocity field peaks at the galaxy major axis ($\psi = 0$) and goes to zero along the minor axis ($\psi = \pi/2$). Hence, the power in the $B_{1,v}$ term therefore represents the *circular* velocity in each ring r, while power in other coefficients represent deviations from circular motion. On the other hand, the zeroth-order term, A_0, gives the *systemic velocity* of each ring, while the A_1 term represents velocity gradients found along the minor axis (i.e., *radial* velocity) on the plane of the galaxy (e.g., inflows/outflows). As shown in Fig. 4.2 the observed velocity field of the galaxy IRAS F12115-4656 has been reconstructed using *kinemetry*, and the residuals are shown on the top right of the same panel[3]. On the bottom part, we reconstruct the maps of the zeroth and first order Fourier coefficients, respectively, A_0, A_1 and B_1. All these images are centered using the continuum map (see App. A for details).

On the other hand, the velocity dispersion field is an *even* moment (μ_{even}) of the velocity distribution, so that its kinematic analysis is identical to traditional surface photometry. In an ideal rotating disk, the velocity dispersion has to be constant along each ring of the ellipse

$$\mu_{even}(\psi, r) \approx A_0(r) \tag{4.5}$$

and decreases when the semi-major axis length increases. In this context, the A_0 term represents the velocity dispersion profile. Higher order terms (A_n, B_n) indicate deviations from symmetry (Krajnović et al. 2006).

We use the algorithm described in detail in Krajnović et al. (2006) to extract and characterize the profiles along each best fitting ellipse for all the objects in our VIMOS (U)LIRG sample. In particular, we investigate the power of this methodology in studying the kinematic asymmetries. First we apply the *kinemetry* method to the aforementioned subsample, drawing preliminary conclusions about the kinematics of the objects. We then apply the same criteria as those proposed by Shapiro et al. (2008) and also explore the potential of a new criterion to study kinematic asymmetries. In the particular case of Shapiro et al. (2008), they use the kinematic process of Krajnović et al. (2006) measuring the asymmetries of the velocity fields and velocity dispersion maps in order to quantify the

[3]The residuals range between $\pm$ 40 km s^{-1}, with a median absolute value of $\sim$ 4 km s^{-1}.

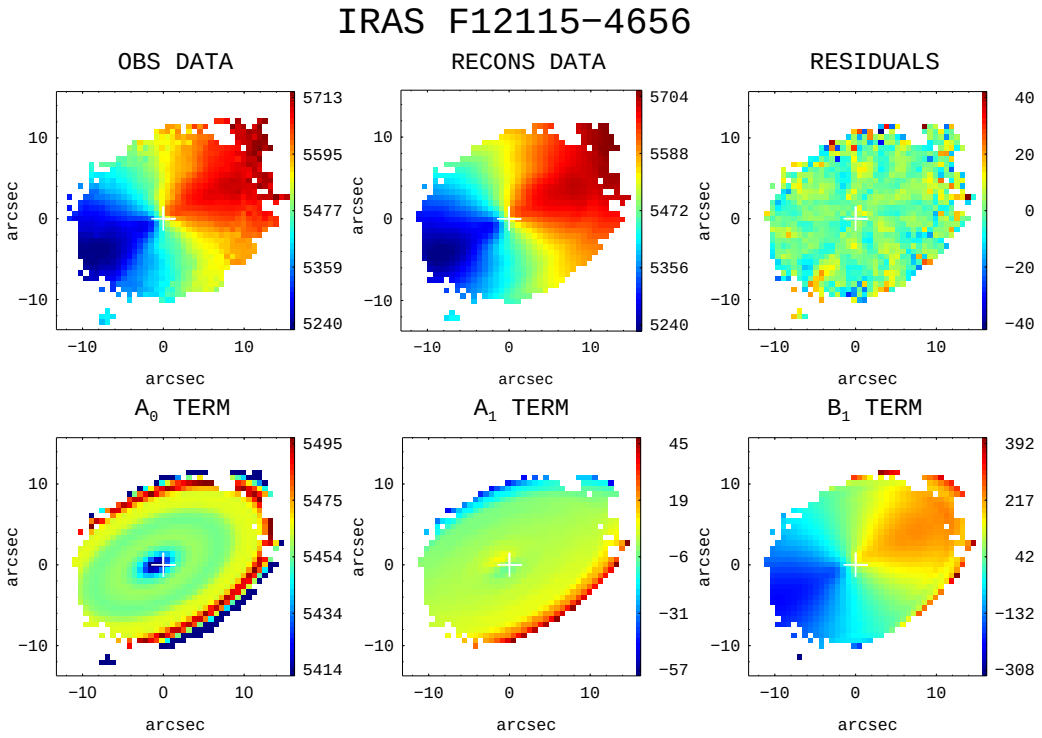

Figure 4.2: Example of reconstructed maps for the galaxy IRAS F12115-4656 from the observed data (top left panel). *Top:* The observed, the reconstructed and the residual maps are shown. *Bottom:* The reconstructed maps respectively associated to the A_0, A_1 and B_1 terms are presented. They represent, respectively, the systemic, radial and circular velocities.

kinematic asymmetries with respect to an ideal rotating thin disk case. Any asymmetries in these fields represent deviations from the idealized model. The combined asymmetry (i.e., K_{tot}) of the two fields can fully describe how accurately a system is represented by an idealized disk.

There are two effects that limit the reliability with which coefficients in the expansion can be determined: (i) the absolute number of points sampled along the ellipse, and (ii) the regularity with which these points sample the ellipse as a function of angle, θ. Ellipse parameters (i.e., position angle Γ, centre, and flattening $q = b/a$) can be determined by minimizing a small number of harmonic terms; in the code, some of them can be constrained (e.g., fixing the center allows the position angle Γ and flattening q to freely change or remain fixed). The choice of a correct center is important in the analysis in order to avoid artificial overestimations of the asymmetries. In Sect. 4.2.5 the dependence on the input parameters is discussed in detail.

4.2.3 The *kinemetry* results: reconstructed maps and radial profile of the Fourier coefficients

We investigate the potential of the *kinemetry* method developed by Krajnović et al. (2006) (hereafter K06), in analyzing the kinematic maps of (U)LIRGs. In particular, we want to investigate the power of this methodology in studying the kinematic asymmetries. First we apply the *kinemetry* method to the subsample, drawing preliminary conclusions about the kinematics of these objects. We then apply the same criteria as those proposed by Shapiro et al. (2008) and also explore the potential of a new criterion to study kinematic asymmetries. We therefore expect to measure lower asymmetries for our two post-coalescence merger systems than to those considered by Shapiro et al. (2008), which are more kinematically disturbed because of their recent merger activity. In our post-coalescence systems, the inner parts are expected to be relaxed into an almost virialized disk with a large rotational component, while the outer parts should still retain asymmetries associated with the merger events. Finally, we analyze the resolution and redshift effects on these results.

In our analysis, the position of the galaxy's center is assumed to correspond the peak of the Hα flux intensity map. In the two class 0 objects, the Hα peak is in good positional agreement with the center of symmetry of the velocity field (i.e. kinematic center). For the class 2 objects, the kinematic center of the velocity field is not so well-defined, but the Hα peak is also in a reasonable symmetric position. The position angle Γ is allowed to vary. The flattening q is also allowed to vary, but across a physically meaningful range (i.e. 0.2-1). This allows us to consider general cases, such as tilted/wrapped disks. In Sect. 4.3.4 (i.e., Fig. 4.8), we discuss further the effects of the different choices on these input parameters.

In Figs. 4.3 - 4.6, we present for the four galaxies the original kinematic maps (i.e., velocity field and velocity dispersion), along with their reconstructed maps (i.e., obtained using all the coefficients of the harmonic expansion up to the fifth order corrections). The residual maps (i.e., original - model) are also shown with a typical RMS of 10 km s^{-1}. Therefore, in all four cases, the fits are good and the reconstructed maps recover the properties of the original data in great detail. We also present the behavior of the kinematic parameters defined in the previous section (i.e., position angle, Γ, and the flattening, q), along with some of the *kinemetry* coefficients (k_1 and k_5 normalized to the k_1).

As for the ellipse parameters, we find in general a good optimization for Γ at the different radii for the four objects. As for q, there are several cases that reach the boundary of the range of acceptable values. In general, this happens in the innermost regions where the rotation component, and therefore the amplitude of the sinusoidal velocity profile

along the ellipse, are small. The irregularities in the velocity field are therefore far larger than the (rotational) amplitude of the velocity profile. Since the problem of finding the best-fit ellipse (i.e., best-fit q and Γ combination) can be quite degenerate with many local minima, a low q (high ellipticity) facilitates the minimization of χ^2 because the latter is sensitive to a change in Γ. In contrast, if q is high (circular ellipse), the fit (χ^2) is insensitive to a change in Γ increasing the difficulty of the χ^2 minimization process. As a result, q tends to have small values in the inner regions, reaching in some cases the minimum acceptable value. In addition, the q parameter is more weakly constrained at smaller radii as a consequence of the relatively fewer data points involved and the seeing smearing, and has larger errors[4]. This does not mean, however, that the harmonic expansion to describe the kinematics is not well-constrained. The reconstructed velocity maps are indeed in excellent agreement with the real velocity field for the inner regions (i.e., low q values), even for the innermost region (see Figs. 4.3 - 4.6). At larger r, the amplitude of the velocity profile along the ellipse is larger; more data points contribute to constrain the ellipse, that are less sensitive to local kinematic irregularities, hence provide a more optimal fitting of the parameters. At large radii, we also find good agreement between the fit and the data. We now provide some comments on the *kinemetry* results for each galaxy of the sample.

- IRAS F11255-4120

  The position angle Γ is quite stable ($\sim 200^\circ \pm 15$) over most the sampled radius. In the inner part (i.e. $r < 3''$), q has values of 0.2-0.4 and it has some instabilities at $r \sim 5''$, which are likely due to the inner bar structure. However, the expansion recovers very well the data in all this region. We find that k_1 is mainly dominated by rotation (i.e, B_1) and increases radially up to a value of 140 km s^{-1}. The k_5/k_1 term, which measures the small-scale kinematic asymmetries, has small values up to a maximum of 0.15, which is indicative of minor peculiarities. These asymmetries become smaller in the outer parts. The error bars are not visible because they are smaller than the black points in the plot.

- IRAS F10567-4310

  The position angle Γ is quite stable over the sampled radii, with values between 220

[4]Note that *kinemetry* provides the errors in the ellipse parameters (i.e., q, Γ), which are determined by the Levenberg-Marquardt least squares minimization (MPFIT) fit with the formal 1σ uncertainties computed from the covariance matrix. Similarly, the harmonic terms have their formal 1σ errors estimated from the diagonal elements of the corresponding covariance matrix obtained with a linear least squares fit.

and 250 degrees. The q parameter reaches the value of 0.2 in the inner region (i.e., $r < 2''$), where the reconstructed map shows a very good agreement with the data. The parameter k_1 is mainly dominated by rotation (i.e, B_1) and increases radially up to a value of 140 km s^{-1}, revealing a possible minor anomaly at $r \sim 4''$. The k_5/k_1 term has very small values, with a maximum of 0.05 over the sampled radii, meaning that this object is close to being an ideal rotating disk structure.

- IRAS F04315-0840

  The position angle Γ typically spans from 350° to 380°[5], except for ($r \sim 3''$), which drops to around 320° as a consequence of one of two distinct redshifted peaks present in the velocity field map. For most of the radii, q is close to 1 (circle-ellipses). The parameter k_1 increases radially up to a value of 120 km s^{-1} ($r < 5''$) and then decreases to reach a value of 100 km s^{-1} at $r \sim 15''$. The k_5/k_1 term is between 0 and 0.3, and has a constant increasing behavior. This illustrates that departures from rotation are mainly found in the outer parts of the galaxy.

- IRAS F21453-3511

  The position angle Γ remains almost constant to $\sim 250°$ for $r > 6''$, while it has lower and more unstable values for $r < 6''$. The values of q reaches 0.2 in the region within a radius of $r < 4''$, mainly owing to the relatively small rotation component in this region. However, the agreement between the kinematic fit and data is very good for these radii. At $r = 4''$, q reaches a maximum (~ 1) and then decreases to a value of 0.6 at larger radii. k_1 does not reveal any strong rotational component ranging between 10 km s^{-1} and 50 km s^{-1}. In the inner region it increases for $r < 4''$ and then remains quite constant. The k_5/k_1 term ranges between 0 and 0.2, showing a quite stable trend. In this object, the deviations from pure rotation are larger than those for the class 0 objects and as large as those of IRAS F04315-0840.

In general, we have found that for class 0 sources the higher order deviations (from pure rotation) are small (i.e., $k_5/k_1 < 0.1$), while for class 2 objects the deviations are larger, particularly in the outer regions ($k_5/k_1 \leq 0.4$). For all of these sources, the rotation curve (i.e., k_1 parameter) seems to imply that these objects are rotating. As discussed before, these galaxies do not display extreme asymmetries in their kinematic maps as confirmed by the *kinemetry* results obtained so far.

In the following sections, we study several kinematic criteria to enhance our classification of these systems.

[5]The position angle is measured from north (0°=360°) anti-clockwise. To ensure that the two values become more easily comparable, we choose to add 360° in one case.

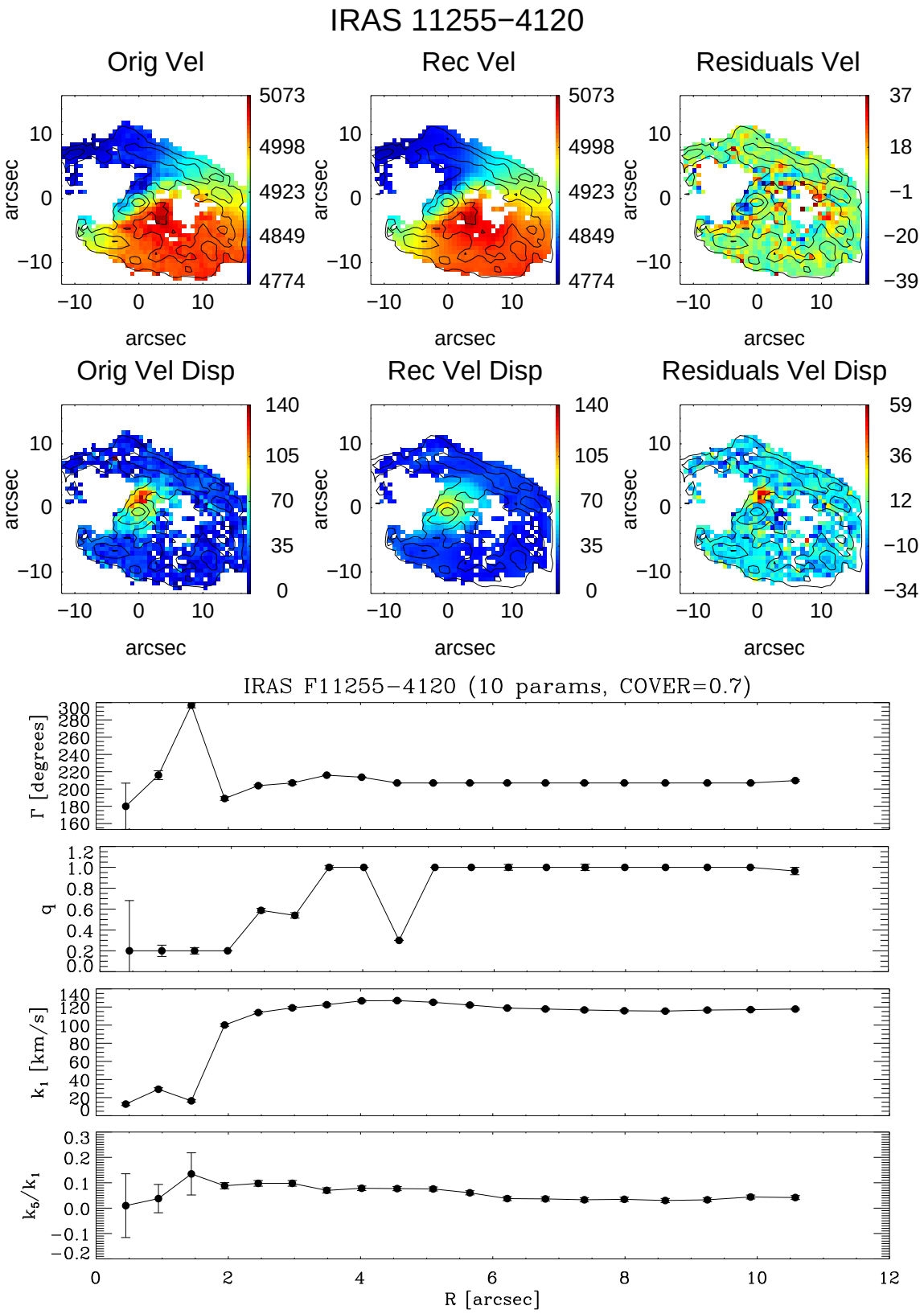

Figure 4.3: **Upper panel:** Maps of Hα Gaussian fit velocities (top left), Hα Gaussian fit dispersion (bottom left) and their respective reconstructed (middle) and residual (data-model) maps (on the right) for IRAS F11255-4120. **Lower panel:** Radial profiles of the kinematic properties, obtained using *kinemetry* program. The position angle Γ and the flattening q of the best-fit ellipses, as well as the first and the fifth order Fourier terms (respectively, k_1 and k_5) are plotted as a function of the radius.

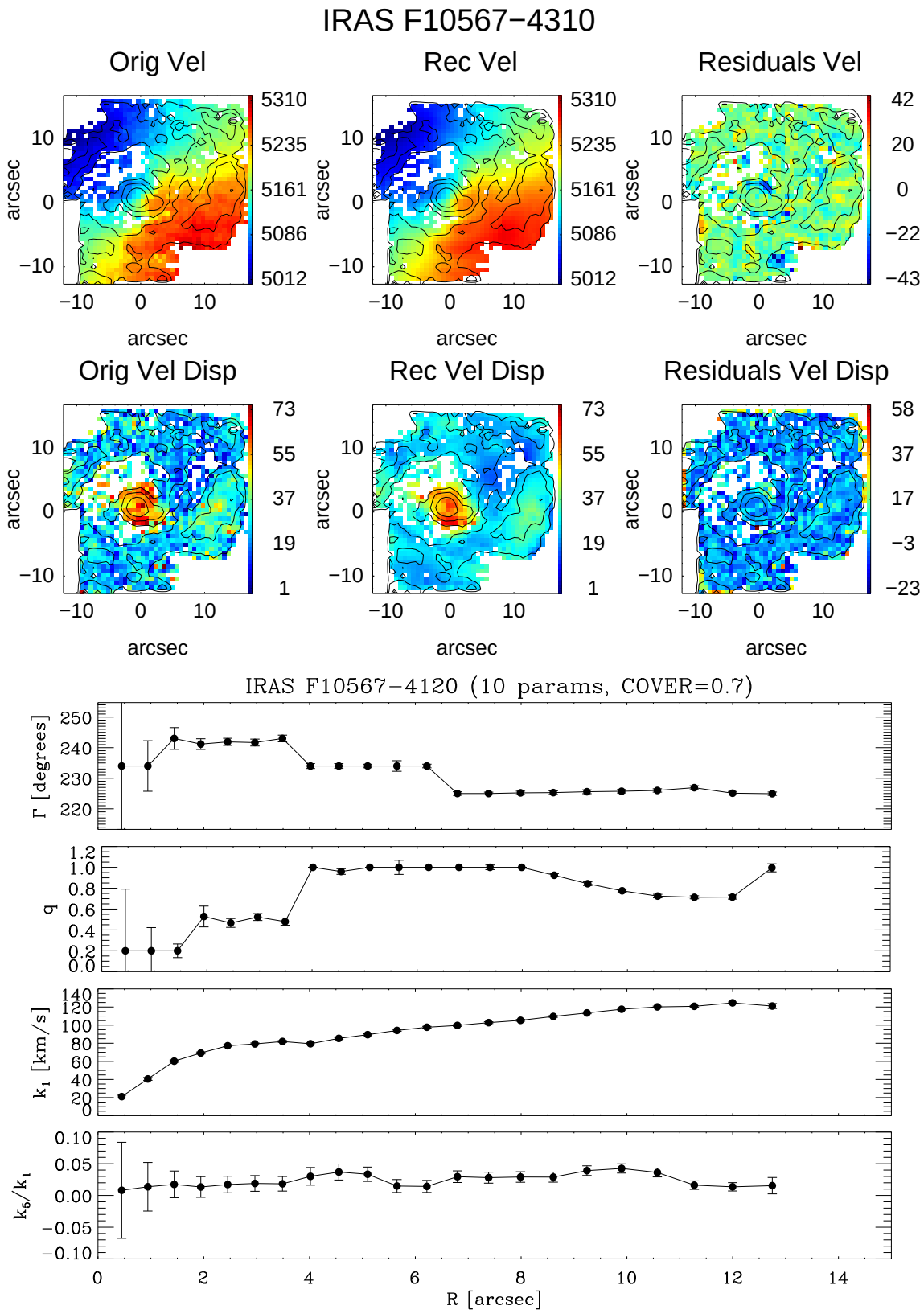

Figure 4.4: **Upper panel:** Maps of Hα Gaussian fit velocities (top left), Hα Gaussian fit dispersion (bottom left) and their respective reconstructed (middle) and residual (data-model) maps (on the right) for IRAS F10567-4310. **Lower panel:** Radial profiles of the kinematic properties, obtained using *kinemetry* program. The position angle Γ and the flattening q of the best-fit ellipses, as well as the first and the fifth order Fourier terms (respectively, k_1 and k_5) are plotted as a function of the radius.

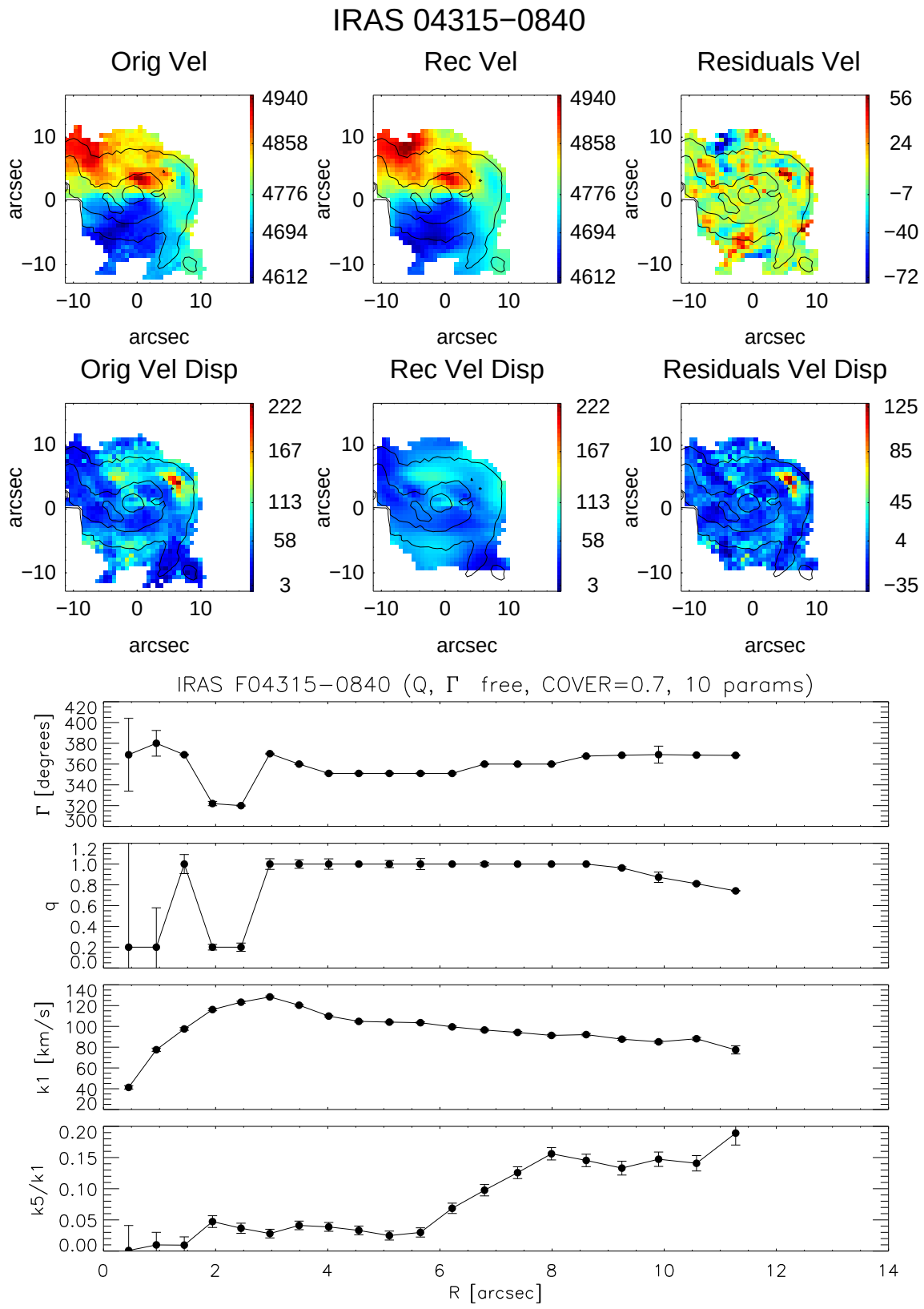

Figure 4.5: **Upper panel:** Maps of Hα Gaussian fit velocities (top left), Hα Gaussian fit dispersion (bottom left) and their respective reconstructed (middle) and residual (data-model) maps (on the right) for IRAS F04315-0840. **Lower panel:** Radial profiles of the kinematic properties, obtained using *kinemetry* program. The position angle Γ and the flattening q of the best-fit ellipses, as well as the first and the fifth order Fourier terms (respectively, k_1 and k_5) are plotted as a function of the radius.

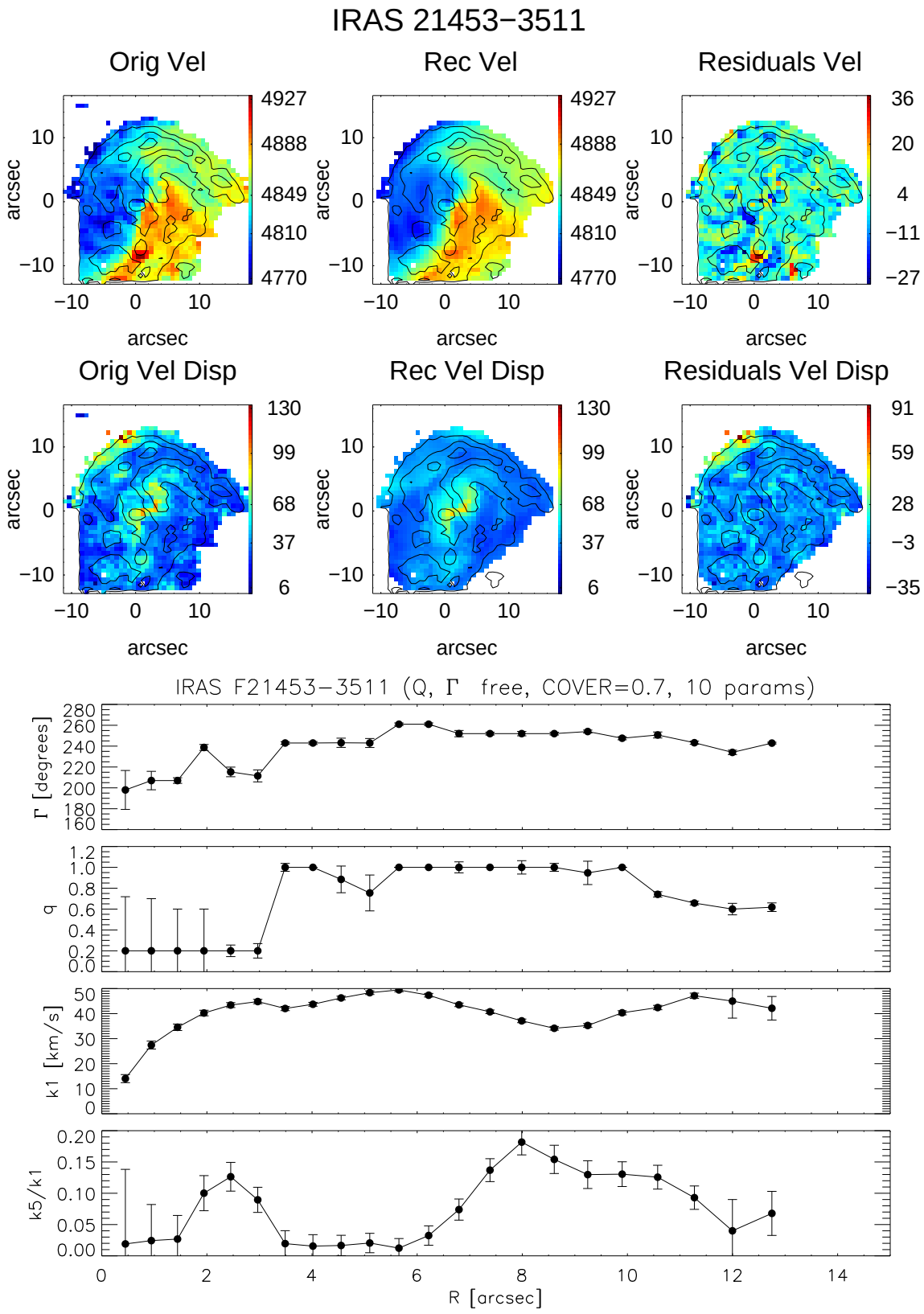

Figure 4.6: **Upper panel:** Maps of Hα Gaussian fit velocities (top left), Hα Gaussian fit dispersion (bottom left) and their respective reconstructed (middle) and residual (data-model) maps (on the right) for IRAS F21453-3511. **Lower panel:** Radial profiles of the kinematic properties, obtained using *kinemetry* program. The position angle Γ and the flattening q of the best-fit ellipses, as well as the first and the fifth order Fourier terms (respectively, k_1 and k_5) are plotted as a function of the radius.

4.2.4 The [σ_a- v_a] plane: the Shapiro et al. (2008) criteria

To reveal rotational/non-rotational motion within the dynamics of the gas in each galaxy, we first consider the same criteria as the ones proposed by Shapiro et al. (2008). We note that they compare two main classes of systems: those that have suffered a recent major merger event (i.e., *mergers*) and those without any signs of interacting or merger activity (i.e., *disks*). For further details, we refer to Shapiro et al. (2008). They define the asymmetries in the velocity and velocity dispersion fields as

$$v_{asym} = \left\langle \frac{k_{avg,v}}{B_{1,v}} \right\rangle_r \qquad \sigma_{asym} = \left\langle \frac{k_{avg,\sigma}}{B_{1,v}} \right\rangle_r, \tag{4.6}$$

where $k_{avg,v} = (k_{2,v}+k_{3,v}+k_{4,v}+k_{5,v})/4$ and $k_{avg,\sigma} = (k_{1,\sigma}+k_{2,\sigma}+k_{3,\sigma}+k_{4,\sigma}+k_{5,\sigma})/5$. For an ideal rotating disk, we expect the velocity profile to be perfectly antisymmetric if the B_1 term dominates the Fourier expansion, while the velocity dispersion map is expected to be perfectly symmetric and therefore all terms except A_0 should vanish.

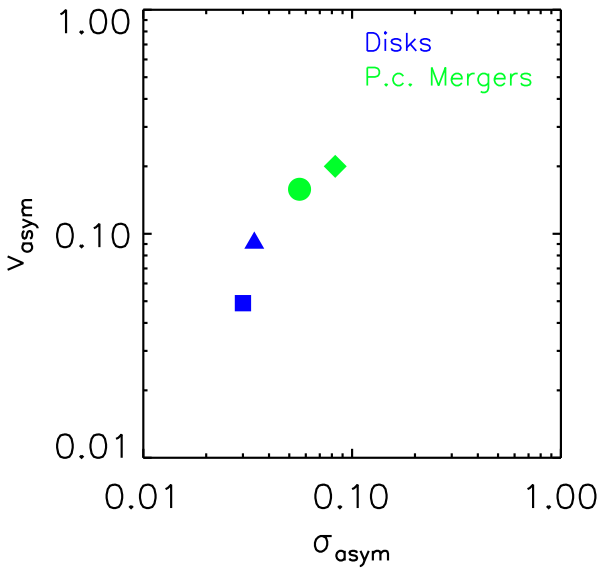

Figure 4.7: Asymmetry measure of the velocity v_{asym} and velocity dispersion σ_{asym} fields for the four galaxies analyzed here. Symbol types distinguish the different systems: the square represents IRAS F10567-4310, the triangle is IRAS F11255-4120, the circle is IRAS F04315-0840, and the diamond represents IRAS F21453-3511. Blue and green symbols represent different morphological types, respectively class 0 and class 2 objects.

In Fig. 4.7, we show the results for our galaxies in the [$\sigma_a - v_a$] plane. As expected, class 0 objects have lower values of the asymmetries than class 2 objects. Looking at their velocity and velocity dispersion maps, the class 0 maps (Figs. 4.3 - 4.4) resemble those

of an ideal rotating disk (i.e., 'spider diagram' structure for the velocity field and centrally peaked velocity dispersion map), while class 2 objects have more distorted velocity fields and irregular dispersion maps (Figs. 4.5 - 4.6). Therefore, taking into account that the objects in the present sample were classified as either class 0 or class 2 based on pure morphological arguments, we can conclude that their morphological and kinematical classifications in the [σ_a - v_a] plane are consistent.

To analyze the robustness of the results in Fig. 4.7, we now analyze their dependence on the considered input parameters as well as the errors in the radial velocities and velocity dispersion measurements. We note that *kinemetry* uses the full 2D kinematic information of the velocity field and velocity dispersion map, allowing us to perform a good characterization of the asymmetries, something that is more efficient than using 1D parameters such as v_c/σ_c and v_{shear}/Σ as seen in Sect 4.2.

4.2.5 Dependence on the input parameters

As pointed out by K06, a good choice of input parameters is important to avoid an artificial overestimation of the asymmetries. To perform the *kinemetry* analysis, we need to define the dynamical center, as well as specify different levels of constraints of the input parameters. For instance, the kinematic position angle, Γ, and the flattening, q, of the ellipses can be fixed or allowed to vary in the fitting at different radii. The COVER parameter, which controls the radius at which the process stops by setting the fraction of the ellipse that has to be covered by data[6], also has to be assigned.

In Fig. 4.8, we present the results in the [σ_a - v_a] plane of our galaxies for different sets of input parameters. In each panel, one parameter at a time is changed, respectively, the COVER (top-left), the position angle Γ (or PA, top-right), the flattening q (bottom-left), and the CENTER (bottom-right) of the ellipses. We can find that the results are stable for a reasonable choice of values. When considering the COVER panel, the four galaxies give similar results up to cover=0.5, whereas IRAS F11255-4120 deviates significantly for COVER = 0.3. Our results for IRAS F21453-3511 seem to be sensitive to our choice of galaxy center but it remains stable within the region of high-asymmetries in all the (extreme) cases considered. As shown, the choice of either free or fixed position angle Γ or flattening q do not have a strong effect on the final results. In particular, the computed asymmetries are quite insensitive to the choice for q, especially for the class 0 galaxies.

[6]For instance, COVER = 0.7 means that if fewer than 70% of the points along an ellipse are not covered by data the program stops. This value ensures sure that kinematic coefficients are robust. It is sometimes necessary to relax this condition, especially when reconstructing maps. For further details, we refer to Krajnović et al. (2006).

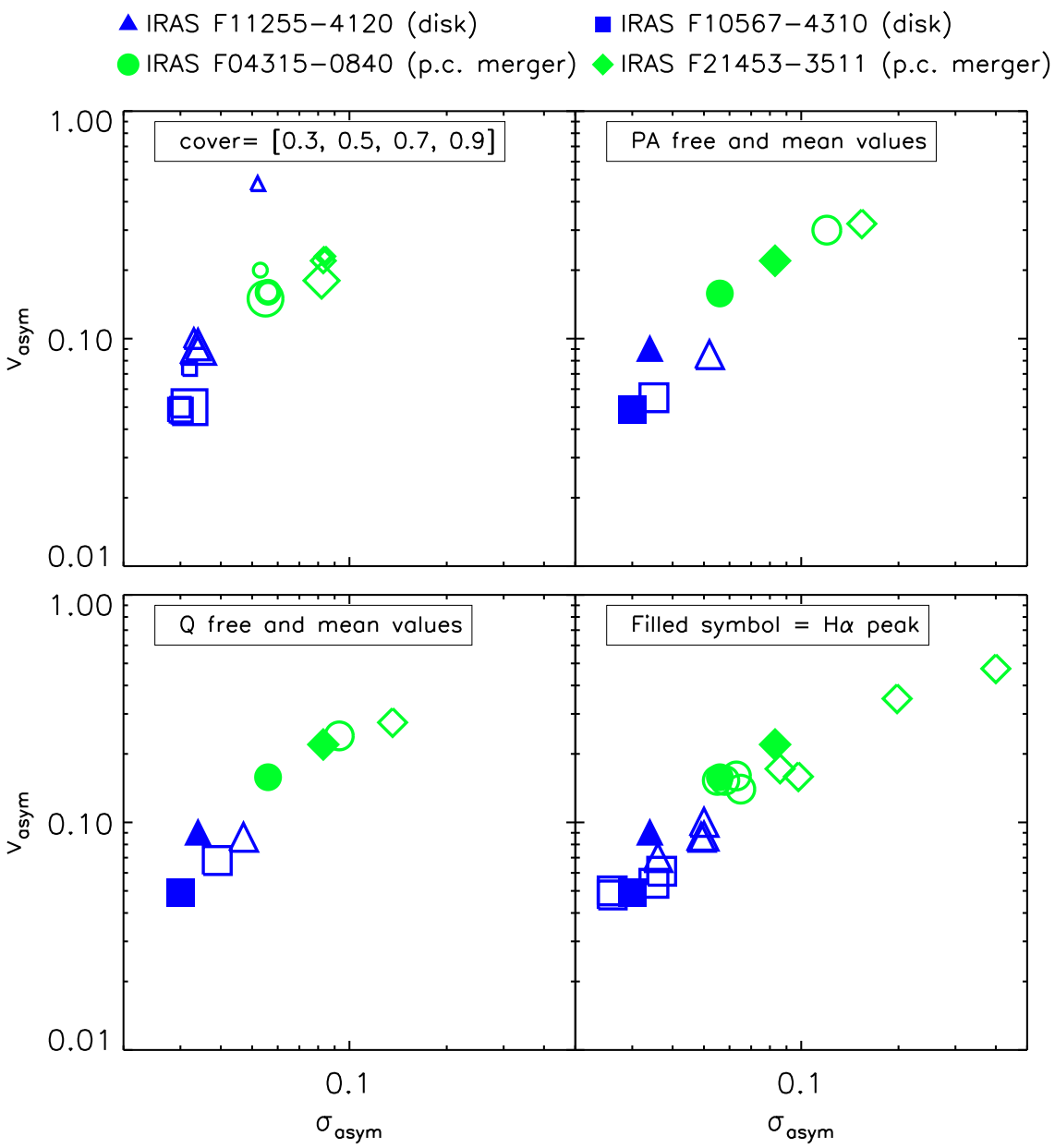

Figure 4.8: Results for the asymmetry measures when different sets of input parameters are considered with a ten harmonic term analysis. Symbol types and colors help us to distinguish among the different systems as explained in the legend. In each panel, one parameter at a time is changed, namely respectively, COVER, Γ (or PA), q, and the CENTER of the ellipses. *Top-left:* Different results for the COVER parameter (i.e., 0.3, 0.5, 0.7, 0.9) where the size of the symbol is proportional to the COVER value (the biggest symbol corresponds to the highest cover value and vice versa). *Top-right:* The results obtained when we allow a *position angle* Γ to vary (filled symbols) or be fixed to its mean value (empty symbols) are shown. *Bottom-left:* The results shown are obtained when we allow q to either vary or remain constant with radius at its mean value. *Bottom-right:* Results achieved choosing five different centers for each galaxy: filled symbols represent results obtained from the 'standard' analysis (Hα flux peak), and empty symbols the results obtained by shifting their center by one pixel (horizontally *and* vertically, with respect to the Hα peak pixel corresponding to a shift of 0.95″).

In general, the asymmetries obtained for a fixed Γ/q are somewhat higher because there is smaller degree of freedom such that the asymmetries cannot be accurately taken into account in the fitting. A similar trend is shown when reconstructing the kinematic maps. As an example, we reconstruct the velocity field map of the galaxy IRAS F21453-3511 considering the possible combinations for the position angle Γ and flattening q (free or fixed to vary). The results are shown in Fig. 4.9, along with their corresponding residual (i.e., observed-model) maps. The root mean square (RMS) value in each residual map is computed: the lowest one is reached when Γ and q are let free to vary. Although with somewhat higher residuals, *kinemetry* is able to properly reconstruct the velocity field of this type 2 object even when one (or both) of the parameter is (are) fixed.

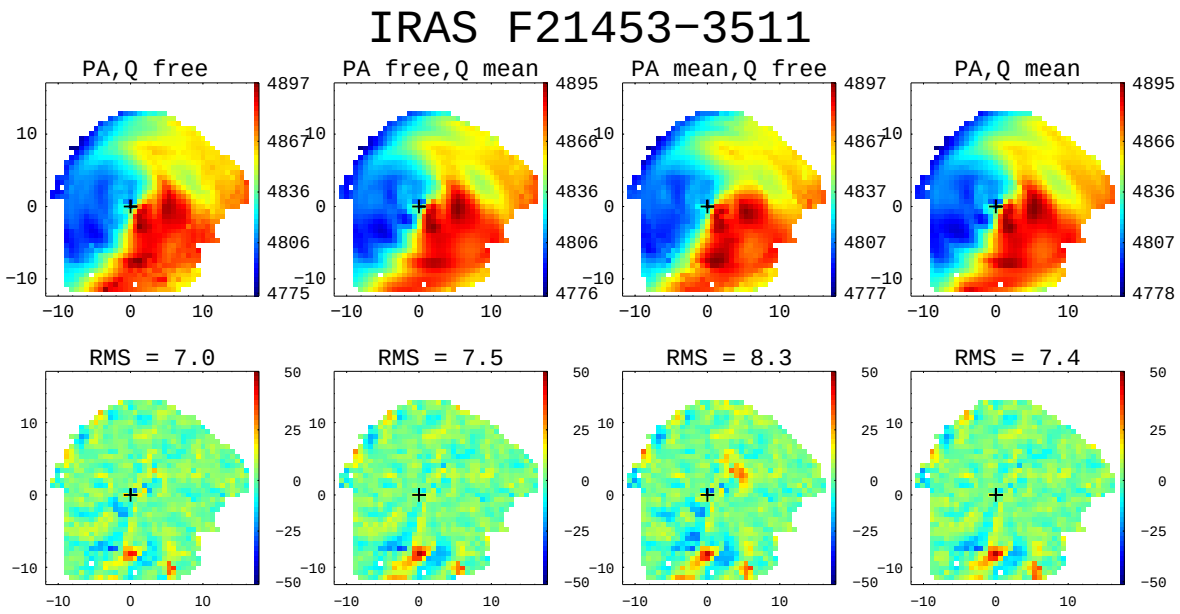

Figure 4.9: Reconstructed velocity field and residual maps of IRAS F21453-3511 when using different Γ (PA) and q combinations. The root mean square (RMS) in the residual map is computed in each case. The best reconstructed map is obtained when both Γ (PA) and q are free to vary (top and bottom left). In the other cases, *kinemetry* is also able to reconstruct properly the velocity field, although producing somewhat higher residuals.

The proper choice of free/fixed parameters obviously depends on the level of S/N (i.e., if the deviations are associated with a true feature or noise). In accordance with these results, we select the input parameters for our analysis as COVER = 0.7, Γ is completely allowed to vary, q is free to vary in the range $[0.2 - 1]$, and the center = Hα flux peak.

4.2.6 Monte Carlo simulations

To analyze the dependence of the *kinemetry* results on the uncertainties in the radial velocities and velocity dispersion values, we measure the probability distribution functions (PDFs) of the asymmetries in these systems using Monte Carlo (MC) simulations, as done in S08, since the *kinemetry* method does not lend itself to a straightforward error propagation.

Therefore, for each template, we create 150 different realizations of the moment maps (i.e., velocity field and velocity dispersion) based on their corresponding error maps. These error maps correspond to the measurement errors in the velocity moments, as derived when fitting the kinematics in the data cube along with wavelength calibration errors[7] (see Tab. 4.3). For each moment map, we perturb the observed data points by randomizing them, using Gaussian noise parameterized by the measured 1σ errors. The new maps created are then used to rerun *kinemetry* and apply the analysis described before. In figure 4.10, our results are shown. We find that our results in the [σ_a - v_a] plane are almost unaffected by the velocity errors and that there are relatively well-defined regions for disks and merger galaxies.

Table 4.3: Results of the calibration check using the [OI]λ6300.3 Å sky line.

IRAS Galaxy	$<\lambda_c> \pm \Delta\lambda_c$ [Å]	$<\sigma_{INS}> \pm$ std [Å]
F11255-4120	6300.42 $\pm$ 0.15	0.78 $\pm$ 0.09
F10567-4310	6300.17 $\pm$ 0.13	0.77 $\pm$ 0.09
F04315-0840	6300.24 $\pm$ 0.10	0.78 $\pm$ 0.08
F21453-3511	6300.27 $\pm$ 0.11	0.77 $\pm$ 0.06

Typical values of the central wavelength and width distribution of the [OI]λ6300.3 Å sky line registered in the data cubes along with their standard deviations (errors).

[7]The wavelength calibration, the instrumental profile, and fiber-to-fiber transmission correction are checked for the four galaxies using the [OI]λ6300.3 Å sky line as in Arribas et al. (2008). Our interest is focused on the Hα and [NII]$\lambda\lambda$6548.1, 6583.4 Å emission lines, hence the sky line here considered is suitable because of its proximity to these lines. In table 4.3, the average values for the central wavelength $<\lambda_c>$ and (instrumental) width $<\sigma_{INS}>$, with their standard deviations, are shown for the four galaxies.

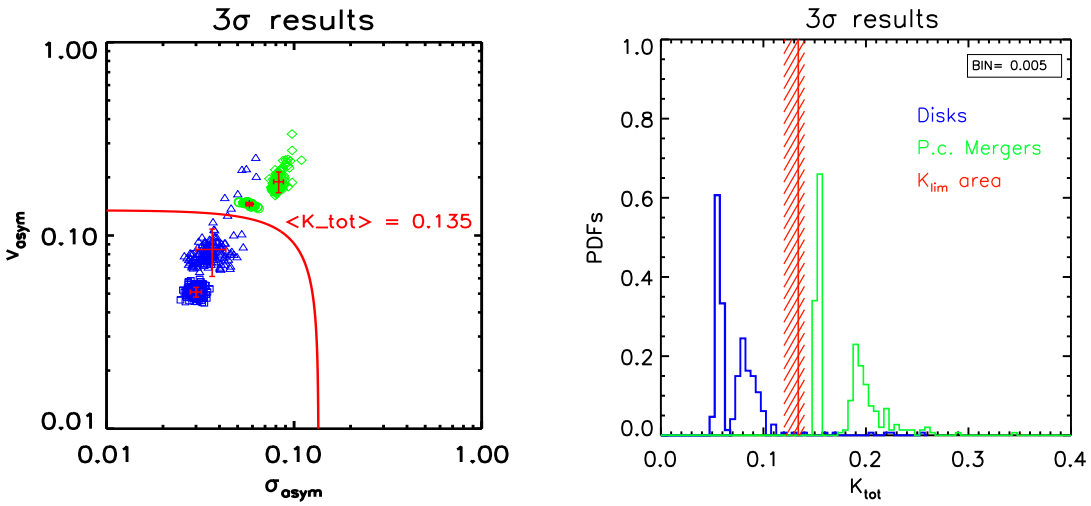

Figure 4.10: **Left:** Asymmetry measures of the velocity v_{asym} and velocity dispersion σ_{asym} fields derived from the Monte Carlo realizations for the four objects. For each source, 150 MC simulations are run but here only the $\pm 3\sigma$ results are shown. The solid red line indicates the division between class 0 (disks) and class 2 (post-coalescence mergers) at $<K_{tot}> = 0.135$. **Right:** The probability distribution function (PDFs) as derived from MC realizations. The empirical delineation where K_{lim}=0.135 can cleanly separate the two classes (i.e., K_{lim} area). The symbols are the same as those used before.

4.2.7 Total kinematic asymmetry of disk, ongoing and post-coalescence merger systems

As done in Shapiro et al. (2008), we compute the total kinematic asymmetry K_{tot}[8] border in order to separate class 0 (disks) and class 2 (post-coalescence merger) objects. For the four objects, we obtained a mean value of $< K_{tot} >= 0.135$ which is significantly lower value than that previously obtained in Shapiro et al. (2008) (i.e., $<K_{tot}> = 0.5$). The difference could arise because our *mergers* are in a post-coalescence phase displaying relaxation in the innermost regions with a large rotation component, while in Shapiro et al. (2008) they are mostly pre-coalescence merger systems dominated by irregular velocity field and high velocity dispersion. In addiction, the limit defined in their work comes out after excluding IRAS F12112+0305, a pre-coalescence merger pair (i.e., García-Marín et al. 2009) which resembles a *disk* at high redshift. If the classification of this object had considered, they would have derived a total kinematic asymmetry border considerably lower (i.e., $<K_{tot}> \sim 0.3$, see Figure 5 in Shapiro et al. (2008)), hence the discrepancy from our findings may be smaller.

In any case, the border *disk/merger* for the Shapiro et al. (2008) sample is so dependent

[8] As defined in Shapiro et al. (2008), the total kinematic asymmetry includes both the kinematic asymmetry contribution coming from the velocity field and velocity dispersion maps, such as $K_{tot} = \sqrt{(\sigma^2_{asym} + v^2_{asym})}$.

on the classification of a single object (i.e., IRAS F12112+0305) illustrates its relatively large associated uncertainties. A reduction in the total asymmetry border K_{tot}, as our results (and Shapiro et al. (2008), after reclassifying IRAS F12112+0305) suggest, may also lead to a change in the relative frequency of *disks* and *mergers* in a given sample, hence an increase in the fraction of *mergers*. Changing the relative frequencies of *disks* and *mergers* has obvious implications for the interpretation of our data in terms of the different evolutionary scenarios mentioned in the introduction. On the other hand, our sample is admittedly too small and consists of objects with relatively homogeneous properties (i.e., LIRGs classified as disks and post-coalescence mergers) for a robust determination of general use. Therefore, additional efforts to constrain its value as well as understand how it depends on several instrumental and observational factors are required.

4.2.8 A new criterion to distinguish *disks* from post-coalescence *mergers*

In this section we explore a new kinematic criterion in order to better assess the presence of asymmetries in the kinematic maps. As described in Kronberger et al. (2007), when considering recent (i.e., $\leq$ 100 Myr after the first encounter) or ongoing major mergers of equal mass galaxies (i.e., Milky Way type), the inner regions[9] of the galaxy are usually affected by more chaotic motions, as revealed by a quite irregular rotational curve and higher order deviations (i.e., k_5/k_1) at small radii. As the major merger evolves, the inner regions rapidly relax into a rotating disk, while the outer parts remain out of equilibrium. This implies that the velocity field in a post-coalescence system might be dominated by rotation in the inner regions but have large kinematic asymmetries in the outer parts, as is actually observed in our systems. Provided that the outer regions retain better the memory of a merger event, we propose a criterion that enhances the relative importance of the asymmetries at larger radii.

Instead of simply averaging the asymmetries over all radii (as in Shapiro et al. (2008)), we then weight these according to the number of data points used in their determination. Since the number of data points of the outer ellipses is larger than for the inner ones, the asymmetries found in the outer ellipses contribute more significantly to the average when deriving v_{asym} and σ_{asym}. As the number of data points is to first approximation proportional to the circumference of the ellipse, for practical reasons we used this to weight the asymmetries found for the different ellipses.

[9] If a galaxy covers a FoV of 30 kpc $\times$ 30 kpc, the regions more affected by chaotic motions are those at galactocentric distances smaller than 10 kpc.

The circumferences of the ellipses are computed using the truncated 'infinite sum' formula, which is a function of the ellipticity (i.e., $e = \sqrt{1 - q^2}$) and the semi-major axis of the ellipse (r)

$$C(e, r) \approx 2\pi r \left[1 - \left(\frac{1}{2} \right)^2 e^2 - \left(\frac{1 \cdot 3}{2 \cdot 4} \right)^2 \cdot \frac{e^4}{3} \right]. \tag{4.7}$$

The final formula to compute the weighted velocity and velocity dispersion asymmetries are respectively

$$v_{asym} = \sum_{n=1}^{N} \left(\frac{k^v_{avg,n}}{B^v_{1,n}} \cdot C_n \right) \cdot \frac{1}{\sum_{n=1}^{N} C_n}, \tag{4.8}$$

$$\sigma_{asym} = \sum_{n=1}^{N} \left(\frac{k^\sigma_{avg,n}}{B^v_{1,n}} \cdot C_n \right) \cdot \frac{1}{\sum_{n=1}^{N} C_n}, \tag{4.9}$$

where N is the total number of radii considered, C_n the value of the circumference for a given ellipse, the different k_n (k^v_n and k^σ_n) are the deviations concerning respectively the velocity field and velocity dispersion maps, and B^v_1 is the rotational curves. We refer to this approach as the *'weighted'* method and its associated plane W-[σ_a - v_a]). In Fig. 4.11, the results in the W-[σ_a - v_a] plane for our four galaxies are shown, where MC were performed as described above.

The results follow the same general trend but the two classes are distinguished somewhat more clearly than in the unweighted case. For class 0 objects, the *weighted* velocity asymmetries are lower, while for class 2 objects these asymmetries are somewhat higher than in the [σ_a - v_a] plane. Therefore, this highlights that post-coalescence mergers have larger deviations at larger radii with respect to pure rotational motions, while disks have still smaller deviations than those obtained using [σ_a - v_a]. In this case, the total kinematic asymmetry border, which distinguishes the two disks and the two post-coalescence mergers, is characterized by a mean value of 0.146.

4.2.9 Angular resolution/redshift dependence

The effects of angular resolution on the distortions of the velocity fields produced by mergers were discussed by Kronberger et al. (2007) based on simulated velocity fields as a function of redshift (i.e., $0 < z < 1$). They found that for large (Milky Way type) galaxies the distortions are clearly visible at intermediate redshifts but partially smeared

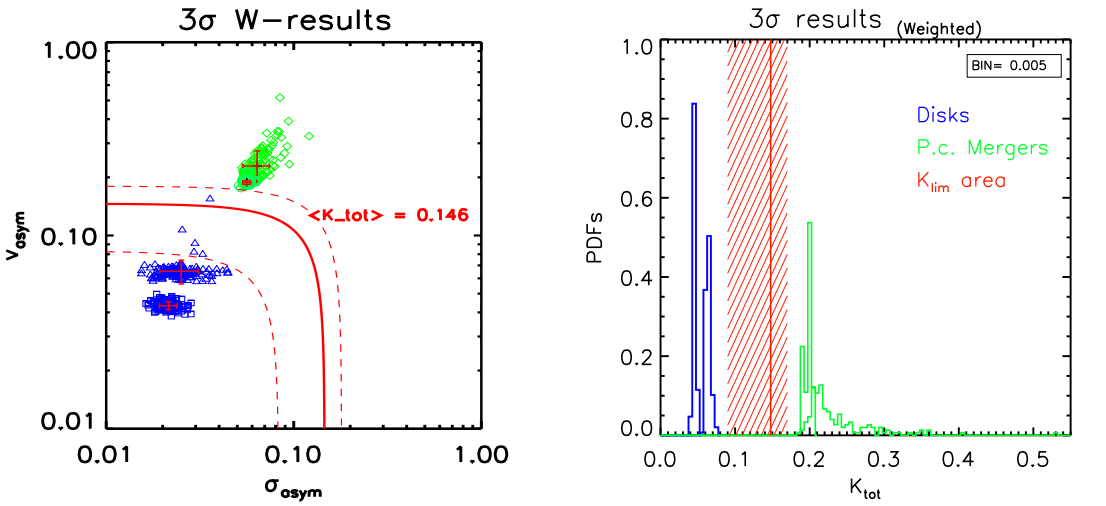

Figure 4.11: **Left:** Weighted asymmetry measures of the velocity $v^{(w)}_{asym}$ and velocity dispersion $\sigma^{(w)}_{asym}$ fields derived from the Monte Carlo realizations for the four objects. For each source, 150 MC simulations are run but only the $\pm 3\sigma$ results are shown. The solid red line indicates the empirical division between disks and post-coalescence mergers at $<K_{tot}> = 0.146$. **Right:** The probability distribution function (PDFs) as derived from MC realizations. The empirical delineation $K_{lim} = 0.146$ clearly distinguishes the two classes along with a large range of other values (i.e., dashed K_{lim} area).

out, while for small galaxies even strong distortions cannot be seen in the velocity field at z $\approx$ 0.5. Gonçalves et al. (2010), simulating LBAs at redshift $z \sim 2$, found that, in general, galaxies at high-z have smaller values of K_{tot}, i.e., they appear more disky than they actually are. Although their originally reported percentages of galaxies classified as mergers, locally and at z = 3, are, respectively, $\sim$ 70% and $\sim$ 38%, in our own analysis we end up with somewhat different percentages, respectively, $\sim$ 60% and $\sim$ 30%.

To investigate the effects of resolution on our results, we simulate the observation of these systems at $z = 3$ with a typical pixel scale of 0.1″ (the same pixel scale as the IFU *NIRSpec/JWST*). At this redshift, the current FoV of our images is about 1″ x 1″ with a typical scale of 7.83 kpc/arcsec, assuming a ΛCDM cosmology with $H_0 = 70$ km s^{-1} Mpc^{-1}, $\Omega_M = 0.3$, and $\Omega_\Lambda = 0.7$. The simulated maps are shown in Fig. 4.12. We apply *kinemetry* using these maps and, following the same procedures as before, obtain the results shown in the [σ_a - v_a] (Fig. 4.13) and W-[σ_a - v_a] (Fig. 4.14) planes. The [σ_a - v_a] plane shows the expected trend, where both classes appear to be more symmetric when observed at high redshift. In this case, a lower value of the total kinematic asymmetry K_{asym} border is derived (red dashed line), as expected (i.e., $K_{tot} = 0.096$). Thus, shifting the sample from $z = 0$ to $z = 3$, the frontier between *disks/post-coalescence mergers* in the [σ_a - v_a] plane changes from 0.135 to 0.096.

The W-[σ_a - v_a] plane is less sensitive to resolution effects after redshifting our sample $z = 3$ (see Fig. 4.14). This is because the larger / outer regions are the ones less affected

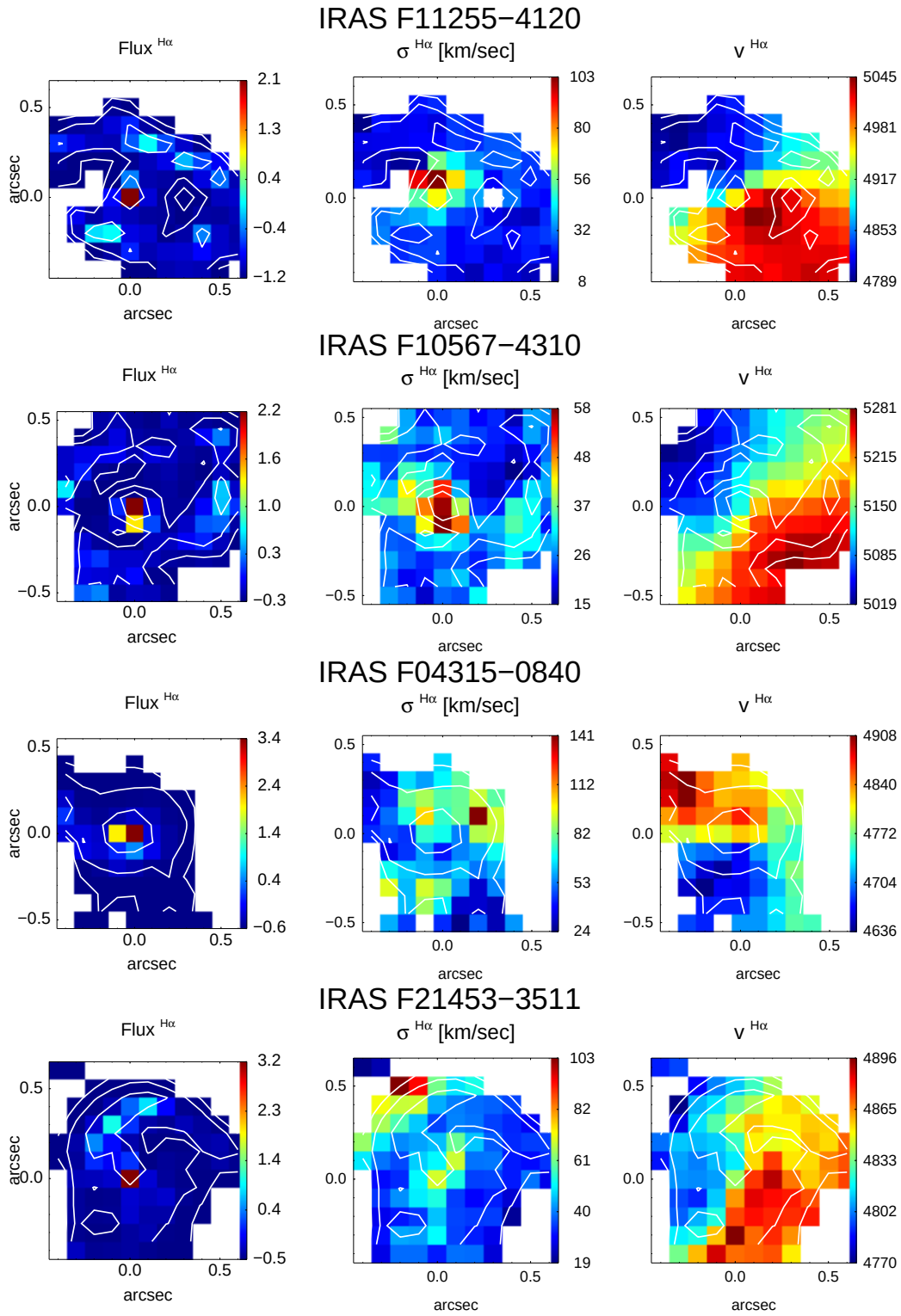

Figure 4.12: Hα maps for the four objects observed at $z = 3$ with a spatial sampling of 0.1″. The flux intensity, velocity dispersion σ (km s^{-1}), and velocity fields v maps (km s^{-1}) for the main component are shown. The flux intensity maps are represented on a logarithmic scale and in arbitrary flux units. All the images are centered using the Hα peak and the iso-contours of the Hα flux are over-plotted.

by resolution effects. As with this new criterion, the associated asymmetries weight more than those present at inner radii, the computed asymmetries (i.e., v_{asym}, σ_{asym}) are less affected by resolution. Therefore, the total kinematic asymmetry distinguishing the two classes changes only from 0.146 to 0.130 between z=0 and z=3. Summarizing, resolution effects tend to smooth kinematic deviations making objects appear more disky than they actually are. These effects are more significant when analyzing the kinematic asymmetries in the (unweighted) [σ_a -v_a] plane than in the W-[σ_a - v_a] one. In particular, when comparing our local seeing limited observations with simulated data at $z = 3$ (and 0.1″/spaxel), the total kinematic asymmetry border value is reduced by a 30% from $z = 0$ to $z = 3$ in the [σ_a - v_a] plane, while it is only shifted by 11% in the W-[σ_a - v_a] plane.

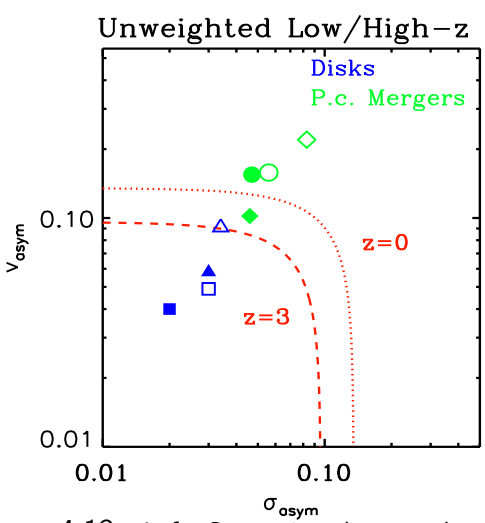

Figure 4.13: *Left:* Comparison between local and z=3 results in the [σ_a - v_a] plane. Empty symbols represent low-z results, while filled ones are for z=3. Symbols have the same meaning as in Fig. 4.7. The red dashed line is the *high-z* frontier with a value of 0.096 as explained in the text while the dotted one is for the local analysis (i.e., 0.135).

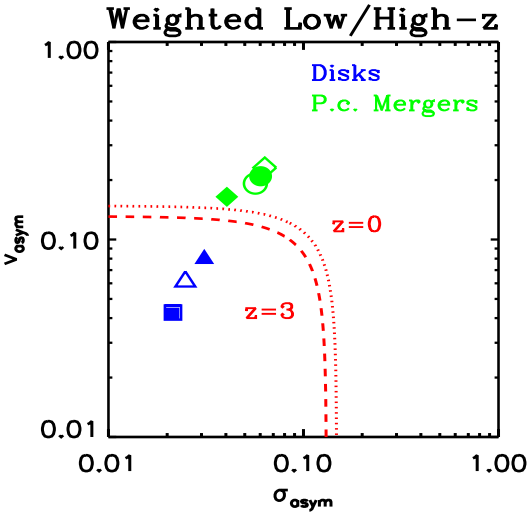

Figure 4.14: *Right:* Comparison between local and z=3 results in the W-[σ_a - v_a] plane. Empty symbols represent low-z results, while filled ones are for z=3. The red dashed line represents the *high-z* frontier, while the dotted one is for the local case.

Comparing our results with those obtained in Shapiro et al. (2008) when considering local spirals and toy-disk models as *observed* at high-z, we note that the low value of our K_{tot} (~ 0.1) classifies those galaxies as *mergers* and, on the other hand, the frontier defined in S08 classifies our post-coalescence mergers and IRAS F12112+0305 as *disk*. This illustrates that the definition of a *mergers* is a crucial point when defining the asymmetry frontier. A lower value of the fraction merger/disk (i.e., a higher value of the K_{tot} parameter) can be derived when only pre-coalescence ongoing mergers are considered as 'true' mergers. The *weighted* criterion proposed here should be applied to larger and more diverse samples in order to understand the uncertainties associated with this type

of classifications.

4.3 *Kinemetry*-based characterization of the entire (U)LIRG sample

As commented at the beginning of this chapter, in this section we are going to apply the *kinemetry* technique to the whole sample in order to characterize the kinematic asymmetries in local (U)LIRG systems. In particular, the same analysis as described in Sects. 4.2.1 and 4.2.9 is applied, thus comparing and discussing the Shapiro et al. (2008) (hereafter, 'unweighted') and Bellocchi et al. (2012) (hereafter, 'weighted') methods.

4.3.1 Distinguishing local (U)LIRGs as *disk/merger*

As largely described in Chapter 2, our sample consists of 51 individual galaxies covering a large L_{IR} range and encompasses a wide variety of morphologies which allow us to discuss the kinematic asymmetries as a function of the galaxy properties (e.g., infrared luminosity L_{IR}, morphological class).

In order to better interpret and discuss our data we recall the Veilleux et al. (2002) classification, according to which the Interacting (type 1) galaxies can be sub-classified as *Wide- or Close-Interacting* according to their projected nuclear separation. The presence (or not) of tidal tails and/or other structures interconnecting the nuclei using continuum maps (e.g., HST, DSS) is considered as well since it could help us to better distinguish the merger phase. In particular, if the nuclear projected separation is $>$ 10 kpc, the emission of the two galaxies can be well separated in the VIMOS maps, and there is no presence of tidal tails and/or other structures between the nuclei in their continuum maps (e.g., HST, DSS), the sources are considered as *Wide-Interacting pairs* (or *paired-disks*). A few systems (i.e., IRAS F06035-7102, IRAS F06206-6315, IRAS F12596-1529, IRAS F22491-1808, IRAS F23128-5919) are classified as *Close-Interacting* pairs (or *ongoing mergers*), defined as pairs with projected nuclear separation smaller than 10 kpc (but larger than 1.5 kpc, at which the limit for the coalescence phase is defined) and when the individual contributions cannot be disentangled in the VIMOS maps[10]. These galaxies have a common envelope, and they are likely in a more advanced merger phase than the wide-interacting pairs. Therefore, we have distinguished four dynamical phases, where the first two are referred as 'disk', while the second two as 'mergers':

[10] The galaxy IRAS F08520-6850 is considered as *wide-pair* because the two galaxy can be well separated in the VIMOS maps although showing a nuclear separation slightly smaller than 10 kpc.

- Isolated disk
- Paired disk (Wide-interacting pair)

} `disks'

- Ongoing merger (Close-interacting pair)
- Post-coalescence merger

} `mergers'

Similarly to Shapiro et al. (2008) and what done in Sect. 4.2.7, we quantify the total kinematic asymmetry degree K_{tot} of the each galaxy, as the combination of both the kinematic asymmetry contributions of the velocity field (v_{asym}) and velocity dispersion (σ_{asym}) maps, i.e. $K_{tot} = \sqrt{(\sigma^2_{asym} + v^2_{asym})}$. We find that the ongoing merger systems have the largest kinematic asymmetry (K_{tot}), while (isolated and paired) disks and post-coalescence mergers are characterized by lower K_{tot} values. In a similar way, ULIRGs show higher K_{tot} with respect to LIRGs. The mean values for the different groups are shown in Tab. 4.4.

Table 4.4: Mean (median) K_{tot} asymmetry values of the (U)LIRG VIMOS subsamples.

Systems (1)	K_{tot} (2)	# objects (3)
class 0 (Isolated disk)	0.13 ± 0.03 (0.11)	13/50
class 1 (Paired disk)	0.14 ± 0.03 (0.10)	21/50
class 1 (Ongoing merger)	1.9 ± 0.47 (1.95)	5/50
class 1 (Pair d. & Ongoing m.)	0.48 ± 0.16 (0.12)	26/50
class 2 (Post-coalescence merger)	0.64 ± 0.22 (0.29)	11/50
LIRGs	0.27 ± 0.08 (0.11)	43/50
ULIRGs	1.37 ± 0.42 (1.03)	7/50
(U)LIRG	0.43 ± 0.10 (0.16)	50

Col (1): System. Col(2): Mean (and median) total kinematic asymmetry. Col (3): Fraction of galaxies in each subsample.

The kinematic asymmetry results (i.e., v_{asym} and σ_{asym}) derived for the whole local sample are shown in Fig. 4.15 when applying, respectively, the unweighted (left panels, [σ_a-v_a]) and weighted (right panels, [σ^w_a-v^w_a]) criteria. The same general trend is found

in both the planes, where *disks* (i.e., isolated and paired disks) are characterized by lower kinematic asymmetries than *mergers* (i.e., ongoing and post-coalescence).

Determining a frontier

In order to distinguish *disks* from *mergers* in the two kinematic asymmetry planes we try to find out a value of the frontier applying the following approach. Since a quite large scatter is found in the asymmetry values of each kinematic class (i.e., disk and merger populations), the median value (instead of the mean) of each K_{tot} distribution is considered (hereafter, $K_{tot}^{med(disk)}$ and $K_{tot}^{med(merger)}$). Then, the total kinematic asymmetry for the frontier (K_{tot}^{F}) is computed as the mean value of these two quantities:

$$K_{tot}^{F} = \frac{1}{2} \times (K_{tot}^{med(disk)} + K_{tot}^{med(merger)}). \quad (4.10)$$

The uncertainty associated to this value has been computed as the mean value of each *Median Absolute Deviation (or MAD)*[11] estimate associated to each distribution. As shown in Fig. 4.15, for $K_{tot} < K_{tot}$ -1 MAD no mergers are found, while for $K_{tot} > K_{tot} + 1$ MAD disks do not exist. Indeed, the more disturbed objects are those classified as *ongoing-mergers* (i.e., IRAS F06035-7102, IRAS F06206-6315, IRAS F12596-1529, IRAS F22491-1808, IRAS F23128-5919)[12] along with post-coalescence sources which show high asymmetries (i.e., IRAS F05189-2524, IRAS 09022-3615, IRAS F10257-4339, IRAS F13001-2339), characterized by very disturbed kinematic maps. There is a 'transition region' for which K_{tot} - 1 MAD $< K_{tot} < K_{tot} + 1$ MAD, where the distinction between *disk/merger* is difficult. The middle panels in the same figure show the corresponding probability distribution functions (PDFs) of each morphological class normalized to the number of objects in each bin.

Both the unweighted and weighted methods give similar results, although the weighted one allows to distinguish slightly better disks and mergers. This is better visible if, apart from the statistical approach, we determine the optimal value of the frontier able to classify our local sources in disk and merger galaxies: to this aim, the number of well classified galaxies as a function of the K_{tot} is derived. Since in our sample the number of disks dominates on the number of mergers, we then define an 'index' parameter (I) as

[11] The respective uncertainty associated to the *median* value of the total kinematic asymmetry has been computed as median-absolute-deviation (hereafter, MAD). It returns a data set' s median absolute deviation from the median, that is median(|data - median(data)|). It is a proxy for the standard deviation, but is more resistant against outliers.

[12] These sources may appear as such either because they are actually in the early phase of merging or because the limited angular resolution of VIMOS does not allow to separate the contribution of each galaxy.

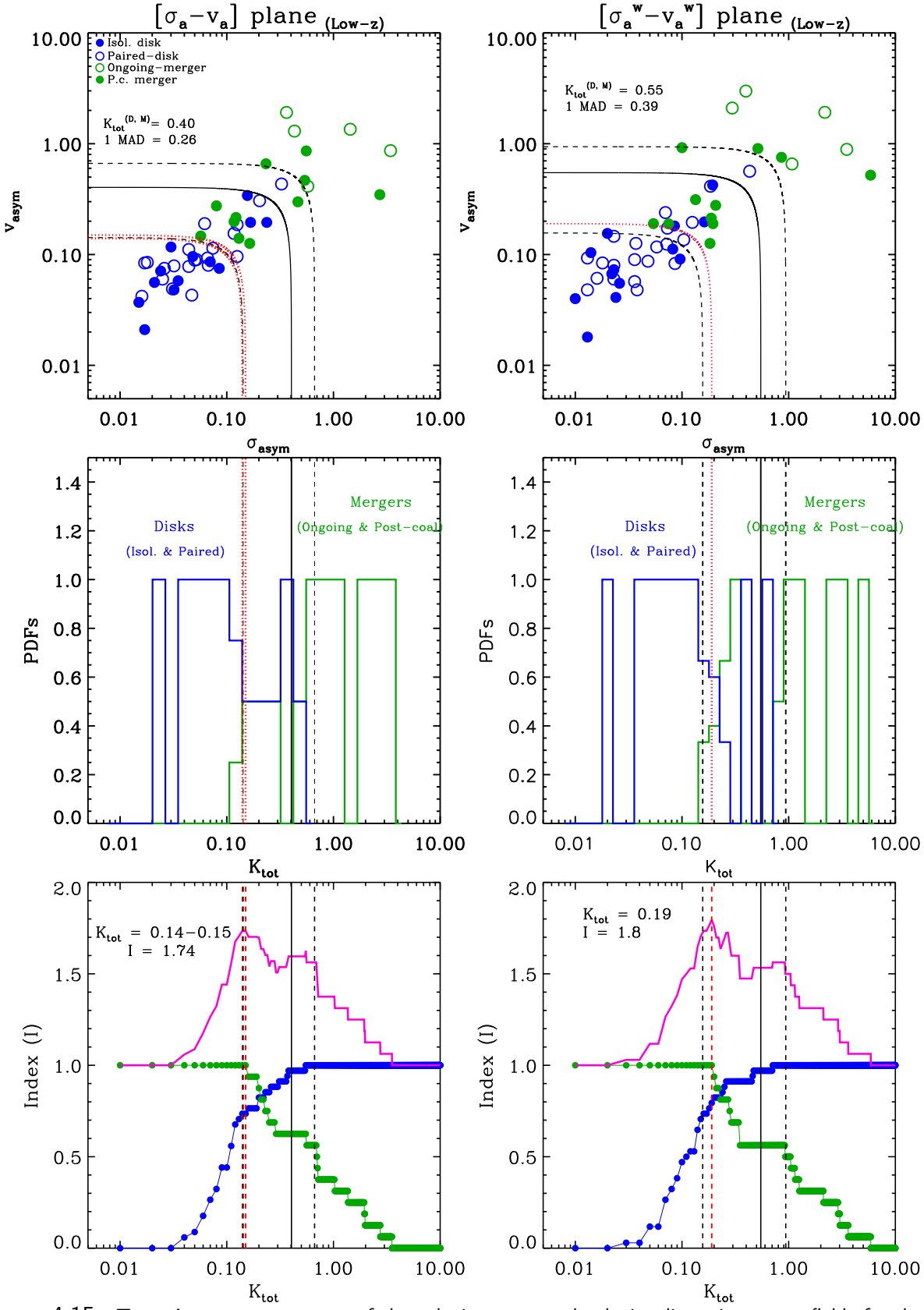

Figure 4.15: **Top:** Asymmetry measure of the velocity v_{asym} and velocity dispersion σ_{asym} fields for the whole sample observed at low-z when applying the unweighted (left) or the weighted (right) methods. Different colors distinguish the different morphological types: the solid dark blue dots are the morphologically classified isolated disks, in open blue dots the wide-pairs, in solid dark green dots the post-coalescence mergers and in open green dots the close-pairs. **Middle:** The respective probability distribution functions (PDFs) of the respective planes normalized to the number of objects in each bin. **Bottom:** Distribution of the total number of well classified galaxies at low-z as a function of the total kinematic asymmetry K_{tot} in the unweighted (left) and weighted (right) planes.
The K_{tot} value which identifies the maximum index I is identified using a red line in all the plots: both these values are shown in the bottom panels. The statistical frontiers ($K_{tot} \pm 1$ MAD) are shown in black (dashed lines) in all the panels.

the sum of the respective fractions of well classified systems in each morphological class (i.e., I_{disk} for disks and I_{merger} for mergers). In particular, I is defined in Eq. 4.11:

$$I = I_{disk} + I_{merger} = \frac{\#well\ class\ disks}{total\ \#\ disks} + \frac{\#well\ class\ mergers}{total\ \#\ mergers} \quad (4.11)$$

The results are shown in the bottom panels in Fig. 4.15 in the two cases (i.e., unweighted and weighted methods): the disk contribution is represented in blue, the merger one is shown in green and the total one in magenta. The total observed distribution allows to determine the optimal K_{tot} frontier value for which the largest fraction of well classified systems (I) is achieved: this value is also shown in the figure. In each distribution two peaks are found and we refer to them as 'main' and 'secondary' peaks. The main peak identifies the K_{tot} value(s) which well classifies the largest fraction of systems, where $K_{tot} \sim 0.15$ and 0.19, in the unweighted and weighted planes, respectively. As visible in the figure, the statistical K_{tot} values (i.e., $K_{tot} \pm 1$ MAD) well approximate the main and secondary peaks, well defining the region where the distinction between disk/merger is difficult.

Thus, at low-z the largest value of I is derived when the weighted method is applied (i.e., I = 1.8, $K_{tot} \sim 0.19$), although it is only slightly larger than that derived in the unweighted plane (I = 1.74). When considering the frontier considered by Shapiro et al. (2008) (i.e., $K_{tot} = 0.5$) the index I reaches the value of ~ 1.6, clearly lower than our optimal value and close to the secondary peak. If we consider this frontier half of the post-coalescence mergers are misclassified as disks, leading to an overestimation of the disk/merger ratio.

4.3.2 Total kinematic asymmetries of high-z simulated (U)LIRGs

In order to investigate the effects of resolution, we simulate observations at z = 3 as done in Sect. 4.2.9. The 'simulated' FoV of the maps ranges between $\sim 1'' \times 1''$ up to $\sim 5'' \times 5''$ with the scale of ~ 7.7 kpc arcsec^{-1} corresponding to z = 3. We apply *kinemetry* to these kinematic maps and the results are shown in Fig. 4.16, respectively, for the unweighted (left) and weighted (right) planes (i.e., $[\sigma_a\text{-}v_a]_{Hz}$ and $[\sigma_a^w\text{-}v_a^w]_{Hz}$). As expected, the results are characterized by lower kinematic asymmetries than those obtained locally (e.g., Gonçalves et al. 2010; Bellocchi et al. 2012). This result is due to the fact that when lowering the linear resolution the kinematic deviations are smoothed, making objects to appear more symmetric than they actually are. However, a few sources among

the ongoing- (i.e., IRAS F06035-7102, IRAS F2249-1808, IRAS F23128-5919) and post-coalescence mergers (i.e., IRAS F09022-3615, IRAS F05189-2524, IRAS F10257-4339, IRAS F13001-2339) still preserve quite high values.

Thus, the distribution of the number of well classified objects as a function of the K_{tot} is considered (bottom panels in Fig. 4.16). The main and secondary peaks are identified as well. The maximum index I of 1.7 is reached when the K_{tot} assumes the (average) value of $\sim$0.14 and $\sim$0.16 in the unweighted and weighted planes, respectively. The value adopted by Shapiro et al. (2008) would imply an index I of $\sim$ 1.4, clearly lower than the optimal value derived by us. In this case about two thirds of our 'mergers' would be classified as 'disks', largely overestimating the disk/merger ratio.

As a result, the comparison between local and high-z results obtained using both the unweighted and weighted methods allows to draw the following conclusions:

- At low-z similar results are found for the unweighted and the weighted methods, although for the weighted one 'disks' and 'mergers' are slightly better separated. The optimal K_{tot} value able to classify the largest number of objects is $\sim$ 0.19;

- A 'transition region' is found in the asymmetry plane with the total kinematic values (at low-z) in the range 0.19 (0.15) $< K_{tot} <$ 0.9 (0.6) for the weighted (unweighted) plane, while outside we are able to well classify with 'kinemetry' *disks* and *mergers*.

- At high-z, a trend similar to that found locally is obtained but characterized by lower total kinematic asymmetries K_{tot}, as a consequence of the resolution effects. Slightly better results are derived when using the weighted method, in which the main peak in the I distribution is better defined, ending up with a $K_{tot} \sim$ 0.16;

- Finally, if the frontier obtained by Shapiro et al. (2008) (i.e., K_{tot} = 0.5) is considered, the fraction of well classified objects (I) would be clearly lower than our optimal values, both locally and at high-z. This limit implies that at least half of the post-coalescence mergers would be misclassified as disks thus leading to an overestimation of the disk/merger ratio, both locally and at high-z.

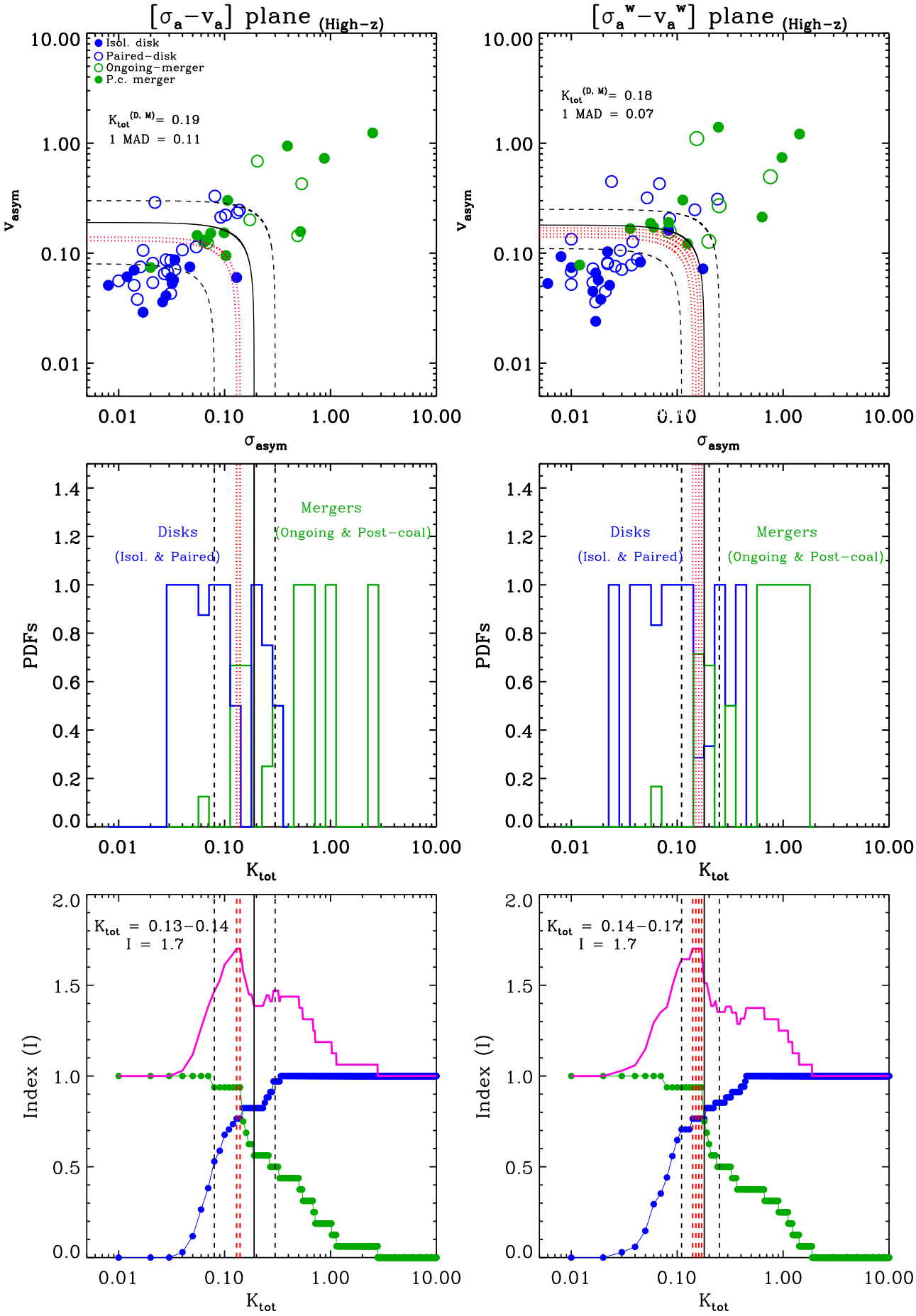

Figure 4.16: High-z results in the (σ_a-v_a) and (σ_a^w-v_a^w) planes for the whole sample simulated at z = 3. The panels are the same as those shown in Fig. 4.15.

4.3.3 Correlations between total kinematic asymmetry and some kinematical and dynamical parameters

The relation between the K_{tot} and the infrared luminosity L_{IR}

In this section the relation between the total kinematic asymmetry K_{tot} and some kinematical and dynamical parameters is considered. In particular, some trends are found when considering the K_{tot} as a function of the infrared luminosity L_{IR}, the dynamical ratio v^*/σ and the projected nuclear separation. Since at low-z the K_{tot} values for the unweighted and weighted planes are only slightly different and the same general trend is conserved, we take into account the unweighted values for a possible comparison with other previous high-z works.

Although our analysis is mainly focused on the VIMOS sample, as part of the discussion, additional galaxies with available IFS data have been included to increase the number of systems in the ULIRG luminosity range. These data correspond to the observations taken with INTEGRAL/WHT (i.e., Colina et al. 2005) which will allow us to discuss in a more complete (statistical) way our results. Their kinematic maps have been resampled as if they were observed at the VIMOS spatial sampling and then analyzed as done for the VIMOS sources. In particular, we consider the eight mergers analyzed in Shapiro et al. (2008) for a more focused comparison. Their individual K_{tot} values are shown in Tab. 4.5.

Table 4.5: Individual total kinematic asymmetries K_{tot} of the INTEGRAL/WHT ULIRG sub-sample.

ID (IRAS) (1)	log L_{IR} (2)	Class (3)	K_{tot} (4)
08572+3915	12.15	Ongoing merger	0.67
12112+0305	12.35	Ongoing merger	0.23
14348-1447	12.37	Ongoing merger	0.27
15206+3342	12.25	Post-coalescence merger	0.19
15250+3609	12.07	Post-coalescence merger	0.58
17208-0014	12.41	Post-coalescence merger	0.16
Arp220	12.17	Post-coalescence merger	0.20
Mrk273	12.16	Post-coalescence merger	1.19

Col (1): System. Col(2): Infrared luminosity as in Chapter 2 (Tab. 2.1, Column 6). Col (3): Morphological class as defined in this section. Col (4): total kinematic asymmetry.

In Fig. 4.17 the linear trend between the total kinematic asymmetries K_{tot} as a function of the infrared luminosity L_{IR} is shown. This plot clearly shows the (morphological

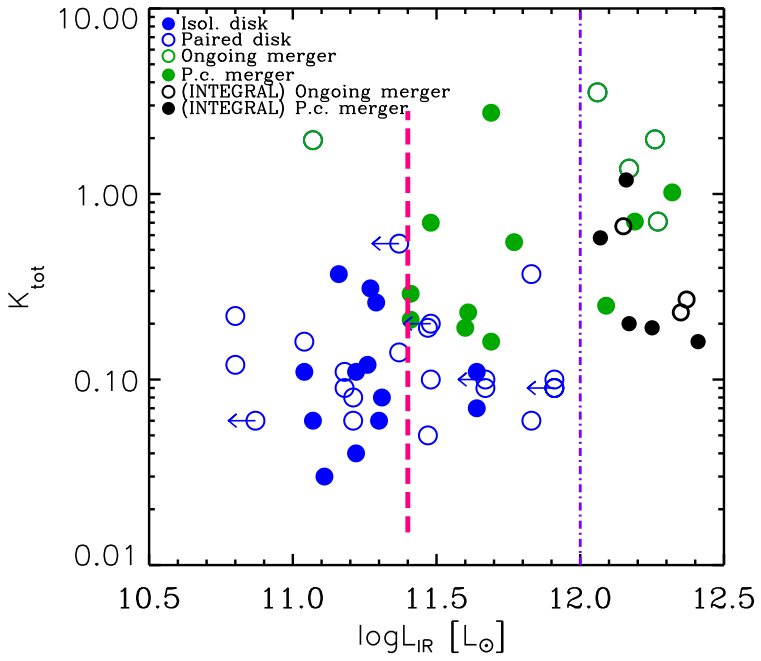

Figure 4.17: Relation between the total kinematic asymmetry values K_{tot} as a function of the infrared luminosity L_{IR}. The vertical dot-dashed violet line separates the LIRG-ULIRG domain, while the dashed pink line possibly separates 'disks' and 'mergers'.

and kinematical) results summarized in Tab. 4.4 (see also Tab. 3.1). Indeed, the more luminous objects (ULIRGs, including those from INTEGRAL) are those showing the higher total kinematic asymmetries, while the less luminous ones (LIRGs) have lower kinematic asymmetries. Indeed, the majority of the more luminous galaxies are classified as *mergers*, while the less luminous objects are classified as *disks*. Furthermore, $L_{IR} \sim 11.4$ $L_{\odot}$ seem to be a critical infrared luminosity as it separates these two morphological classes.

The relation between K_{tot} and v^*/σ

As discussed in Chapter 3 we found a clear correlation between the different phases of the merging process and the mean kinematic properties inferred from the kinematic maps in our sample. In particular, isolated disks, interacting galaxies, and merging systems define a sequence of increasing mean velocity dispersion and decreasing velocity field amplitude, which is characterized by intrinsic average dynamical ratios (v^*/σ) of 4.7, 3.0, and 1.8, respectively.

In a similar way, the total kinematic asymmetry K_{tot} quantifies the kinematic asymmetry degree in a galaxy with respect to the ideal rotating disk case. In Fig. 4.18 the relation between (unweighted) K_{tot} and v^*/σ for each source is considered. A (linear)

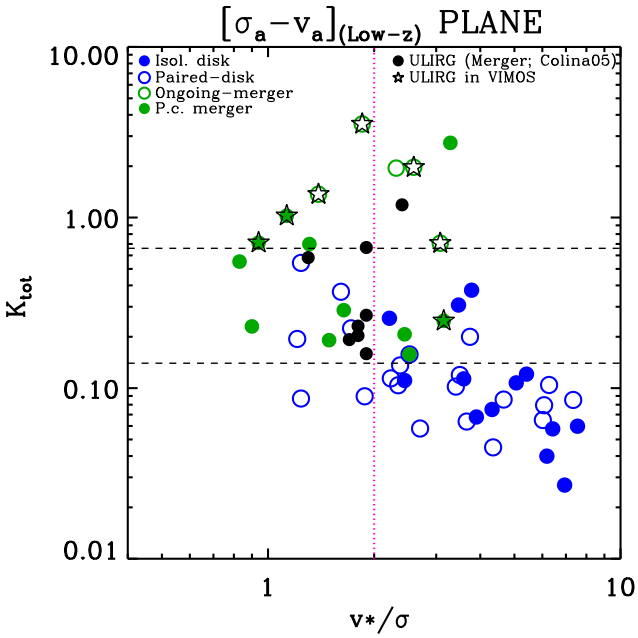

Figure 4.18: The relation between the total kinematic asymmetry K_{tot} and the intrinsic dynamical ratio v^*/σ is shown. The more rotation dominated objects are those showing the lower kinematic asymmetry, while an opposite trend is found for the dispersion-dominated objects. The colors and symbols used are the same as in the previous figures. Black dots identify ULIRGs observed with INTEGRAL, while black stars represent ULIRGs from VIMOS.

inverse trend is found: the more rotation-dominated objects (i.e., $v^*/\sigma \geq 2$, dashed vertical line) generally show lower values of the kinematic asymmetries with respect to those derived for dispersion-dominated systems (i.e., $v^*/\sigma < 2$), as expected. In order to quantify how well the 1D parameter v^*/σ classifies disks and mergers in our sample with respect to the *kinemetry* results, we compute the fraction of well classified objects as before (i.e., Sect. 4.3.1 and 4.3.2) deriving an index I = 1.4. This is smaller than the one obtained using the total kinematic asymmetry K_{tot}, which is an indication that when the full 2D information is taken into account to study the asymmetries better classifications are obtained. In Fig. 4.18 the ULIRGs observed with INTEGRAL are identified by black dots while ULIRGs observed with VIMOS are identified by black stars. All these ULIRGs are well classified as *mergers* according to our *kinemetry* frontier while a lower fraction is well classified according to the v^*/σ parameter. This confirms the importance of the 2D kinematic analysis in unveiling the real status of these systems.

Kinematic asymmetries as a function of the nuclear separation along the merger process

In this section we analyze the relation between the projected nuclear separation and the total kinematic asymmetry K_{tot} for those pair of galaxies for which a nuclear separation can

be computed. The INTEGRAL subsample has been considered as well. In particular, the nuclear separation can be estimated for 19 systems[13]. An upper limit has been computed for the majority of the type 2 galaxies (assuming a nuclear separation smaller than the resolution element of the image considered). The HST and VIMOS continuum images have been used to derive the projected nuclear separation. In three cases (i.e., IRAS F01341-3735 , IRAS F09437+0317, IRAS F14544-4255) the DSS images have been used since a larger FoV was needed to cover the whole system.

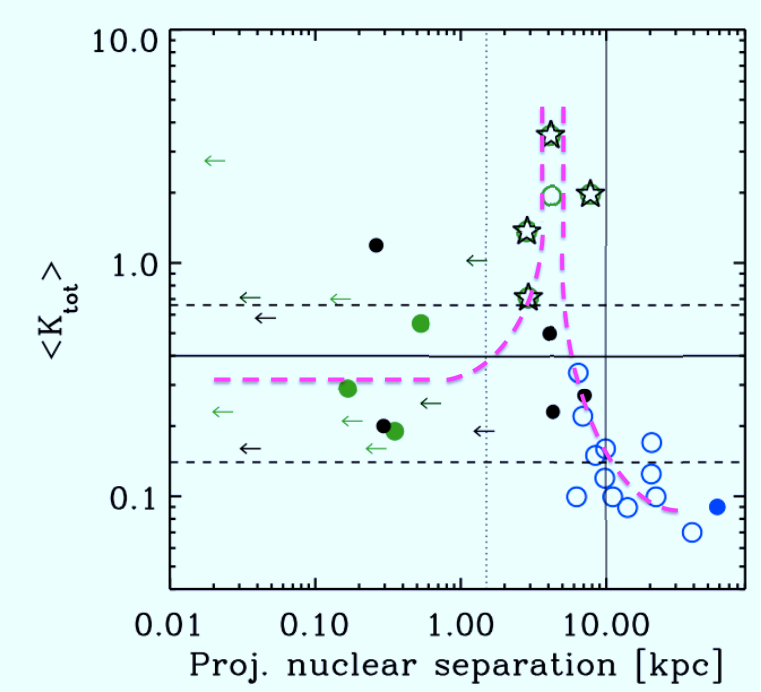

Figure 4.19: Relation between the mean total kinematic asymmetry K_{tot} and the nuclear projected separation in (wide and close) interacting and merging systems. The K_{tot} of a system generally increases with the decreasing of the nuclear separation: it reaches its maximum value in ongoing (pre-coalescence) mergers, then decreasing for post-coalescence mergers. The colors and symbols used are the same as in the previous figure (Fig. 4.18). The pink dashed line helps to highlight the evolutionary trend found when a galaxy goes from the wide-interacting phase to the post-coalescence one.

In Fig. 4.19 the mean value of the (unweighted) K_{tot} (i.e., $<K_{tot}>$) of each system is related with its nuclear projected separation. This plot highlights the fact that, during the first phases of the merging process, the smaller the nuclear separation of a system

[13]We refer to the type 1 systems IRAS F07027-6011, IRAS 08424-3130, IRAS F12043-3140, IRAS F01159-4443, IRAS F06035-7102, IRAS F06076-2139, IRAS F06206-6315, IRAS F06259-4780, IRAS F08520-6850, IRAS 12596-1529, IRAS F22491-1808, IRAS F23128-5919, IRAS F01341-3735, IRAS F09437+0317, IRAS F14544-4255, IRAS F18093-5744 and to a few type 2 objects IRAS 08355-4944, IRAS F10038-3338 and IRAS F21453-3511.

the higher its total kinematic asymmetry. Moreover, the maximum asymmetry value K_{tot} is reached for the ongoing mergers with nuclear separation $\sim$ 2-5 kpc, in which the merger phase is currently taking place. Then, a more unclear trend is shown for the post-coalescence mergers (i.e., type 2; nuclear separation less than 1.5 kpc), although their values are generally lower than those characterizing ongoing mergers. The virialization of the inner parts of these objects explains such results. The pink dashed line in Fig. 4.19 helps to highlight the possible evolutionary sequence obtained when a galaxy goes from the wide-interacting to the post-coalescence phase.

4.4 Summary and conclusions from *kinemetry*

This chapter has been divided into two parts: in the first one, we select a small subsample of four LIRGs (two disks and two post-coalescence mergers) located at similar distance (to minimize relative resolution effects). These systems offer the opportunity to explore the potential of the 'kinemetry' method when analyzing the velocity fields and velocity dispersion maps in moderately disturbed and partially relaxed systems. A new optimized criterion (i.e., weighted, Bellocchi et al. 2012) is also proposed and discussed along with the used of the criteria defined by Shapiro et al. (2008). We then apply these criteria to the four simulated observations at high-z, at the resolution of NIRSpec/JWST. In the second part, the same 'kinemetry' analysis is applied to the whole (U)LIRG sample (i.e., 51 individual galaxies) and the results are discussed.

From the first part, we draw the following conclusions from this study:

- The general kinematic properties of the four LIRGs are consistent with their morphological classification: *isolated disks* are found to have quite regular velocity fields and centrally peaked velocity dispersion maps consistent with a single rotating disk interpretation, while the remaining two galaxies have slightly different properties. In particular, we found that post-coalescence *mergers* have more irregular velocity fields and velocity dispersion maps that have off-nuclear velocity dispersion peaks (up to 220 km s^{-1} at 2.4 kpc from the H_α peak for IRAS F04315-0840) or nuclear asymmetric structures.

- We have found double-peaked emission-line profiles in the inner regions of the four galaxies. The secondary broad components (i.e., $\sigma \sim$ 70 - 450 km s^{-1}) are in all cases blue-shifted ($\Delta v \sim$ 50 - 150 km s^{-1}) and, taking into account the large velocities involved, they can be well explained by the presence of an *outflow* in a dusty environment. The pattern of the 2D kinematic maps of the secondary broad component for the two post-coalescence *mergers* (with kinematic axes perpendicular to those of the main component) further supports this interpretation. In the particular case of IRAS F04315-0840, the broad component is found over a quite extended area ($\sim$ 2.4 x 2.7 kpc^2).

- Our measured values of the v_c/σ_c parameter classify the four sources as *rotation dominated*. Similar results are obtained when using the quantity v_{shear}/Σ. This shows that our post-coalescence mergers have a large rotation component and that the sole use of these parameters does not allow us to discriminate their kinematic differences from those of disks.

- When the full 2D kinematics information provided by the spatially resolved velocity field and velocity dispersion maps is considered, the kinematic asymmetries are well characterized with *kinemetry*, making the morphological and kinematic classifications consistent for the four objects. Disks have lower kinematic asymmetries than those derived for post-coalescence mergers;

- We have explored a new criterion to characterize the kinematic asymmetries using *kinemetry*. In particular, we introduce a new weighting method that gives weight to the kinematics of the outer regions when computing the total asymmetries v_{asym} and σ_{asym}. This step is important because post-coalescence mergers have relatively small kinematic asymmetries in the inner parts as a consequence of the rapid relaxation into a rotating disk, with the outer parts being still out of equilibrium (i.e., having larger asymmetries). The 'frontier' between *disks* and *post-coalescence* systems only changes by 11% when considering the local and z=3 cases suggests that this new criterion dependents less on angular resolution effects. Thus, the W-[σ_a - v_a] plane differentiates in a more robust way *disks* from *post-coalescence mergers*.

- Classifying *disk/merger* systems using *kinemetry* is difficult, and clearly depends on the definition of a *merger*. The 'asymmetry frontier' depends on the 'type' of mergers considered: if only pre-coalescence ongoing mergers are considered as 'true' mergers, a lower value of the fraction of *merger/disk* systems can be derived.

- Our two post-coalescence systems would have been classified as *disks* if we would have used the previously defined criteria to classify *disks* and *mergers*. This suggests that the number of mergers to disk systems at high-z may have been underestimated by some previous works.

From the analysis applied to the whole sample we draw the following conclusions:

- The kinematic properties of our low-z (U)LIRGs derived using the *kinemetry* method are consistent with their morphology. Indeed, the majority of the isolated disks and paired-disks have low kinematic asymmetries in both their velocity field and velocity dispersion maps, while post-coalescence and ongoing-mergers show higher kinematic asymmetry values in both the velocity field and velocity dispersion maps. We are able to well separate regular *disks* from complex *mergers*, though a 'transition region' (i.e., $0.19 < K_{tot} < 0.9$) is found where *disks* show kinematic asymmetries as high as those derived for post-coalescence *mergers*. The best frontier able to well distinguish these two classes has a total kinematic asymmetry $K_{tot} \sim 0.19$ (weighted case). This value depends on the the definition of *disk/merger* systems. However, there is

not a value for the frontier able to separate in a categorical way such classes. This is found for both the weighted and unweighted methods, which give similar results when the whole sample is considered.

- A linear trend is found between the K_{tot} and the infrared luminosity L_{IR}, with the most luminous objects (ULIRGs) showing the highest total kinematic asymmetries. Furthermore, $L_{IR} \sim 11.4\ L_{\odot}$ seems to be a critical infrared luminosity as it separates these two morphological classes.

  A linear (inverse) trend is derived between the K_{tot} and the intrinsic dynamical ratio v^*/σ: morphologically classified *disks* show the higher dynamical ratio and the lower total kinematic asymmetry K_{tot}. Contrary, for the *mergers* v^*/σ is low while K_{tot} is high.

  An interesting trend is also found between the K_{tot} and the projected nuclear separation along the merger process. Initially, the smaller the nuclear separation the larger the K_{tot}, which reaches its maximum value during the 'ongoing merger phase' (nuclear separations of 2-5 kpc) and then decreases during the post-coalescence mergers phase, although with a relatively large dispersion.

- The K_{tot} limit derived by Shapiro et al. (2008) to separate *disks* from *mergers* is significantly larger than the one found by us for the whole sample, with both the unweighted and weighted methods. This would classify as *merger* only the ongoing mergers and some post-coalescence mergers with more complex kinematics, lowering the value of the fraction of merger/disk systems since it overestimates the fraction of disks according to the results found in this work.

Chapter 5

Future work

In this chapter we present some preliminary analyses and results of topics that will be developed in the future. First, the stellar mass estimates for a subsample of 25 systems are derived from the Spectral Energy Distribution (SED) fit, obtained using the **MAGPHYS** *package. These results are compared with the dynamical mass estimates previously derived in Chapter 3 for the whole sample, whose comparison allows to estimate the gas fraction in our local systems. This work has been done in collaboration with Prof. Stephane Charlot and Dr. Camilla Pacifici at Institut d' Astrophysique de Paris (IAP).*

We also present preliminary results based on the comparison between our local kinematic results and those derived for high-z SFGs in previous IFS-based works. This allows us to study the similarities (or discrepancies) in the kinematics and dynamics between low-z (U)LIRGs and high-z SFGs.

5.1 Stellar masses in local (U)LIRGs: comparison with the dynamical masses

In recent years multi-wavelength surveys enabled a more complete study of the universe both locally and at high-z. The study of the observed spectral energy distributions (SEDs) using multi-wavelength data helps us to constrain some of the key physical parameters which characterize the systems (e.g., stellar mass, star formation rate, dust mass).

The comparison between the stellar and dynamical masses allows us to estimate the gas mass in our systems. We thus use the model developed by da Cunha et al. (2008), in which the galaxy emission, from the ultraviolet to optical and infrared wavelengths, is interpreted in terms of star formation histories and dust content. This model relies on the Bruzual & Charlot (2003) population synthesis code to compute the spectral evolution of

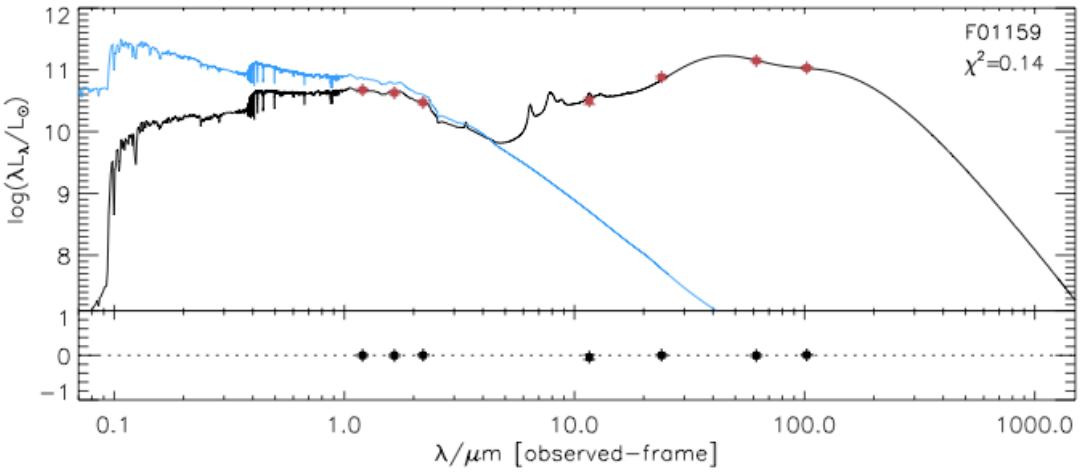

Figure 5.1: Best model fits (in black) to the observed spectral energy distributions (red dots) of the galaxy IRAS F01159-4443. The blue line shows the unattenuated stellar population spectrum. *Below:* The residuals (L_{obs} - L_{mod})/L_{obs} are shown.

stellar populations. The package *Multi-wavelength Analysis of Galaxy Physical Properties* (hereafter, MAGPHYS[1]) has been used to interpret observed spectral energy distributions (in our case at rest wavelengths in the range 1.22 μm $\leq \lambda \leq$ 100 μm) of galaxies in terms of galaxy-wide physical parameters pertaining to the stars and the interstellar medium (e.g., stellar and dust masses, star formation rate, etc.).

In order to derive the stellar masses $M_\star$ in our systems, the Near-IR 2MASS fluxes (i.e., J, H, K bands) along with those obtained from the Far-IR IRAS bands (i.e., 12, 25, 60, 100 μm) are considered. Such analysis is applied to 25 of the 38 systems considered, since the emission of individual galaxies in some interacting systems (i.e., IRAS F07027-6011, IRAS F01341-3735, IRAS F06259-4780, IRAS F08424-3130, IRAS F08520-6850, IRAS F12596-1529, IRAS F18093-5744) cannot be disentangled due to the limited angular resolution in the IRAS bands. As first step, we also exclude the systems with uncertain morphological classification (i.e., IRAS F09437+0317, IRAS 12116-5615, IRAS F13001-2339, IRAS F17138-1017). In Fig. 5.1 an example of the results of the SED fitting is shown for IRAS F01159-4443 (i.e., the best -attenuated- fit model is shown in black while the unattenuated fit is in blue).

When comparing these results with the dynamical mass values derived in Chapter 3, we find that the stellar masses are consistent with the expectation that $M_\star \leq M_{dyn}$, ending up with a linear (log-log) relation:

$$log(M_\star/M_\odot) = 5.7 + 0.4 \times log(M_{dyn}/M_\odot)\ . \qquad (5.1)$$

[1] *http://www.iap.fr/magphys.*

For a few peculiar cases[2] this discrepancy could be explained as due to a underestimation of the dynamical mass, possibly caused by the presence of an AGN which may affect the kinematic properties of the objects, or an overestimation of the stellar mass, due to uncertainties associated to the photometry or stellar models. However, the $M_{\star}/M_{dyn}$ ratios decrease from the least massive to the most massive galaxies. In Fig. 5.2 we also compare our result (blue line fit) with those derived for a sample of early-type galaxies (ETGs) analyzed by Gallazzi et al. (2006) (red dashed area), as shown in Fig. 5.2. They found a steeper slope (coef $\sim$ 0.8) than what derived for our sample (coef $\sim$ 0.7). Assuming that the $M_{dyn} = M_{\star} + M_{gas} + M_{DM}$, a different slope in the fit can be interpreted as due to a larger gaseous contribution in (U)LIRGs with respect to what found in ETGs, supposed to be characterized by little contents of gas and dust. As a result, in our systems about half of the dynamical mass is due to the stellar mass contribution. This topic will be investigated in more detail in the future.

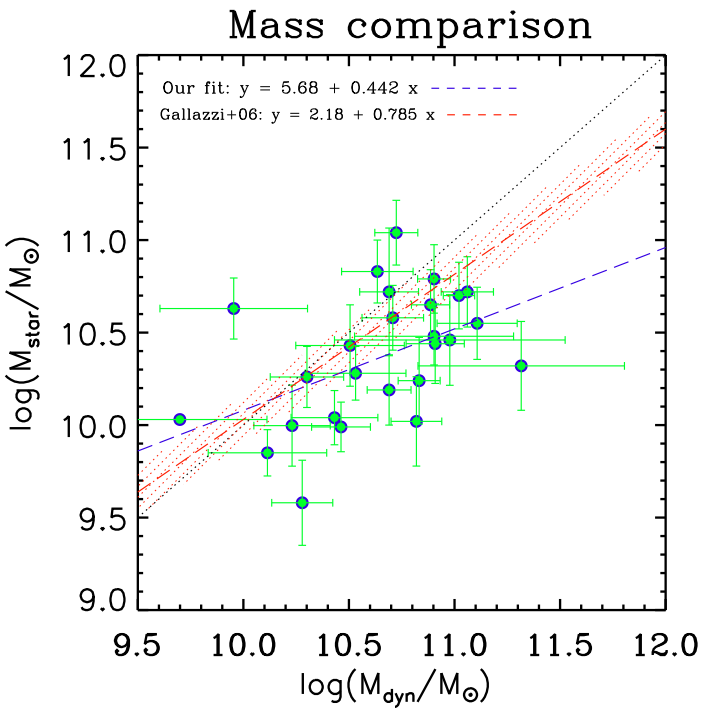

Figure 5.2: Comparison between the stellar and dynamical mass estimates for the (U)LIRG sample. The stellar masses are derived by the SED fitting (see text) while the dynamical ones are derived as explained in Sect. 3.3.5. The dashed blue line represents our trend. The different lines follow the same code as in the previous figure.

[2]For the galaxies IRAS F06206-6315, IRAS 08355-4944, IRAS F10409-4556, IRAS F13229-2934 and IRAS F21453-3511 we find that $M_{\star} > M_{dyn}$ within the 2σ uncertainties.

5.2 Kinematic comparison with IFS-based high-z SFGs

In this section we compare our local IFS kinematic results with those derived at high-z when observing different SFG samples. As done in Chapter 3, the observed v/σ ratio as a function of the effective radius and dynamical mass is derived and shown in Fig. 5.3. Our data are represented as explained in the figure caption (i.e., pink dots represent LIRGs drawn from the VIMOS sample; cyan dots are ULIRGs from the VIMOS and INTEGRAL samples). As visible in Fig. 5.3, most of the high-z systems show lower observed dynamical ratio v/σ with respect to the values derived for local (U)LIRGs. On the one hand, LIRGs are the more rotation-dominated systems, while ULIRGs share similar kinematic properties with high-z systems.

In Tab. 5.1 the mean (and median) kinematic values derived for our and high-z samples are summarized. SINS galaxies at $z \sim 2$ along with SFGs observed at $2 \leq z \leq 3.3$ by Law et al. (2009) are objects that show quite low dynamical ratio (i.e., $v/\sigma \sim 0.4$ and 0.6). In between this redshift range, there are the SMGs which seem to be systems characterized by rotation, according to their $v/\sigma \sim 1$. For the SMGs the dynamical measure of v/σ is higher than in more quiescent SFGs at the same redshift (e.g., from Law et al. 2009; Lemoine-Busserolle et al. 2010): this highlights a difference in the dynamics of these populations. The sources analyzed in Law et al. 2009 and Lemoine-Busserolle et al. (2010) are characterized by low velocity amplitude ($\sim$ 30 - 40 km s^{-1}) and much higher velocity dispersion, possibly being dominated by star formation events.

As a result, systems found at $z < 2$ are more rotation dominated ($v/\sigma > 1$), showing a dynamical ratio in between 1 and $\sim$ 3, while systems at $z > 2$ are characterized by dynamical ratios 0.4-1, although most of them show a 'disk-like' velocity field pattern. The dynamical mass does not show a clear trend among all the different systems: however, some of these systems have a quite large value, as in the case of SFGs from Epinat et al. (2009), SINS and SMG systems.

All these results may suggest that SFGs, located at similar redshift, may not be dominated by the same mechanisms. This topic deserves further investigation and will be developed in the next future.

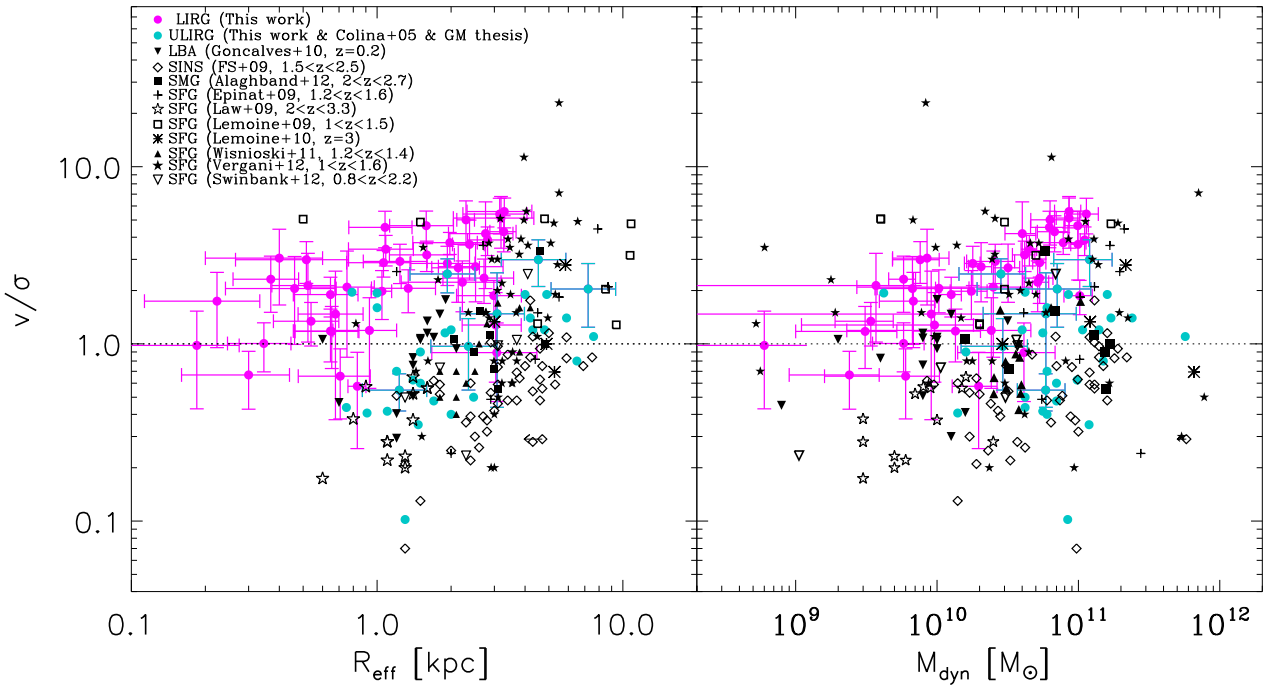

Figure 5.3: The v/σ ratio as a function of the effective radius and dynamical mass is shown. Pink dots represent LIRGs drawn from the VIMOS sample; ULIRGs from the INTEGRAL and VIMOS data are in cyan. **LBAs** are represented with black filled downward triangles. The **SINS** SFGs from Förster Schreiber et al. (2009) (FS09) are represented with black open diamonds. Alaghband-Zadeh et al. (2012) analyzed a sample of **SMG** at redshift $2 < z < 2.7$ studying their Hα emission line using 1-D spectra. These galaxies are shown using filled black squares. Epinat et al. (2009) studied a sample of 9 star-forming galaxies at redshifts $1.2 < z < 1.6$ observed with SINFONI on VVDS. They are represented using the cross symbols. Law et al. (2009) studied a sample of **SFG** at high redshift (i.e., $2 < z < 3.3$) studying the Hα or [OIII] emission. The are represented using the empty star symbols. Lemoine-Busserolle & Lamareille (2010) analyzed a sample of star-forming disk galaxies at redshifts $1.0 < z < 1.5$ observed with SINFONI. They are represented using the empty squares. Lemoine-Busserolle et al. (2010) studied the properties of four SFGs at redshifts $z = 3$, here represented by the stylized stars. **SFGs** at redshift $1.2 < z < 1.4$ drawn from Wisnioski et al. (2011) are represented with black upward triangles. Vergani et al. (2012) derived the kinematical parameters for a sample of 46 MASSIV galaxies at $1 < z < 1.6$, represented using filled star symbols. Swinbank et al. (2012) studied a sample of high-z disk galaxies ($z = 0.8$ - 2.2) represented by empty downward triangles.

Table 5.1: Mean (and median) kinematic results for high-z systems.

System	z	v (km s^{-1})	σ (km s^{-1})	v/ σ	R_{eff} (kpc)	M_{dyn} (10^{10} $M_{\odot}$)	K class (R; D; M)/T
(1)	(2)	(3)	(4)	(5)	(6)	(7)	(8)
LBA	0.2	67 ± 11 (63)	71 ± 6 (67)	0.95 ± 0.11(1.1)	1.4 ± 0.1 (1.5)	1.0 ± 0.2 (1.0)	(2; 10; 6)/19
SFG[a]	0.8-2.2	144 ± 28 (160)	93 ± 20 (75)	1.7 ± 0.4 (1.9)	2.7 ± 0.5 (3.1)	3.1 ± 1.0 (3.6)	(5; 1)/6[1]
SFG[b]	1-1.5	177 ± 24 (182)	59 ± 8 (58)	3.4 ± 0.6 (4.8)	6.3 ± 1.4 (8.5)	4.1 ± 1.9 (3.0)	(4; 4)/8[2]
SFG[c]	1-1.6	114 ± 12 (107)	54 ± 3 (51)	2.9 ± 0.6 (1.9)	3.5 ± 0.2 (3.4)	9.4 ± 2.5 (3.9)	(23; 23)/46[3]
SFG[d]	1.2-1.4	85 ± 10 (74)	98 ± 4 (93)	0.94 ± 0.13 (0.7)	2.7 ± 0.2 (2.5)	4.1 ± 0.6 (3.8)	(4; 6; 3)/13
SFG[e]	1.2-1.6	157 ± 33 (147)	64 ± 6 (70)	2.9 ± 0.9 (2.1)	4.4 ± 0.9 (4.4)	14.2 ± 2.6 (13.0)	(2; 4; 3)/9
SINS	∼ 2	82 ± 8 (67)	133 ± 7 (133)	0.6 ± 0.05 (0.6)	3.5 ± 0.2 (3.1)	9.0 ± 1.3 (7.4)	(∼ 1/3 each)[4]
SMG	2-2.7	136 ± 22 (150)	140 ± 19 (150)	1.0 ± 0.1 (1.0)	3.0 ± 0.3 (2.9)	10.4 ± 0.2 (13.0)	(3; 4; 1)/8
SFG[f]	2-3.3	31 ± 5 (29)	87 ± 8 (73)	0.35 ± 0.05 (0.31)	1.2 ± 0.1 (1.3)	0.9 ± 0.2 (0.7)	(3; 6; 4)/13
SFG[g]	3	39 ± 5 (46)	65 ± 6 (72)	0.6 ± 0.1 (0.7)	4.8 ± 0.6 (5.3)	34 ± 13 (41)	(3; 1)/4

Col (1): High-z systems, identified as follows: [a]SFGs at redshift $0.8 \leq z \leq 2.2$ studied by Swinbank et al. (2012). [b]SFGs with $1 \leq z \leq 1.5$ analyzed by Lemoine-Busserolle & Lamareille (2010) [c]SFGs with $1 \leq z \leq 1.6$ analyzed by Vergani et al. (2012) (this is the same sample studied in Epinat et al. (2012), but here they computed the dynamical mass) taken from MASSIVE sample. [d]SFGs analyzed by Wisnioski et al. (2011) having redshift $1.2 \leq z \leq 1.4$. [e]SFGs observed with SINFONI of VVDS with $1.2 \leq z \leq 1.6$ analyzed by Epinat et al. (2009). [f]SFGs with $2 \leq z \leq 3.3$ analyzed by Law et al. (2009). [g]SFGs by Lemoine-Busserolle et al. (2010) at redshift z=3. Col (2): Redshift. Col (3): Observed velocity amplitude. Col (4): Mean velocity dispersion derived as explained in the text. Col (5): Observed dynamical ratio as the ratio between the value in Col. (2) and Col. (3). Col(6): Half light radius (see text). Col (7): Dynamical masses computed as explained in the text. Col (8): Fraction of galaxies with kinematics characterized by a Rotation (R), Dispersion (D) or Merger (M) patterns, based on the peculiarities of their kinematic maps. In particular, (1) The kinematic classification has been done using the criteria applied in Shapiro et al. (2008) (i.e., $K_{tot} = 0.5$ as the value of the frontier able to separate disks from mergers). (2) They only derived the kinematic parameters for those galaxies that can be fitted using the rotational model (i.e., 8/10). (3) In this work they only distinguish between *Rotating* and *Non-Rotating* systems. (4) For the SINS sample we considered the fractions of different kind of objects as derived in their work.

Chapter 6

Summary and Main Conclusions

Luminous infrared galaxies (LIRGs) and ultraluminous infrared galaxies (ULIRGs) are galaxies that emit most of their light in the infrared (IR) wavelength range where LIRGs have IR luminosities (L_{IR}) in between 10^{11} and 10^{12} $L_{\odot}$, whereas ULIRGs have L_{IR} in between 10^{12} and 10^{13} $L_{\odot}$. (U)LIRGs host the most extreme star-forming events in the present universe. They are powered by strong star-formation and/or an active galactic nucleus (AGN). Although (U)LIRGs are rare in the local universe, they are much more numerous at high-z and are relevant contributors to the whole past star formation beyond $z \sim 1$.

In this thesis work we have focused on the 2D kinematic characterization of a local sample of (U)LIRGs as traced by the Hα emission line. For this study we have analyzed a sample observed with the IFU of the VIMOS instrument on the VLT, which consists of 38 systems (51 individual galaxies) found at $z < 0.1$, encompassing a wide variety of morphological types (i.e., from isolated disks for low-luminosity LIRGs to a majority of merger remnants for ULIRGs) and nuclear excitations (HII, Seyfert and LINER). This is the largest sample for which a detail 2D kinematic study on (U)LIRGs has been performed so far. It is the first attempt to obtain statistically significant results of the kinematic properties of these systems as a function of the infrared luminosity, morphology (i.e., interaction phase) and dynamical status. Furthermore, a large fraction (i.e., 31/38) of sources cover the less studied LIRG luminosity range. Though the LIRG range represents the *core* sample, for parts of the analysis we have also included a subsample mainly formed by ULIRGs (i.e., 25 galaxies) observed with INTEGRAL/WHT (i.e., Colina et al. 2005; García-Marín et al. 2007, 2009) to extend the luminosity range.

This thesis work represents a detailed kinematic study of this important galaxy population and it is focused on two main topics: (i) the 2D characterization of the two main kinematic components found in these objects (i.e., a 'narrow' one, linked to the systemic

ionized ISM, and a 'broad' one, associated to the outflow phenomenon); (ii) the analysis of the kinematic asymmetries with the goal of distinguishing between *disks* and *mergers*, as their relative fraction is a key observational parameter for constraining galaxy evolutionary models. The main conclusions for the analysis of these two topics are summarized below.

2D kinematic characterization of (U)LIRGs

- The Hα emission line profile fitting allowed us to identify two kinematically distinct components in the systems. One of these components (i.e., 'systemic' or 'narrow' component) is found over the whole line-emitting region of the systems and it is characterized by mean velocity dispersions of $\sigma_{mean} \approx$ 30-160 km s^{-1}. The secondary component ('broad' component) is generally found in the inner (spatially resolved) regions of most of LIRGs and ULIRGs. It is characterized by relatively large line widths $\sigma_{mean} \sim$ 320 km s^{-1}, and its central velocity is blueshifted with respect to the systemic component for most of the objects with values up to $\sim$ 400 km s^{-1}. The largest extensions and most extreme kinematic properties of the broad component are observed in interacting and merging systems. This component likely traces nuclear outflows.

- The systemic component traces the overall velocity field and shows a large variety of kinematic 2D structures, from very regular velocity patterns typical of pure rotating disks (RD, 29%) to kinematically perturbed disks (PD, 47%), and highly disrupted and complex kinematics (CK, 24%). Thus, most of the objects (76%) are dominated by rotation. This fraction is larger than previously found in samples of ULIRGs. In fact, we found that the importance of rotation anti-correlates with the infrared luminosity, with a higher fraction of objects with complex kinematics among ULIRGs than in LIRGs (respectively, 6/7 vs. 6/42).

- We find a clear correlation between the different phases of the merging process and the mean kinematic properties inferred from the velocity maps. In particular, isolated disks, interacting galaxies, and merging systems define a sequence of increasing mean velocity dispersion and decreasing velocity field amplitude, which is characterized by intrinsic average dynamical ratios (v*/σ) of 4.7, 3.0, and 1.8, respectively. We also find that the σ_c/σ_{mean} vs. σ_{mean} plane is an good discriminator between disks and interacting/merging systems, with disks showing higher σ_c/σ_{mean} and lower σ_{mean} values by factors of 1.5 to 2, on average.

- The dynamical mass estimates for the present (U)LIRG sample range from $\sim$ 0.04 to 1.4 $m_\star$, with ULIRGs ($\sim$ 0.5 $\pm$ 0.2 $m_\star$) more massive than LIRGs by, on average, a factor of about 2. The mass ratio of individual pre-coalescence galaxies is < 2.5 for most of the systems, confirming that most (U)LIRG mergers involve sub-$m_\star$ galaxies of similar mass.

- The subclass of (U)LIRGs classified as mergers and the LBAs share similar kinematic properties, although the dynamical mass of LBAs is a factor 5 smaller, on average. This is a clear indication that, independent of the mass of the system and of whether it is dusty or dust-free, starburst winds and tidally induced forces produce dynamically hot systems characterized by $\sigma \sim$ 70-80 km s^{-1} and $v/\sigma \sim$ 1-2.

Distinguishing *disks* from *mergers* in (U)LIRG-like systems

As for the study of the kinematic asymmetries in (U)LIRG-like systems to distinguish between *disks* and *mergers* we highlight the following conclusions:

- In general, the kinematic properties of (U)LIRGs derived using the *kinemetry* method are consistent with their morphology. Indeed, the majority of the isolated disks and paired-disks are found to have low kinematic asymmetries in both their velocity field and velocity dispersion maps (i.e., regular 'point -antisymmetric' velocity fields and 'centrally peaked' velocity dispersion maps), while post-coalescence and ongoing-mergers show higher kinematic asymmetry values in both their velocity field and velocity dispersion maps (i.e., irregular pattern). The 2D 'kinemetry' analysis improves the classification of the dynamical phases with respect to the 1D analysis (e.g., v/σ).

  However, some discrepancies between the morphological and kinematical classifications exist, making the analysis subjected to relatively large uncertainties when objects have a total kinematic asymmetry (K_{tot}) in the range $0.19 < K_{tot} < 0.9$. Outside this range, regular disks and complex mergers are well identified.

- We have explored a new criterion to characterize the kinematic asymmetries using *kinemetry*. In particular, we introduce a new method that gives weight to the kinematics of the outer regions when computing the total asymmetries v_{asym} and σ_{asym}. This step is important because post-coalescence mergers have relatively small kinematic asymmetries in the inner parts as a consequence of the rapid relaxation

into a rotating disk, with the outer parts being still out of equilibrium (i.e., having larger asymmetries). However, we find similar results when the unweighted and weighted methods are applied to the whole sample.

- A linear trend is found between the K_{tot} and the infrared luminosity L_{IR} with the most luminous objects showing the highest total kinematic asymmetries. The $L_{IR} \sim 11.4\ L_{\odot}$ seems to be a critical infrared luminosity as it separates the two morphological and kinematical classes.

  A linear (inverse) trend is also derived between the K_{tot} and the intrinsic dynamical ratio v^*/σ: morphologically classified *disks* show higher dynamical ratio and lower total kinematic asymmetry K_{tot}. Contrary, v^*/σ is low while K_{tot} is high in *merger* systems.

  A interesting trend is found between the K_{tot} and the projected nuclear separation along the merger process. The K_{tot} increases from 'paired-disk' to 'ongoing mergers', where it reaches its maximum value at nuclear separations of 2-5 kpc, and then decreases during the post-coalescence mergers phase with a relatively large dispersion.

- From this analysis, we can conclude that in some cases it is uncertain to classify systems as *disk/merger* using *kinemetry*-based criteria, and this clearly depends on the definition of *disk* and *merger*. The K_{tot} limit imposed by Shapiro et al. (2008) to separate *disks* from *mergers* is significantly larger than the one found by us for the whole (U)LIRG sample, either with the unweighted or weighted methods. Shapiro's limit classifies as *merger* only the ongoing and some of the post-coalescence mergers with complex kinematics, thus overestimating the fraction of disks. As a consequence, our analysis suggests that previous studies may have underestimated the fraction of mergers in the early universe.

Chapter 7

Conclusiones

Las galaxias luminosas (LIRGs) y ultraluminosas infrarrojas (ULIRGs) son galaxias que emiten la mayor parte de su luminosidad en el infrarrojo (IR). Las LIRGs tienen luminosidades IR (L_{IR}) entre 10^{11} y 10^{12} $L_{\odot}$, mientras que las ULIRGs tienen L_{IR} en el rango 10^{12} y 10^{13} $L_{\odot}$. Las (U)LIRGs alojan los eventos más extremos de formación estelar en el universo cercano y están dominadas por fuerte formación estelar y/o la presencia de un nucleo galáctico activo (AGN). Aunque las (U)LIRGs son raras en el universo cercano, son mucho más numerosas a alto *redshift (z)* y contribuyen de forma importante a la tasa de formación estelar del universo más allá de $z \sim 1$.

Esta tesis está enfocada a la caracterización cinemática 2D de una muestra de (U)LIRGs locales usando la línea de emisión de Hα. Para este estudio se ha considerado una muestra observada con la unidad de espectroscopía de campo integral (IFU) del instrumento VIMOS/VLT, que consiste en 38 sistemas (51 galaxias individuales) situadas a $z < 0.1$, que abarcan una amplia variedad de tipos morfológicos (desde los discos aislados para las LIRGs de baja luminosidad a restos de *merger* para la mayoría de las ULIRGs) y excitaciones nucleares (HII, Seyfert y LINER). Esta muestra extiende significativamente otras muestras previas en número y en características. Es el primer intento para obtener un estudio estadísticamente significativo de las propiedades cinemáticas 2D de estos sistemás en función de la luminosidad infrarroja, morfología (fase de interacción) y estado dinámico. Además, la mayoría de las fuentes (31/38) cubre el rango de baja luminosidad (LIRG). Aunque el rango de luminosidad de las LIRGs representa el 'nucleo' de la muestra, en parte del análisis se ha incluido también una submuestra principalmente formada por ULIRGs (25 objetos) observadas con INTEGRAL/WHT (Colina et al. 2005; García-Marín et al. 2007, 2009) para extender el rango de luminosidad.

Esta trabajo representa un estudio cinemático detallado de esta importante población de galaxias y está enfocado en dos temas principales: (i) la caracterización 2D de dos com-

ponentes cinemáticas principales presentes en estos objetos (una 'estrecha', relacionada al medio interestelar (ISM), y una 'ancha', asociada al fenomeno de *outflow*); (ii) el análisis de las asimetrías cinemáticas con el objetivo de distinguir entre discos y *merger*, siendo su fracción relativa un parámetro observacional clave para acotar los diferentes escenarios evolutivos.

Caracterización cinemática de las (U)LIRGs

- El ajuste del perfil de la línea de emisión Hα permite identificar dos componentes cinemáticas distintas en estos sistemas. Una de estas ('sistémica' o 'estrecha') se encuentra en todo el campo de emisión del sistema y está caracterizada por una velocidad de dispersión promedio de $\sigma_{mean} \approx$ 30-160 km s^{-1}. La componente secundaria (componente 'ancha') está localizada en las regiones centrales (resueltas espacialmente) en la mayoría de las LIRGs y ULIRGs. Esta componente está caracterizada por anchuras de línea relativamente grandes, $\sigma_{mean} \sim$ 320 km s^{-1}, y su velocidad central está desplazada hacia el azul con respecto a la componente sistémica en la mayoría de los objetos, con valores que llegan hasta $\sim$ 400 km s^{-1}. Las extensiones más grandes y las propiedades cinemáticas más extremas de la componente ancha se observan en las galaxias en interacción y en fase de fusión. Esta componente probablemente traza *outflows*.

- La componente sistémica traza el campo de velocidad global y muestra una gran variedad de estructuras cinemáticas 2D, desde campos de velocidad muy regulares típicos de un disco puramente rotante (RD, 29%) a discos perturbados cinemáticamente (PD, 47%), y altamente perturbados con cinemática compleja (CK, 24%). Por lo tanto, la mayoría de los objetos (76%) están dominados por rotación, cuya fracción es más grande de la que se ha encontrado previamente en muestras de ULIRGs. De hecho, encontramos que la importancia de la rotación anti-correla con la luminosidad infrarroja, con una más alta fracción de objetos con cinemática compleja en las ULIRGs que en las LIRGs (6/7 y 6/42, respectivamente)

- Se ha encontrado una clara correlación entre las diferentes fases en el proceso de fusión y las propiedades cinemáticas promedio inferidas a partir de los mapas de velocidad. En particular, discos aislados, galaxias en interacción y sistemas en fase de fusión definen una secuencia caracterizada por una dispersión de velocidad promedio creciente y una amplitud del campo de velocidad decreciente, los cuales están caracterizados por un cociente dinámico promedio (v$^*/\sigma$) de 4.7, 3.0, y 1.8, respec-

tivamente. Además, el plano σ_c/σ_{mean} vs. σ_{mean} discrimina bien entre los discos y las galaxias en fase de interacción/*mergers*. Los discos muestran un σ_c/σ_{mean} más alto y valores de σ_{mean} más bajos por un factor 1.5-2 en promedio.

- Las estimaciones de las masas dinámicas de las (U)LIRGs están en el rango de $\sim$ 0.04 - 1.4 $m_\star$, siendo las ULIRGs ($\sim 0.5 \pm 0.2$ $m_\star$) más masivas de las LIRGs por un factor 2 en promedio. El cociente entre las masas de las galaxias en fase de pre-coalescencia es < 2.5 para la mayor parte de los sistemas, confirmando que la mayoría de los (U)LIRGs clasificados como *merger* involucran galaxias sub-$m_\star$ con masas similares.

- La subclase de galaxias (U)LIRG clasificadas como *mergers* y los *Lyman break analogs* (LBAs) tienen propiedades cinemáticas similares, aunque la masa dinámica de las LBA es 5 veces más pequeña en promedio. Este resultado indica claramente que, independientemente de la masa de un sistema y de su cantidad de polvo, los vientos generados por eventos de formación estelar y fuerzas de marea producen sistemas dinámicos calientes caracterizados por $\sigma \sim$ 70-80 km s^{-1} y $v/\sigma \sim$ 1-2.

Diferenciando los discos de los *mergers* en sistemas de tipo (U)LIRG

El estudio de las asimetrías cinemáticas en sistemas de tipo (U)LIRG para distinguir entre discos y *mergers* permite resaltar las siguientes conclusiones:

- En general, las propiedades cinemáticas de las (U)LIRGs derivadas usando el método de *kinemetry* son consistentes con su morfología. De hecho, las mayor parte de los discos aislados y emparejados tienen asimetrías cinemáticas bajas en el campo de velocidad y dispersión de velocidad (campo de velocidad regular 'anti-simétrico' con respecto al centro cinemático y mapa de dispersión de velocidad con un pico en el centro). Por otro lado, las galaxias en fase de pre- y post-fusión muestran asimetrías cinemáticas más altas en ambos mapas (estructura irregular). El análisis de *kinemetry* en 2D mejora la clasificación de las fases dinámicas con respecto al análisis 1D (v/σ).

  Sin embargo, se han encontrado discrepancias entre la clasificación morfológica y cinemática, lo que hace que el análisis esté sujeto a incertidumbres relativamente grandes cuando los objetos tienen una asimetría cinemática global (K_{tot}) en el rango $0.19 < K_{tot} < 0.9$. Fuera de este rango, discos regulares y galaxias en fase de fusión muy complejas son fácilmente identificables.

- Se ha desarrollado un nuevo criterio basado en *kinemetry* optimizado ('ponderado', Bellocchi et al. 2012) para caracterizar las asimetrías cinemáticas. En particular, con el nuevo método se da más peso a las asimetrías cinemáticas en las regiones más externas de las galaxias en el cálculo de las asimetrías v_{asym} y σ_{asym}. Esto es importante porque las galaxias en la fase de post-fusión tienen asimetrías cinemáticas relativamente pequeñas en las regiones más internas como consecuencia de la rápida relajación a un disco rotante, mientras que las partes externas no se encuentran en equilibrio (mayores asimetrías). Sin embargo, se derivan resultados similares cuando ambos métodos (no-ponderado y ponderado) se aplican a la muestra completa.

- Se encuentra una relación lineal entre el K_{tot} y la luminosidad infrarroja L_{IR}. Los objetos más luminosos (ULIRGs) están caracterizados por una asimetría cinemática global más alta. La $L_{IR} \sim 11.4\ L_{\odot}$ parece ser una luminosidad infrarroja crítica capaz de separar las dos clases morfológica y cinemática.

  También se deriva una relación lineal inversa entre el K_{tot} y el cociente intrínseco dinámico v^*/σ: galaxias clasificadas morfológicamente como discos muestran un cociente dinámico más alto y asimetría cinemática global K_{tot} más baja. Lo contrario sucede con los *mergers*.

  Una tendencia interesante se encuentra también entre la asimetría cinemática global K_{tot} y la separación nuclear proyectada a lo largo del proceso de fusión. Inicialmente, cuanto menor es la separación nuclear mayor es su K_{tot}, que alcanza su valor máximo durante la fase de fusión (separaciones nucleares $\sim$ 2-5 kpc). En la fase de post-fusión el K_{tot} decrece, aunque con una dispersión relativamente grande.

- Finalmente, de este análisis se puede concluir que, en unos casos, clasificar los sistemas como discos/'mergers' con criterios basados en *kinemetry* tiene sus incertidumbres, y que el resultado claramente depende de la definición de disco y de 'merger'. El límite K_{tot} impuesto por Shapiro et al. (2008) para separar los discos de los *mergers* es mucho más alto que el valor derivado por nosotros considerando toda la muestra de (U)LIRGs, tanto con el método no-ponderado como con el ponderado. El límite de Shapiro clasifica como *merger* sólo las galaxias en fase de pre-fusión y unas pocas en la fase de post-fusión que muestran cinemática compleja, sobreestimando así la fracción de discos. Como consecuencia, nuestro análisis sugiere que estudios previos podrían haber infraestimando la fracción de galaxias en fase de fusión en el universo lejano.

Publications

Referred Publications related to this thesis

1. *VLT/VIMOS integral field spectroscopy of luminous and ultraluminous infrared galaxies: 2D kinematic properties*
   Bellocchi, E., Arribas, S., Colina, L., Miralles-Caballero, D. 2013, A&A, 557, A59.

2. *Studying the kinematic asymmetries of disks and post-coalescence mergers using a new kinemetry criterion*
   Bellocchi, E., Arribas, S., and Colina, L. 2012 A&A, 542, A54.

3. *Distinguishing disks from mergers: tracing the kinematic asymmetries in local (U)LIRGs using kinemetry-based criteria*
   Bellocchi, E., Arribas, S., and Colina, L. 2014 in prep.

Other collaborative related papers

1. *Ionized gas outflows and global kinematics of low-z luminous star forming galaxies*
   Arribas, S., Colina, L., **Bellocchi, E.**, Maiolino, R., Villar-Martin, M. 2014 accepted in A&A

2. *Spatially resolved kinematics, galactic wind, and quenching of star formation in the Luminous InfraRed Galaxy IRAS F11506-3851*
   Cazzoli, S., Arribas, S., Colina, L., Piqueras-López, J., **Bellocchi, E.**, Emonts, E., Maiolino, R., Villar-Martin, M. submitted

Other collaborative papers

1. *The HELLAS2XMM survey. XIII. Multi-component analysis of the spectral energy distribution of obscured AGN*
   Pozzi, F., Vignali, C., Comastri, A., **Bellocchi, E.**, Fritz, J., Gruppioni, C., Mignoli,

M., Maiolino, R., Pozzetti, L., Brusa, M., Fiore, F., Zamorani, G. 2010 A&A, 571, 11

2. *The HELLAS2XMM survey - XII. The infrared/submillimetre view of an X-ray selected type 2 quasar at $z \sim 2$*
   Vignali, C., Pozzi, F., Fritz, J., Comastri, A., Gruppioni, C., **Bellocchi, E.**, Fiore, F., Brusa, M., Maiolino, R., Mignoli, M., La Franca, F., Pozzetti, L., Zamorani, G., Merloni, A. 2009, MNRAS, 395, 2189.

Bibliography

Alaghband-Zadeh, S., Chapman, S. C., Swinbank, A. M., et al. 2012, ArXiv e-prints

Allington-Smith, J. R. 2007, in Revista Mexicana de Astronomia y Astrofisica Conference Series, Vol. 28, Revista Mexicana de Astronomia y Astrofisica Conference Series, ed. S. Kurtz, 17–23

Alonso-Herrero, A., Pereira-Santaella, M., Rieke, G. H., & Rigopoulou, D. 2012, *Astrophys. J.*, 744, 2

Alonso-Herrero, A., Ramos Almeida, C., Mason, R., et al. 2011, *Astrophys. J.*, 736, 82

Alonso-Herrero, A., Rieke, G. H., Rieke, M. J., et al. 2006, *Astrophys. J.*, 650, 835

Arribas, S., Bushouse, H., Lucas, R. A., Colina, L., & Borne, K. D. 2004, *Astron. J.*, 127, 2522

Arribas, S. & Colina, L. 2003, *Astrophys. J.*, 591, 791

Arribas, S., Colina, L., Alonso-Herrero, A., et al. 2012, *Astron. Astrophys.*, 541, A20

Arribas, S., Colina, L., & Borne, K. D. 2000, *Astrophys. J.*, 545, 228

Arribas, S., Colina, L., & Clements, D. 2001, *Astrophys. J.*, 560, 160

Arribas, S., Colina, L., Monreal-Ibero, A., et al. 2008, *Astron. Astrophys.*, 479, 687

Arribas, S., Mediavilla, E., & Fuensalida, J. J. 1998, *Astrophys. J. L.*, 505, L43

Basu-Zych, A. R., Gonçalves, T. S., Overzier, R., et al. 2009, *Astrophys. J. L.*, 699, L118

Baugh, C. M. 2006, Reports on Progress in Physics, 69, 3101

Bedregal, A. G., Colina, L., Alonso-Herrero, A., & Arribas, S. 2009, *Astrophys. J.*, 698, 1852

Bellocchi, E., Arribas, S., & Colina, L. 2012, *Astron. Astrophys.*, 542, A54

Bellocchi, E., Arribas, S., Colina, L., & Miralles-Caballero, D. 2013, *Astron. Astrophys.*, 557, A59

Bershady, M. A., Verheijen, M. A. W., Swaters, R. A., et al. 2010, *Astrophys. J.*, 716, 198

Blain, A. W., Smail, I., Ivison, R. J., Kneib, J.-P., & Frayer, D. T. 2002, *Physics Reports*, 369, 111

Borne, K. D., Bushouse, H., Lucas, R. A., & Colina, L. 2000, *Astrophys. J. L.*, 529, L77

Bouché, N., Dekel, A., Genzel, R., et al. 2010, *Astrophys. J.*, 718, 1001

Bournaud, F., Chapon, D., Teyssier, R., et al. 2011, *Astrophys. J.*, 730, 4

Bournaud, F., Combes, F., & Jog, C. J. 2004, *Astron. Astrophys.*, 418, L27

Bournaud, F., Daddi, E., Elmegreen, B. G., et al. 2008, *Astron. Astrophys.*, 486, 741

Bournaud, F., Jog, C. J., & Combes, F. 2007, *Astron. Astrophys.*, 476, 1179

Bouwens, R. J., Illingworth, G. D., Blakeslee, J. P., & Franx, M. 2006, *Astrophys. J.*, 653, 53

Bridge, C. R., Appleton, P. N., Conselice, C. J., et al. 2007, *Astrophys. J.*, 659, 931

Brinchmann, J., Charlot, S., White, S. D. M., et al. 2004, *Mon. Not. R. astr. Soc.*, 351, 1151

Bruzual, G. & Charlot, S. 2003, *Mon. Not. R. astr. Soc.*, 344, 1000

Burkert, A., Genzel, R., Bouché, N., et al. 2010, *Astrophys. J.*, 725, 2324

Bushouse, H. A., Borne, K. D., Colina, L., et al. 2002, *Astrophys. J. Suppl.*, 138, 1

Cappellari, M., Bacon, R., Bureau, M., et al. 2006, *Mon. Not. R. astr. Soc.*, 366, 1126

Cappellari, M., Emsellem, E., Bacon, R., et al. 2007, *Mon. Not. R. astr. Soc.*, 379, 418

Cappellari, M., Emsellem, E., Krajnović, D., et al. 2011, *Mon. Not. R. astr. Soc.*, 416, 1680

Caputi, K. I., Lagache, G., Yan, L., et al. 2007, *Astrophys. J.*, 660, 97

Ceverino, D., Dekel, A., & Bournaud, F. 2010, *Mon. Not. R. astr. Soc.*, 404, 2151

Chabrier, G. 2003, *Astrophys. J. L.*, 586, L133

Chapman, S. C., Blain, A. W., Ivison, R. J., & Smail, I. R. 2003, *Nature*, 422, 695

Chapman, S. C., Blain, A. W., Smail, I., & Ivison, R. J. 2005, *Astrophys. J.*, 622, 772

Cole, S., Aragon-Salamanca, A., Frenk, C. S., Navarro, J. F., & Zepf, S. E. 1994, *Mon. Not. R. astr. Soc.*, 271, 781

Cole, S., Lacey, C. G., Baugh, C. M., & Frenk, C. S. 2000, *Mon. Not. R. astr. Soc.*, 319, 168

Cole, S., Norberg, P., Baugh, C. M., et al. 2001, *Mon. Not. R. astr. Soc.*, 326, 255

Colina, L., Arribas, S., & Borne, K. D. 1999, *Astrophys. J. L.*, 527, L13

Colina, L., Arribas, S., & Clements, D. 2004, *Astrophys. J.*, 602, 181

Colina, L., Arribas, S., & Monreal-Ibero, A. 2005, *Astrophys. J.*, 621, 725

Colina, L., Borne, K., Bushouse, H., et al. 2001, *Astrophys. J.*, 563, 546

Combes, F. 2004, in Astrophysics and Space Science Library, Vol. 319, Penetrating Bars Through Masks of Cosmic Dust, ed. D. L. Block, I. Puerari, K. C. Freeman, R. Groess, & E. K. Block, 57

Combes, F., García-Burillo, S., Braine, J., et al. 2011, *Astron. Astrophys.*, 528, A124

Conselice, C. J. 2006, *Mon. Not. R. astr. Soc.*, 373, 1389

Conselice, C. J., Chapman, S. C., & Windhorst, R. A. 2003, *Astrophys. J. L.*, 596, L5

Conselice, C. J., Mortlock, A., Bluck, A. F. L., Grützbauch, R., & Duncan, K. 2013, *Mon. Not. R. astr. Soc.*, 430, 1051

Corbett, E. A., Kewley, L., Appleton, P. N., et al. 2003, *Astrophys. J.*, 583, 670

Cox, T. J., Jonsson, P., Primack, J. R., & Somerville, R. S. 2006, *Mon. Not. R. astr. Soc.*, 373, 1013

Cresci, G., Hicks, E. K. S., Genzel, R., et al. 2009, *Astrophys. J.*, 697, 115

Cresci, G., Mannucci, F., Maiolino, R., et al. 2010, *Nature*, 467, 811

da Cunha, E., Charlot, S., & Elbaz, D. 2008, *Mon. Not. R. astr. Soc.*, 388, 1595

da Cunha, E., Charmandaris, V., Díaz-Santos, T., et al. 2010, *Astron. Astrophys.*, 523, A78

Daddi, E., Dannerbauer, H., Stern, D., et al. 2009, *Astrophys. J.*, 694, 1517

Daddi, E., Dickinson, M., Morrison, G., et al. 2007, *Astrophys. J.*, 670, 156

Daddi, E., Elbaz, D., Walter, F., et al. 2010, *Astrophys. J. L.*, 714, L118

Dasyra, K. M., Tacconi, L. J., Davies, R. I., et al. 2006a, *Astrophys. J.*, 638, 745

Dasyra, K. M., Tacconi, L. J., Davies, R. I., et al. 2006b, *Astrophys. J.*, 651, 835

Dasyra, K. M., Yan, L., Helou, G., et al. 2008, *Astrophys. J.*, 680, 232

Davé, R. 2008, *Mon. Not. R. astr. Soc.*, 385, 147

Davé, R., Finlator, K., Oppenheimer, B. D., et al. 2010, *Mon. Not. R. astr. Soc.*, 404, 1355

Davies, R., Förster Schreiber, N. M., Cresci, G., et al. 2011, *Astrophys. J.*, 741, 69

Dekel, A. & Birnboim, Y. 2006, *Mon. Not. R. astr. Soc.*, 368, 2

Dekel, A., Birnboim, Y., Engel, G., et al. 2009a, *Nature*, 457, 451

Dekel, A., Sari, R., & Ceverino, D. 2009b, *Astrophys. J.*, 703, 785

Di Matteo, P., Bournaud, F., Martig, M., et al. 2008, *Astron. Astrophys.*, 492, 31

Di Matteo, T., Springel, V., & Hernquist, L. 2005, *Nature*, 433, 604

Downes, D. & Solomon, P. M. 1998, *Astrophys. J.*, 507, 615

Duc, P.-A., Mirabel, I. F., & Maza, J. 1997, *Astron. Astrophys. Suppl.*, 124, 533

Egami, E., Dole, H., Huang, J.-S., et al. 2004, *Astrophys. J. Suppl.*, 154, 130

Eisenhauer, F., Abuter, R., Bickert, K., et al. 2003, in Society of Photo-Optical Instrumentation Engineers (SPIE) Conference Series, Vol. 4841, Society of Photo-Optical Instrumentation Engineers (SPIE) Conference Series, ed. M. Iye & A. F. M. Moorwood, 1548–1561

Elbaz, D., Cesarsky, C. J., Chanial, P., et al. 2002, *Astron. Astrophys.*, 384, 848

Elbaz, D., Daddi, E., Le Borgne, D., et al. 2007, *Astron. Astrophys.*, 468, 33

Elbaz, D., Dickinson, M., Hwang, H. S., et al. 2011, *Astron. Astrophys.*, 533, A119

Elbaz, D., Hwang, H. S., Magnelli, B., et al. 2010, *Astron. Astrophys.*, 518, L29

Emsellem, E., Cappellari, M., Peletier, R. F., et al. 2004, *Mon. Not. R. astr. Soc.*, 352, 721

Epinat, B. 2011, ArXiv e-prints

Epinat, B., Amram, P., Balkowski, C., & Marcelin, M. 2010, *Mon. Not. R. astr. Soc.*, 401, 2113

Epinat, B., Contini, T., Le Fèvre, O., et al. 2009, *Astron. Astrophys.*, 504, 789

Epinat, B., Tasca, L., Amram, P., et al. 2012, *Astron. Astrophys.*, 539, A92

Farrah, D., Bernard-Salas, J., Spoon, H. W. W., et al. 2007, *Astrophys. J.*, 667, 149

Farrah, D., Rowan-Robinson, M., Oliver, S., et al. 2001, *Mon. Not. R. astr. Soc.*, 326, 1333

Flores, H., Hammer, F., Puech, M., Amram, P., & Balkowski, C. 2006, *Astron. Astrophys.*, 455, 107

Förster Schreiber, N. M., Genzel, R., Bouché, N., et al. 2009, *Astrophys. J.*, 706, 1364

Förster Schreiber, N. M., Genzel, R., Lehnert, M. D., et al. 2006, *Astrophys. J.*, 645, 1062

Förster Schreiber, N. M., Genzel, R., Newman, S. F., et al. 2013, ArXiv e-prints

Förster Schreiber, N. M., Shapley, A. E., Genzel, R., et al. 2011, *Astrophys. J.*, 739, 45

Frayer, D. T., Armus, L., Scoville, N. Z., et al. 2003, *Astron. J.*, 126, 73

Gallazzi, A., Charlot, S., Brinchmann, J., & White, S. D. M. 2006, *Mon. Not. R. astr. Soc.*, 370, 1106

García-Marín, M., Colina, L., & Arribas, S. 2007, phD thesis, Universidad Autonoma de Madrid, Spain

García-Marín, M., Colina, L., Arribas, S., Alonso-Herrero, A., & Mediavilla, E. 2006, *Astrophys. J.*, 650, 850

García-Marín, M., Colina, L., Arribas, S., & Monreal-Ibero, A. 2009, *Astron. Astrophys.*, 505, 1319

Gehrz, R. D., Sramek, R. A., & Weedman, D. W. 1983, *Astrophys. J.*, 267, 551

Genel, S., Genzel, R., Bouché, N., et al. 2008, *Astrophys. J.*, 688, 789

Genzel, R., Burkert, A., Bouché, N., et al. 2008, *Astrophys. J.*, 687, 59

Genzel, R., Lutz, D., Sturm, E., et al. 1998, *Astrophys. J.*, 498, 579

Genzel, R., Newman, S., Jones, T., et al. 2011, *Astrophys. J.*, 733, 101

Genzel, R., Tacconi, L. J., Gracia-Carpio, J., et al. 2010, *Mon. Not. R. astr. Soc.*, 407, 2091

Genzel, R., Tacconi, L. J., Rigopoulou, D., Lutz, D., & Tecza, M. 2001, *Astrophys. J.*, 563, 527

Gnerucci, A., Marconi, A., Cresci, G., et al. 2011, *Astron. Astrophys.*, 528, A88

Goldader, J. D., Joseph, R. D., Doyon, R., & Sanders, D. B. 1997a, *Astrophys. J. Suppl.*, 108, 449

Goldader, J. D., Joseph, R. D., Doyon, R., & Sanders, D. B. 1997b, *Astrophys. J.*, 474, 104

Gonçalves, T. S., Basu-Zych, A., Overzier, R., et al. 2010, *Astrophys. J.*, 724, 1373

González, V., Labbé, I., Bouwens, R. J., et al. 2010, *Astrophys. J.*, 713, 115

Gruppioni, C., Pozzi, F., Rodighiero, G., et al. 2013, *Mon. Not. R. astr. Soc.*, 432, 23

Guyon, O., Sanders, D. B., & Stockton, A. 2006, *Astrophys. J. Suppl.*, 166, 89

Haan, S., Surace, J. A., Armus, L., et al. 2011, *Astron. J.*, 141, 100

Heckman, T. M., Armus, L., & Miley, G. K. 1990, *Astrophys. J. Suppl.*, 74, 833

Heckman, T. M., Hoopes, C. G., Seibert, M., et al. 2005, *Astrophys. J. L.*, 619, L35

Helou, G. 1986, *Astrophys. J. L.*, 311, L33

Helou, G. & Walker, D. W., eds. 1988, Infrared astronomical satellite (IRAS) catalogs and atlases. Volume 7: The small scale structure catalog, Vol. 7

Heyl, J. S., Hernquist, L., & Spergel, D. N. 1994, *Astrophys. J.*, 427, 165

Hinz, J. L. & Rieke, G. H. 2006, *Astrophys. J.*, 646, 872

Holland, W. S., Robson, E. I., Gear, W. K., et al. 1999, *Mon. Not. R. astr. Soc.*, 303, 659

Hopkins, A. M. & Beacom, J. F. 2006, *Astrophys. J.*, 651, 142

James, P. A., Shane, N. S., Beckman, J. E., et al. 2004, *Astron. Astrophys.*, 414, 23

Jesseit, R., Naab, T., Peletier, R. F., & Burkert, A. 2007, *Mon. Not. R. astr. Soc.*, 376, 997

Jones, T., Ellis, R., Jullo, E., & Richard, J. 2010, *Astrophys. J. L.*, 725, L176

Karim, A., Schinnerer, E., Martínez-Sansigre, A., et al. 2011, *Astrophys. J.*, 730, 61

Kartaltepe, J. S., Dickinson, M., Alexander, D. M., et al. 2012, *Astrophys. J.*, 757, 23

Kartaltepe, J. S., Sanders, D. B., Le Floc'h, E., et al. 2010, *Astrophys. J.*, 721, 98

Kauffmann, G., Heckman, T. M., Tremonti, C., et al. 2003, *Mon. Not. R. astr. Soc.*, 346, 1055

Kennicutt, Jr., R. C. 1998, *Astrophys. J.*, 498, 541

Kennicutt, Jr., R. C., Tamblyn, P., & Congdon, C. E. 1994, *Astrophys. J.*, 435, 22

Kereš, D., Katz, N., Fardal, M., Davé, R., & Weinberg, D. H. 2009, *Mon. Not. R. astr. Soc.*, 395, 160

Kereš, D., Katz, N., Weinberg, D. H., & Davé, R. 2005, *Mon. Not. R. astr. Soc.*, 363, 2

Kessler, M. F., Steinz, J. A., Anderegg, M. E., et al. 1996, *Astron. Astrophys.*, 315, L27

Kewley, L. J., Groves, B., Kauffmann, G., & Heckman, T. 2006, *Mon. Not. R. astr. Soc.*, 372, 961

Kewley, L. J., Heisler, C. A., Dopita, M. A., & Lumsden, S. 2001, *Astrophys. J. Suppl.*, 132, 37

Kim, D.-C. 1995, PhD thesis, UNIVERSITY OF HAWAII.

Kim, D.-C., Sanders, D. B., Veilleux, S., Mazzarella, J. M., & Soifer, B. T. 1995, *Astrophys. J. Suppl.*, 98, 129

Krajnović, D., Cappellari, M., de Zeeuw, P. T., & Copin, Y. 2006, *Mon. Not. R. astr. Soc.*, 366, 787

Kronberger, T., Kapferer, W., Schindler, S., & Ziegler, B. L. 2007, *Astron. Astrophys.*, 473, 761

Kroupa, P. 2008, in Astronomical Society of the Pacific Conference Series, Vol. 390, Pathways Through an Eclectic Universe, ed. J. H. Knapen, T. J. Mahoney, & A. Vazdekis, 3

Lagache, G., Puget, J.-L., & Dole, H. 2005, *Ann. Rev. Astron. Astr.*, 43, 727

Larson, R. B. & Tinsley, B. M. 1978, *Astrophys. J.*, 219, 46

Law, D. R., Steidel, C. C., Erb, D. K., et al. 2007, *Astrophys. J.*, 669, 929

Law, D. R., Steidel, C. C., Erb, D. K., et al. 2009, *Astrophys. J.*, 697, 2057

Le Fèvre, O., Saisse, M., Mancini, D., et al. 2003, in Presented at the Society of Photo-Optical Instrumentation Engineers (SPIE) Conference, Vol. 4841, Society of Photo-Optical Instrumentation Engineers (SPIE) Conference Series, ed. M. Iye & A. F. M. Moorwood, 1670–1681

Le Floc'h, E., Papovich, C., Dole, H., et al. 2005, *Astrophys. J.*, 632, 169

Lehnert, M. D., Nesvadba, N. P. H., Le Tiran, L., et al. 2009, *Astrophys. J.*, 699, 1660

Lemoine-Busserolle, M., Bunker, A., Lamareille, F., & Kissler-Patig, M. 2010, *Mon. Not. R. astr. Soc.*, 401, 1657

Lemoine-Busserolle, M. & Lamareille, F. 2010, *Mon. Not. R. astr. Soc.*, 402, 2291

Lilly, S. J., Tresse, L., Hammer, F., Crampton, D., & Le Fevre, O. 1995, *Astrophys. J.*, 455, 108

Lípari, S., Terlevich, R., Díaz, R. J., et al. 2003, *Mon. Not. R. astr. Soc.*, 340, 289

Lotz, J. M., Jonsson, P., Cox, T. J., & Primack, J. R. 2008, *Mon. Not. R. astr. Soc.*, 391, 1137

Lutz, D., Veilleux, S., & Genzel, R. 1999, *Astrophys. J. L.*, 517, L13

Madau, P., Ferguson, H. C., Dickinson, M. E., et al. 1996, *Mon. Not. R. astr. Soc.*, 283, 1388

Magnelli, B., Elbaz, D., Chary, R. R., et al. 2009, *Astron. Astrophys.*, 496, 57

Magnelli, B., Popesso, P., Berta, S., et al. 2013, *Astron. Astrophys.*, 553, A132

Maíz-Apellániz, J. 2004, *Pub. Astron. Soc. Pac.*, 116, 859

Mannucci, F., Cresci, G., Maiolino, R., Marconi, A., & Gnerucci, A. 2010, *Mon. Not. R. astr. Soc.*, 408, 2115

Martig, M. & Bournaud, F. 2010, *Astrophys. J. L.*, 714, L275

Mihos, J. C. & Hernquist, L. 1996, *Astrophys. J.*, 464, 641

Mirabel, I. F. & Sanders, D. B. 1989, *Astrophys. J. L.*, 340, L53

Monreal-Ibero, A., Arribas, S., & Colina, L. 2006, *Astrophys. J.*, 637, 138

Monreal-Ibero, A., Arribas, S., Colina, L., et al. 2010, *Astron. Astrophys.*, 517, A28+

Murphy, E. J., Chary, R.-R., Dickinson, M., et al. 2011, *Astrophys. J.*, 732, 126

Murphy, Jr., T. W., Armus, L., Matthews, K., et al. 1996, *Astron. J.*, 111, 1025

Muzzin, A., van Dokkum, P., Kriek, M., et al. 2010, *Astrophys. J.*, 725, 742

Naab, T. & Burkert, A. 2003, *Astrophys. J.*, 597, 893

Naab, T., Burkert, A., & Hernquist, L. 1999, *Astrophys. J. L.*, 523, L133

Naab, T., Johansson, P. H., & Ostriker, J. P. 2009, *Astrophys. J. L.*, 699, L178

Nardini, E., Risaliti, G., Salvati, M., et al. 2008, *Mon. Not. R. astr. Soc.*, 385, L130

Nardini, E., Risaliti, G., Watabe, Y., Salvati, M., & Sani, E. 2010, *Mon. Not. R. astr. Soc.*, 405, 2505

Neugebauer, G., Habing, H. J., van Duinen, R., et al. 1984, *Astrophys. J. L.*, 278, L1

Noeske, K. G., Weiner, B. J., Faber, S. M., et al. 2007, *Astrophys. J. L.*, 660, L43

Nordon, R., Lutz, D., Shao, L., et al. 2010, *Astron. Astrophys.*, 518, L24

Ocvirk, P., Pichon, C., & Teyssier, R. 2008, *Mon. Not. R. astr. Soc.*, 390, 1326

Overzier, R. A., Heckman, T. M., Kauffmann, G., et al. 2008, *Astrophys. J.*, 677, 37

Pannella, M., Gabasch, A., Goranova, Y., et al. 2009, *Astrophys. J.*, 701, 787

Papovich, C., Rudnick, G., Le Floc'h, E., et al. 2007, *Astrophys. J.*, 668, 45

Peng, C. Y., Ho, L. C., Impey, C. D., & Rix, H.-W. 2010, *Astron. J.*, 139, 2097

Pérez-González, P. G., Rieke, G. H., Egami, E., et al. 2005, *Astrophys. J.*, 630, 82

Pérez-González, P. G., Rieke, G. H., Villar, V., et al. 2008, *Astrophys. J.*, 675, 234

Pilbratt, G. L., Riedinger, J. R., Passvogel, T., et al. 2010, *Astron. Astrophys.*, 518, L1

Piqueras López, J., Colina, L., Arribas, S., & Alonso-Herrero, A. 2013, ArXiv e-prints

Pope, A., Scott, D., Dickinson, M., et al. 2006, *Mon. Not. R. astr. Soc.*, 370, 1185

Puech, M. 2010, *Mon. Not. R. astr. Soc.*, 406, 535

Puech, M., Hammer, F., Lehnert, M. D., & Flores, H. 2007, *Astron. Astrophys.*, 466, 83

Ren, D. & Allington-Smith, J. 2002, *Pub. Astron. Soc. Pac.*, 114, 866

Rieke, G. H. & Lebofsky, M. J. 1979, *Ann. Rev. Astron. Astr.*, 17, 477

Rieke, G. H. & Low, F. J. 1972, *Astrophys. J. L.*, 176, L95+

Risaliti, G., Maiolino, R., Marconi, A., et al. 2006, *Mon. Not. R. astr. Soc.*, 365, 303

Rodighiero, G., Daddi, E., Baronchelli, I., et al. 2011, *Astrophys. J. L.*, 739, L40

Rodighiero, G., Vaccari, M., Franceschini, A., et al. 2010, *Astron. Astrophys.*, 515, A8

Rodríguez-Zaurín, J., Arribas, S., Monreal-Ibero, A., et al. 2011, *Astron. Astrophys.*, 527, A60+

Rodríguez Zaurín, J., Tadhunter, C. N., & González Delgado, R. M. 2009, *Mon. Not. R. astr. Soc.*, 400, 1139

Rodríguez Zaurín, J., Tadhunter, C. N., & González Delgado, R. M. 2010, *Mon. Not. R. astr. Soc.*, 403, 1317

Roth, M. M., Kelz, A., Fechner, T., et al. 2005, *Pub. Astron. Soc. Pac.*, 117, 620

Rothberg, B. & Fischer, J. 2010, *Astrophys. J.*, 712, 318

Rothberg, B., Fischer, J., Rodrigues, M., & Sanders, D. B. 2013, *Astrophys. J.*, 767, 72

Rowan-Robinson, M. 1986, *Mon. Not. R. astr. Soc.*, 219, 737

Rujopakarn, W., Rieke, G. H., Eisenstein, D. J., & Juneau, S. 2011, *Astrophys. J.*, 726, 93

Rupke, D. S. N. & Veilleux, S. 2013, ArXiv e-prints

Sajina, A., Yan, L., Fadda, D., Dasyra, K., & Huynh, M. 2012, *Astrophys. J.*, 757, 13

Salim, S., Rich, R. M., Charlot, S., et al. 2007, *Astrophys. J. Suppl.*, 173, 267

Salpeter, E. E. 1955, *Astrophys. J.*, 121, 161

Sánchez, S. F., Kennicutt, R. C., Gil de Paz, A., et al. 2012, *Astron. Astrophys.*, 538, A8

Sanders, D. B., Mazzarella, J. M., Kim, D.-C., Surace, J. A., & Soifer, B. T. 2003, *Astron. J.*, 126, 1607

Sanders, D. B. & Mirabel, I. F. 1996, *Ann. Rev. Astron. Astr.*, 34, 749

Sanders, D. B., Soifer, B. T., Elias, J. H., Neugebauer, G., & Matthews, K. 1988, *Astrophys. J. L.*, 328, L35

Sargent, M. T., Béthermin, M., Daddi, E., & Elbaz, D. 2012, *Astrophys. J. L.*, 747, L31

Scoville, N. Z., Evans, A. S., Thompson, R., et al. 2000, *Astron. J.*, 119, 991

Shapiro, K. L., Falcón-Barroso, J., van de Ven, G., et al. 2010, *Mon. Not. R. astr. Soc.*, 402, 2140

Shapiro, K. L., Genzel, R., Förster Schreiber, N. M., et al. 2008, *Astrophys. J.*, 682, 231

Shapiro, K. L., Genzel, R., Quataert, E., et al. 2009, *Astrophys. J.*, 701, 955

Sijacki, D., Springel, V., & Haehnelt, M. G. 2011, *Mon. Not. R. astr. Soc.*, 414, 3656

Skrutskie, M. F., Cutri, R. M., Stiening, R., et al. 2006, *Astron. J.*, 131, 1163

Soifer, B. T. & Neugebauer, G. 1991, *Astron. J.*, 101, 354

Soifer, B. T., Neugebauer, G., & Houck, J. R. 1987, *Ann. Rev. Astron. Astr.*, 25, 187

Somerville, R. S., Primack, J. R., & Faber, S. M. 2001, *Mon. Not. R. astr. Soc.*, 320, 504

Soto, K. T. & Martin, C. L. 2012, *Astrophys. J. Suppl.*, 203, 3

Steidel, C. C., Adelberger, K. L., Giavalisco, M., Dickinson, M., & Pettini, M. 1999, *Astrophys. J.*, 519, 1

Swinbank, A. M., Sobral, D., Smail, I., et al. 2012, *Mon. Not. R. astr. Soc.*, 426, 935

Tacconi, L. J., Genzel, R., Lutz, D., et al. 2002, *Astrophys. J.*, 580, 73

Tacconi, L. J., Genzel, R., Smail, I., et al. 2008, *Astrophys. J.*, 680, 246

Tacconi, L. J., Neri, R., Chapman, S. C., et al. 2006, *Astrophys. J.*, 640, 228

Takagi, T., Ohyama, Y., Goto, T., et al. 2010, *Astron. Astrophys.*, 514, A5

Takagi, T., Ono, Y., Shimasaku, K., & Hanami, H. 2008, *Mon. Not. R. astr. Soc.*, 389, 775

Taylor, E. N., Franx, M., Brinchmann, J., van der Wel, A., & van Dokkum, P. G. 2010, *Astrophys. J.*, 722, 1

Tecza, M., Genzel, R., Tacconi, L. J., et al. 2000, *Astrophys. J.*, 537, 178

Telesco, C. M. & Harper, D. A. 1980, *Astrophys. J.*, 235, 392

Toomre, A. & Toomre, J. 1972, *Astrophys. J.*, 178, 623

U, V., Sanders, D. B., Mazzarella, J. M., et al. 2012, *Astrophys. J. Suppl.*, 203, 9

Valiante, E., Lutz, D., Sturm, E., Genzel, R., & Chapin, E. L. 2009, *Astrophys. J.*, 701, 1814

van Starkenburg, L., van der Werf, P. P., Franx, M., et al. 2008, *Astron. Astrophys.*, 488, 99

Veilleux, S., Kim, D.-C., & Sanders, D. B. 1999a, *Astrophys. J.*, 522, 113

Veilleux, S., Kim, D.-C., & Sanders, D. B. 2002, *Astrophys. J. Suppl.*, 143, 315

Veilleux, S., Kim, D.-C., Sanders, D. B., Mazzarella, J. M., & Soifer, B. T. 1995, *Astrophys. J. Suppl.*, 98, 171

Veilleux, S., Rupke, D. S. N., Kim, D.-C., et al. 2009, *Astrophys. J. Suppl.*, 182, 628

Veilleux, S., Sanders, D. B., & Kim, D.-C. 1999b, *Astrophys. J.*, 522, 139

Vergani, D., Epinat, B., Contini, T., et al. 2012, *Astron. Astrophys.*, 546, A118

Vieira, J. D., Marrone, D. P., Chapman, S. C., et al. 2013, *Nature*, 495, 344

Werner, M. W., Roellig, T. L., Low, F. J., et al. 2004, *Astrophys. J. Suppl.*, 154, 1

Westmoquette, M. S., Clements, D. L., Bendo, G. J., & Khan, S. A. 2012, *Mon. Not. R. astr. Soc.*, 424, 416

Williams, M. J., Bureau, M., & Cappellari, M. 2010, *Mon. Not. R. astr. Soc.*, 409, 1330

Wisnioski, E., Glazebrook, K., Blake, C., et al. 2011, *Mon. Not. R. astr. Soc.*, 417, 2601

Wolf, J., Martinez, G. D., Bullock, J. S., et al. 2010, *Mon. Not. R. astr. Soc.*, 406, 1220

Wright, E. L. 2006, *Pub. Astron. Soc. Pac.*, 118, 1711

Wu, H., Cao, C., Hao, C.-N., et al. 2005, *Astrophys. J. L.*, 632, L79

Wuyts, S., Förster Schreiber, N. M., van der Wel, A., et al. 2011, *Astrophys. J.*, 742, 96

Yang, Y., Flores, H., Hammer, F., et al. 2008, *Astron. Astrophys.*, 477, 789

Yuan, T.-T., Kewley, L. J., & Sanders, D. B. 2010, *Astrophys. J.*, 709, 884

Yun, M. S., Reddy, N. A., & Condon, J. J. 2001, *Astrophys. J.*, 554, 803

Zamojski, M., Yan, L., Dasyra, K., et al. 2011, *Astrophys. J.*, 730, 125

Zanichelli, A., Garilli, B., Scodeggio, M., et al. 2005, *Pub. Astron. Soc. Pac.*, 117, 1271

List of Tables

List of Figures

Glossary

2MASS	Two Microns All Sky Survey
A&A	Astronomy and Astrophysics
ACS	Advanced Camera for Surveys
AGN	Active Galactic Nucleus
AJ	Astronomical Journal
AO	Adaptive Optics
ApJ	Astrophysical Journal
ApJS	Astrophysical Journal Supplement
BGS	Bright Galaxy Survey
CAHA	Centro Astronòmico Hispano-Alemàn Calar Alto
CALIFA	Calar Alto Legacy Integral Field Area survey
ESO	European Southern Observatory
EsoRex	ESO Recipe Execution Tool
ETG	Early Type Galaxy
EW	Equivalent Width
FITS	Flexible Image Transport System
FLAMES	Fibre Large Array Multi Element Spectrograph
FoV	Field of View
FWHM	Full Width at Half Maximum
GHASP	Gassendi Hα survey of SPirals
GMOS	Gemini Multi-Object Spectrographs
HST	Hubble Space Telescope
IDL	Interactive Data Language
IFS	Integral Field Spectroscopy/Spectrograph
IFU	Integral Field Unit
IMF	Initial Mass Function
IR	Infrared
IRAS	Infrared Astronomical Satellite
IRIS	Infrared Imaging Spectrograph
ISO	Infrared Space Observatory
JWST	James Webb Space Telescope

KMOS	K-band Multi-Object Spectrograph
LBA	Lyman Break Analog
LINER	Low-Ionization Nuclear Emission-line Region
LIRG	Luminous Infrared Galaxy
MAD	Median Absolute Deviation
MASSIV	Mass Assembly Survey with SINFONI in VVDS
MIPS	Multiband Imaging Photometer for Spitzer
MIRI	Mid-Infrared Instrument
MOS	Multi-Object Spectrograph
MUSE	Multi Unit Spectroscopic Explorer
NASA	National Aeronautics and Space Administration
NED	NASA/IPAC ExtragalacticDatabase
NFGS	Nearby Field Galaxy Survey
NGC	New General Catalogue
NICMOS	Near Infrared Camera and Multi-Object Spectrometer
NIRSpec	Near-Infrared Spectrograph
OSIRIS	OH-Suppressing Infra-Red Imaging Spectrograph
PDF	Probability Distribution Function
PMAS	Potsdam MultiAperture Spectrophotometer
PSF	Point Spread Function
QSO	Quasi Stellar Object
S/N	Signal-to-Noise
SAURON	Spectroscopic Areal Unit for Research on Optical Nebulae
SED	Spectral Energy Distribution
SFG	Star-Forming Galaxy
SFR	Star Formation Rate
SINFONI	Spectrograph for INtegral Field Observations in the Near Infrared
SINGS	Spitzer Infrared Nearby Galaxies Survey
SINS	Spectroscopic Imaging survey in the Near-infrared with SINFONI
SMG	Sub-Millimetre Galaxy
SOF	Set-of-Frames
TIGER	Traitement Intégral des Galaxies par l'Etude de leurs Raies
TIR	Total Infrared
ULIRG	Ultraluminous Infrared Galaxy
UV	Ultraviolet
VIMOS	VIsible MultiObject Spectrograph
VLT	Very Large Telescope
VVDS	The VIMOS VLT Deep Survey
WFPC2	Wide-Field Planetary Camera 2
WHT	William Herschel Telescope

Appendices

Appendix A

Kinematic maps

In this appendix we present the Hα flux, velocity field, and the velocity dispersion maps of the different kinematic components for the galaxies of the sample. When available, the HST image is also included. The spatial offsets between the peaks of the continuum and the Hα flux emission are shown in Table A.1.

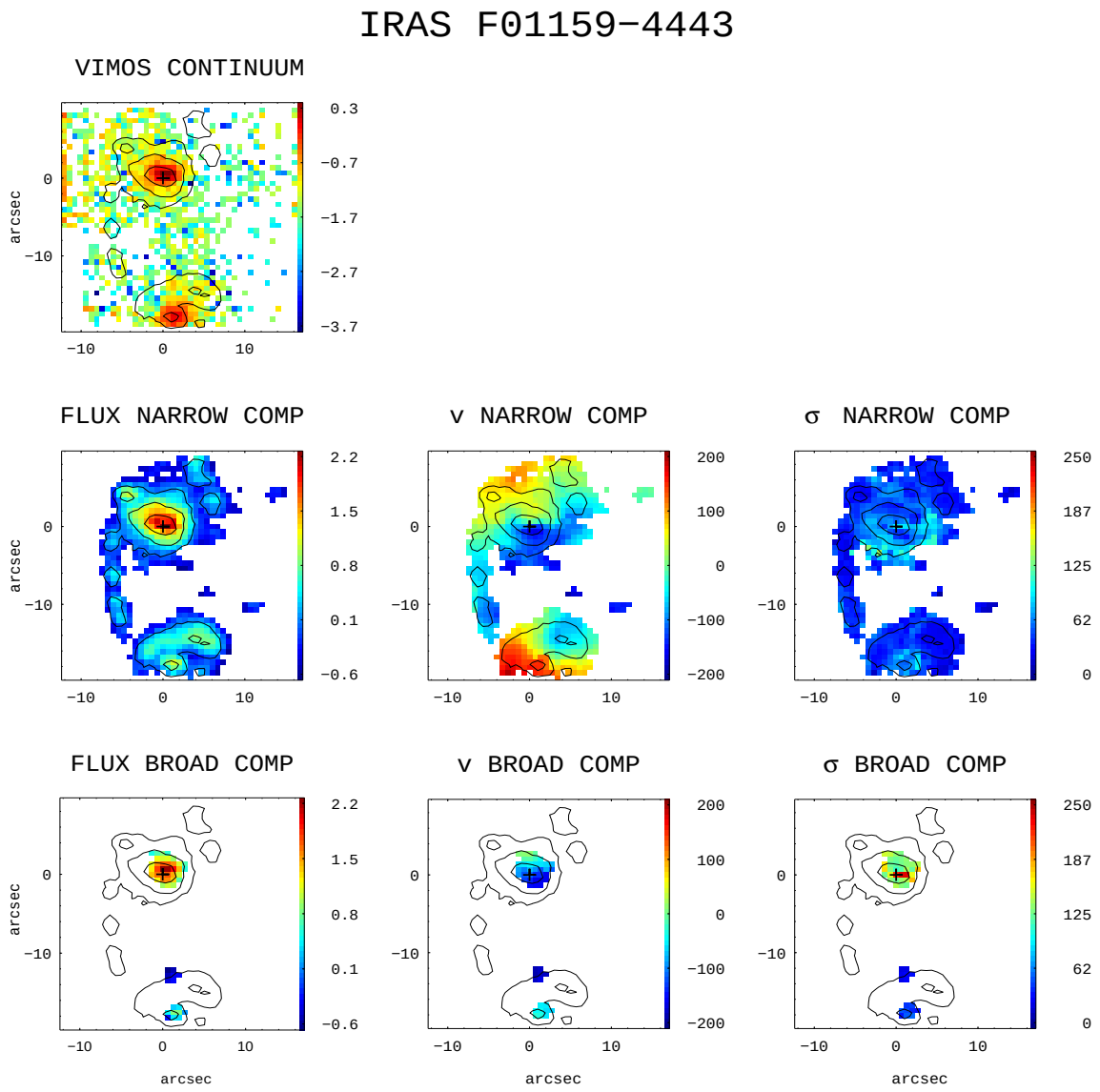

Figure A.1: *Top panel:* VIMOS continuum (6390-6490) Å image within the rest-frame wavelength range. When available, the HST continuum image is also shown. *Middle panel:* the Hα flux intensity, velocity field, v (km s^{-1}), and velocity dispersion, σ (km s^{-1}), for the narrow component. *Bottom panel:* similar maps for the broad component. The flux intensity maps are represented in logarithmic scale (applying a factor of -13) in units of erg s^{-1} cm^{-2} for the Hα flux maps and erg s^{-1} cm^{-2} Å^{-1} for the continuum map. The center (0,0) is identified with the Hα flux intensity peak and the iso-contours of the Hα flux map are overplotted. North is at the top and East to the left in all the panels.

IRAS F01159-4443 (ESO 244-G012): this is an interacting pair with a nuclear separation $\sim$ 8.4 kpc, where the northern galaxy shows the brightest nuclear emission in both the Hα and continuum maps. The two galaxies show regular velocity fields in the narrow component. The scale is 0.462 kpc/″.

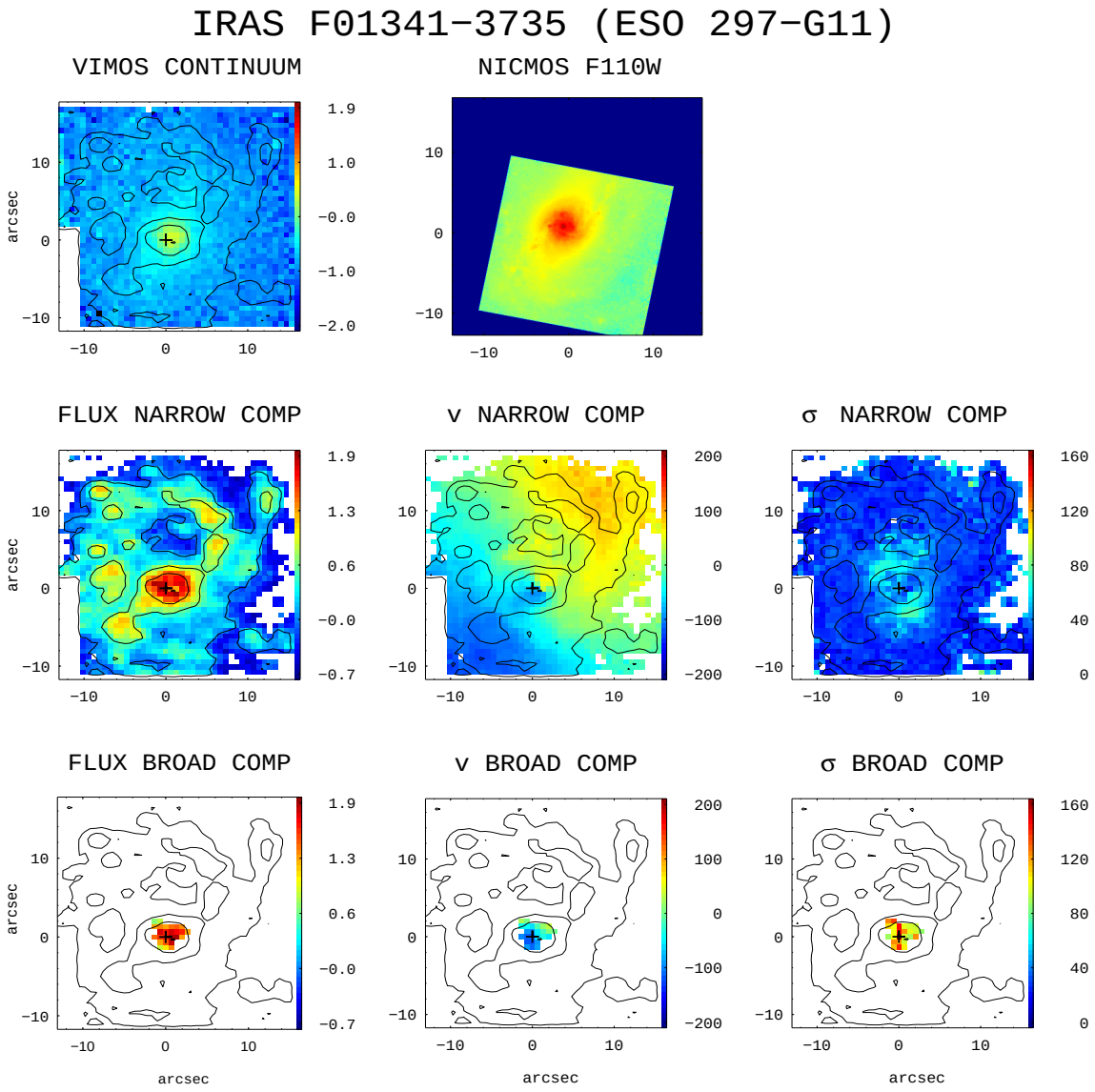

Figure A.2: (General comments about the panels as in Fig. A.1.) IRAS F01341-3735 (ESO 297-G011/G012): this system is composed of two galaxies (i.e., northern, southern) separated by $\sim$ 25 kpc, implying the need of two VIMOS pointings. The present maps correspond to the northern galaxy, which shows a regular velocity field. The velocity dispersion map has two symmetric local maxima of $\sim$ 70 km s^{-1} around the nucleus, which are well fitted using one Gaussian model. These regions have low Hα surface brightness and are associated with high excitation and high σ, as reported by Monreal-Ibero et al. (2010). In the innermost regions (i.e., $\sim$ 1.5 kpc^2), the Hα-[NII] emission lines need a secondary broad component. The spatial scale is of 0.352 kpc/″.

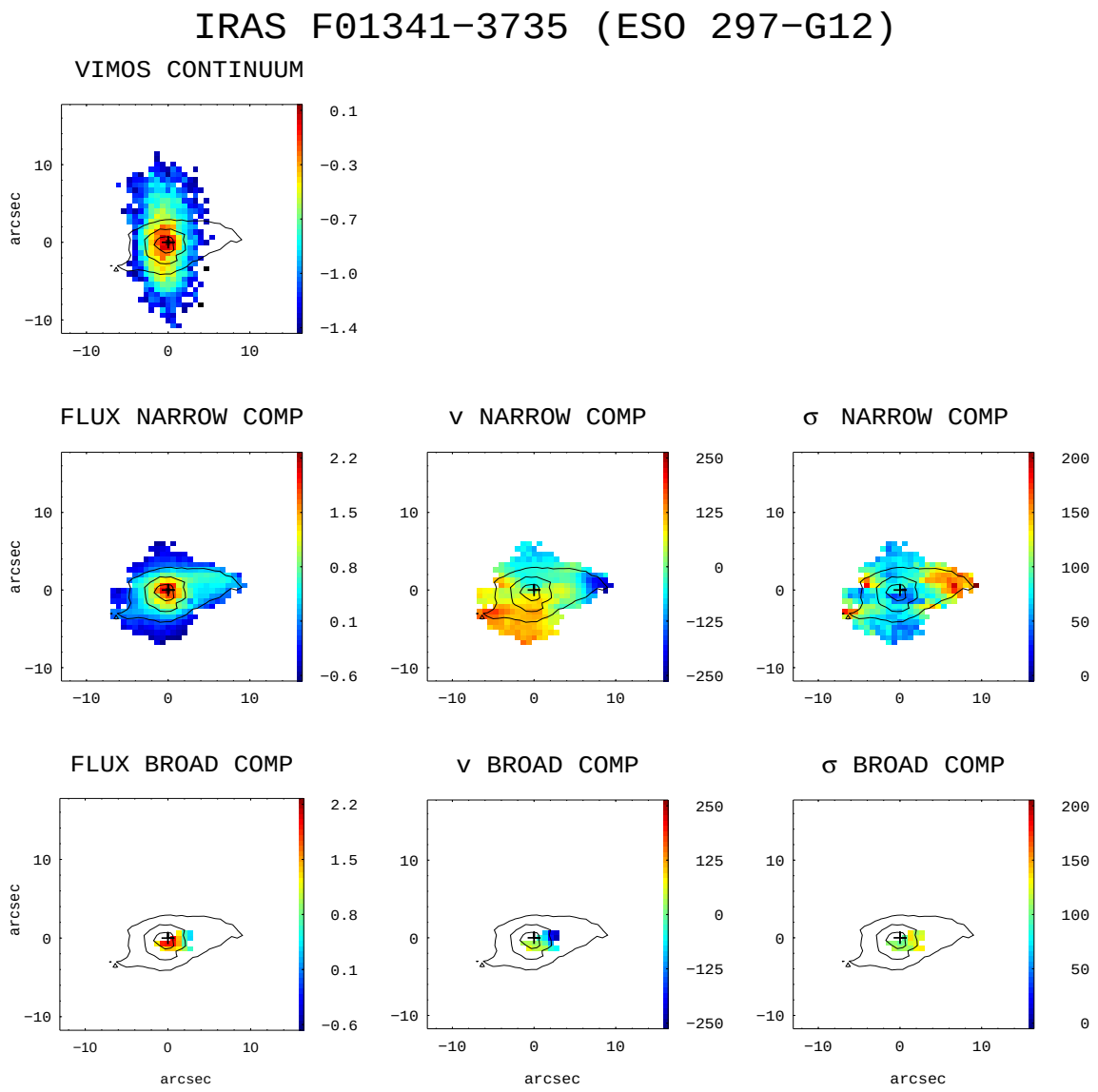

Figure A.3: (General comments about the panels as in Fig. A.1.). ESO 297-G012: this is the southern galaxy of the system IRAS F01341-3735. The Hα emission is oriented perpendicular to the major stellar axis as traced by the continuum image. Although a rotation component is visible in the velocity field along the major photometrical axis, its structure, as well as that of the velocity dispersion map, is irregular. In an inner region ($\sim$ 1 kpc^2), the spectra have been fitted with two components, with the broad component blueshifted by $\sim$ 50 km s^{-1}. The scale is 0.352 kpc/″.

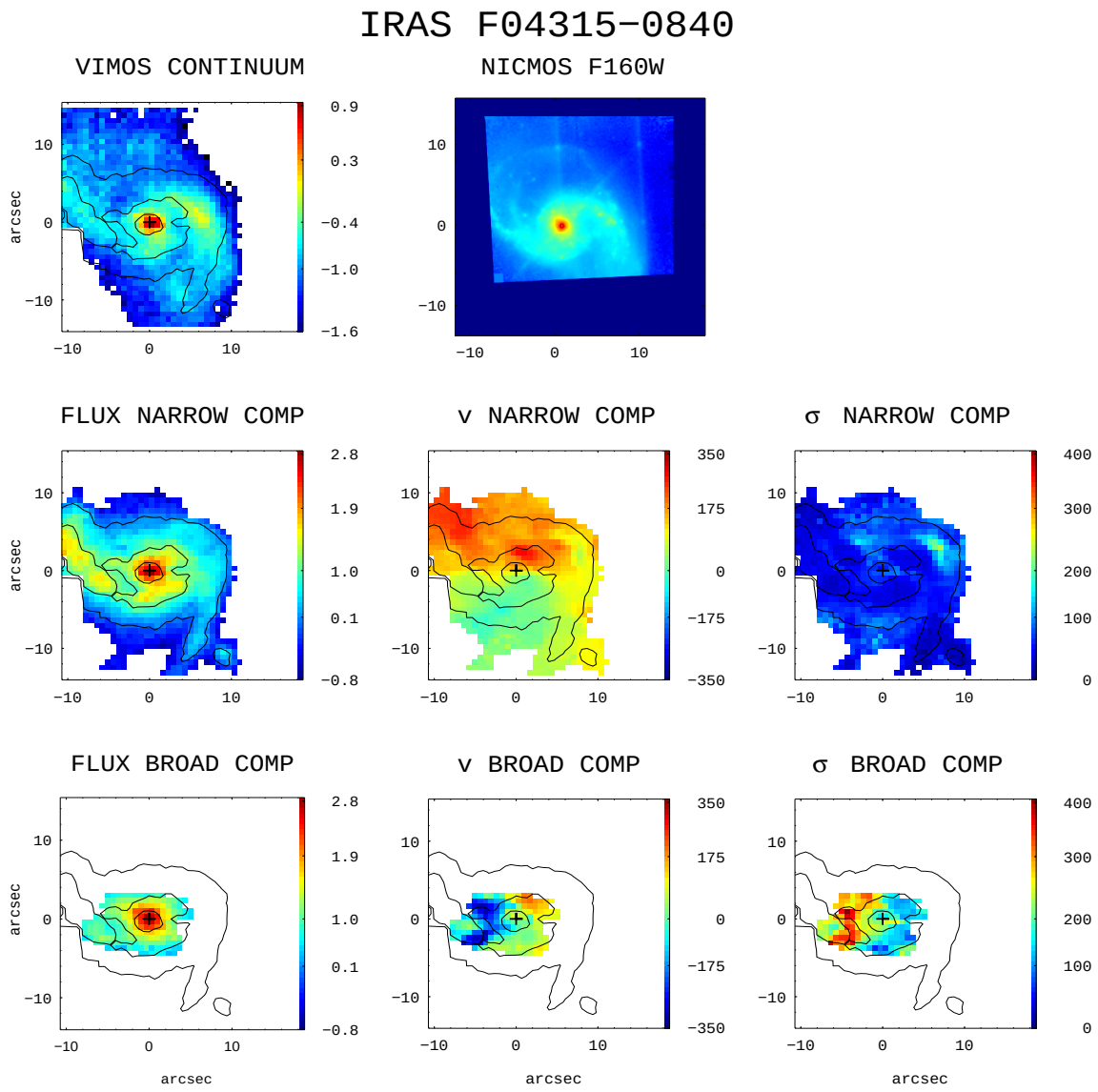

Figure A.4: (General comments about the panels as in Fig. A.1.) IRAS F04315-0840 (NGC 1614): this is a well-studied, post-coalescence late merger, with a bright, spiral structure of a length scale of few kpcs. The velocity field of the narrow component is somewhat distorted and chaotic with an amplitude of 324 km s^{-1}. Its velocity dispersion map shows an offset peak of $\sim$ 220 km s^{-1} at around 2.4 kpc from the nucleus in the western arm. The spectra in the inner regions are complex, and a secondary broad component covers a relatively large area of about 8.6 kpc^2. The projection of the kinematic major axes of the narrow (main) and broad components differs by $\sim 90°$. The blueshifted region of the velocity field of the broad component has the largest velocity dispersion (i.e., $\sim$400 km s^{-1}). All this supports the hypothesis of a dusty outflow, where the receding components (which are behind the disk) are obscured, making the whole profile relatively narrow with respect to the approaching component. This object has been analyzed in Bellocchi et al. (2012). The spatial scale is 0.325 kpc/″.

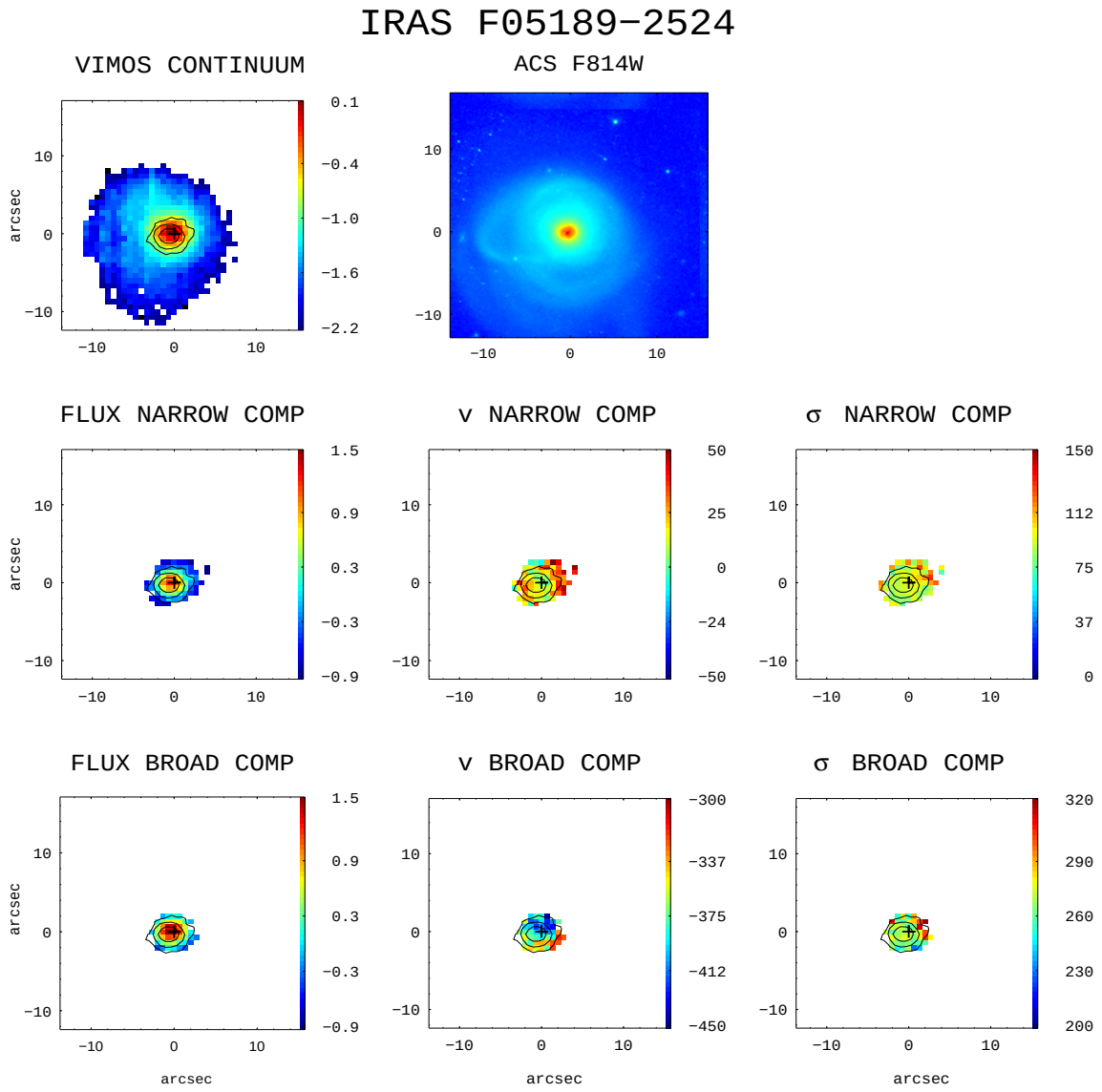

Figure A.5: (General comments about the panels as in Fig. A.1.) IRAS F05189-2524: this galaxy shows a compact Hα emission, both in the narrow and broad components.Their velocity fields and velocity dispersion maps do not show regular patterns. The broad component is blueshifted up to $\sim$ 400 km s^{-1} with respect to the narrow one and is dominant in terms of flux in the innermost spaxels. The scale is of 0.839 kpc/″.

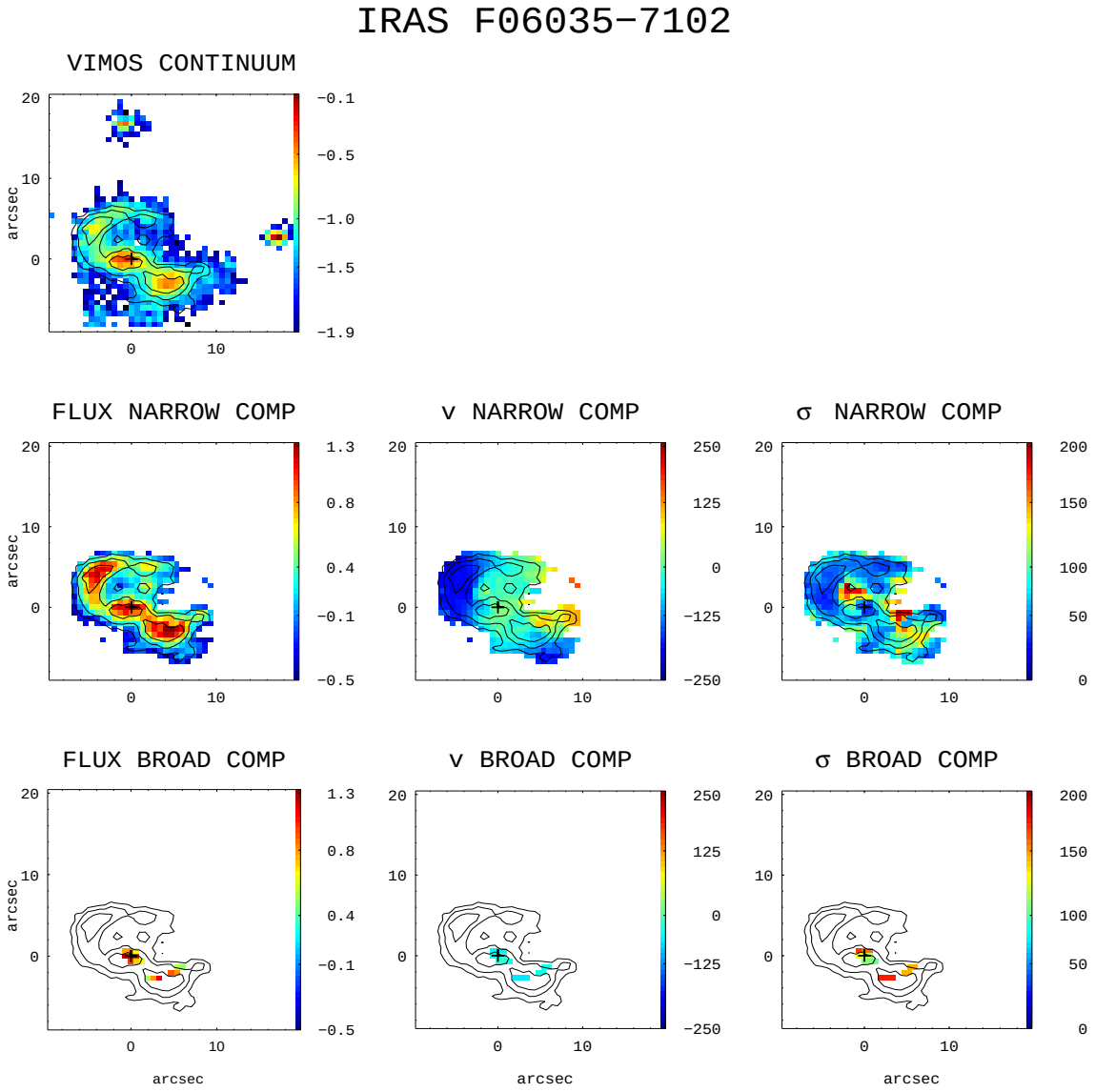

Figure A.6: (General comments about the panels as in Fig. A.1.) IRAS F06035-7102: this system consists of two pre-coalescence galaxies with a nuclear separation of $\sim$ 8 kpc. The velocity dispersion map of the narrow component clearly shows an irregular pattern, in which the two local maxima correspond to low Hα surface brightness regions. The spatial scale is 1.5 kpc/″.

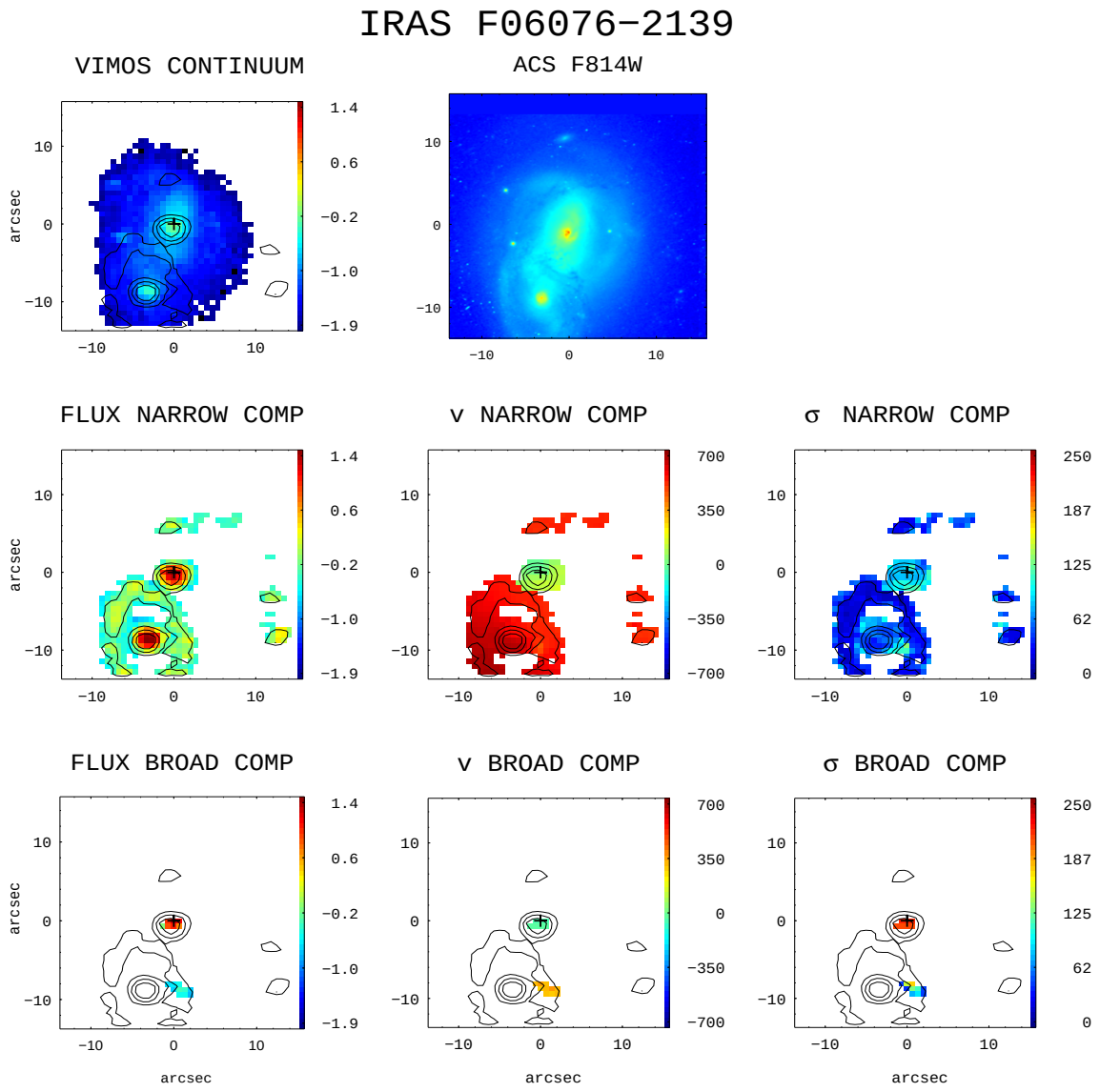

Figure A.7: (General comments about the panels as in Fig. A.1.) IRAS F06076-2139: this system consists of two galaxies in interaction with a rather complex morphology. The Hα image shows a rather different structure than that shown by the VIMOS continuum and the HST-ACS image. The southern galaxy is characterized by a ring and a tidal tail-like structures extending towards the west and northwest part from the nucleus. The faint broad component found in a small region of the ring in the southern object is likely due to the superposition of the emission of the two galaxies along the line-of-sight. This system was already studied in Arribas et al. (2008). The scale is 0.743 kpc/″.

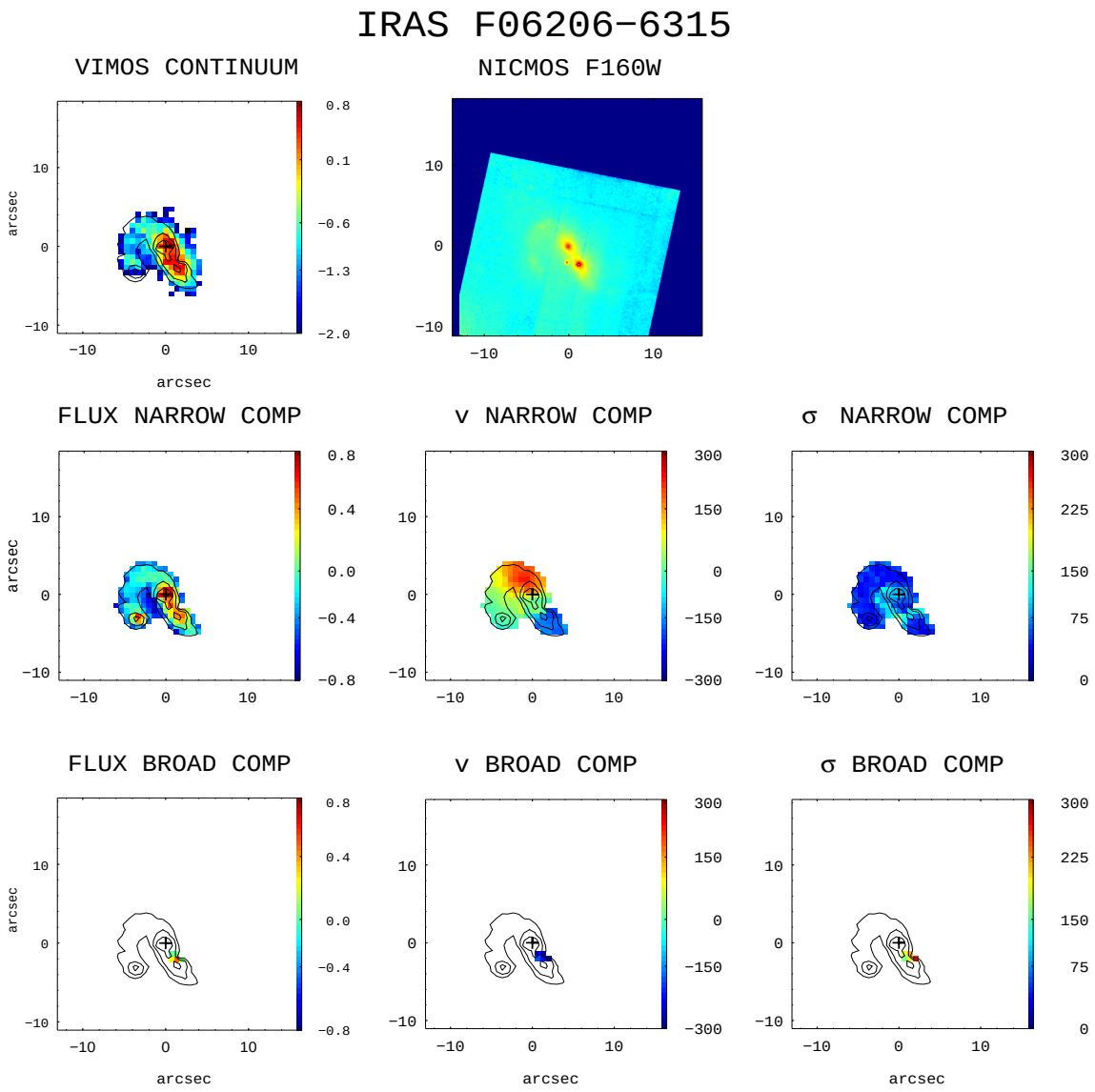

Figure A.8: (General comments about the panels as in Fig. A.1.) IRAS F06206-6315: this system has a double nuclei separated by $\sim$ 4 kpc, as clearly seen in the the Near Infrared Camera and Multi-Object Spectrometer (NICMOS/HST) image. There is a tidal tail starting in the north and bending towards the southeast, which contains a local peak of Hα emission (i.e., a possible tidal dwarf galaxy candidate). The brightest nucleus seems to be in positional agreement with the kinematic center. The velocity field is regular, and most of the spectra are well fitted using one component. The scale is of 1.72 kpc/″.

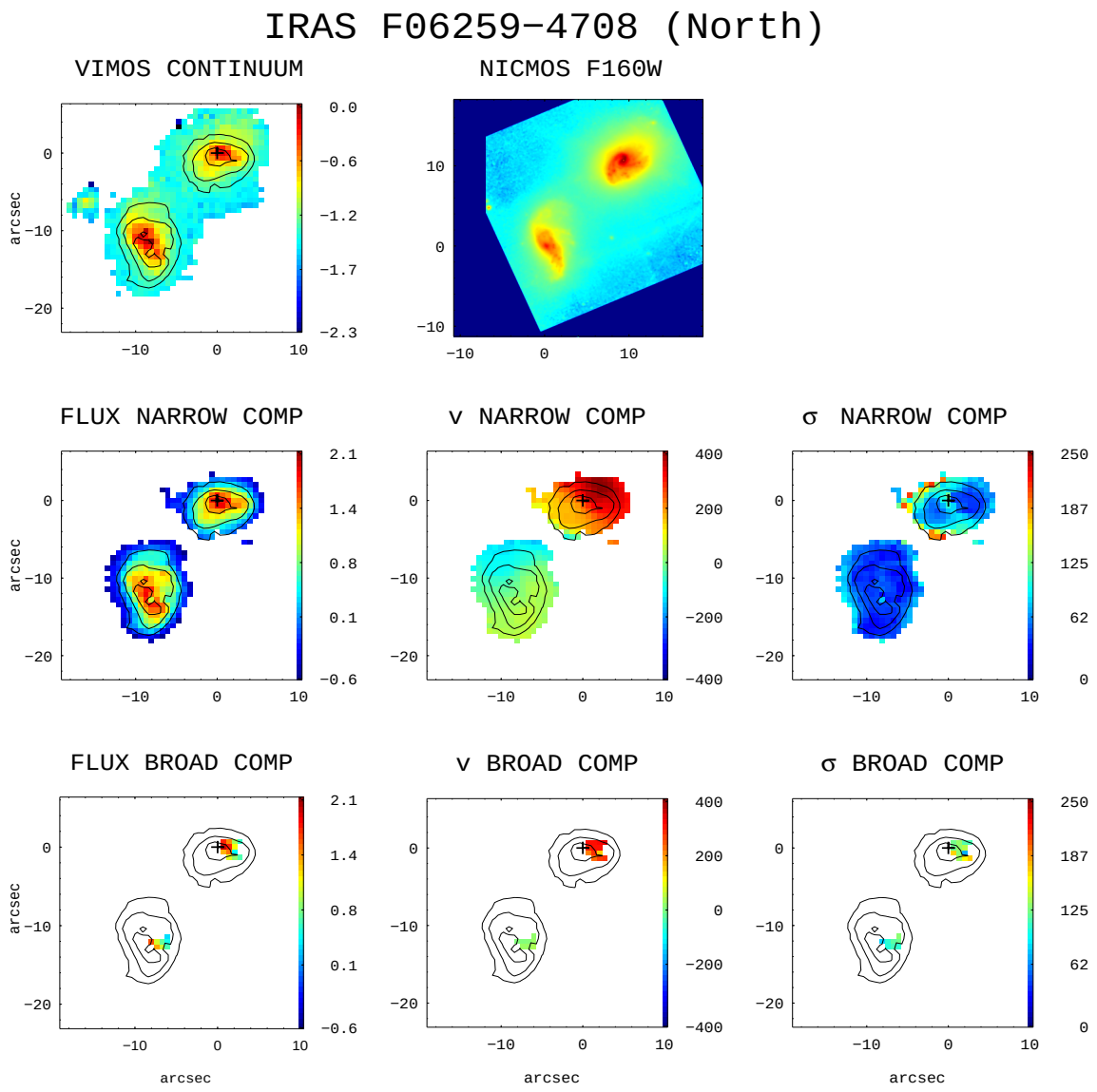

Figure A.9: (General comments about the panels as in Fig. A.1.) IRAS F06259-4708 (ESO 255-IG007): two VIMOS pointings were used during the observation of this triple system. The two brightest galaxies, the northern and the central ones, are separated by a distance of ∼11 kpc, while the third one is located at ∼ 13 kpc to the south from the central galaxy (see next panel). The present panels correspond to the northern and central galaxies, which show a regular velocity field pattern. The scale is of 0.769 kpc/″.

IRAS F06259−4708 (South)

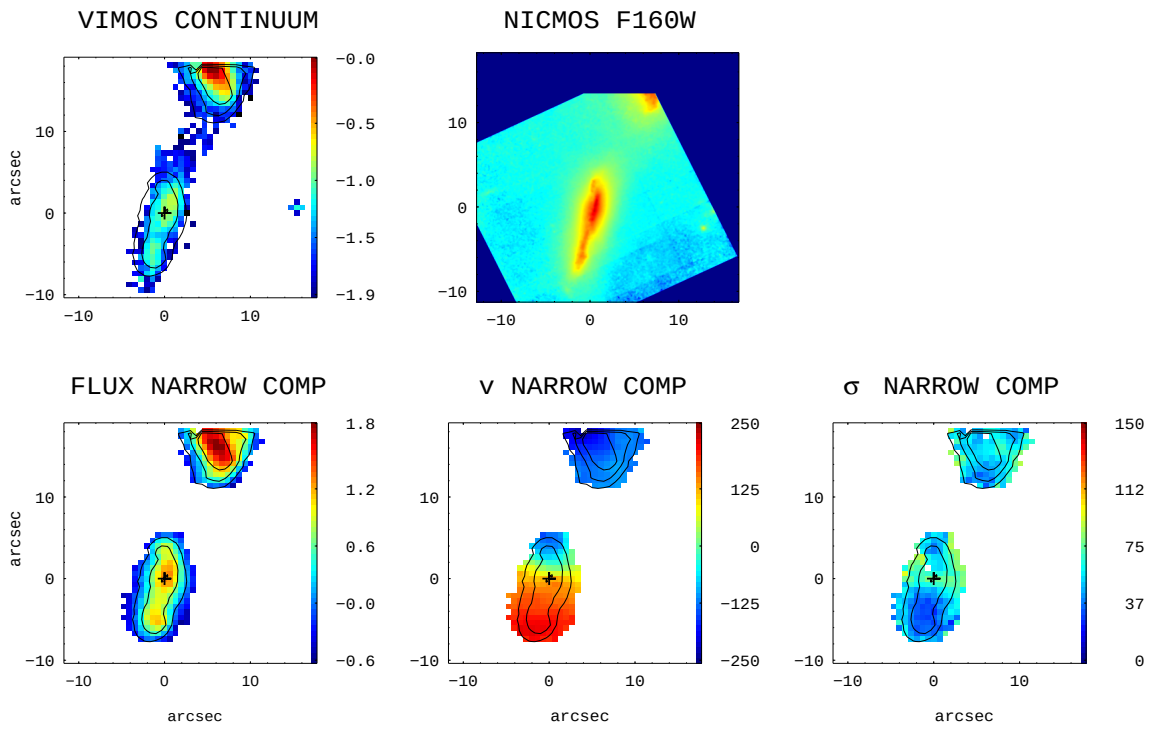

Figure A.10: (General comments about the panels as in Fig. A.1.) ESO 255-IG007: this is the southern galaxy of the system IRAS F06259-4708. It has a regular velocity field and the velocity dispersion map. One single Gaussian component is adequate to fit the Hα-[NII] emission lines of this galaxy. The scale is 0.769 kpc/″.

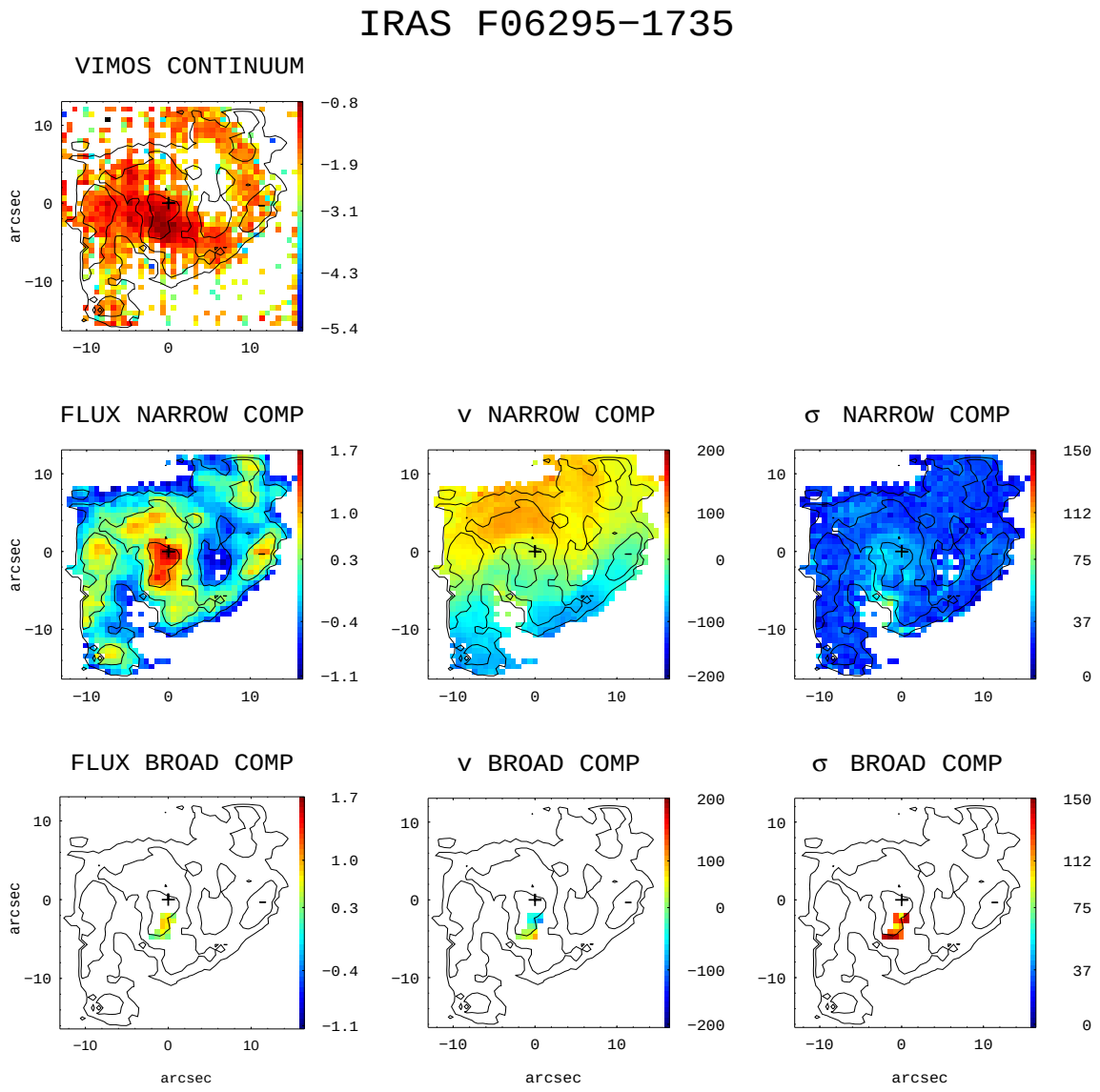

Figure A.11: (General comments about the panels as in Fig. A.1.) IRAS F06295-1735 (ESO 557-G002): the continuum image of this barred spiral shows vertical strips, which were not possible to remove during the reduction process (see Rodríguez-Zaurín et al. 2011). However, the Hα maps are not affected by this problem. Interestingly, neither the arms nor the bar in the Hα image coincide with those in the continuum image. The velocity field shows a regular structure, while its velocity dispersion map reaches the highest values (i.e., $\sigma \sim$ 70-80 km s^{-1}) at about 2 kpc to the south of the nucleus, in a region of relatively low emission. The scale is of 0.431 kpc/″.

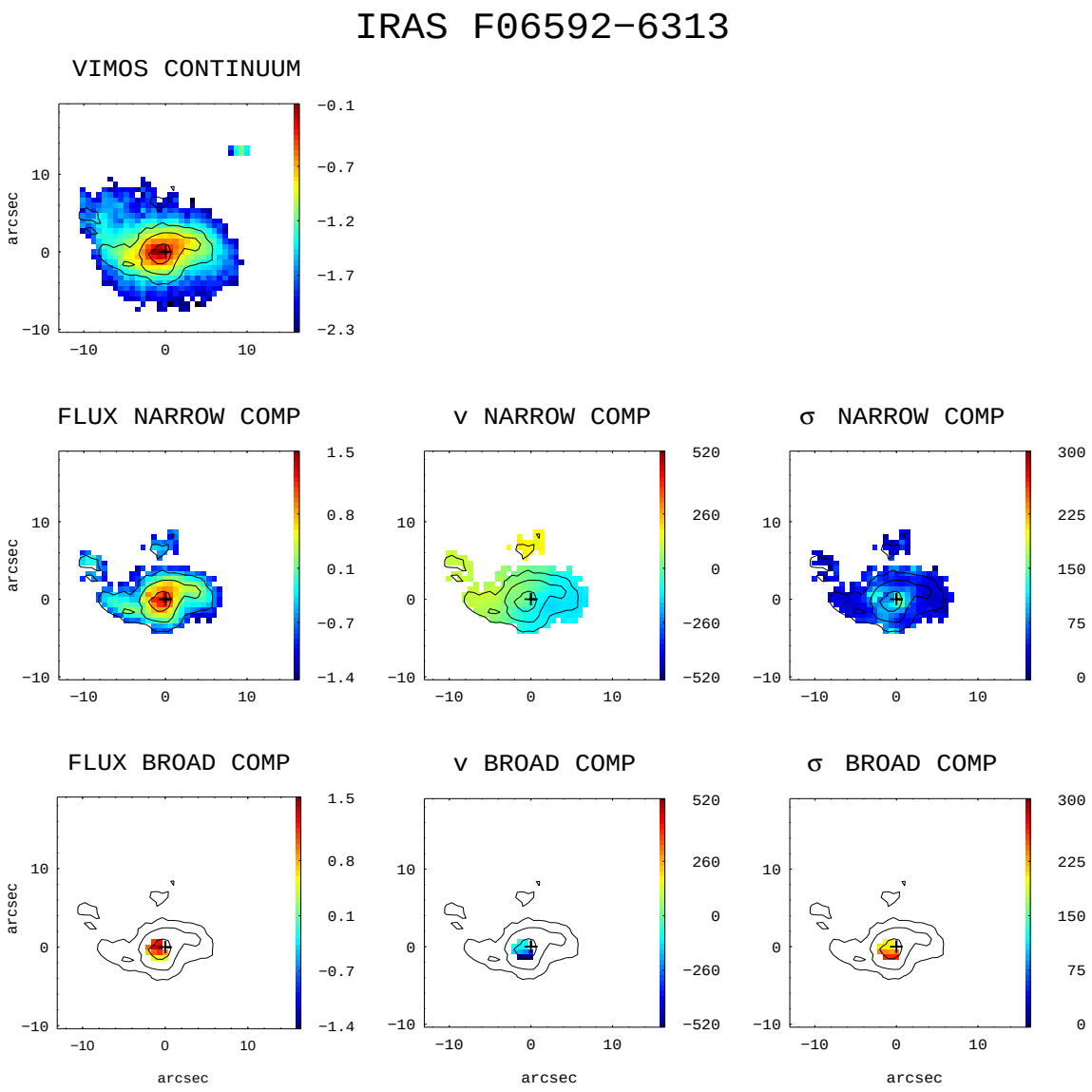

Figure A.12: (General comments about the panels as in Fig. A.1.) IRAS F06592-6313: this spiral galaxy shows a minor kinematic axis not aligned with the corresponding photometric one. Its velocity field shows a regular pattern with an amplitude of 160 km s^{-1}, while the velocity dispersion map shows some structure around the nucleus. A broad component blueshifted up to $\sim$ 300 km s^{-1} has been found in the inner regions. The scale is of 0.464 kpc/″.

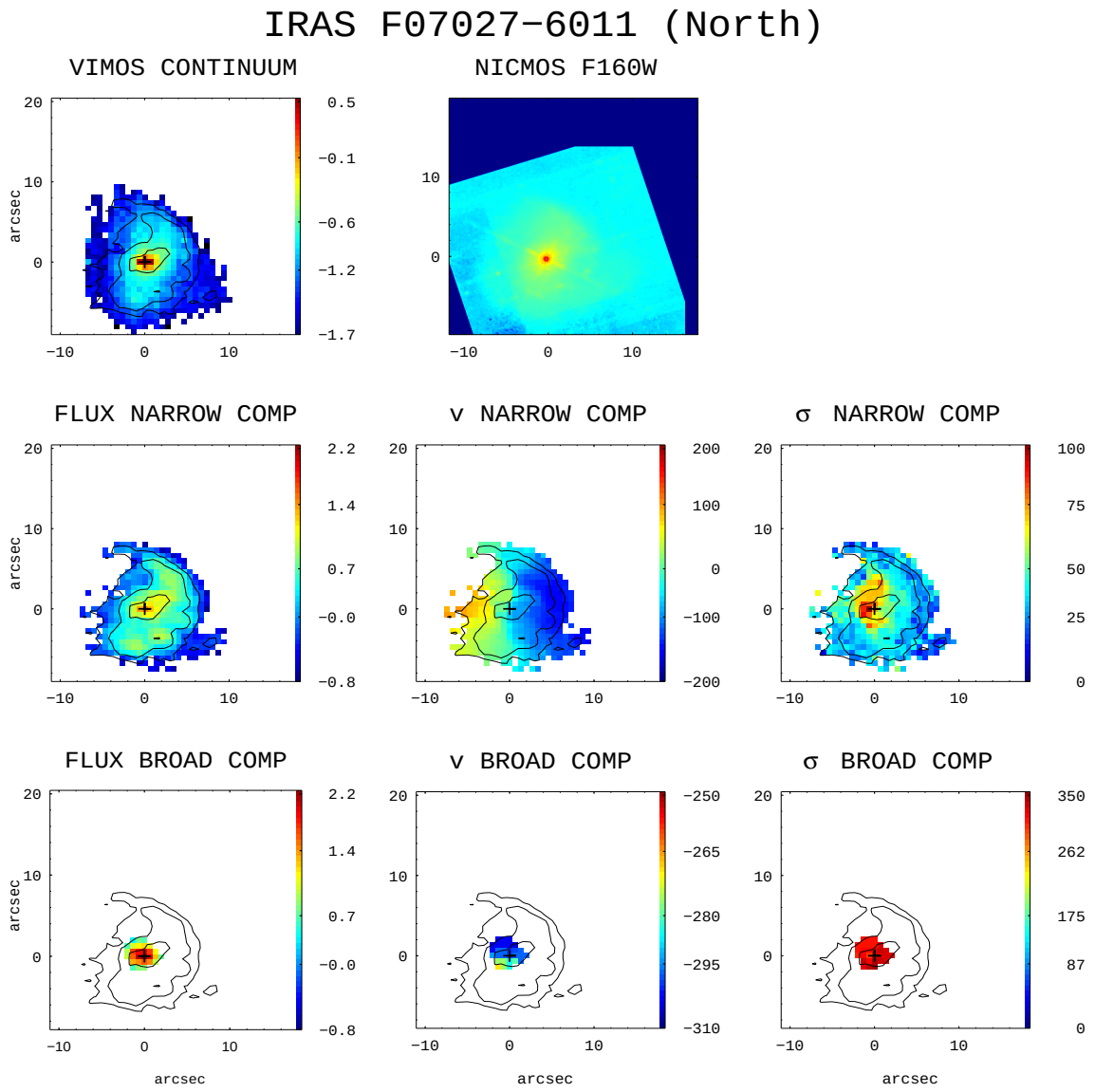

Figure A.13: (General comments about the panels as in Fig. A.1.) IRAS F07027-6011 (AM 0702-601): this system consists of two galaxies separated by $\sim$ 54 kpc. The present maps correspond to the northern galaxy. This object has a regular velocity field, while the velocity dispersion map shows a local maximum offset by $\sim$ 0.4 kpc with respect to the nucleus (or Hα flux peak). The secondary component found in the inner part shows a σ_{mean} of about 320 km s^{-1}, which can be explained by the fact that this galaxy possibly hosts an AGN (see Arribas et al. 2012). The spatial scale is of 0.626 kpc/″.

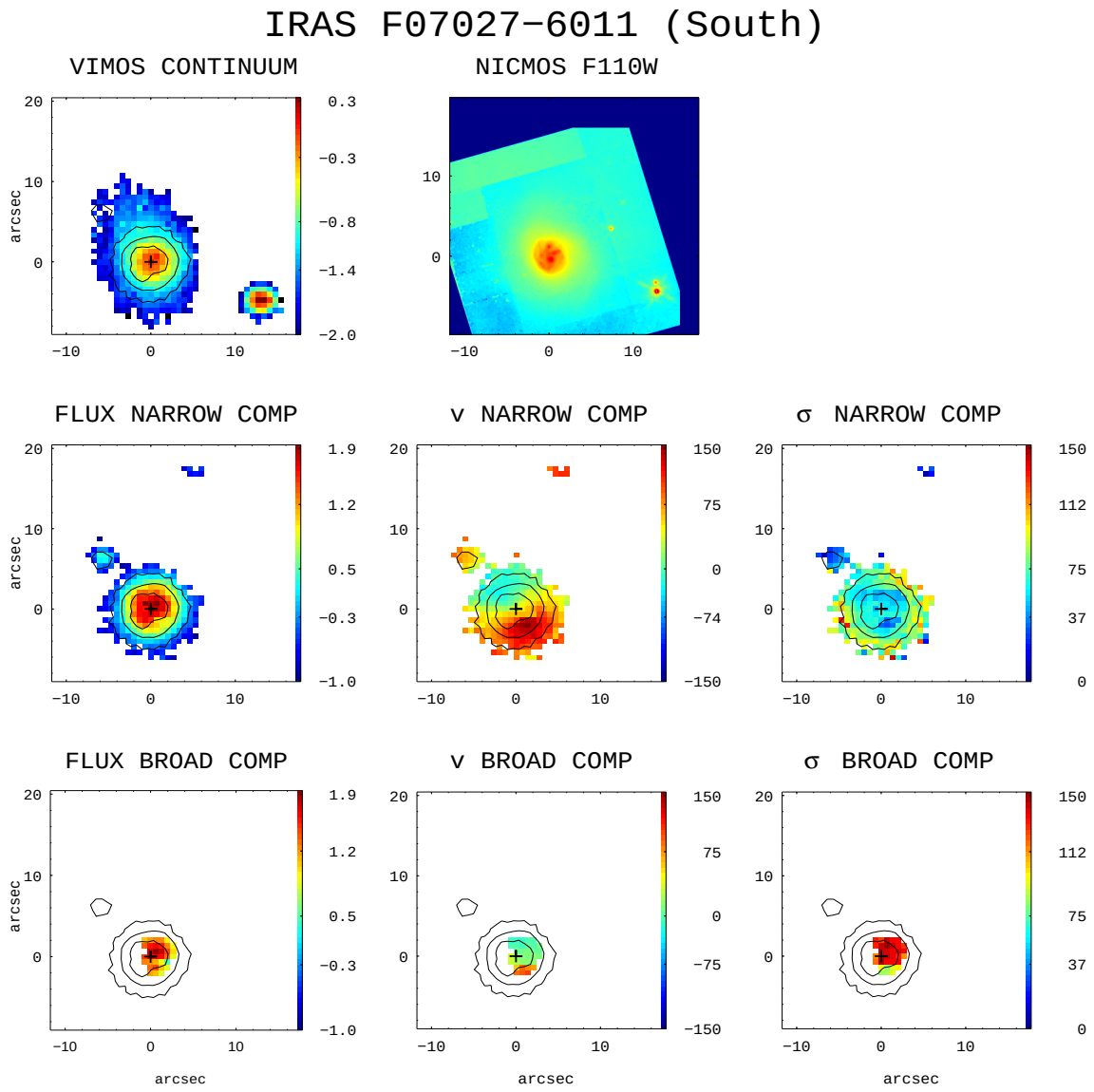

Figure A.14: (General comments about the panels as in Fig. A.1.) IRAS F07027-6011 (AM 0702-601): these maps correspond to the southern galaxy of the system. The velocity field of the narrow component is rather regular. In the velocity dispersion map a local maximum is found in correspondence of the nucleus (or Hα peak). The spatial scale is of 0.626 kpc/″.

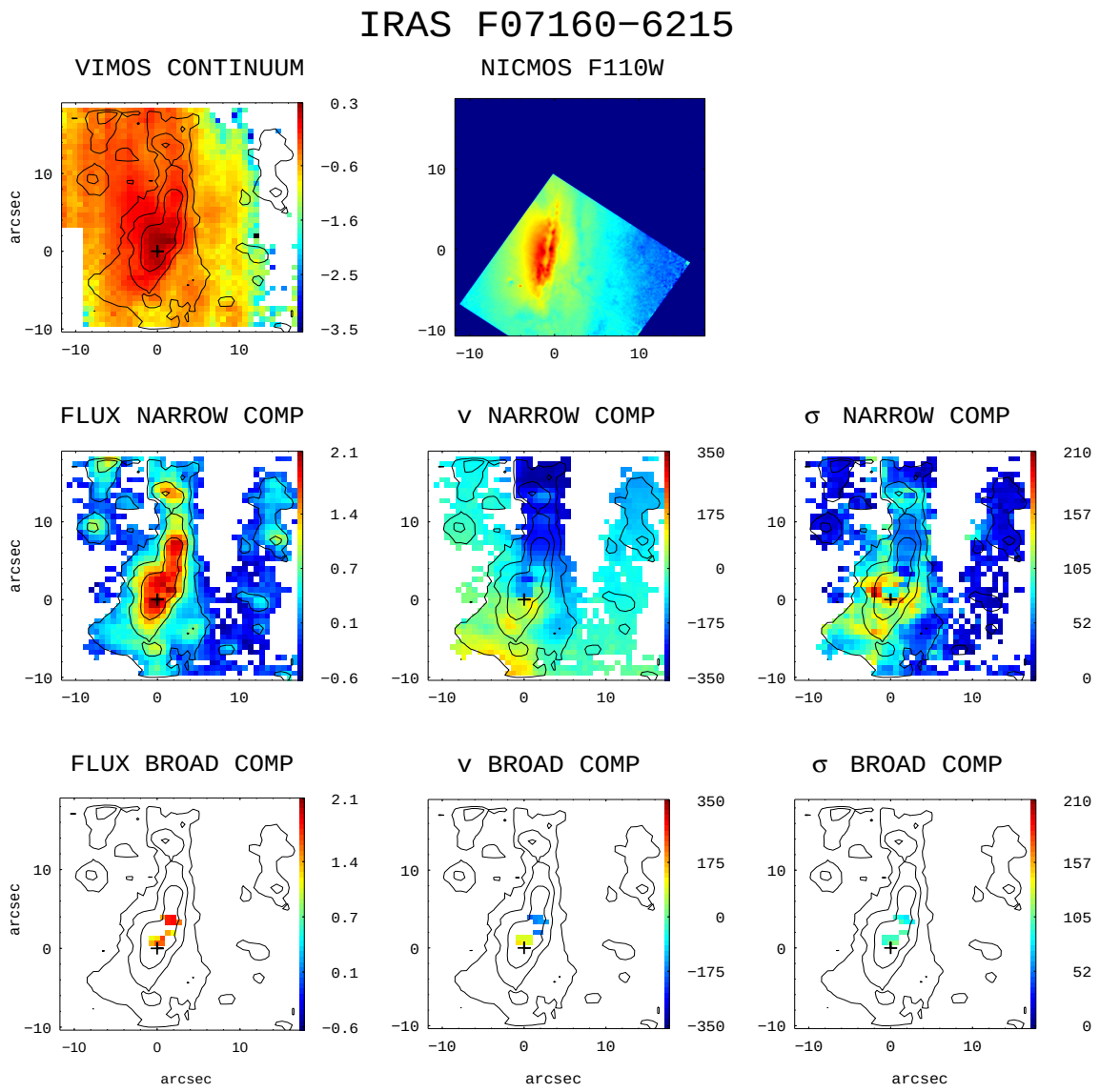

Figure A.15: (General comments about the panels as in Fig. A.1.) IRAS F07160-6215 (NGC 2369): this is an edge-on dusty galaxy, whose structure could strongly affect the pattern of its velocity field and velocity dispersion map. Indeed, the velocity field has a clear rotation component with some irregularities, and the velocity dispersion map shows distorted inner ($\sim$ 1 kpc) regions, with values ranging between 120 and 200 km s^{-1}, where a broad component has been considered to properly fit the spectra. The scale is 0.221 kpc/″.

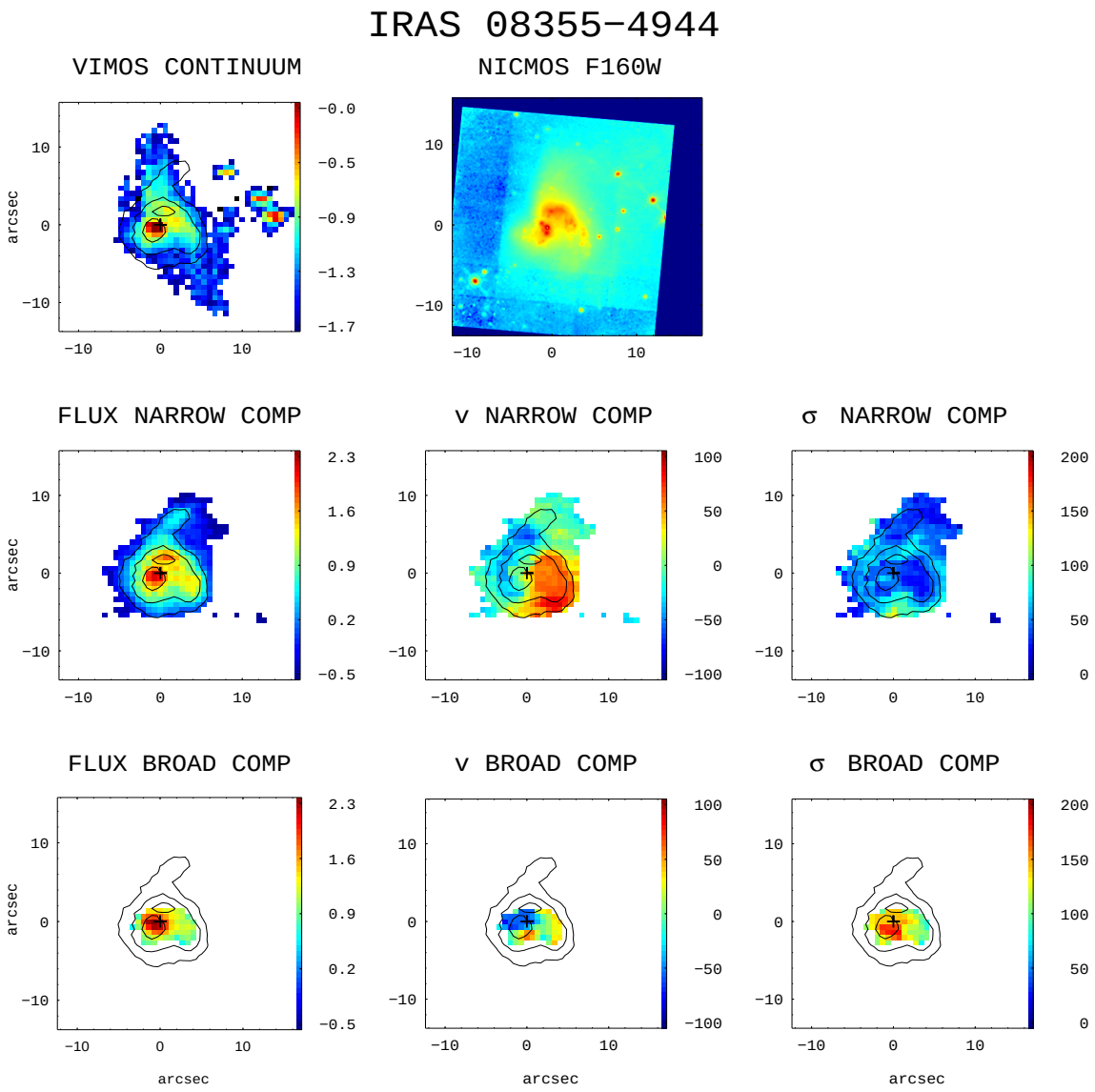

Figure A.16: (General comments about the panels as in Fig. A.1.) IRAS 08355-4944: this galaxy is morphologically classified as a post-coalescence merger. It has a quite regular velocity pattern and a relatively disturbed structure in the velocity dispersion map. Most of the spectra in the inner region have been fitted applying 2-Gaussian fit. The spatial scale is 0.521 kpc/″.

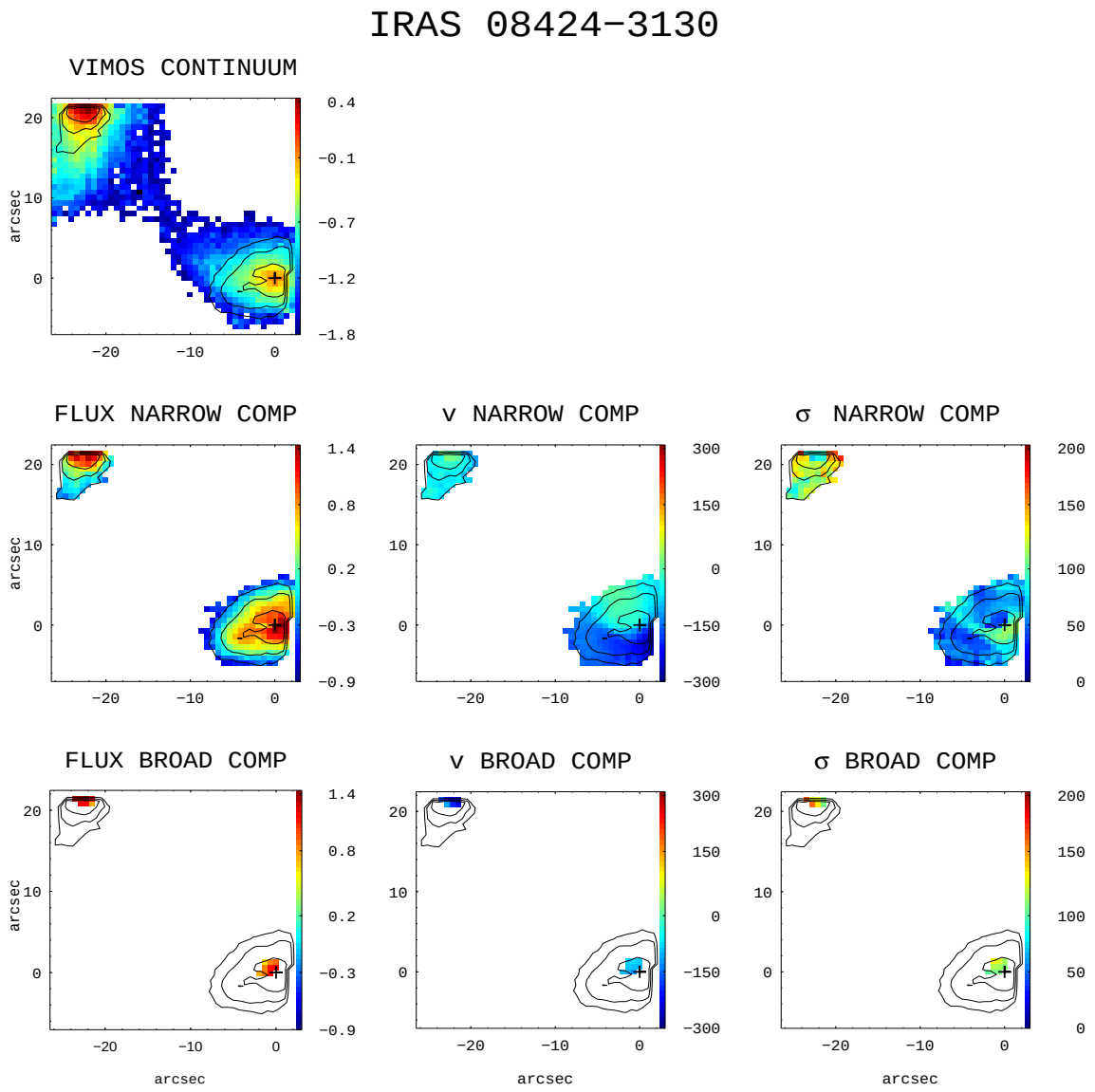

Figure A.17: (General comments about the panels as in Fig. A.1.) IRAS 08424-3130 (ESO 432-IG006): the Digital Sky Survey (DSS) image shows a pair of spiral galaxies (nuclear separation of $\sim$ 9 kpc) in interaction. Only part of the nuclear region of both galaxies is covered by our VIMOS FoV. The area covered by the Hα emission line for the northern galaxy is very small, so that its kinematical classification was not possible. The southern object reveals a relatively regular velocity field with an amplitude of 133 km s^{-1} and an almost centrally peaked velocity dispersion map. The spatial scale is 0.329 kpc/″.

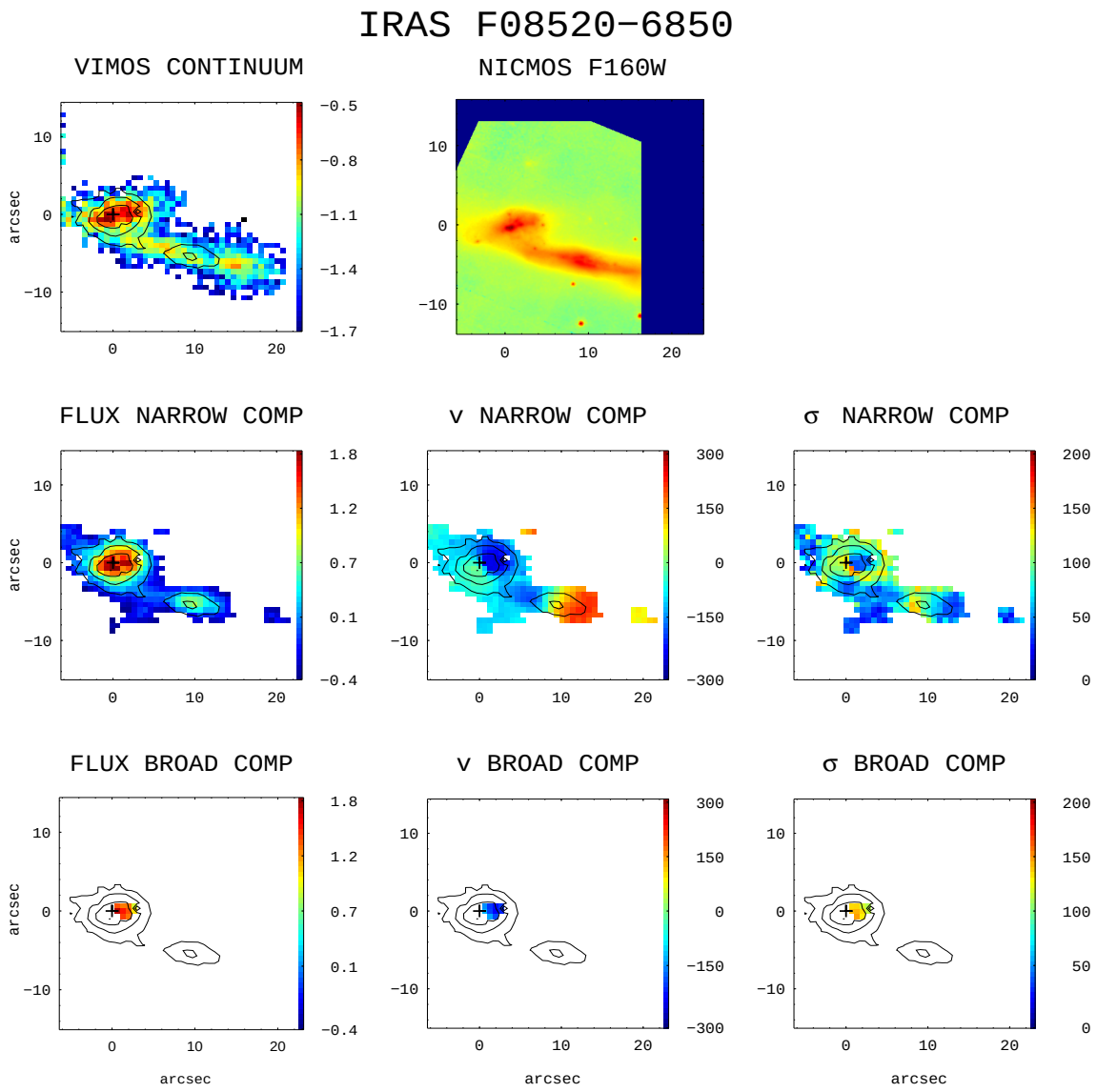

Figure A.18: (General comments about the panels as in Fig. A.1.) IRAS F08520-6850 (ESO 60-IG016): this system is composed of two disk galaxies in interaction with a nuclear separation of 10 kpc. The Hα flux peak and the kinematic center of the eastern source are in positional agreement. The velocity fields of the respective galaxies are regular. The spatial scale is 0.909 kpc/″.

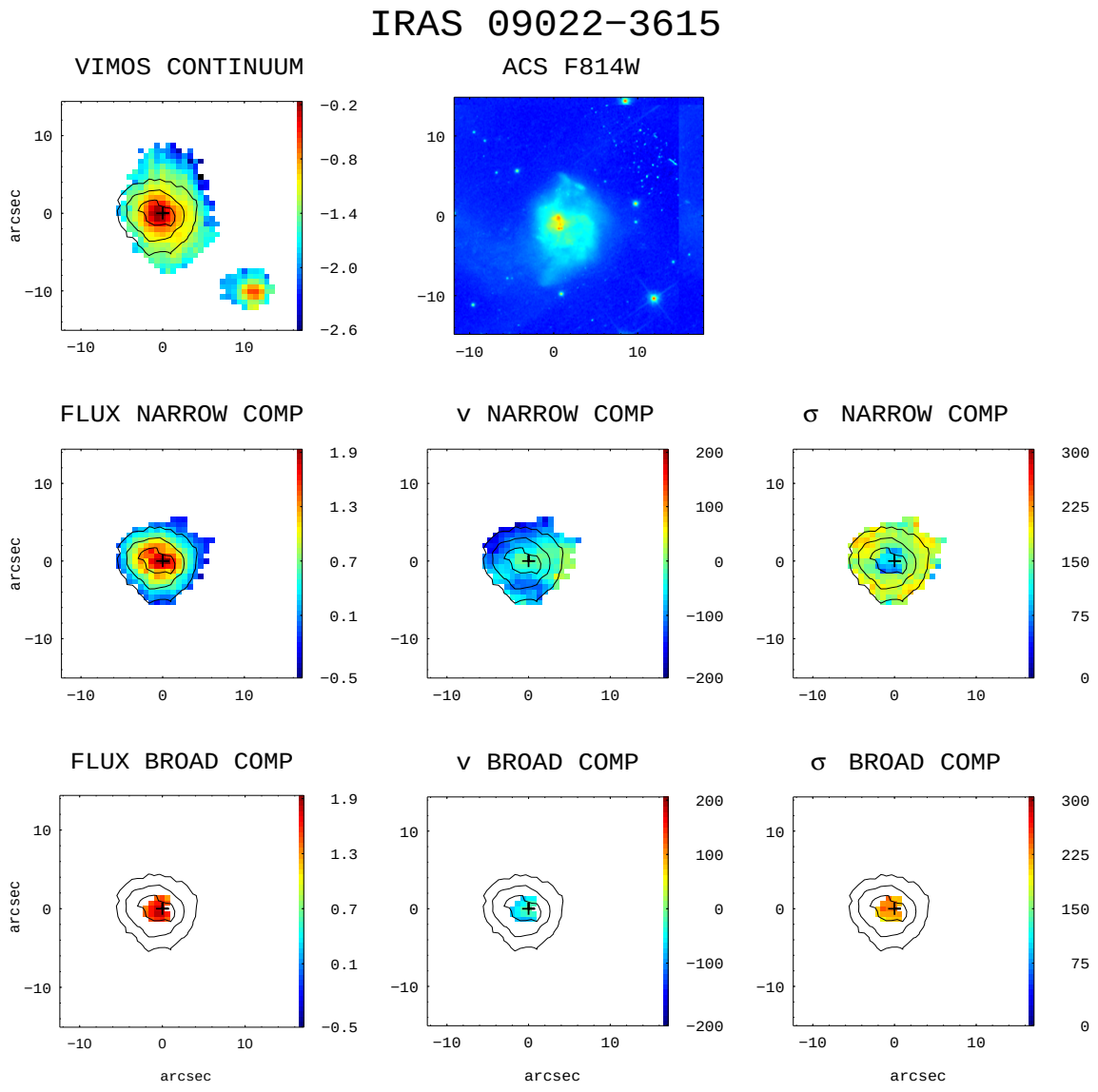

Figure A.19: (General comments about the panels as in Fig. A.1.) IRAS 09022-3615: the velocity field is quite distorted and irregular with poorly defined kinematic axes. The ring of high-velocity dispersion around the nucleus has several local peaks. A broad component is present in the inner parts. The spatial scale is of 1.153 kpc/″.

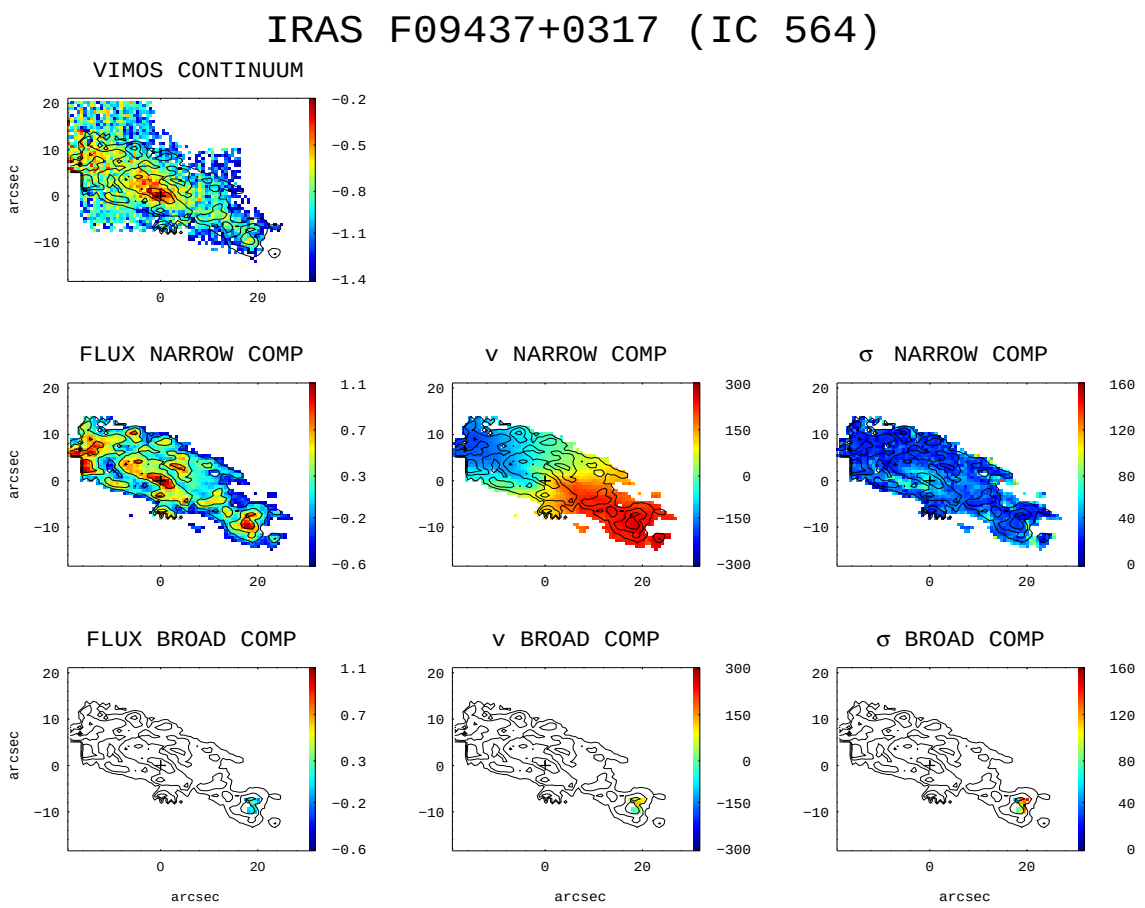

Figure A.20: (General comments about the panels as in Fig. A.1.) IRAS F09437+0317 (IC 564/IC 563): this system is formed by two galaxies (north: IC564/ south: IC563) with a nuclear separation of about 39 kpc. Three VIMOS pointings were carried out for observing this system. For the northern galaxy (IC 564), two pointings sample the northeast (NE) and the southwest (SW) parts of the galaxy (see Fig.1 Paper III); both of them have been used to derived the mean kinematic values (Table 3.3). These panels (i.e., $\sim 50'' \times 40''$) were generated by combining the NE and NW pointings. A faint broad component was found in correspondence of an offset Hα peak in the SW direction, possibly due to the presence of a star-forming region. The velocity field is regular, and the kinematic center seems to be in positional agreement with the continuum and Hα flux peaks. The spatial scale is 0.415 kpc/$''$.

IRAS F09437+0317 (IC 563)

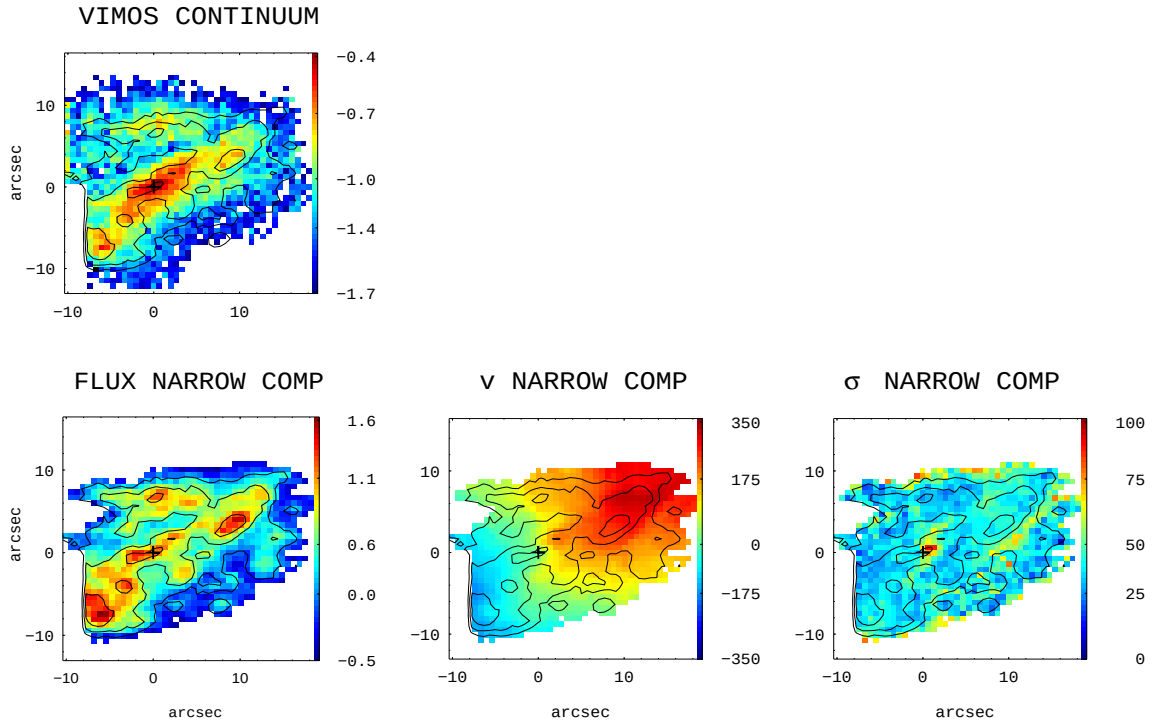

Figure A.21: (General comments about the panels as in Fig. A.1.) IRAS F09437+0317 (IC 563): this object shows a very regular velocity field and a centrally peaked velocity dispersion map. The VIMOS continuum image is considered the center of the image since the Hα peak is offset due to a knot of star formation and does not properly define the center. The spatial scale is 0.415 kpc/″.

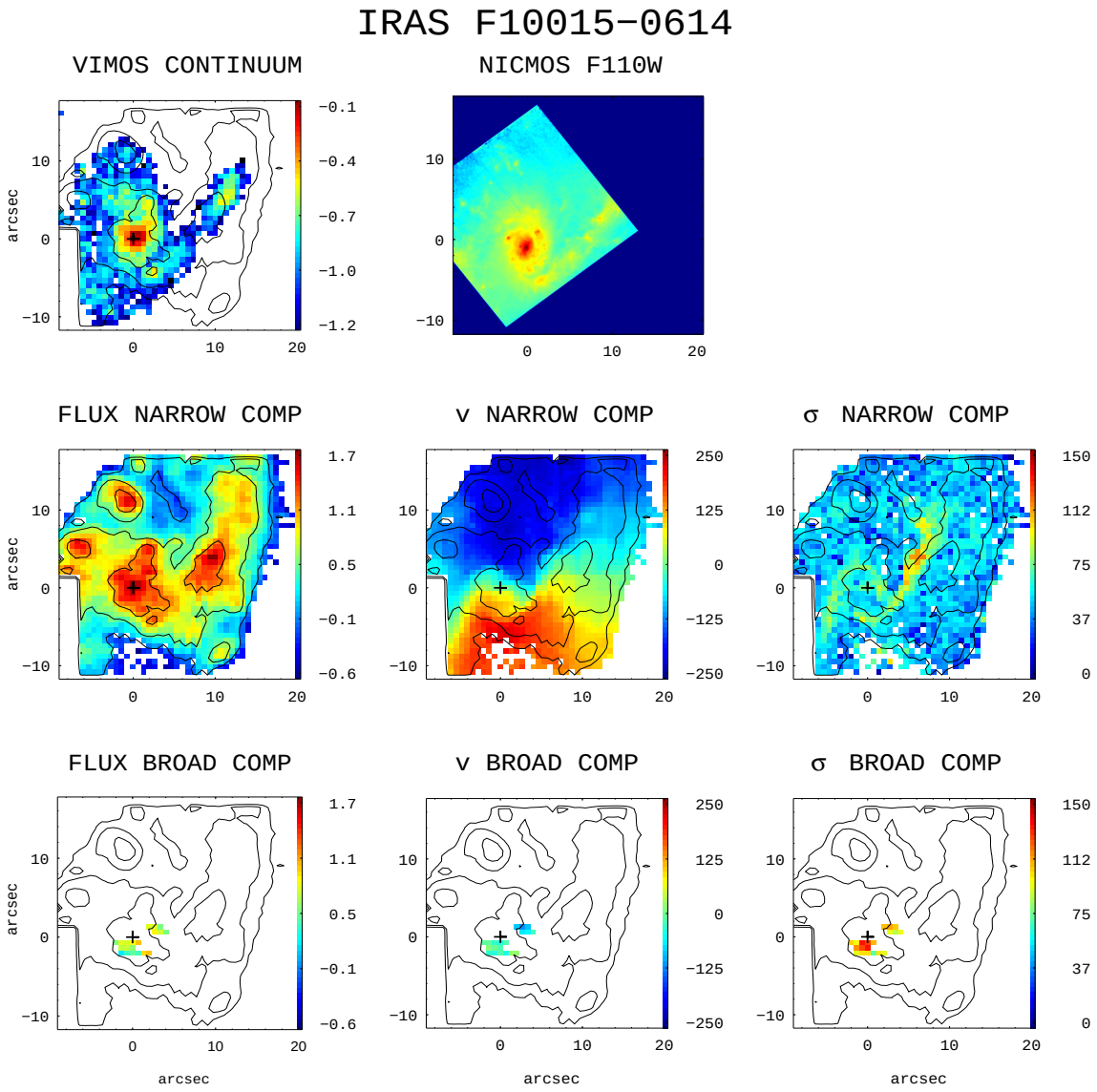

Figure A.22: (General comments about the panels as in Fig. A.1.) IRAS F10015-0614 (NGC 3110): this galaxy shows two well-defined spiral arms in NICMOS/HST image. The velocity field and the velocity dispersion maps reproduce the spiral structure of this galaxy. Broad-profile spectra are found in regions of low-Hα surface brightness round the nucleus.The spatial scale is 0.343 kpc/″.

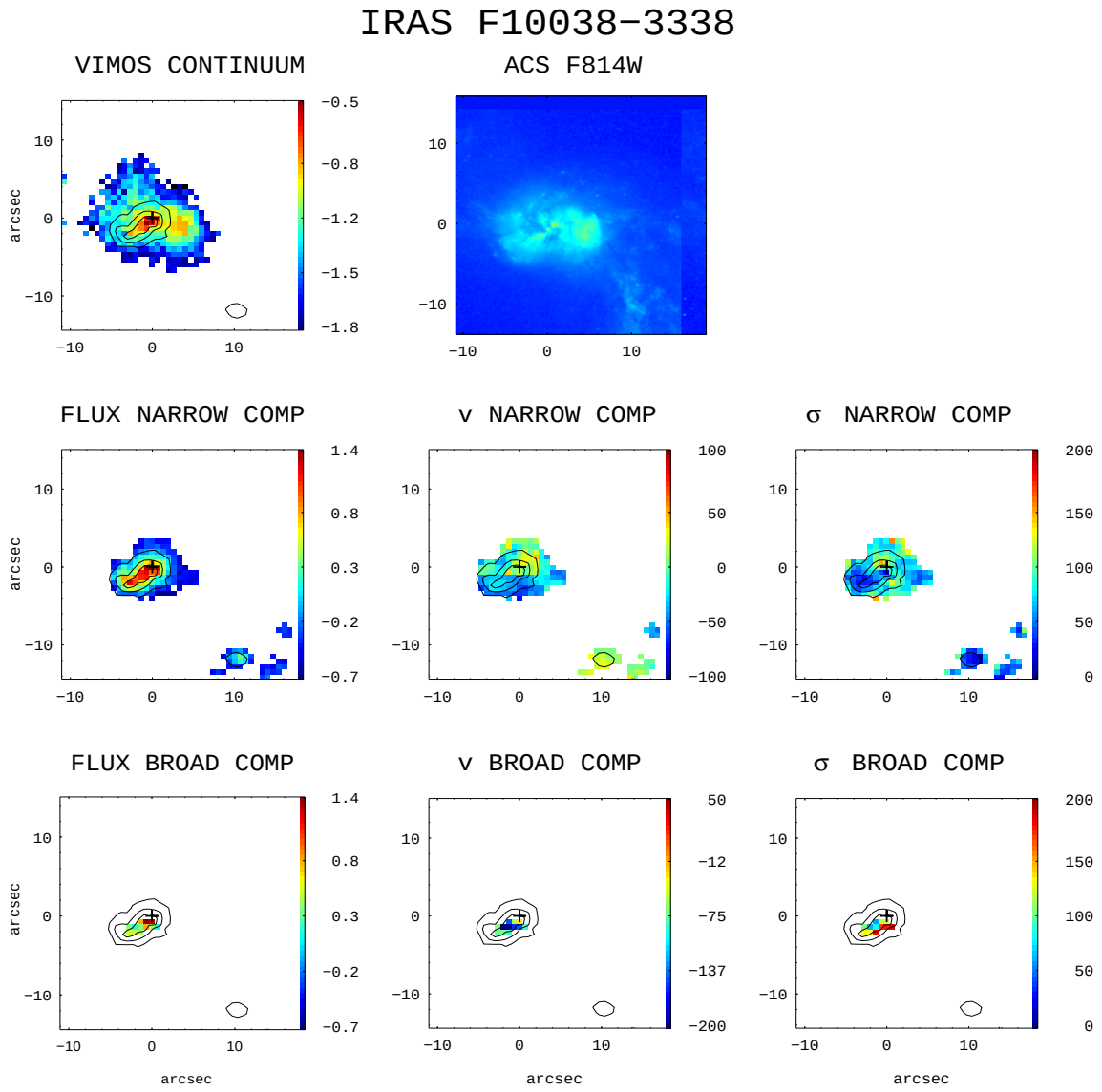

Figure A.23: (General comments about the panels as in Fig. A.1.) IRAS F10038-3338 (IC 2545): the VIMOS continuum image shows two nuclei separated by $\sim$ 3 kpc. The Hα peak corresponds to the eastern nucleus. The velocity field and velocity dispersion maps are quite disturbed. The broad component is blueshifted by 100 km s^{-1}. The scale is of 0.679 kpc/″.

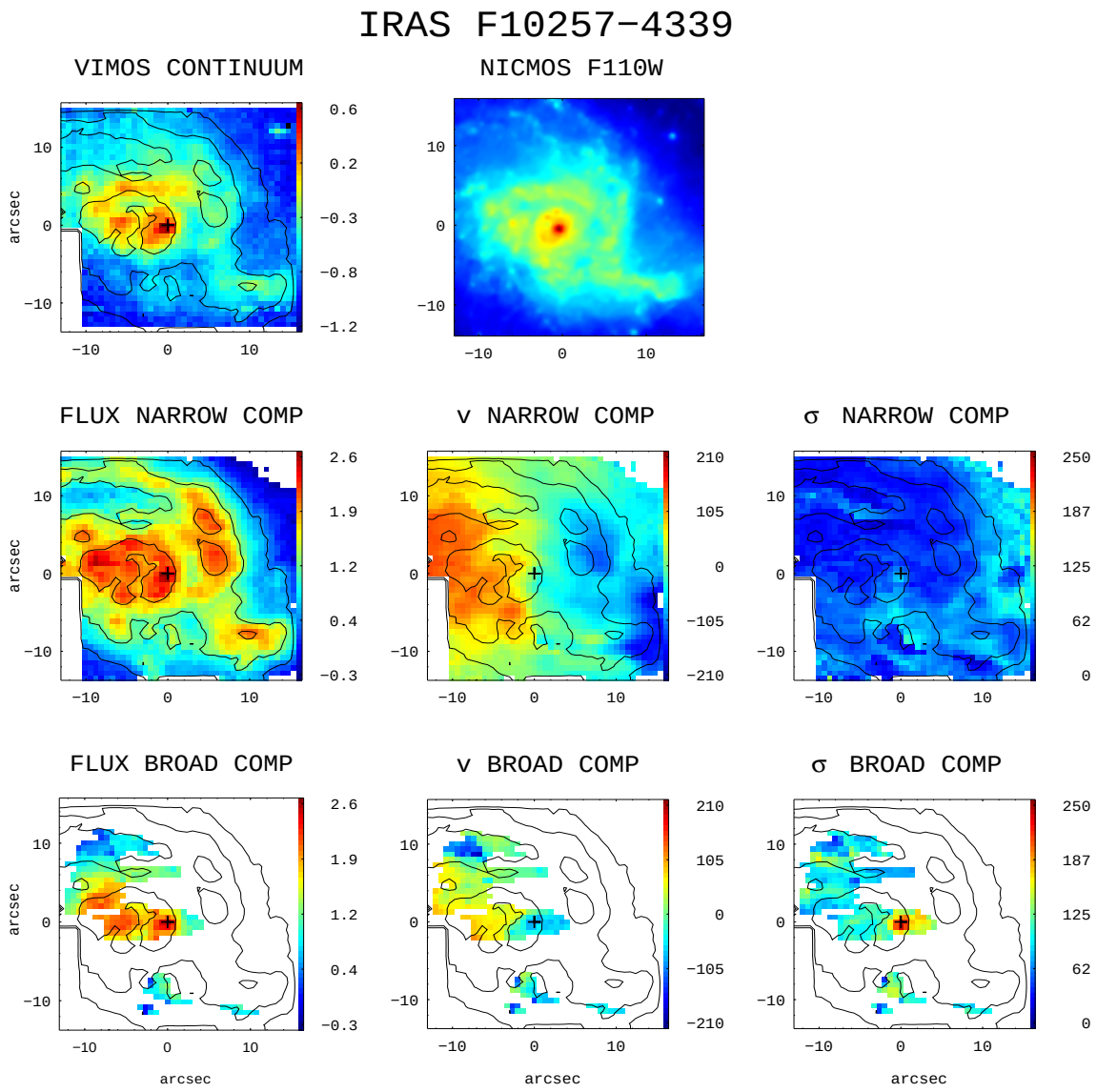

Figure A.24: (General comments about the panels as in Fig. A.1.) IRAS F10257-4338 (NGC 3256): this galaxy has a somewhat complex morphological structure. It shows a clumpy pattern in the Hα flux intensity map. The velocity field of the narrow component has the kinematic axes not well defined, though a rotation component with an amplitude of 170 km s^{-1} can be identified. The velocity dispersion map shows high values in regions where high ionized gas is found (see Monreal-Ibero et al. 2010). The broad component has been found in a quite large and irregular area. The scale is of 0.192 kpc/″.

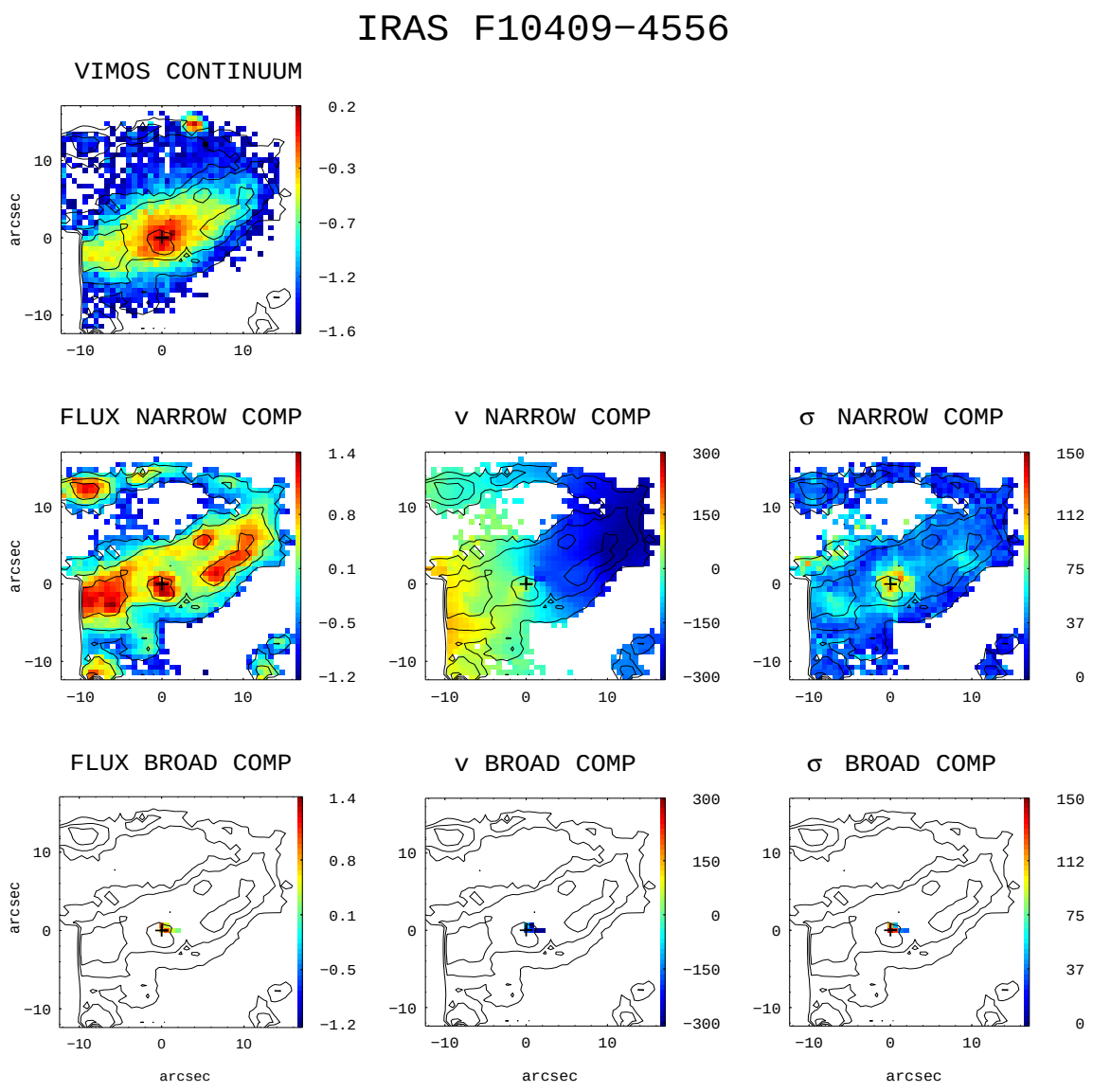

Figure A.25: (General comments about the panels as in Fig. A.1.) IRAS F10409-4556 (ESO 264-G036): this is an isolated barred spiral galaxy morphologically classified as type 0 (i.e., *isolated disk*). Its velocity field is very regular and the velocity dispersion map is centrally peaked. The spatial scale is 0.425 kpc/″.

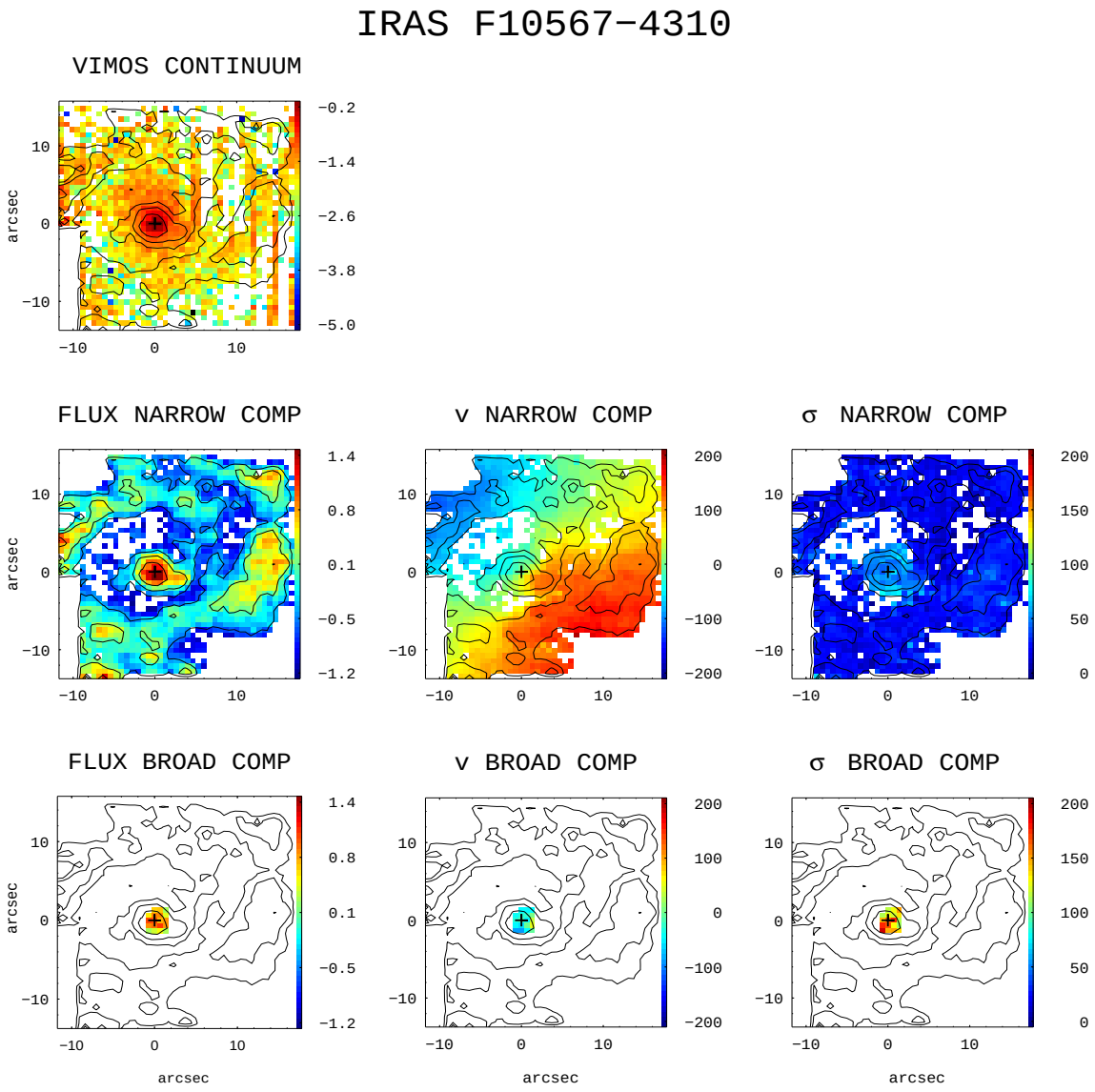

Figure A.26: (General comments about the panels as in Fig. A.1.) IRAS F10567-4310 (ESO 264-G057): the continuum image shows vertical patterns, which were not possible to remove during the reduction process (see Rodríguez-Zaurín et al. 2011). However, the Hα maps are not affected by this problem. The narrow component shows a very regular velocity field and a centrally peaked velocity dispersion map. This object has been analyzed in Bellocchi et al. (2012). The scale is 0.35 kpc/″.

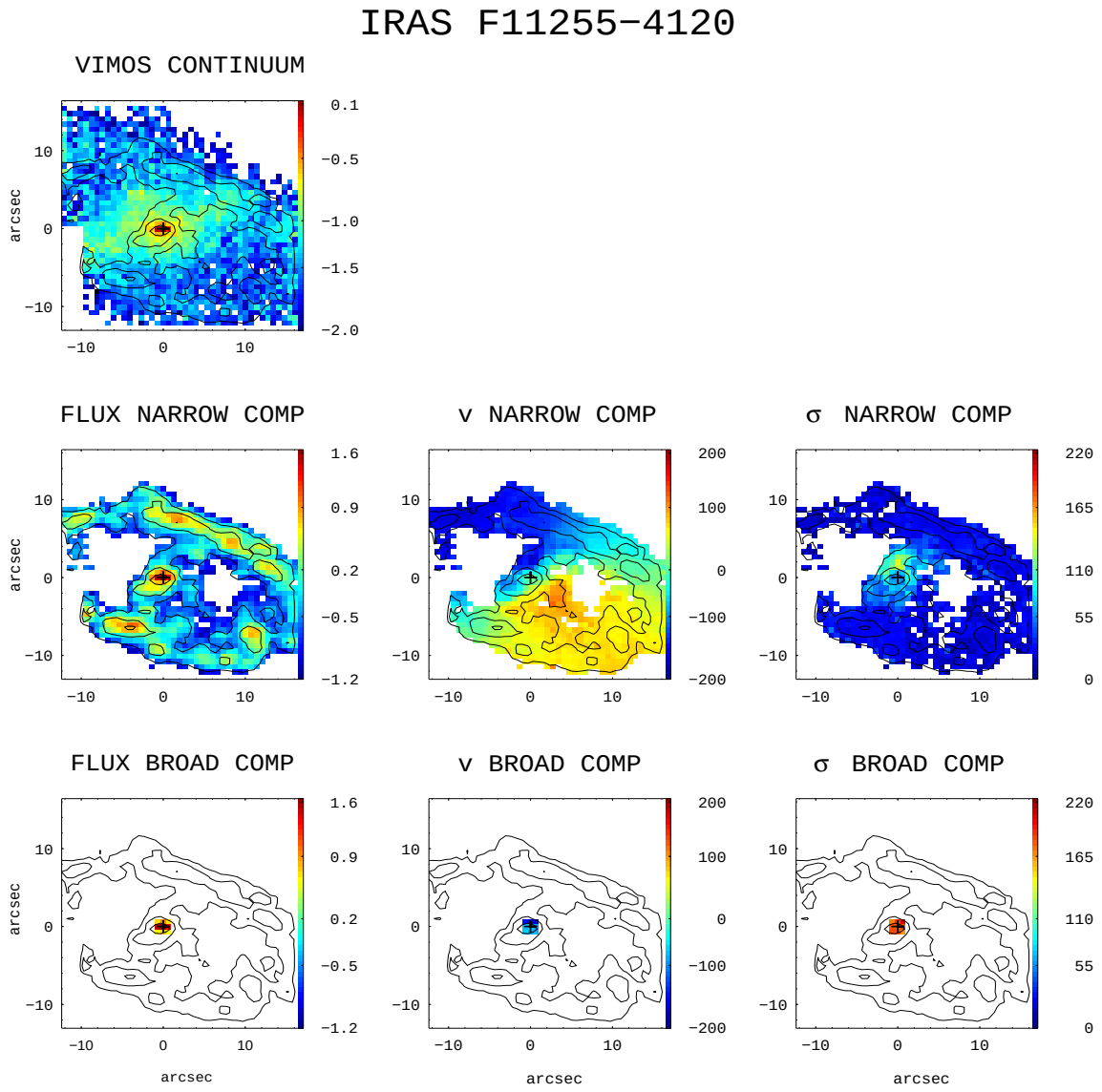

Figure A.27: (General comments about the panels as in Fig. A.1.) IRAS F11255-4120 (ESO 319-G022): this is a barred spiral with a circumnuclear ring structure that is at $\sim$ 4 kpc from the nuclear region in the Hα image but not observed in the continuum images. Interestingly, the orientation of the bar seen in continuum emission (PA $\sim$ 110°) is different from that of the ionized gas emission (PA $\sim$ 150°). The projected orientation of the rotation axis (minor kinematic axis) seems to be different by about 30° from that of the minor photometric axis (and the bar in the Hα flux intensity map) but is well aligned with the bar in the continuum. The kinematic center closely agrees with that of the Hα flux and the continuum peaks. The velocity field is very regular and the velocity dispersion map has an almost centrally peaked structure with a local maximum of 120 km s^{-1} in the bar structure. This object has been previously studied in Bellocchi et al. (2012). The scale is of 0.333 kpc/″.

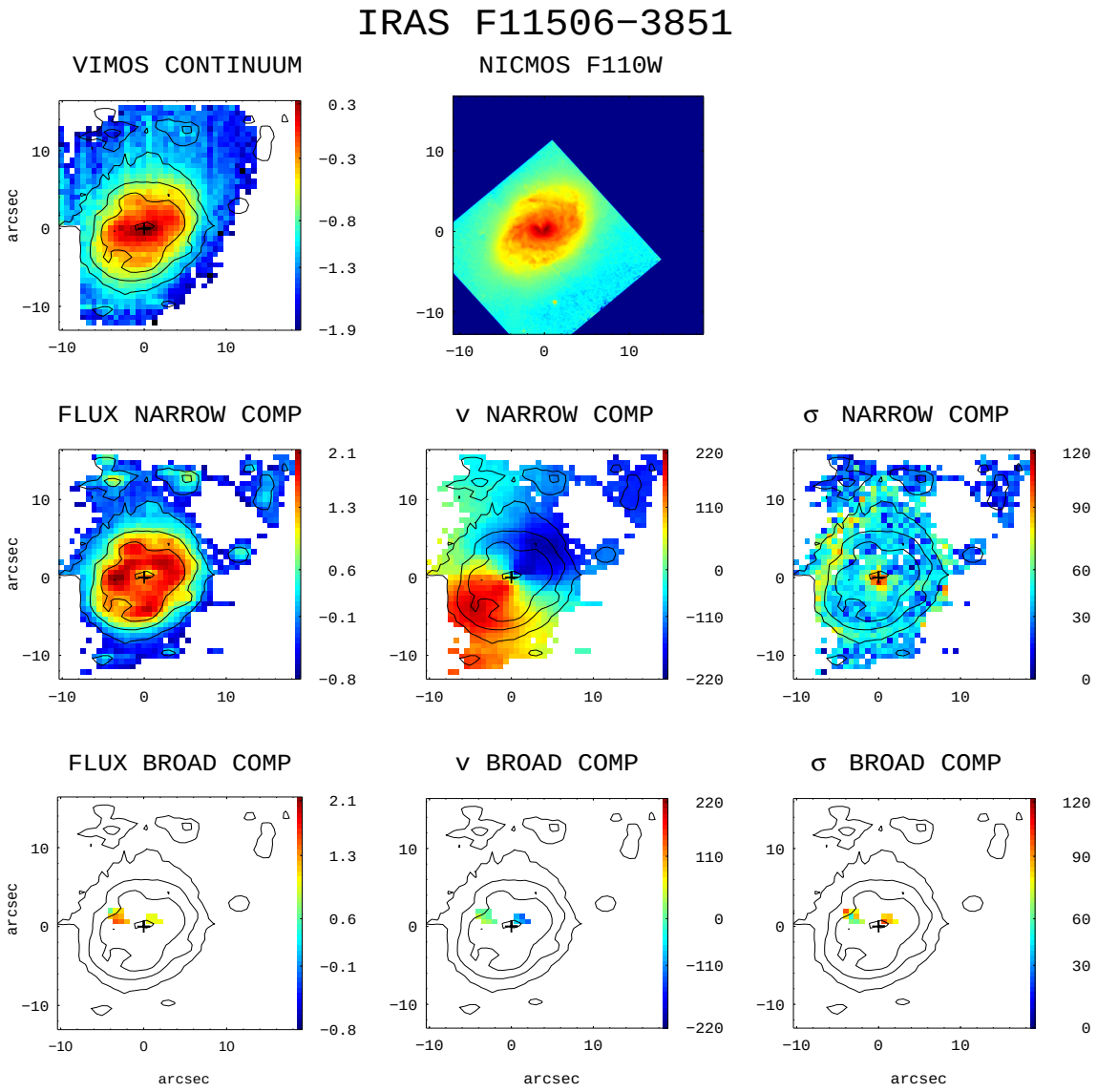

Figure A.28: (General comments about the panels as in Fig. A.1.) IRAS F11506-3851 (ESO 320-G030): a circumnuclear ring structure is detected in the Hα image. The velocity field is extremely regular and the velocity dispersion map is centrally peaked (i.e., σ_c = 81 km s^{-1}) with high values (i.e., $\sim$ 60 km s^{-1}) outwards the ring structure. The spatial scale is of 0.221 kpc/″.

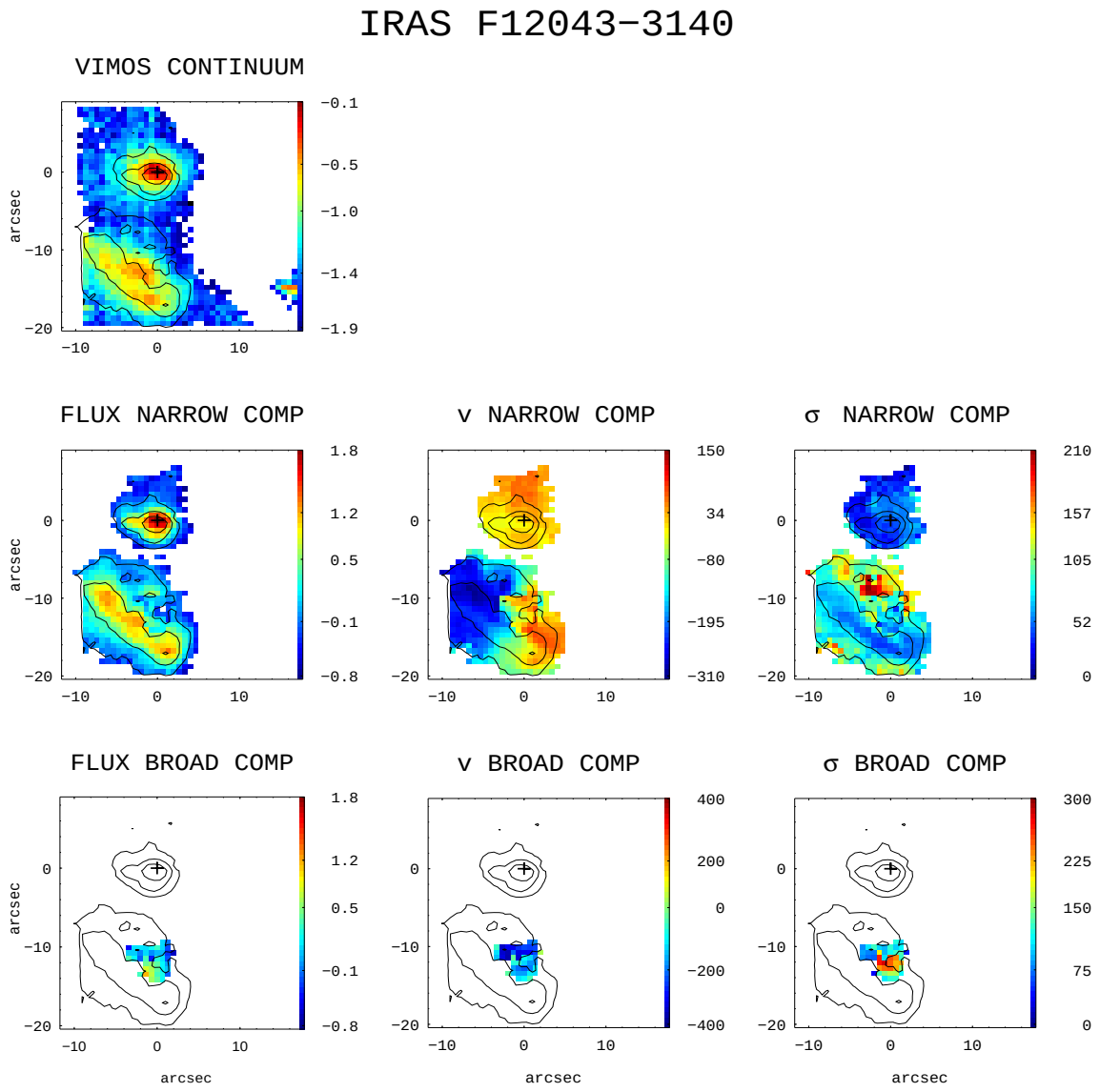

Figure A.29: (General comments about the panels as in Fig. A.1.) IRAS F12043-3140 (ESO 440-IG058): this system consists of two galaxies with a nuclear separation of $\sim$ 6 kpc. The northern galaxy is compact, while the southern source presents several knots in the Hα map. The velocity field of the southern galaxy has two relatively well-defined approaching and receding parts, with the kinematic and photometric axes in relatively good agreement. Its velocity dispersion map reaches the highest values (i.e., $\sigma \sim 250$ km s^{-1}) in the northern part, in correspondence of a local maximum of the Hα intensity map. Around that region, a secondary broad component has been found in some spectra . The stellar distribution (i.e., continuum map) of the northern galaxy suggests that it is almost face-on: this could possibly explain the derived relatively low velocity shear (i.e., $\sim$ 42 km s^{-1}). Its velocity field shows a somewhat irregular pattern. The scale is of 0.468 kpc/″.

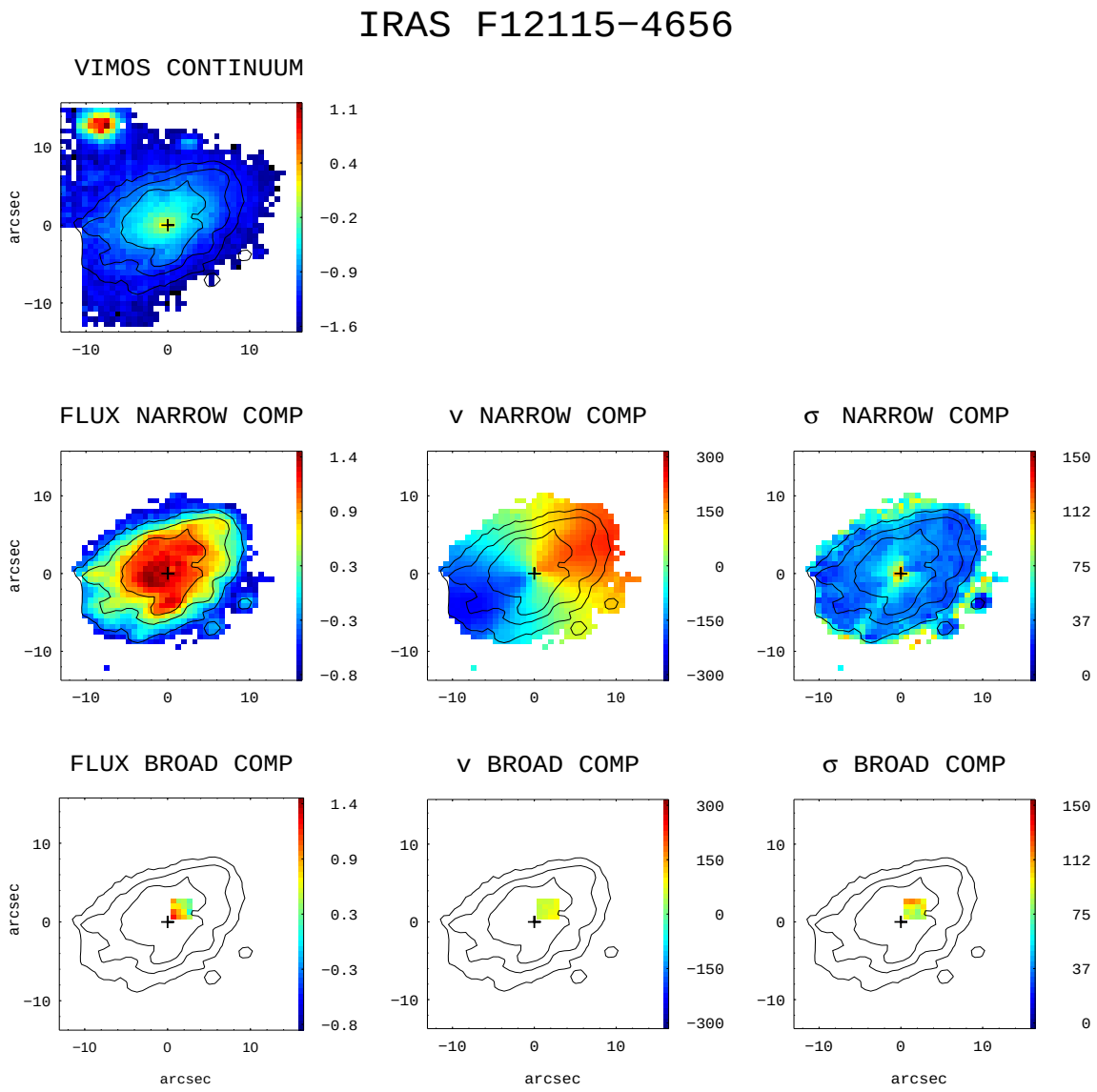

Figure A.30: (General comments about the panels as in Fig. A.1.) IRAS F12115-4656 (ESO 267-G030): the Hα image shows a peak displaced by 0.8 kpc in the southwest direction with respect to the nucleus (continuum maximum). The kinematic center is in positional agreement with the nucleus. The velocity field and velocity dispersion map are those typical of a rotating *disk*-like object. At about $\sim$ 3 kpc northwest from the nucleus, the spectra show the presence of two kinematically distinct components. The scale is of 0.375 kpc/″.

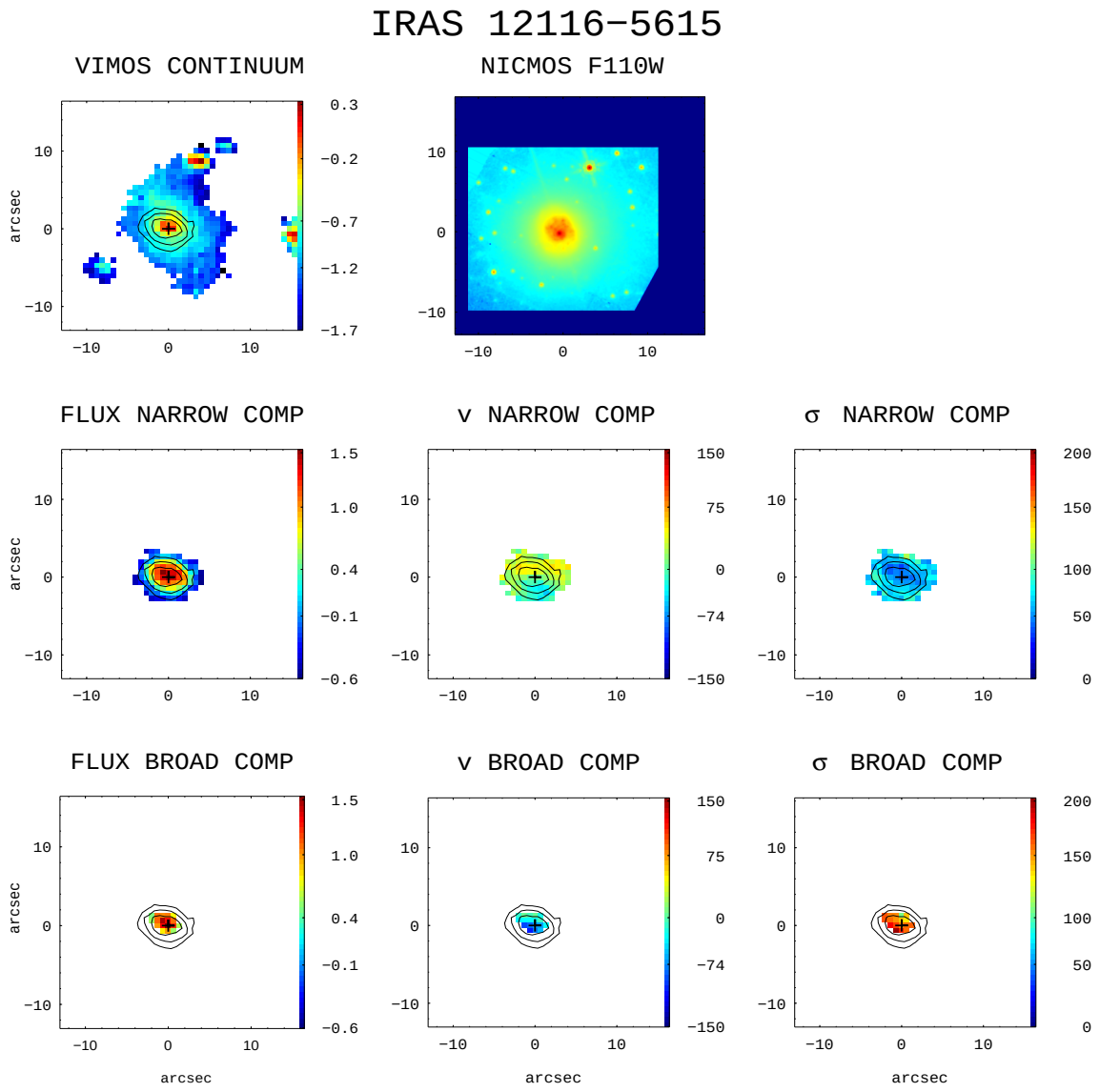

Figure A.31: (General comments about the panels as in Fig. A.1.) IRAS 12116-5615: this is one of the few objects for which the morphological classification is uncertain (class 2 or 0). It shows a very compact Hα emission. The Hα velocity field has a typical rotation pattern, but the velocity dispersion map is not centrally peaked. The latter shows higher values in the outer parts, which also have high excitation and low-Hα surface brightness (see Monreal-Ibero et al. 2010). The scale is of 0.545 kpc/″.

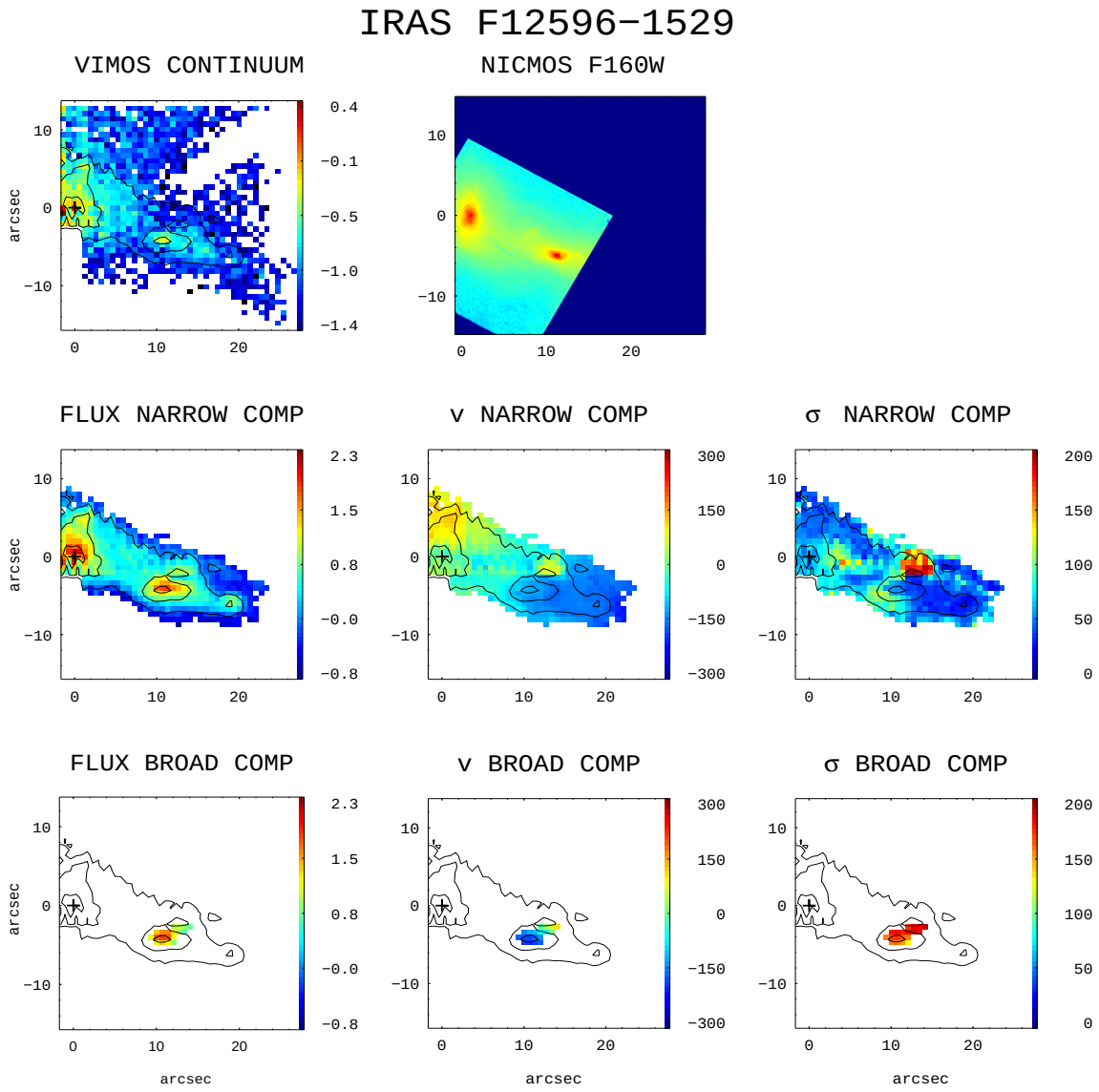

Figure A.32: (General comments about the panels as in Fig. A.1.) IRAS F12596-1529 (MGC-02-33-098): this system is interacting with MCG-02-33-099, at $\sim$ 37 kpc in the southeast direction. The HST image clearly shows two distinct galaxies in interaction, still visible in the VIMOS Hα flux intensity map, where the nuclei are separated by $\sim$ 5 kpc. For this system it was not possible to reliably separate the contribution of each object. The two galaxies have been considered as a whole systems, deriving the mean kinematic values reported in Table 3.3. However, the velocity field shows a quite regular pattern. The velocity dispersion map does not have a well-defined structure with a maximum of $\sim$ 200 km s^{-1} in the northern part of the western galaxy: in this region low-Hα surface brightness spectra are well fitted using one component and for this reason show a broader profile. However, no kinematic classification can be inferred from the whole system. The spatial scale is of 0.324 kpc/″.

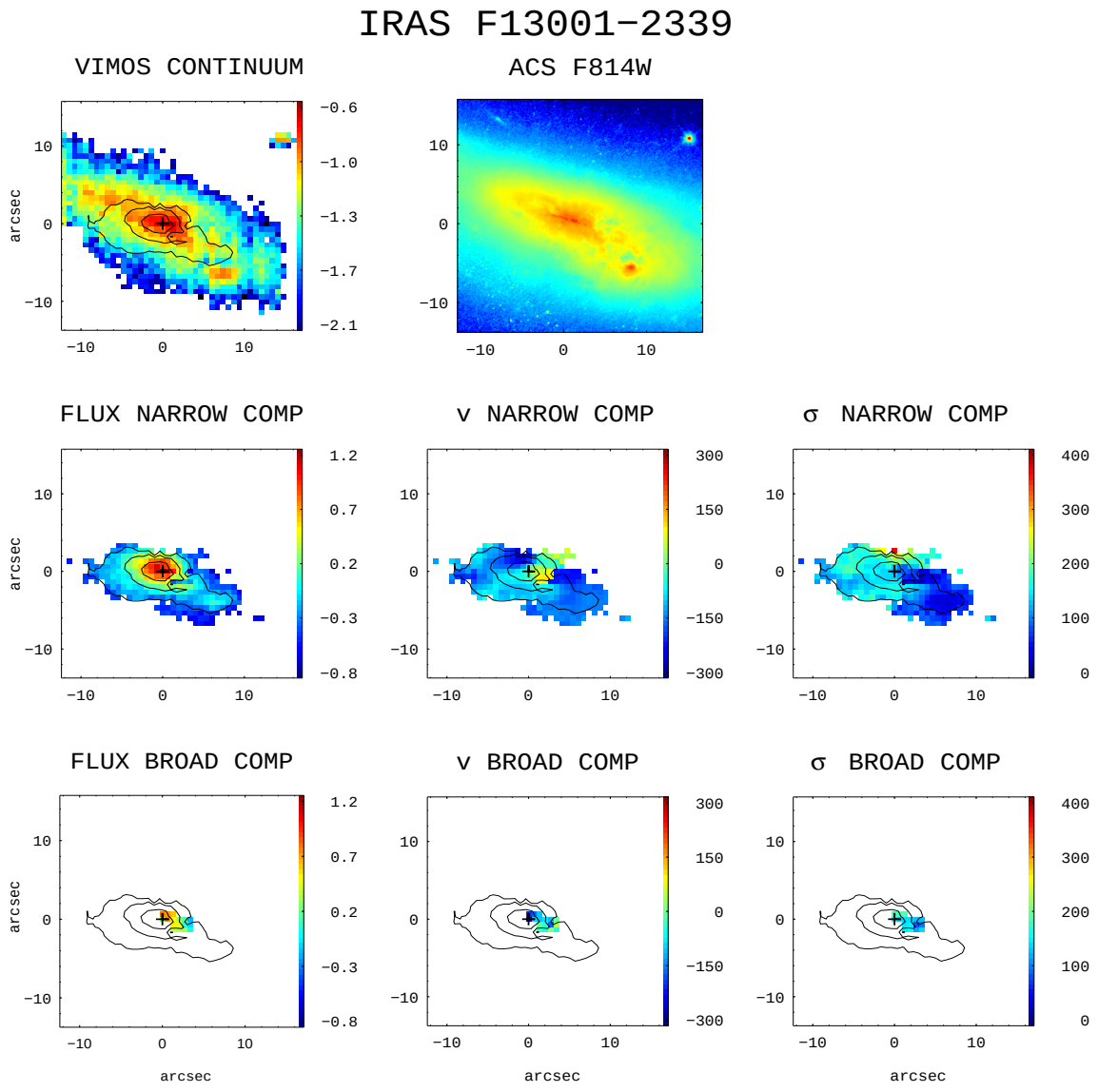

Figure A.33: (General comments about the panels as in Fig. A.1.) IRAS F13001-2339 (ESO 507-G070): the velocity field and velocity dispersion map have an irregular pattern. Some of the spectra in the northern region show a broad profile and relatively high excitation (see Monreal-Ibero et al. 2010). Its scale is of 0.439 kpc/″.

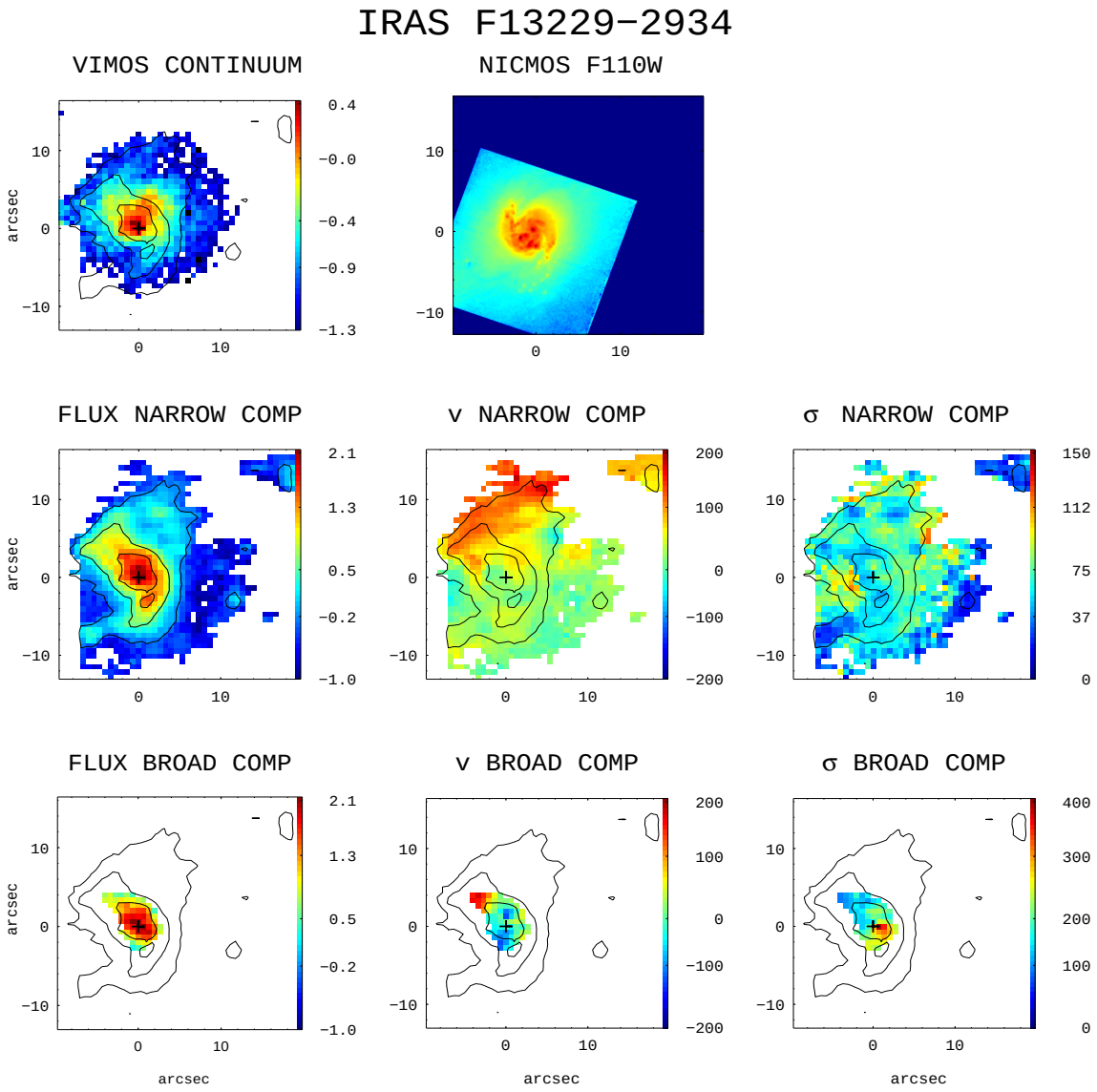

Figure A.34: (General comments about the panels as in Fig. A.1.) IRAS F13229-2934 (NGC 5135): the morphology of the ionized gas emission is substantially different from that of the continuum. Moreover, the photometric major axis of the continuum image seems to be perpendicular with respect to that of the Hα flux intensity in the inner regions. The spatial scale is 0.28 kpc/″.

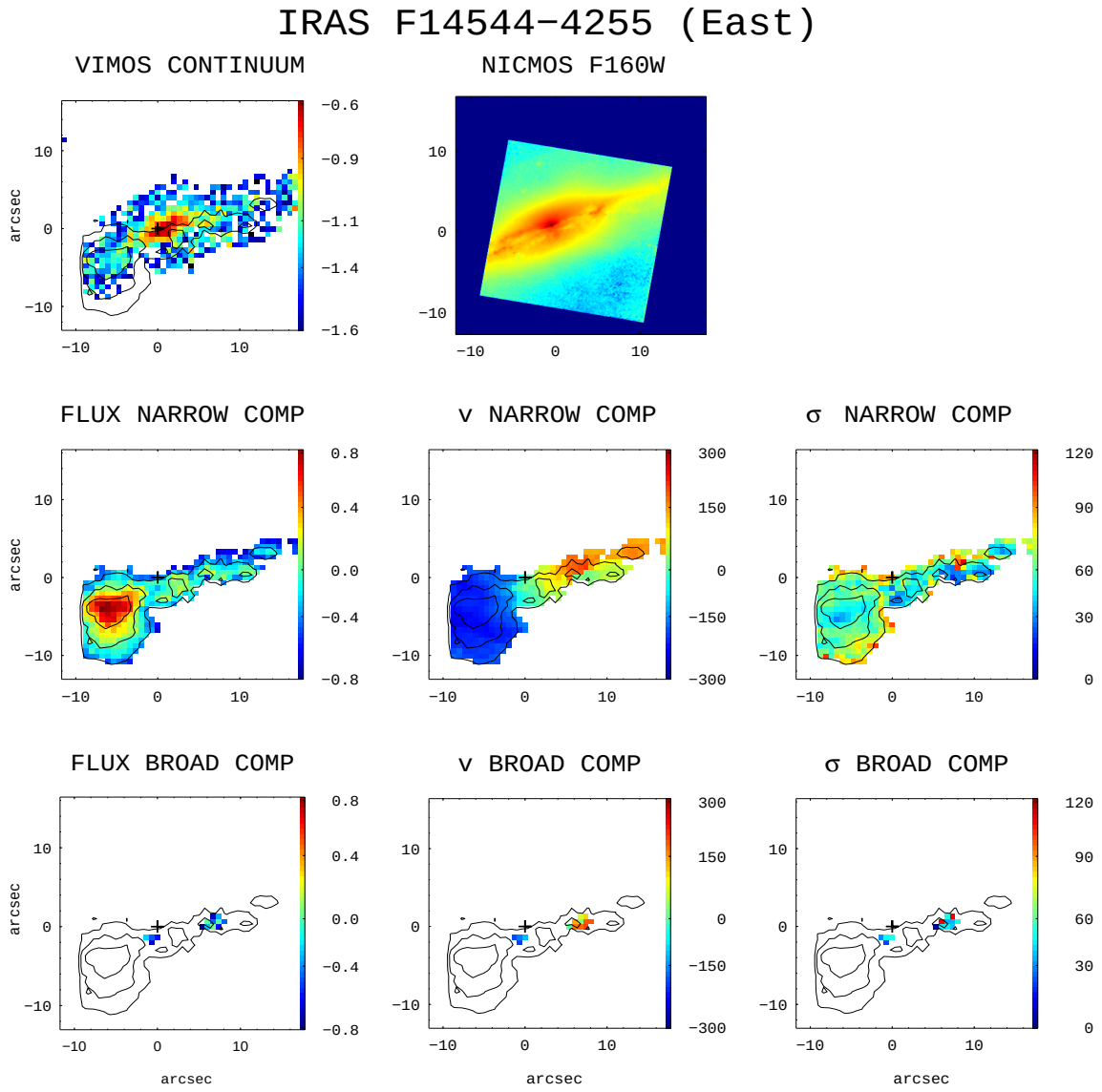

Figure A.35: (General comments about the panels as in Fig. A.1.) IRAS F14544-4255 (IC 4518): this system is formed by two galaxies with a nuclear separation $\sim$ 12 kpc, which were observed separately using two VIMOS pointings. The present panels correspond to the eastern source. This galaxy has a faint tail extended towards the northwest, as seen in the DSS image (see Paper III). The Hα image reveals a very strong knot of star formation towards the southeast of the nucleus ($\sim$ 2.5 kpc): for this reason, the VIMOS continuum peak is used to identify the center (0,0) of the images. The velocity field is rather regular, although some deviations of pure rotation pattern are seen towards the west, probably due to the projection of star-forming knots with peculiar velocity. Its velocity dispersion map has a relatively constant value of $\sigma_{mean} \sim 60$ km s^{-1} in almost the whole FoV. The broad component found in a few spectra has velocity dispersion values similar to those of the narrow component. The spatial scale is of 0.32 kpc/″.

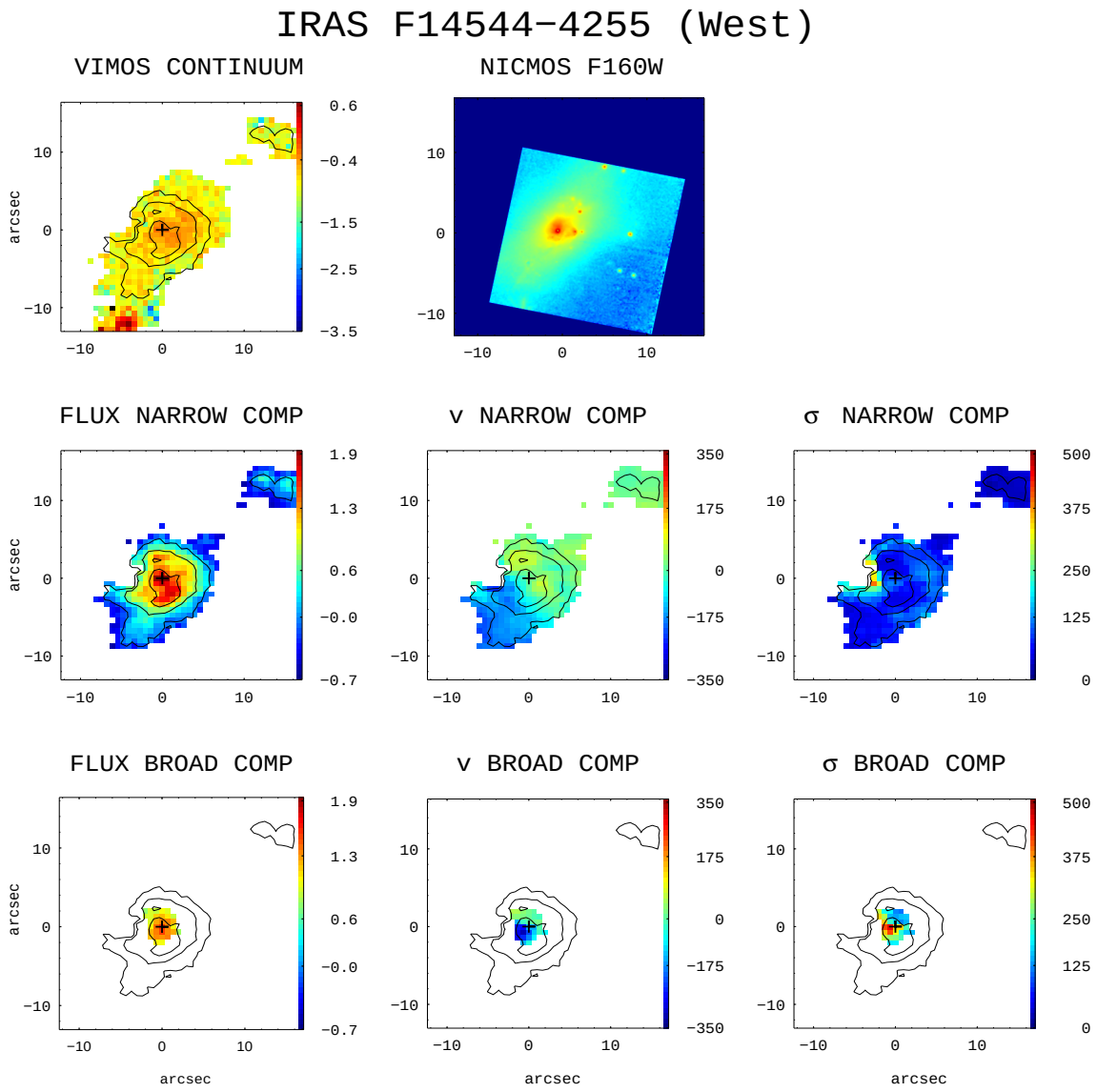

Figure A.36: (General comments about the panels as in Fig. A.1.) IRAS F14544-4255 (IC 4518): this is the western source of the system. It is more compact than the eastern one, although some extended emission is also observed towards the northwest likely associated with two star-forming knots. The velocity field has some irregularities (i.e., two maxima in the redshifted part), although a weak rotation pattern is visible. The velocity dispersion map shows a maximum of 300 km s^{-1} on the eastern part of this galaxy at 0.9 kpc from the Hα flux peak. The high values of the velocity dispersion of the narrow component correspond to low-Hα surface brightness spectra. The spectra showing a secondary broad component in this object are quite complex. The spatial scale is 0.32 kpc/″.

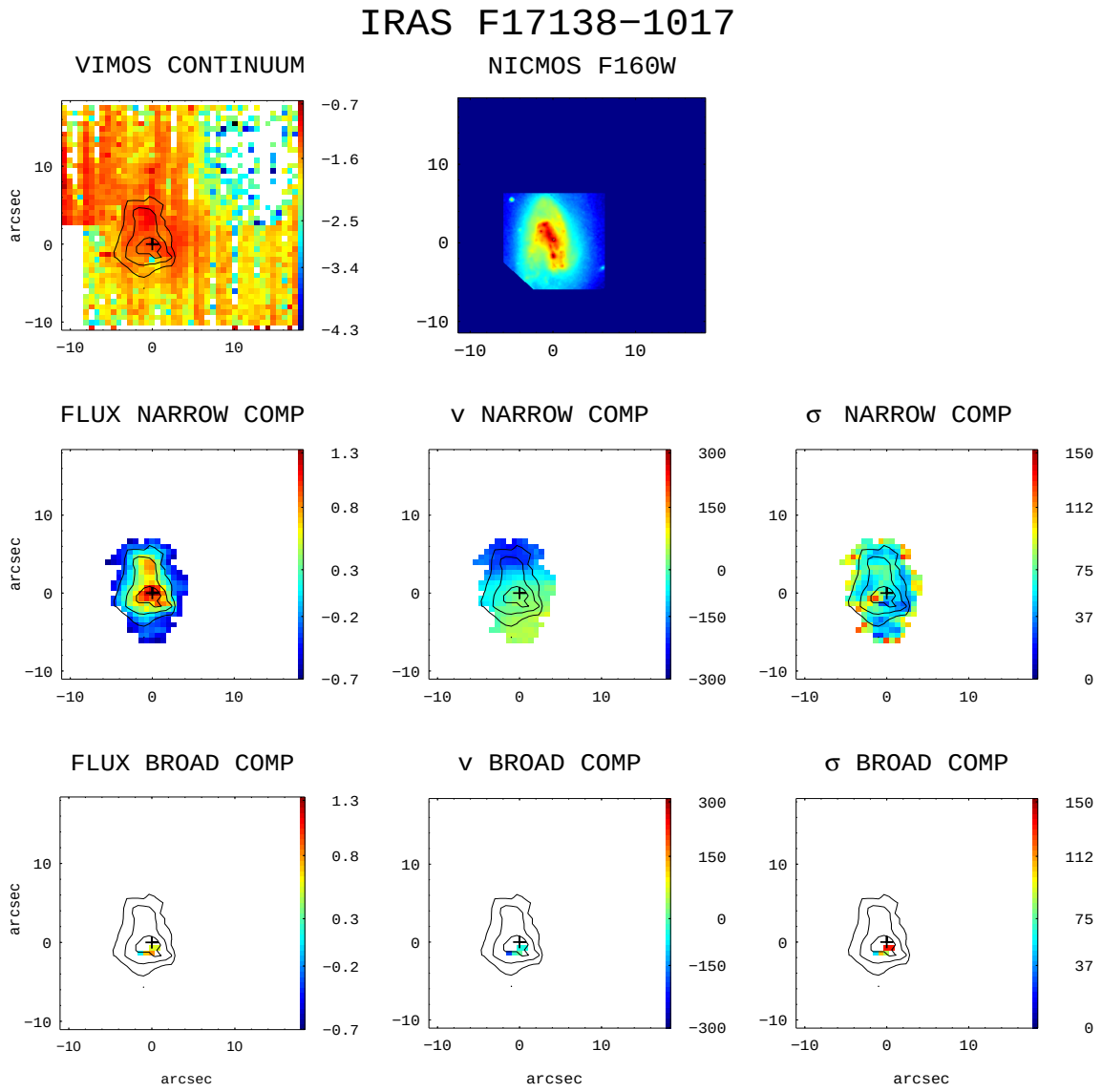

Figure A.37: (General comments about the panels as in Fig. A.1.) IRAS F17138-1017: the velocity field is regular, while the velocity dispersion map has no defined pattern. The continuum image shows vertical patterns that could not be removed during the reduction process (see Rodríguez-Zaurín et al. 2011). However, the Hα maps (flux intensity and velocity field) are not affected by this problem. The spatial scale is 0.352 kpc/″.

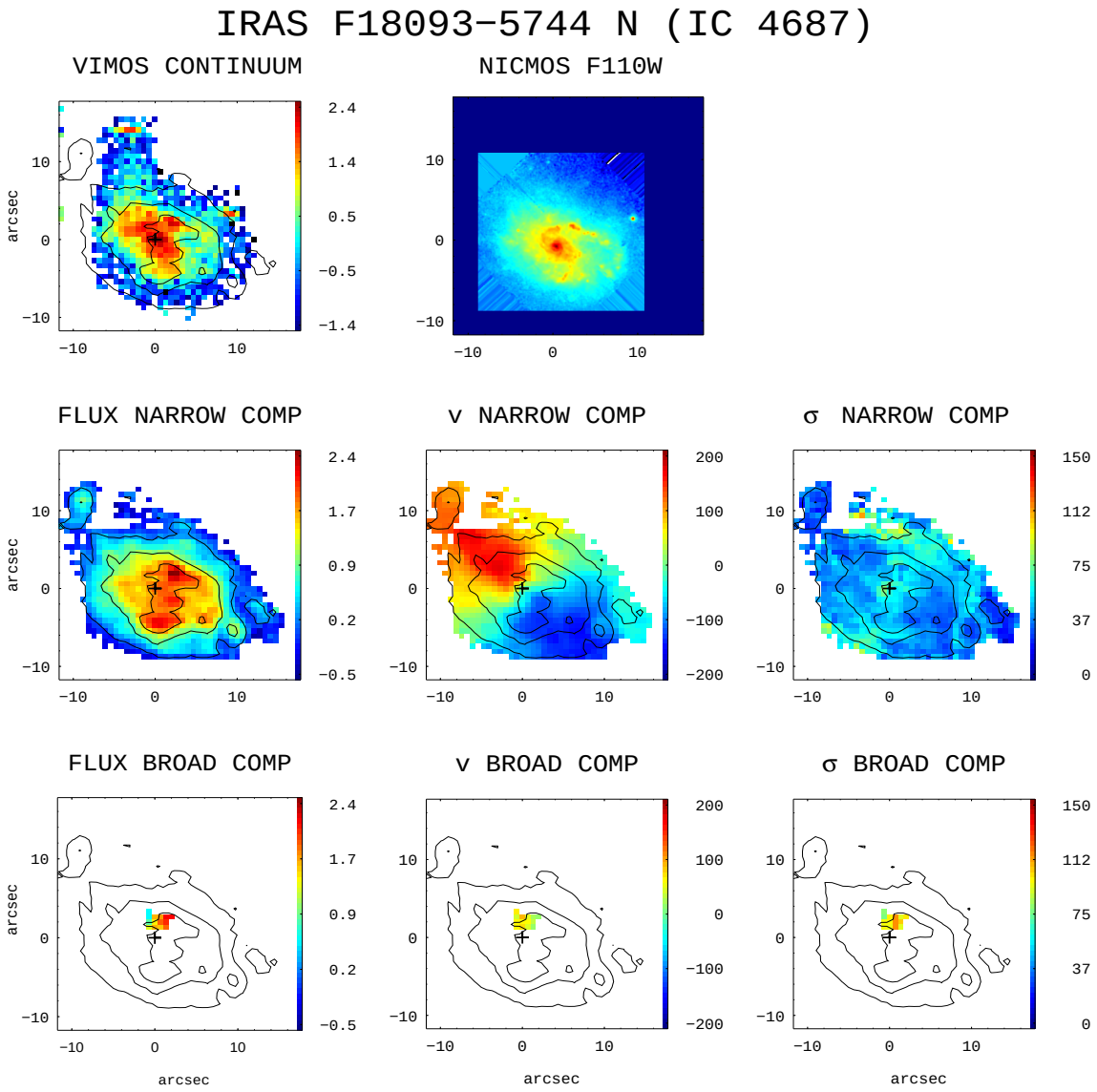

Figure A.38: (General comments about the panels as in Fig. A.1.) IRAS F18093-5744: the whole system consists of three galaxies in interaction, which have been observed separately. The nuclear separations between the northern (IC 4687) and the central galaxy (IC 4686) and between the central and the southern galaxy (IC 4689) are $\sim$ 10 kpc and $\sim$ 20 kpc, respectively. The HST (F110W) image shows a spiral-like morphology for IC 4687, with several knots and concentrations in the nuclear region. IC 4687 shows a velocity field dominated by rotation, with the kinematic center well defined and coincident with the nucleus (continuum maximum). On the other hand, the velocity dispersion map shows an almost centrally peaked map, with higher values in the outer parts of the galaxy, corresponding to ionized regions (see Monreal-Ibero et al. 2010). The scale is 0.353 kpc/″.

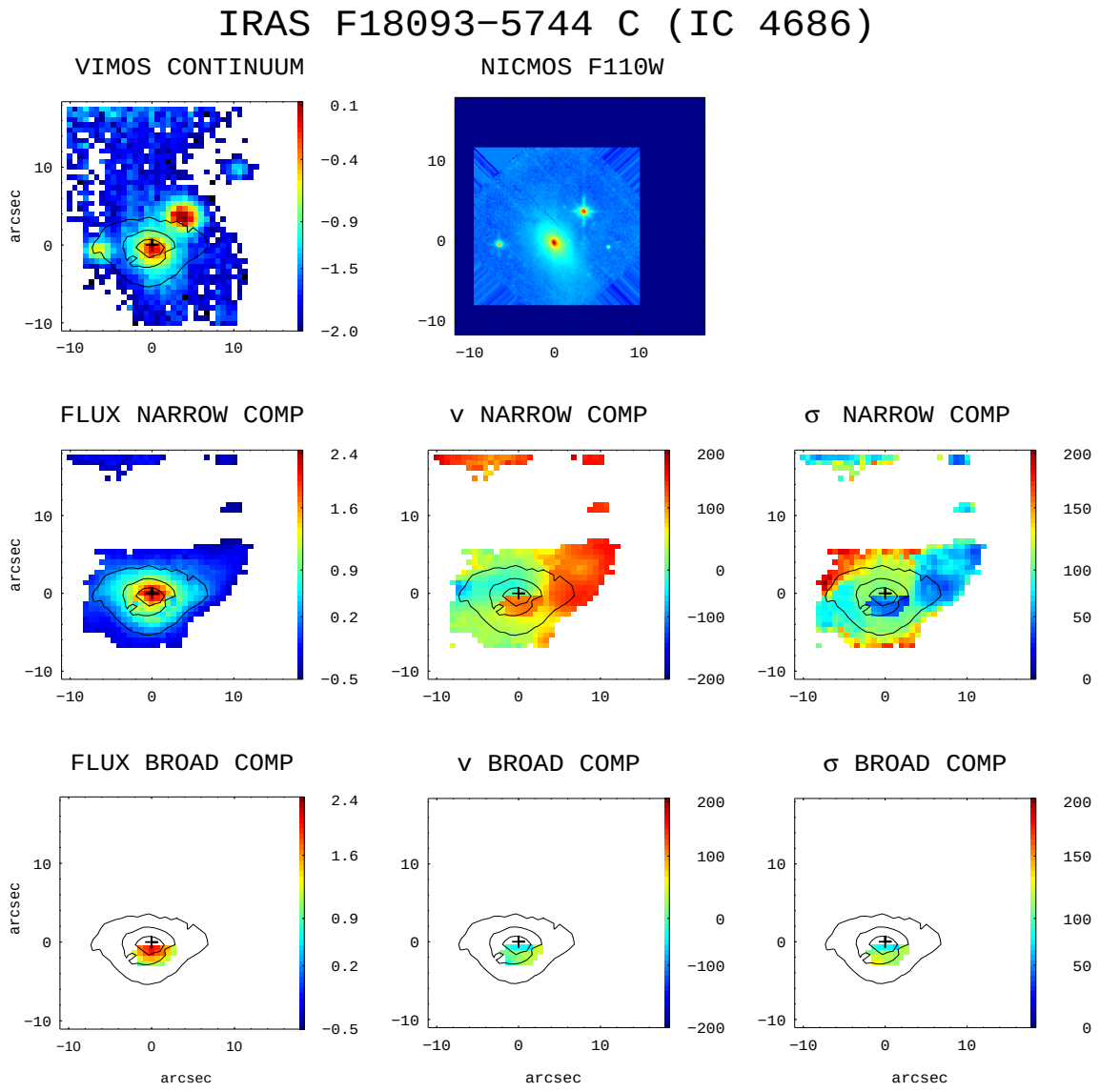

Figure A.39: (General comments about the panels as in Fig. A.1.) IRAS F18093-5744 (C): the Hα emission from the source is highly concentrated in the nuclear region. Ionized gas emission is also observed extending towards the northwest of the nuclear region, probably as part of a tidal tail linking this galaxy with IC 4687. The VIMOS continuum emission is strongly contaminated by a star located in the northwest part with respect to the galaxy. The northern/western part of the velocity field is dominated by the kinematics of the tidal tail, which shows redshifted velocities and very low velocity dispersion: the blue part of the velocity field is not well defined, even excluding the region south of the nucleus. Due to the presence of the tidal tail, the interpretation of the broad component in the innermost region is uncertain (i.e., it may correspond to the main systemic component because it is the narrow one associated with the tidal tail). The scale is 0.353 kpc/″.

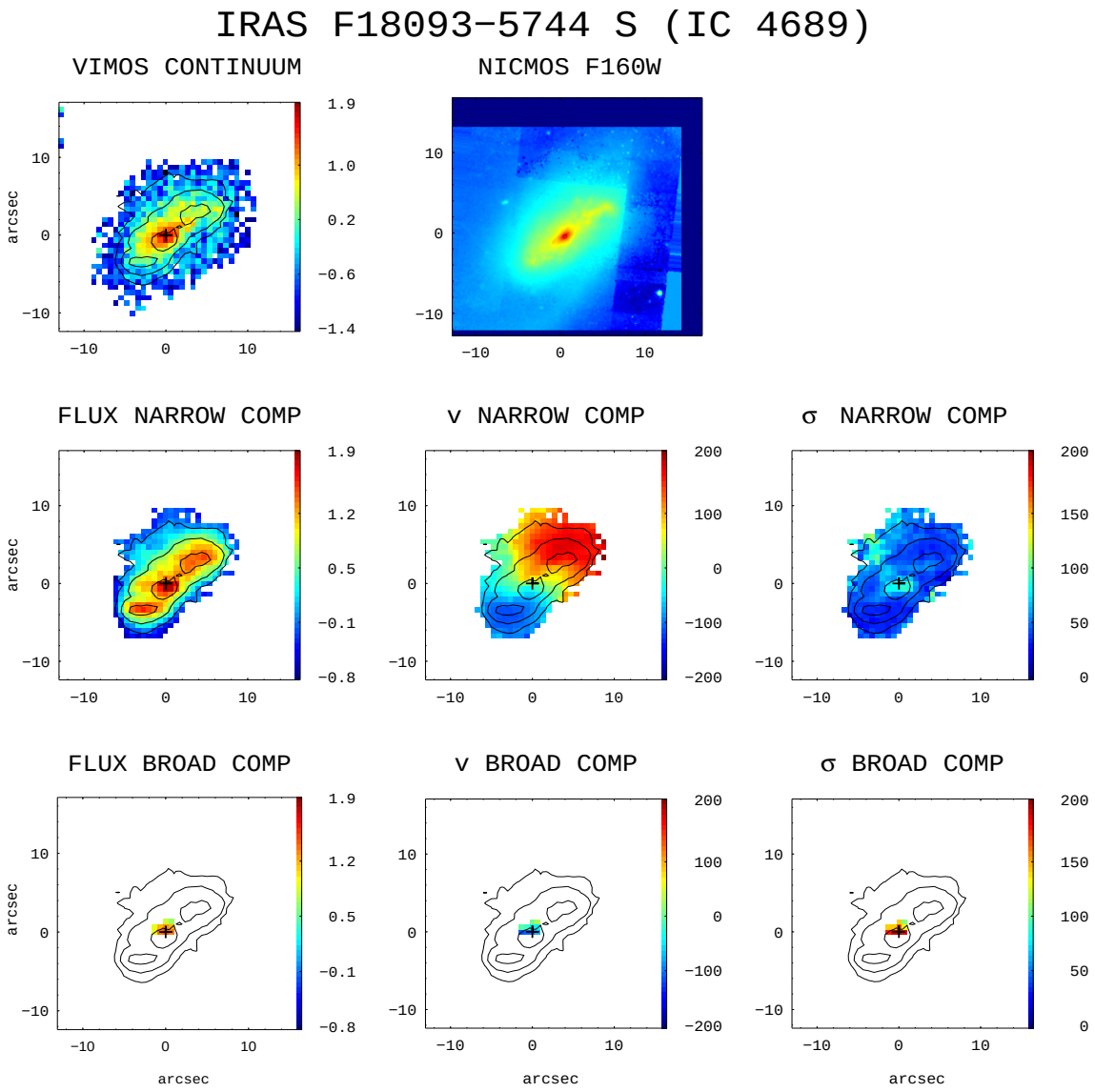

Figure A.40: (General comments about the panels as in Fig. A.1.) IRAS F18093-5744 (S) (IC 4689): this galaxy has a spiral morphology in the NICMOS/HST image, without clear evidence of strong interaction with the other galaxies of the system. The kinematic center seems to be coincident with the VIMOS continuum peak: the velocity field shows a mostly regular pattern, typical of a rotation-dominated *disk*-like object. Its velocity dispersion map shows a centrally peaked structure. It also shows regions in the northern part with relatively large velocity dispersion ($\sim$ 100 km s^{-1}). A small area ($\sim$ 0.6 kpc^2) at the center shows the presence of a broad component, blueshifted by $\sim$ 85 km s^{-1}. The scale is 0.353 kpc/″.

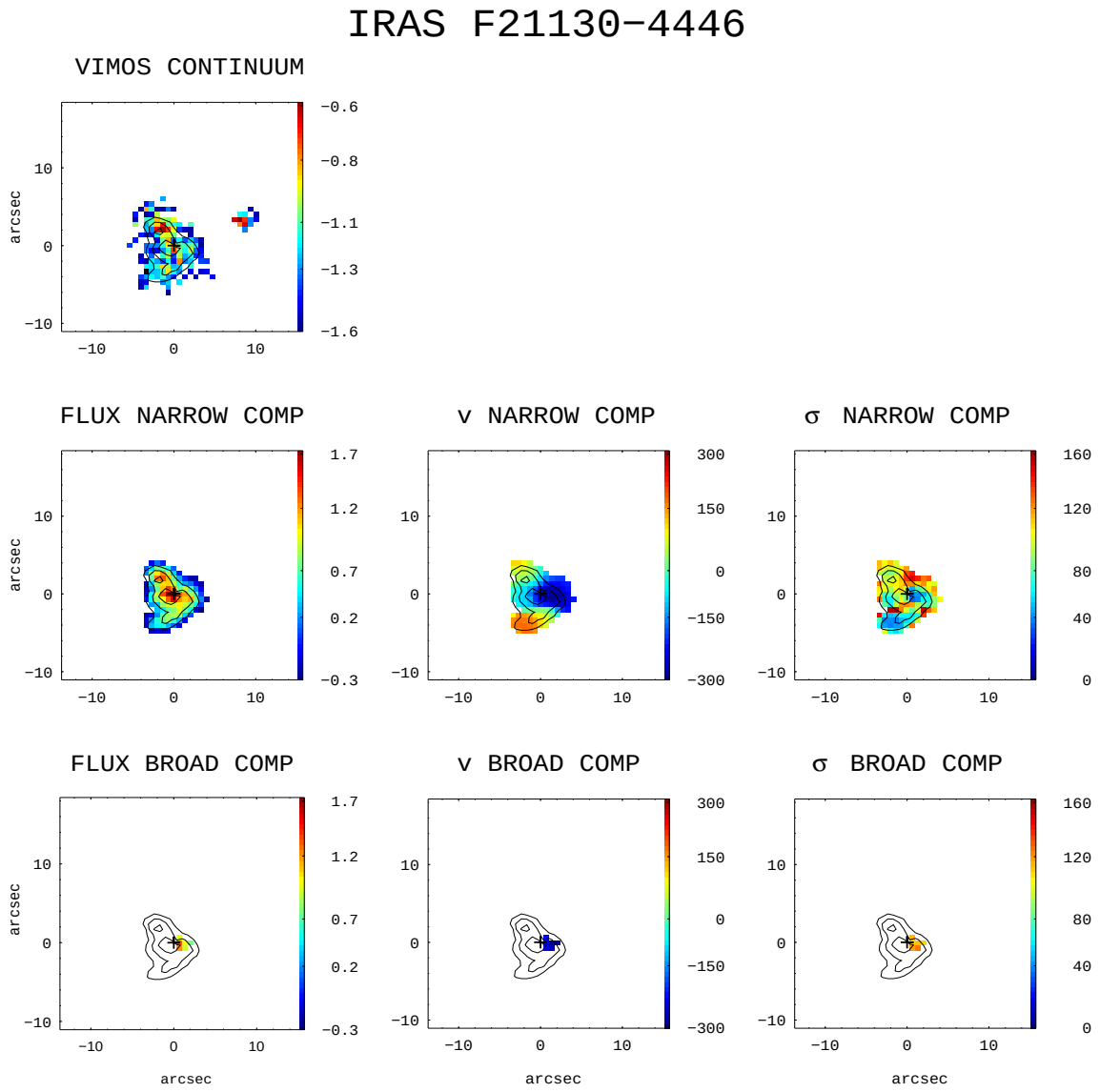

Figure A.41: (General comments about the panels as in Fig. A.1.) IRAS F21130-4446: this system has a double nucleus with a separation of 5.4 kpc (i.e., Dasyra et al. 2006b). The peak of the continuum emission coincides with the location of the northern (weaker) Hα condensation. The velocity field has a quite complex structure. The velocity dispersion map shows a distorted and irregular structure. The scale is of 1.72 kpc/″.

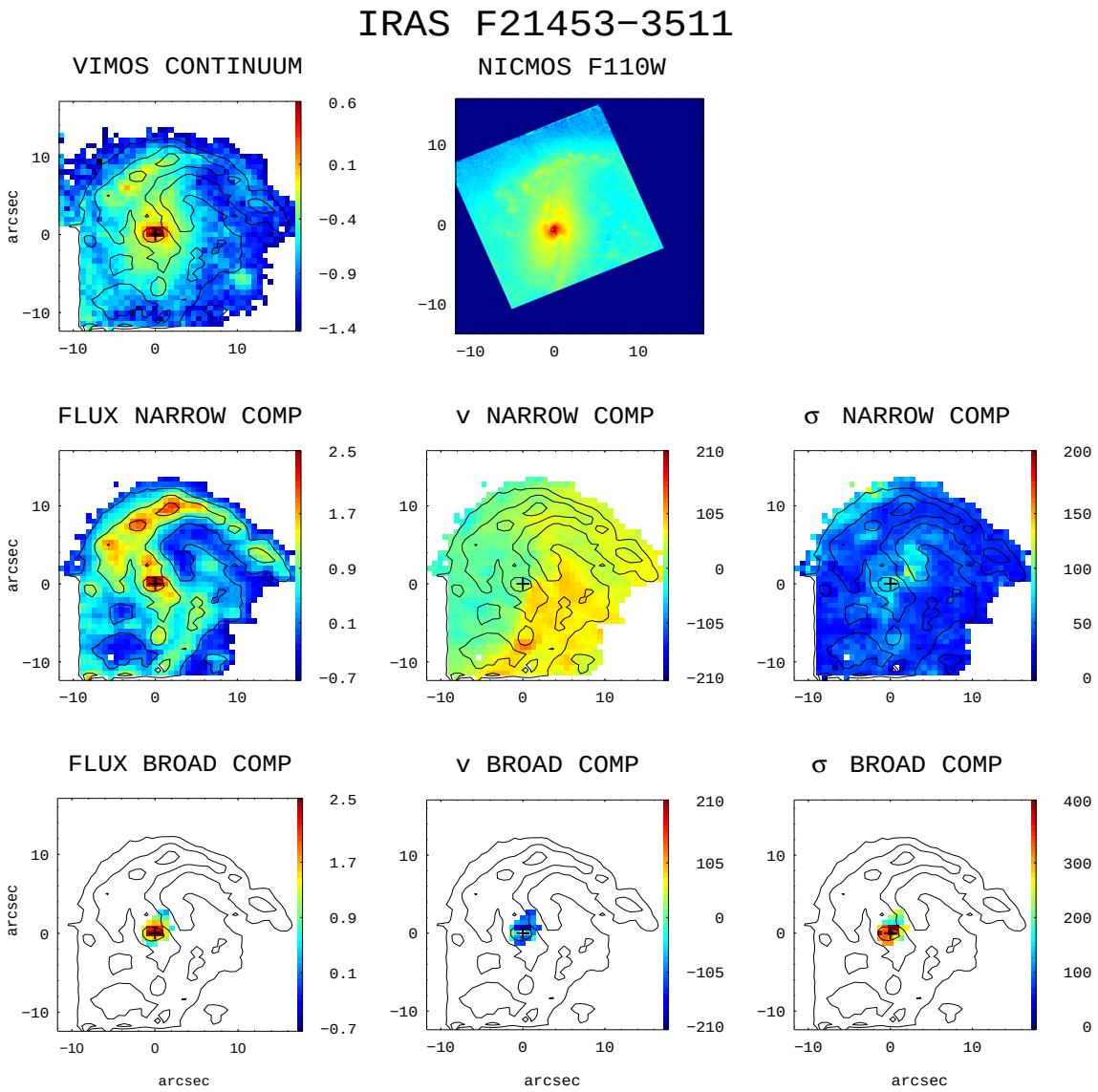

Figure A.42: (General comments about the panels as in Fig. A.1.) IRAS F21453-3511 (NGC 7130): the velocity field and velocity dispersion maps of the narrow component show asymmetric patterns. In the velocity field three main regions can be identified with the rotation axes not well-defined. The velocity dispersion map shows high values in the northern arm and its central part, with values larger than 100 km s^{-1}. This object has been analyzed in Bellocchi et al. (2012). The scale is 0.329 kpc/″.

IRAS F22132−3705

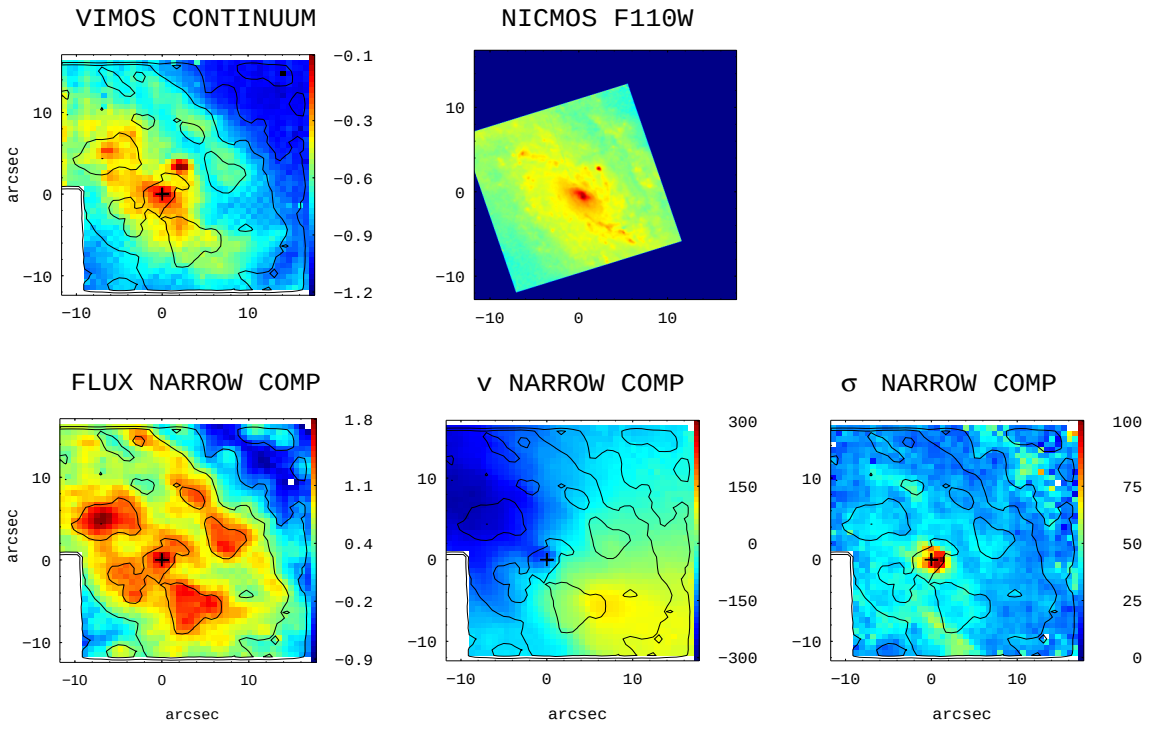

Figure A.43: (General comments about the panels as in Fig. A.1.) IRAS F22132-3705 (IC 5179): the velocity field of this source has the typical 'spider-diagram' shape characterizing a rotating *disk*-like object. The kinematic center and the peak of the velocity dispersion map are well defined and coincident with the VIMOS continuum maximum and the Hα flux peak. In the south and northwest there are regions with velocity dispersion of the order of 50 km s^{-1}. The spatial scale is 0.234 kpc/″.

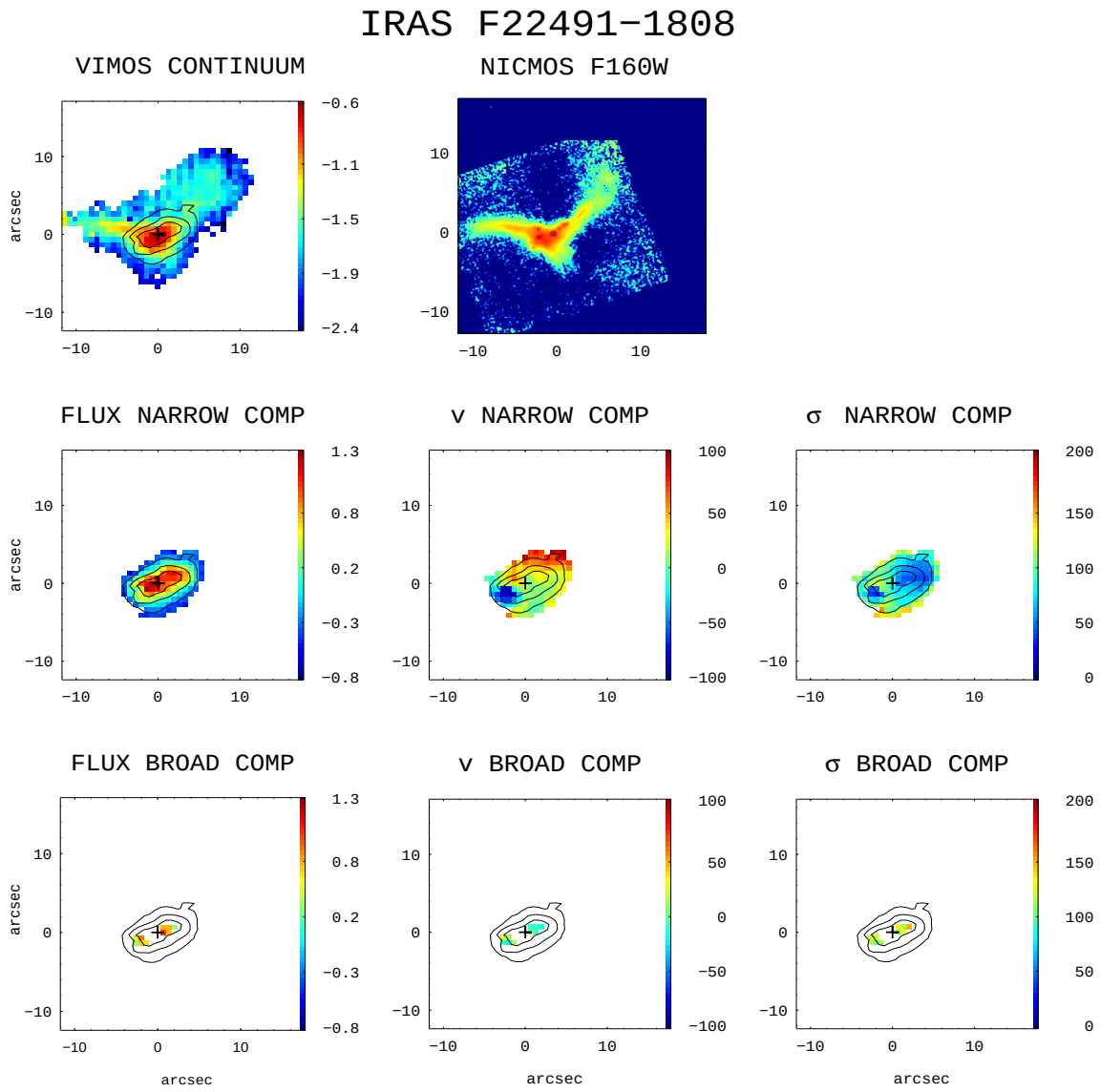

Figure A.44: (General comments about the panels as in Fig. A.1.) IRAS F22491-1808: this is a double nucleus system (separation of 2.6 kpc) with several knots and condensations located in both the nuclear region and the tidal tails observed to the east and northwest of the system. The Hα image shows a more compact morphology than that of the continuum, with no evidence for the already mentioned tidal tails. This system seems to be kinematically disturbed, with a poorly defined minor rotation axis, although a rotation pattern is visible. The velocity dispersion map has a quite irregular structure, with an offset peak with respect to the nucleus and high values in correspondence of low Hα surface brightness. There are two regions where the spectra profiles suggest the presence of an extra broad component. The scale is of 1.47 kpc/″.

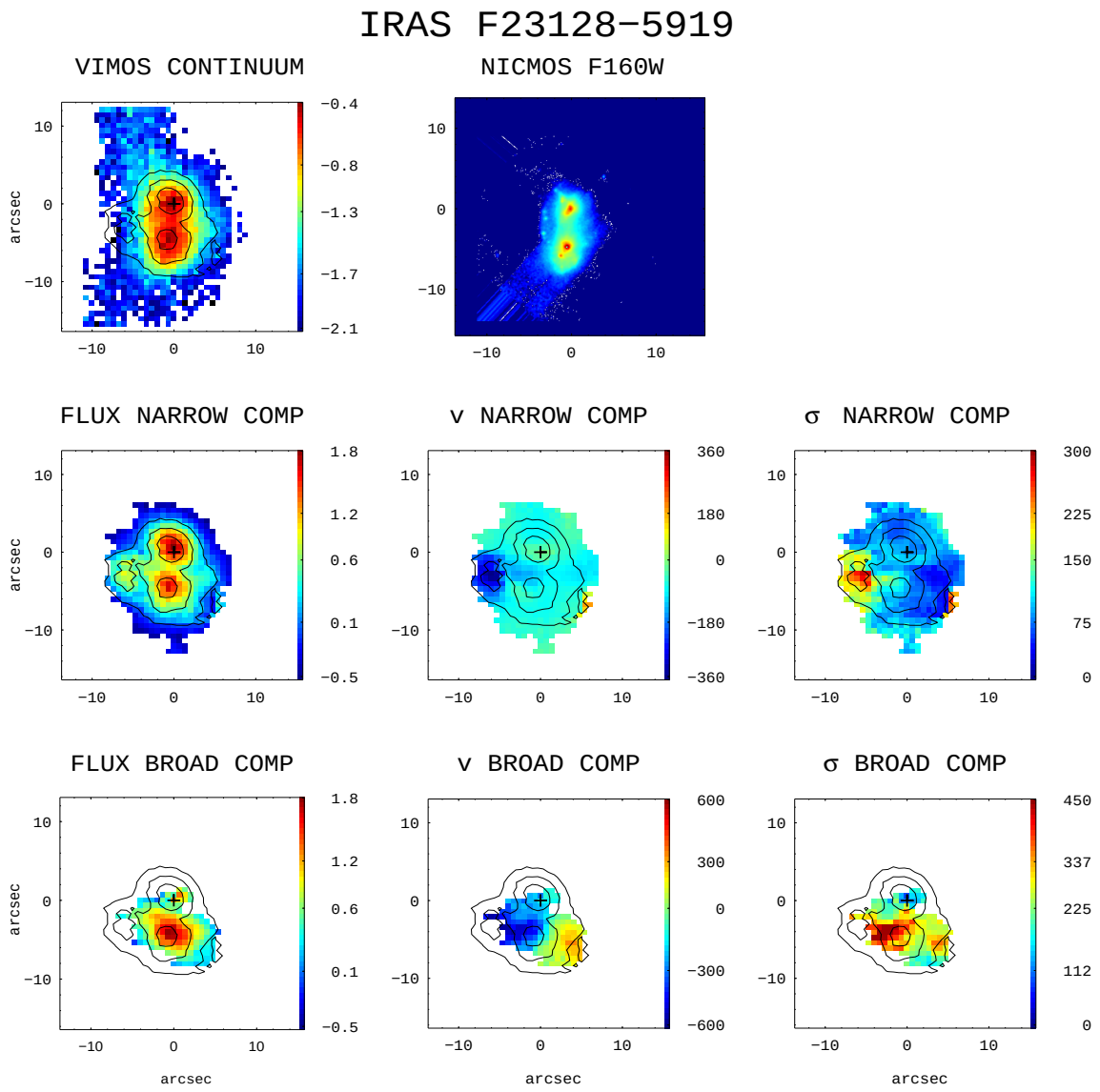

Figure A.45: (General comments about the panels as in Fig. A.1.) IRAS F23128-5919 (AM 2312-591): this is a ULIRG with a double nucleus (separation of $\sim$ 4 kpc). It has not been possible to separate reliably the contribution of each individual galaxy and, therefore, the kinematic values reported in Table 3.3 correspond to the whole system. The velocity field has a quite complex pattern, where the two galaxies merger their velocity fields. A relatively extended broad component has been found in the inner regions of this system, covering an area of 55 kpc^2 and with a mean blueshift of 32 km s^{-1}. The velocity maps of this second component suggest the presence of a strong outflow. The scale is of 0.878 kpc/″.

Table A.1: Spatial offsets between the VIMOS continuum and Hα flux peaks.

Galaxy ID (IRAS)	RA offset ($arcsec$)	DEC offset ($arcsec$)	Notes
(1)	(2)	(3)	
F06295-1735	0.7	-2.5	
F06592-6313	0.6	0	
F07027-6011 S	-0.5	0.4	
F07027-6011 N	0	0	
F07160-6215	-1.4	1.6	
F10015-0614	0	0	
F10409-4556	0	0	
F10567-4310	0	0.3	
F11255-4120	0	0	
F11506-3851	3.4	0.1	(a)
F12115-4656	1.9	-0.7	(a)
F13229-2934	0.6	0.5	
F22132-3705	0	0	
F01159-4443 N	0.6	0.4	
F01341/ESO G12	0	0	
F01341/ESO G11	-0.8	0.6	
F06035-7102	0.7	0	
F06076-2139 N	0	0	
F06206-6315	-0.5	0	
F06259-4780 S	-1.0	1.3	
F06259-4780 N	-0.6	0	
08424-3130 S	0	0	
F08520-6850	0.6	-0.4	
F09437+0317 S	1.5	0	(a)
F09437+0317 N	0.7	0.6	
12043-3140 N	0	0	
F12596-1529	1.7	-0.6	
F14544-4255 E	-6.7	3.9	(a)
F14544-4255 W	-0.6	0	
F18093-5744 S	0	0	
F18093-5744 C	0	0	
F18093-5744 N	-2.2	2.0	(a)
F22491-1808	-0.7	0	
F23128-5919	0	-0.6	
F04315-0840	0	0	
F05189-2524	-0.4	0	
08355-4944	0	0	
09022-3615	1.1	0	
F10038-3338	0.5	-0.4	
F10257-4339	0	0	
12116-5615	-0.5	-0.4	
F13001-2339	0	0	
F17138-1017	-	-	(b)
F21130-4446	1.2	2.2	
F21453-3511	0	0	

Spatial offsets along the right ascension (RA) and declination (DEC) directions: they are defined as the difference between the position of the Hα flux intensity peak and that of the VIMOS continuum (rest frame 6390-6490 Å) intensity peak (i.e., $x_{H\alpha}$ - x_{cont}, $y_{H\alpha}$ - y_{cont}). The coordinates (x_i, y_i) of the peaks in the maps have been derived as the flux-weighted mean position when considering 3×3 spaxels around the maximum intensity value. A typical error of 0.34″ is estimated. For double systems having both galaxies in the VIMOS FoV, the position of the peak refers to the one used as reference to center the images. Col (4): Notes with the following code: (a) The peak of the VIMOS continuum image is considered the center of the images since the Hα peak corresponds to an extranuclear knot of star formation and does not properly define the center of the galaxy. (b) For this galaxy, it was not possible to identify the VIMOS continuum peak due to the S/N.

Appendix B

Near-infrared effective radius determinations

As discussed in Chapter 3 (i.e., Sect.3.3.5), the half-mass radius of a galaxy, R_{hm}, cannot be obtained directly and it has been estimated by measuring the half-light radius, R_{eff}, which encloses half of the total luminosity. We derive the effective radii using near-IR continuum images (i.e., H- and K-bands), which trace the bulk of the galaxy stellar component. This spectral range also has the advantage of reducing the effects of the reddening, which can be significant in (U)LIRGs (i.e., García-Marín et al. 2009, Piqueras López et al. 2013). Specifically, we based our determinations on the 2MASS and HST imaging. We have compiled the K_s-band images from the 2MASS (Skrutskie et al. 2006), and the existing near-IR imaging obtained with HST in H-band (K-band HST imaging is restricted to a reduced number of objects). The 2MASS images have the advantage of being available for all the galaxies in the sample and without limitations by FoV. On the other hand, they have a relatively low angular resolution (i.e., $\sim 2''$), which prevents us from distinguishing kpc-scale structures for many objects in the sample. The HST imaging obviously solves this problem, but in contrast the relatively small FoV of the Near Infrared Camera and Multi-Object Spectrometer (NICMOS) imposes serious limitations for the closest systems. NICMOS/HST H-band infrared imaging existed for about 50 percent of the sample. A few cases were observed with WFC3, which combines good angular resolution and a relatively large FoV.

Two methods have been used to derive the effective radii using 2MASS and HST images: 1) GALFIT (Peng et al. 2010) and 2) the so-called A/2 method, for which the effective radius is defined as $R_{eff} = \sqrt{(A/\pi)}$ and where A is the solid angle subtended by the minimum number of pixels encompassing 50 percent of the galaxy light for the images considered. GALFIT and A/2 methods agree relatively well: in general, radii smaller than

$\sim$ 20% are derived when applying the A/2 method. For those cases with clearly defined disks, the GALFIT radii were preferred to those with the A/2 method. For systems with a high ellipticity or with linear structure, GALFIT tends to interpret them as inclined or edge-on disks. This interpretation is correct in some cases, but in others the actual morphology of the system is distorted by tidal forces or it is uncertain. Also, for highly structured images (generally from HST) the A/2 measurements tend to be smaller than those from GALFIT.

The HST-based measurements tend to be smaller ($\sim$ 10%) than the 2MASS ones as a consequence of the relatively small FoV, which often does not cover the whole galaxy emission. Furthermore, the wavelength dependence of the radius measurements between the H- and K-bands are expected to be very small. In fact, Veilleux et al. (2002), using ground-based K-band imaging for most of the 118 ULIRGs of the IRAS 1 Jy sample, found that the mean values obtained from K-band imaging were about 38% smaller than those obtained in the optical (R-band), i.e., $R^{K}_{eff} = (3.3 \pm 0.5)$ kpc and $R^{R}_{eff} = (4.80 \pm 1.37)$ kpc. Assuming conservatively that this difference is mainly due to reddening, one should expect a minor change between the values inferred at H and K.

The mean R_{eff} for the (U)LIRGs sample is (2.6 ± 1.3) kpc. For the ULIRG subsample, we obtain a mean R_{eff} of (3.3 ± 0.5) kpc, which is in excellent agreement with the value of R^{K}_{eff} obtained by Veilleux et al. (2002). In Chapter 3 the sizes of the (U)LIRGs are also compared with those of other local samples, as shown in Figure 3.4 (left panel). On average, (U)LIRGs have smaller radii than local spirals, though the intrinsic scatter is rather large in both samples. In the present sample of (U)LIRGs, objects with radii as large as 7-20 kpc, such as those in the GHASP survey (i.e., derived in the B-band), are not seen. The E/SOs cover a range in size (measured using the H-band) larger than the (U)LIRGs, with a significant number of sources with R_{eff} smaller than 0.5 kpc and larger than 7 kpc. The ULIRG sample observed with INTEGRAL/WHT (i.e., Colina et al. 2005; García-Marín et al. 2009) covers similar sizes as those of the present sample, with somewhat larger scatter. The derived LBA radii using Paα emission are on average smaller by a factor of 0.7 than (U)LIRG radii. We note that Hα sizes are also somewhat smaller than IR-continuum-based determinations (i.e., Arribas et al. 2012).

In Table B.1 we present the individual results of the derived effective radii when applying the two methods to the 2MASS and HST images, as well as the adopted values and their estimated uncertainties. The table includes a code that indicates the values considered for deriving the adopted one.

Table B.1: Near-IR continuum (stellar) radii determinations.

IRAS name	R_{hl}^{2MASS}(GALFIT) (kpc)	R_{hl}^{2MASS}(A/2) (kpc)	Comm. code	R_{hl}^{HST}(GALFIT) (kpc)	R_{hl}^{HST}(A/2) (kpc)	Comm. code	Adopted (kpc)	code	Previous R_{hl} (kpc)(ref)
(1)	(2)	(3)	(4)	(5)	(6)	(7)	(8)	(9)	(10)
01159 N	0.81 ± 0.32	1.30 ± 0.44	1,7	...	...		1.0 ± 0.4	1100	
01159 S	2.39 ± 0.72	2.09 ± 0.47	1	...	...		2.2 ± 0.6	1100	
01341 N	2.56 ± 0.50	2.20 ± 0.56		1.55 ± 0.65	0.95 ± 0.15	c	2.2 ± 0.6	1110	
01341 S	1.50 ± 0.60	0.93 ± 0.26	4	...	...		1.5 ± 0.6	1000	
04315	1.15 ± 0.35	0.94 ± 0.14	4	0.55 ± 0.30	0.36 ± 0.12	c	1.2 ± 0.4	1000	0.06 (b)
05189	...	(0.67)	6	(0.10)	(0.25)	h	(0.18)	0000	
06035	...	4.71 ± 1.35		...	...		4.7 ± 1.4	0100	
06076 N	3.00 ± 1.40	2.21 ± 0.37	1	3.23 ± 0.06	...	d	3.2 ± 0.6	1110	
06076 S	3.40 ± 1.20	1.73 ± 0.45	1	3.11 ± 0.06	...	d	3.1 ± 0.6	1010	
06206	(3.60)	(4.56)	5	...	2.41 ± 0.60		2.4 ± 0.6	0001	
06259 N	1.09 ± 0.20	1.45 ± 0.58	1	1.15 ± 0.05	1.02 ± 0.02		1.0 ± 0.2	1011	
06259 C	1.67 ± 0.12	1.73 ± 0.35	1	2.91 ± 0.07	1.16 ± 0.04	f	2.6 ± 0.7	1010	
06259 S	2.60 ± 0.50	1.74 ± 0.58	4	...	1.14 ± 0.04	e	2.6 ± 0.7	1000	
06295	...	3.03 ± 0.62	3	...	...		3.0 ± 0.6	0100	
06592	1.53 ± 0.60	1.17 ± 0.26		...	...		1.2 ± 0.4	1100	
07027 N	...	(0.79)	6	...	(0.2)	h	(0.2)	0000	
07027 S	1.61 ± 0.70	1.54 ± 0.69		1.75 ± 0.06	0.96 ± 0.02		1.5 ± 0.5	1111	
07160	3.64 ± 0.35	2.32 ± 0.35	4	...	0.82 ± 0.03	a,e	3.6 ± 0.5	1000	
08355	0.91 ± 0.25	1.21 ± 0.34		2.09 ± 0.38	0.91 ± 0.18	f	1.3 ± 0.8	1110	
08424 N	2.50 ± 1.10	0.81 ± 0.07	1,4	...	...		2.5 ± 0.5	1000	
08424 S	2.20 ± 0.80	1.02 ± 0.10	1	...	...		2.2 ± 0.4	1000	
08520 N	2.87 ± 0.98	...		2.36 ± 0.34	2.17 ± 0.25	g	2.4 ± 0.6	1010	
08520 S	4.00 ± 0.30	...	4	5.95 ± 0.22	2.64 ± 0.30	g	5.3 ± 1.4	1010	
09022	1.96 ± 0.45	1.95 ± 0.40		3.25 ± 0.85	2.40 ± 0.40	d	2.2 ± 0.6	1111	
09437 N	6.10 ± 1.10	3.46 ± 0.71	4	...	...		6.1 ± 1.3	1000	
09437 S	3.09 ± 0.21	2.33 ± 0.39	4	...	...		3.1 ± 0.5	1000	
10015	3.56 ± 0.45	2.75 ± 0.48		1.18 ± 0.18	1.36 ± 0.10	a	3.2 ± 0.6	1100	
10038	2.12 ± 0.70	1.96 ± 0.61		...	...		2.0 ± 0.6	1100	
10257	2.66 ± 0.86	1.76 ± 0.27		1.55 ± 0.04	1.33 ± 0.01	a,d	1.8 ± 0.6	1100	
10409	2.92 ± 0.22	2.25 ± 0.19		...	...		2.5 ± 0.5	1100	
10567	2.88 ± 1.50	3.20 ± 0.40	2	...	...		3.2 ± 0.9	1100	
11254	3.14 ± 0.86	2.40 ± 0.57	2	...	...		2.6 ± 0.7	1100	
11506	1.22 ± 0.20	0.94 ± 0.17		0.67 ± 0.02	0.61 ± 0.02	c	1.1 ± 0.2	1100	
12042 N	1.22 ± 0.20	1.18 ± 0.29	1	...	...		1.2 ± 0.2	1100	
12042 S	2.32 ± 0.32	1.47 ± 0.26	4	...	...		2.3 ± 0.5	1000	
12115	2.97 ± 0.57	2.14 ± 0.36		...	...		2.4 ± 0.6	1100	
12116	1.17 ± 0.35	1.34 ± 0.25	1	1.94 ± 0.88	1.12 ± 0.11	b,f	1.3 ± 0.5	1110	
12596		2.17 ± 0.97	1	...	3.13 ± 0.45	c	2.7 ± 1.0	0101	
13001	3.71 ± 1.00	2.89 ± 1.10	4	5.79 ± 0.15	3.33 ± 0.09	d	5.7 ± 1.5	1010	
13229	3.41 ± 0.85	2.39 ± 0.84	4	1.08 ± 0.09	0.87 ± 0.04	a	3.4 ± 1.2	1000	
14544 E	4.76 ± 0.56	2.63 ± 0.48	4	2.66 ± 0.19	1.24 ± 0.06	c	4.8 ± 1.2	1000	
14544 W	3.04 ± 1.43	2.25 ± 0.51	2	1.55 ± 0.16	1.09 ± 0.12	a	2.3 ± 1.0	1100	
17138	1.78 ± 0.15	1.46 ± 0.25		1.44 ± 0.13	1.06 ± 1.14	a	1.7 ± 0.2	1100	
18093 N	1.75 ± 0.32	1.64 ± 0.35	1	1.57 ± 0.18	1.13 ± 0.08	a	1.8 ± 0.5	1000	
18093 C		(1.04)	5	0.39 ± 0.21	0.26 ± 0.14	c,g	>0.3± 0.2	0011	
18093 S	2.07 ± 0.53	1.46 ± 0.30	4	1.89 ± 0.27	1.32 ± 0.09	c	2.1 ± 0.7	1000	
21130	4.95 ± 0.48	4.56 ± 1.21		...	...		4.9 ± 0.8	1100	
21453	3.68 ± 0.51	2.97 ± 0.82		2.59 ± 0.29	1.34 ± 0.08	a	3.5 ± 0.7	1100	
22132	5.13 ± 0.66	3.12 ± 1.15	2,4	...	1.11 ± 0.04	a,e	5.1 ± 0.7	1000	
22491	3.70 ± 1.00	3.42 ± 2.80	2	...	3.00 ± 2.40	b	3.6 ± 1.5	1101	8.29 (a)
23128	...	1.91 ± 0.22		...	1.60 ± 0.22		1.8 ± 0.3	0101	

Columns: (1) Identification. (2) Half-light radius from the 2MASS K-band image using GALFIT. (3) Half-light radius from the 2MASS K-band image using the A/2 method (see text). (4) Comments associated with the 2MASS images determinations, according to the following code: 1- large uncertainties when applying the A/2 method due to galaxy decomposition; 2- uncertainty due to background value, field stars, and/or complex structure; 3- GALFIT could not obtain a reliable fit; 4- disc with b/a $<$ 0.4, leading to discrepancies between the two methods; 5- unreliable estimates due to background and/or complex structure; 6- point-like source dominating the (unreliable) radius determination; 7- FWHM of the bulge component close to the value for the PSF, making the radii estimates uncertain. (5) Half-light radius from the HST H-band image using GALFIT. (6) Half-light radius from the HST H-band image using the A/2 method. (7) Comments associated with the HST determinations, according to the following code: a- severely limited by FoV; b- very uncertain results due to bad background definition; c- limited by FoV; d- HST image obtained with WFC3 or NIC3 (instead of NIC2); e- bad GALFIT fit; f- rich structure in the HST image; g- uncertainties when applying the A/2 method due to galaxy decomposition; h- point-like source dominating the (unreliable) radius determination. (8) Adopted values. (9) Code indication if the individual values in columns 2, 3, 5, and 6 were used in the adopted value (0 = not used, 1 = used). (10) Previous determinations with the following code: (a) Scoville et al. (2000), model fitting (de Vaucouleurs or exponential) to F160W images; (b) Hinz & Rieke (2006).

Appendix C

Other *kinemetry*-based criteria

In this appendix we describe other criteria that could be useful in distinguishing different systems. Other authors have indeed tried to define criteria able to kinematically classify galaxies at intermediate redshift (i.e., $z \sim 0.6$): for example, Flores et al. (2006) developed a simple kinematic classification scheme for distant galaxies based on their 3D kinematics and their morphology in ACS F775W images. They modeled the velocity field of a rotating disk that matches the observed velocity gradient to obtain the expected σ-map corresponding to the observed velocity field and then compare the observed and model σ-maps, estimating whether the observed kinematics are consistent with a rotating disk (i.e., a rotating disk should show a well-defined peak in the center of the σ map). The spatial separation (Δr, in pixels) between the peaks in the two σ-maps and the relative difference (ϵ) between the amplitudes of the modeled and observed σ peaks are considered to classify the objects. They found that rotating disks have locations near $\Delta r \sim \epsilon \sim 0$, while galaxies with anomalous velocity fields are clearly offset. The same criterion was applied in Yang et al. (2008).

Here we propose some additional criteria, based again on the *kinemetry* method:

1. we consider the normalized higher-order deviations $<k_5/\ k_1>_v$ of the velocity field with respect to those of the velocity dispersion map σ_{asym}, since the k_5 term indicates complex structure in the velocity map, as noted in Krajnović et al. (2006). Small k_5/k_1 values should be found in *disk-like* structures, while large k_5/k_1 are expected for mergers, where more complex structures are assumed to exists. This is confirmed by our results: class 0 objects have $<k_5/k_1>$ close to zero, the amplitude of k_1 is substantial, and the position angle Γ and flattening q remain quite constant such that they can be classified as *disk-like* objects. On the other hand, class 2 objects show a rise in the $<k_5/k_1>$ term of up to 0.6 at outer radii, where peculiar structures can be identified. In Fig. C.1, we present the results obtained from our

MC simulations (150 for each object). This criterion allows us to distinguish the class 0/2 in a similar way as in the [σ_a - v_a] plane, but somewhat worst than in W-[σ_a - v_a] plane.

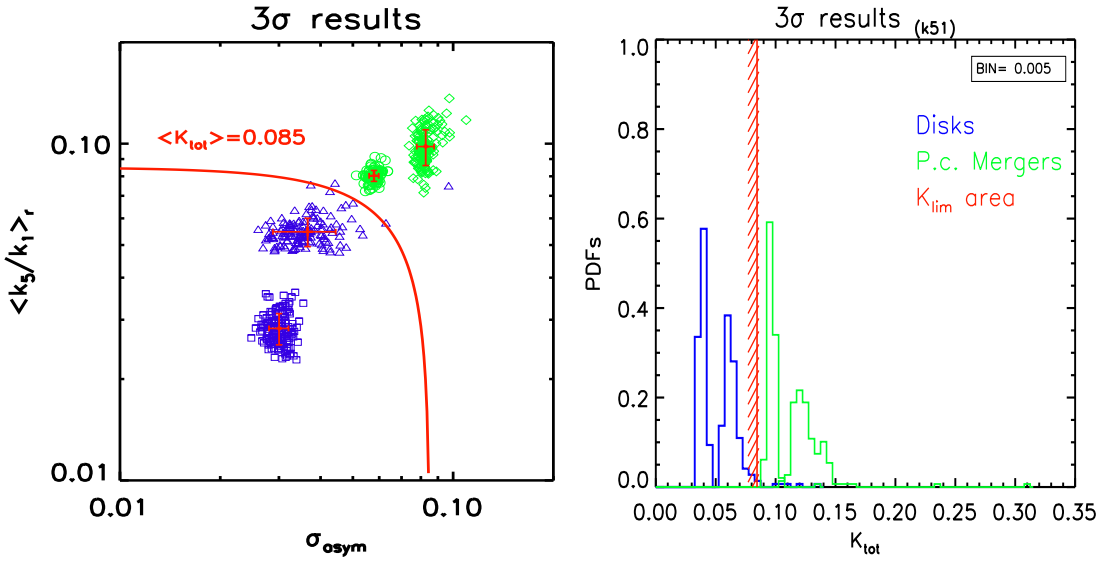

Figure C.1: **Left:** Asymmetry measures of the $<k_5/k_1>$ term and velocity dispersion σ_{asym} as derived from the MC realizations for the four objects. For each source, 150 MC simulations are run but the $\pm 3\sigma$ results are shown. The solid red line indicates the empirical division between disks and mergers at $<K_{lim}> = 0.085$. **Right:** The probability distribution function (PDFs) derived from the respective MC realizations. The empirical delineation clearly separate the two classes defining a small range of possible values (i.e., K_{lim} area). Small deviations $<k_5/k_1>$ are found for *disks*, while higher values are found for *mergers*, which is consistent with our expectation.

2. In some cases, the data quality does not allow us to apply sophisticated criteria to search for asymmetries. In these cases, a simple criterion may be the only possible option. Therefore, we have studied the potential of the *simple*-[σ_a - v_a] plane (hereafter, *S*-[σ_a - v_a]), where only the first-order correction in the harmonic expansion is considered and asymmetries are defined as the ratio of the root mean square (RMS) of the residual map to the mean values of the $B_{1,v}$ term over all the radii. The next formula describes the two asymmetries

$$v_{asym} = \frac{RMS}{\langle B_{1,v} \rangle_r} \qquad \sigma_{asym} = \left\langle \frac{k_{1,\sigma}}{B_{1,v}} \right\rangle_r$$

where the *RMS* gives an estimate of the deviations of the system from the ideal case of simple rotation in the system[1]. In Fig. C.2, we present the results in the *S* - [σ_a - v_a] plane. Comparing this plot with that shown in Fig. 4.7, we note that

[1]Residuals are derived from the measured velocities and the B_1 coefficient.

the RMS/<B_1> term tends to be higher than the v_{asym} values, while the σ_{asym}^{3terms} values are smaller than the $\sigma_{asym}^{10terms}$ range. The σ_{asym}^{3terms} does not seem to clearly characterize the kinematic asymmetries of these systems (i.e., in the case of IRAS F04315-0840, which has a quite distorted morphology). On the other hand, the RMS/<B_1> term by itself can quite clearly distinguish the two classes, where a border dividing them can be estimated to have a value of ~ 0.2.

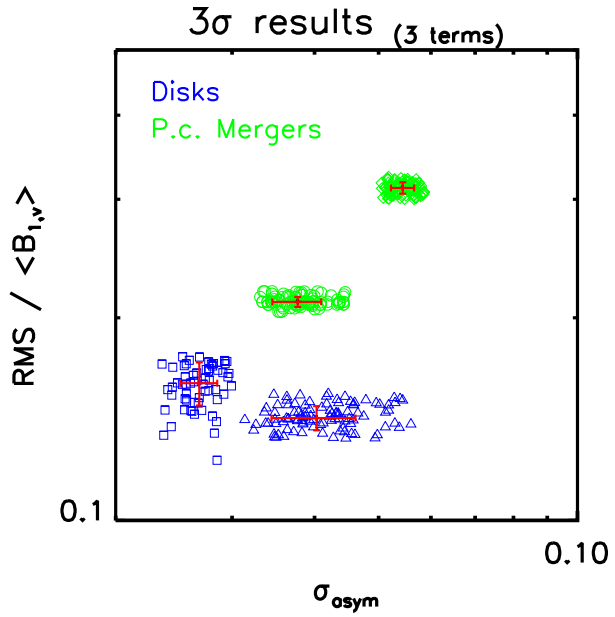

Figure C.2: Subtracting the circular motion (i.e., B_1 coefficient) from the data, we end up with the velocity residual maps, characterized by mean residuals close to zero and a RMS smaller than 20 km s^{-1} for the whole sample. If we assume that the four objects have almost the same RMS, this plot clearly implies higher circular velocities for the class 0 galaxies, while we note that a lower B_1 term is derived for the class 2 ones.

Appendix D

INTEGRAL/WHT kinematic results according to the VIMOS analysis

In this appendix we present the kinematic results obtained for the ULIRG sample (i.e., 18 system, corresponding to 27 individual galaxies; Colina et al. 2005; García-Marín et al. 2007) observed with INTEGRAL/WHT when applying the analysis adopted in this thesis for the (U)LIRG VIMOS sample. The luminosity range covered by the INTEGRAL sources allows to improve the statistics of ULIRG systems and to extend our VIMOS sample. We derive the same kinematic parameters as those discussed in Sects. 3.2 and 3.3 (i.e., v_{shear}, σ_{mean}, M_{dyn}). We thus compare the results with those derived in previous works (i.e., Colina et al. (2005); García-Marín et al. (2007)), which applied a different analysis. In particular, we remind that Colina et al. (2005); García-Marín et al. (2007) adjusted the observed line profiles only using one single component since the relatively low spectral resolution of their INTEGRAL data did not allow to reliably distinguish the presence of multiple components in the lines on a spaxel by spaxel basis. However, in general, the derived kinematical values of v and σ in a 1-Gaussian fit are similar to those of the narrow component when applying 2-Gaussian fit, as done in this thesis.

D.1 The analysis and results

As done in this thesis, we infer some global kinematic properties for the INTEGRAL/WHT ULIRG sample. For instance, the velocity shear v_{shear}, as defined in Sect. 3.1.1, and the uniformly-weighted mean velocity dispersion σ_{mean} are determined. In order to obtain the intrinsic (i.e., inclination corrected) velocity shear, the inclination of each object are

obtained using HST images (i.e., WFPC F814W).

When deriving the dynamical mass of the ULIRG systems the same approach as that used in Chapter 3 has been followed. In brief, Eq. 3.1 has been used for spherical, bound and dynamically relaxed systems dominated by random motions which show a kinematic compatible with slow rotation (i.e., $v^*/\sigma < 2$). For the rest of the systems ('rotation-dominated') we applied the Eq. 3.3. For a relatively small number of objects (i.e., 11/27 galaxies) we applied an average inclination correction following Law et al. 2009 due to their complex morphology. These have a relatively large uncertainty in i, but only for 8/27 objects we apply Eq. 3.3.

All the results are summarized in Tab. D.1. For the majority of the interacting systems we have been able to disentangle the contribution of each galaxy, and then to compute the aforementioned kinematic parameters.

D.2 Differences with previous M_{dyn} estimates

In this section the kinematic values derived following our analysis are compared with those derived in Colina et al. (2005); García-Marín et al. (2007) (see Tab. D.1). Indeed, in their analyses they computed the peak-to-peak velocity amplitude v_{amp}, the nuclear velocity dispersion σ_c and the dynamical mass M_{dyn} according to the formula shown in Colina et al. (2005):

$$M_{dyn} = 1.75 \cdot 10^6 \cdot \sigma_c^2 \cdot R_{eff}[M\odot] \quad \text{(D.1)}$$

In Fig. D.1 three different trends are shown comparing, respectively, the effective radius, the velocity dispersion and the velocity amplitude, which are the three quantities used in the computation of the dynamical mass derived following the two approaches. For the INTEGRAL/WHT data the effective radius is obtained from the I-band (i.e., F814W) images (when available the H-band (i.e., F160W) NICMOS images are used; see García-Marín et al. (2007)). In our analysis we derive the effective radii using near infrared continuum images (i.e. H- and K-bands). These spectral ranges have the advantage of reducing the effects of the reddening, which can be significant in (U)LIRGs (i.e., García-Marín et al. 2009; Piqueras López et al. 2013). Specifically, we based our determinations on the 2MASS and HST imaging, which cover a wide FoV and have high angular resolution, respectively (see App. B).

According to our data, the mean R_{eff} for the ULIRGs sample is (2.4 $\pm$ 1.2) kpc with a median value of 2.1 kpc, which is in good agreement with the value of (3.48 $\pm$ 1.39) kpc obtained by Veilleux et al. (2002) using ground-based K-band imaging for most of

Table D.1: INTEGRAL kinematic results

	This work							GM+07 thesis				
Galaxy ID	v_{shear}	σ_{mean}	R_{eff}	i	v^*/σ	M_{dyn} (10^{10})	Notes	v_{amp}	σ_c	R_{eff}	M_{dyn}^{DISP} (10^{10})	Notes
(1)	(2)	(3)	(4)	(5)	(6)	(7)	(8)	(9)	(10)	(11)	(12)	(13)
Arp 220	195 ± 11	141 ± 3	2.0 ± 0.4	52° ± 26°	1.8 ± 0.8	5.5 ± 1.1	(ii)	191	185	1.2 ± 4.1	7.2 ± 0.2	(a)
Arp 299E (IC694)	114 ± 3	68 ± 2	1.8 ± 0.4	52° ± 26°	2.1 ± 0.9	2.3 ± 1.6	(ii)	132	108	2.0 ± 1.5	4.1 ± 1.0	
Arp 299W (NGC3690)	112 ± 1	102 ± 1	1.2 ± 0.2	52° ± 26°	1.4 ± 0.6	1.7 ± 0.3	(ii, iii)	123	172	1.2 ± 0.2	6.2 ± 3.0	
IRAS 06268	66 ± 3	109 ± 5	5.8 ± 2.1	52° ± 26°	0.8 ± 0.3	9.7 ± 3.6	(ii)					
IRAS 06268 (N)	65 ± 3	138 ± 3	2.7 ± 1.1	47° ± 6°	0.7 ± 0.1	7.1 ± 2.9	(i)	58	128	2.1 ± 0.4	6.0 ± 1.0	
IRAS 06268 (S)	50 ± 6	90 ± 5	2.1 ± 0.5	66° ± 3°	0.6 ± 0.1	2.4 ± 0.6	(i)	74	77	1.1 ± 0.5	1.1 ± 0.5	(a)
IRAS 06487	87 ± 3	172 ± 13	1.5 ± 0.3	52° ± 26°	0.6 ± 0.3	6.2 ± 1.6	(ii)	98	163	1.5 ± 0.3	7.0 ± 1.0	
IRAS 08572 N	123 ± 1	80 ± 1	2.0 ± 0.6	52° ± 26°	1.9 ± 0.9	1.8 ± 0.5	(ii)					
IRAS 08572N (N)	87 ± 4	93 ± 2	0.8 ± 0.3	6° ± 4°	1.1 ± 0.1	0.96 ± 0.4	(i)	70	113	0.6 ± 2.0	1.3 ± 4.0	(a)
IRAS 08572N (S)	114 ± 1	64 ± 1	3.2 ± 1.2	66° ± 4°	2.0 ± 0.1	1.8 ± 0.7	(i)	110	47	0.6 ±0.9	0.2 ± 0.3	(a)
IRAS 11087	89 ± 10	239 ± 5	3.8 ± 0.8	52° ± 26°	0.5 ± 0.2	30.4 ± 6.5	(ii)	105	239	8.9 ± 1.8	89.0 ± 18.0	
IRAS 12112	169 ± 8	120 ± 2	2.3 ± 1.2	52° ± 26°	1.8 ± 0.8	4.6 ± 2.4	(ii)					
IRAS 12112 (N)	183 ± 8	121 ± 2	2.1 ± 0.2	52° ± 26°	1.9 ± 0.9	4.3 ± 0.4	(ii)	200	130	1.7 ± 0.3	5.0 ± 1.0	(a)
IRAS 12112 (S)	105 ± 9	118 ± 2	0.6 ± 0.3	42° ± 7°	1.3 ± 0.2	1.2 ± 0.6	(i)	200	160	1.1 ± 0.5	5.0 ± 1.0	(a)
IRAS 12490	218 ± 2	161 ± 7	2.4 ± 1.2	52° ± 26°	1.7 ± 0.8	8.7 ± 4.4	(ii)	225	207	7.6 ± 1.5	57.0 ± 11.0	
IRAS 13156 (N)	208 ± 5	120 ± 4	1.7 ± 0.8	53° ± 6°	2.2 ± 0.2	6.9 ± 3.4	(i)	218	152	5.9 ± 1.2	23.9 ± 5.0	
IRAS 13156 (S)	203 ± 14	113 ± 22	4.0 ± 1.6	57° ± 3°	2.14 ± 0.5	14.1 ± 6.0	(ii)	258	138	4.9 ± 1.0	16.3 ± 3.0	
IRAS 14060	154 ± 6	76 ± 5	2.4 ± 0.8	50° ± 5°	2.6 ± 0.3	5.4 ± 1.9	(i)	161	130	4.8 ± 1.5	14.2 ± 4.0	
IRAS 14348	174 ± 1	117 ± 1	3.9 ± 1.0	52° ± 26°	1.9 ± 0.8	7.4 ± 1.9	(ii)					
IRAS 14348 (N)	131 ± 1	100 ± 2	3.1 ± 1.0	40° ± 4°	2.0 ± 0.2	7.9 ± 2.8	(i)	104	147	1.5 ± 0.3	5.7 ± 1.0	(a)
IRAS 14348 (S)	143 ± 3	126 ± 1	1.7 ± 0.4	44° ± 5°	1.6 ± 0.2	3.8 ± 0.9	(i)	120	196	1.3 ± 2.5	8.7 ± 10.0	(a)
IRAS 15206	120 ± 1	92 ± 2	2.2 ± 0.5	52° ± 26°	1.7 ± 0.7	2.6 ± 0.6	(ii)	125	90	2.9 ± 0.5	4.1 ± 1.0	
IRAS 15250	109 ± 12	149 ± 4	1.2 ± 0.4	36° ± 5°	1.3 ± 0.2	3.7 ± 1.3	(i)	110	168	1.4 ± 0.7	6.9 ± 3.0	(a)
IRAS 16007	200 ± 9	105 ± 2	8.6 ± 1.8	52° ± 26°	2.4 ± 1.1	31.6 ± 23.7	(ii)					
IRAS 16007 (E)	206 ± 2	118 ± 3	4.0 ± 0.8	68° ± 2°	1.9 ± 0.1	7.8 ± 1.6	(i)	211	110	4.0 ± 0.8	8.5 ± 2.0	
IRAS 16007 (W)	194 ± 9	99 ± 2	4.2 ± 0.8	56° ± 4°	2.4 ± 0.2	13.2 ± 2.5	(i)	211	151	4.2 ± 0.8	16.8 ± 3.0	
IRAS 17208	138 ± 10	91 ± 3	1.8 ± 0.5	52° ± 26°	1.9 ± 0.9	2.1 ± 0.6	(ii)	170	191	1.5 ± 1.7	9.6 ± 10.0	(a)
IRAS 18580	264 ± 1	163 ± 6	6.5 ± 2.4	52° ± 26°	2.0 ± 0.9	44.8 ± 34.3	(ii)					
IRAS 18580 (E)	191 ± 21	147 ± 4	4.5 ± 1.1	52° ± 26°	1.7 ± 0.8	13.5 ± 3.4	(ii)	126	155	6.5 ± 1.0	27.3 ± 4.0	
IRAS 18580 (W)	123 ± 1	176 ± 6	4.5 ± 0.1	52° ± 26°	0.9 ± 0.4	19.4 ± 1.5	(ii)	141	119	4.3 ± 1.0	10.7 ± 2.0	
Mrk 273	332 ± 3	166 ± 7	2.1 ± 0.5	57° ± 4°	2.4 ± 0.14	19.0 ± 4.7	(i)	450	182	2.0 ± 2.6	11.6 ± 15.0	(a)
Mrk 463	233 ± 2	194 ± 1	2.0 ± 0.5	52° ± 26°	1.5 ± 0.7	10.5 ± 2.6	(ii)					
Mrk 463 (E)	251 ± 2	217 ± 1	1.0 ± 1.0	42° ± 8°	1.7 ± 0.3	7.9 ± 6.6	(i, iii)	294	179	1.0 ± 0.6	5.6 ± 1.0	
Mrk 463 (W)	155 ± 2	139 ± 4	1.2 ± 0.1	49° ± 4°	1.5 ± 0.1	3.2 ± 0.3	(i)	294	132	1.0 ± 0.2	3.0 ± 1.0	(a)

Col (1): Identification. Col (2): Velocity shear as computed in the previous analysis. Col (3): (Uniformly-weighted) Mean velocity dispersion. Col (4): Half-light radius from the 2MASS K-band images (see App. B). Col (5): Inclination. Col (6): Ratio between the inclination corrected velocity shear (2) and the mean velocity dispersion (3). Col (7): Dynamical mass. Col (8): Comments with the following code: (i) Inclination derived using the HST image. (ii) A mean inclination (i.e., 52° ± 26°) has been considered. (iii) The value of the effective radius derived in GM07 using the F814W-band HST images has been considered since the 2MASS image does not allow a reliable estimation of the radius. Col (9): Observed peak-to-peak velocity amplitude derived from the work of GM07. Col (10): Central (nuclear) velocity dispersion from GM07. Col (11): Half-light radius from the HST images (i.e., F814W band) from the analysis of GM07. Col (12): Dynamical mass selected using the formula shown in Colina et al. (2005). Col (13): Comments with the following code: (a) For this source the dynamical mass has been computed using the R_{eff} derived from the F160W filter that is shown in Col. (11).

the 118 ULIRGs of the IRAS 1 Jy sample. The effective radii derived in García-Marín et al. (2007) are in general quite similar to our estimations, with some exceptions showing effective radii 3 times larger in the F814W band than those derived in the K band. This is the case of IRAS 11087+5351 and IRAS F12490-1009 which show peculiar structure around the nucleus possibly affecting the effective radius estimation at that wavelength. The first one is a double nucleus (separated by $\sim$ 1.5 kpc) post-coalescence galaxy, which shows some circum-nuclear activity and a strongly ionized outer nebula at about 7 kpc from the nucleus. Then, IRAS F12490-1009 has an arc-like tidal tail towards the north with a total length of $\sim$ 20 kpc. Low surface brightness structures are detected on the East-West direction.

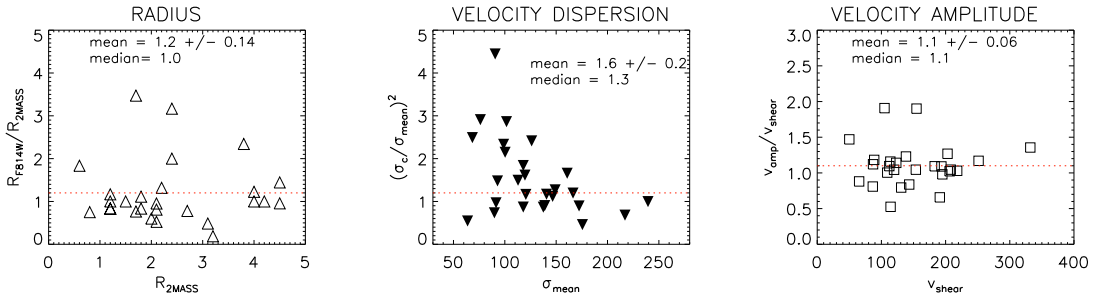

Figure D.1: Effective radius, velocity dispersion and velocity amplitude parameters used in the two formulas of M_{dyn} estimate. Their respective ratios are compared: the effective radii (HST vs 2MASS), the $(\sigma_c/\sigma_{mean})^2$, and the velocity amplitude v_{amp}/v_{shear}. The respective mean (and median) values are shown in the plots.

The mean value of the velocity shear derived from our analysis is of v_{shear} = 151 $\pm$ 63 km s^{-1}(median of 138), while the mean value of the mean velocity dispersion is of σ_{mean} = 127 $\pm$ 43 km s^{-1} (120) km s^{-1}. These values are slightly higher than those derived for the ULIRGs observed with VIMOS (i.e., $v_{shear} \sim$ 130 km s^{-1}, $\sigma_{mean} \sim$ 95 km s^{-1}). This supports the fact that these systems could be more dispersion dominated than those observed with VIMOS. The ratio σ_c/σ_{mean} has slightly different values with a typical mean value of 1.2 $\pm$ 0.1, with a maximum value of 2.1 for the galaxy IRAS F17208-0014, for which a σ_c = 191 km s^{-1} is derived.

The value of K = 6 corresponds to m=1.4 in equation (1) given in Colina et al. (2005), who used m=1.75; therefore, the masses derived in this work are $\sim$ 20 percent lower than those derived with their formula. For a small fraction of galaxies (i.e., 8/27) showing $v^*/\sigma \geq 2$ we derived a mean dynamical mass of 0.54 $\pm$ 0.1 (0.39) $m_\star$ which is in good agreement with that obtained for the ULIRG VIMOS objects (i.e., 0.51 $\pm$ 0.19 $m_\star$). The mean dynamical mass derived by García-Marín et al. (2007) is of the order of M_{dyn} = 0.96 $\pm$ 0.26 (0.5) $m_\star$, a factor of 2 higher with respect to our results. On the

Table D.2: Mean (and median) kinematical properties for the INTEGRAL/WHT ULIRG sample.

Sample	v (km s^{-1})	σ (km s^{-1})	R_{eff} (kpc)	M_{dyn} (10^{10} $M_\odot$)
(1)	(2)	(3)	(4)	(5)
ALL ULIRG (this work)	151 ± 63 (138)	127 ± 43 (120)	2.4 ± 1.2 (2.1)	7.5 ± 1.4 (5.5)
ALL ULIRG (GM07)	164 ± 17 (132)	147 ± 8 (151)	2.8 ± 0.4 (1.7)	13.4 ± 3.6 (7.0)
ULIRG (C05)*	91 ± 17 (70)	146 ± 17 (147)	1.3 ± 0.2 (1.3)	5.6 ± 1.4 (5.5)

Col (1): Sample. Col (2): Velocity amplitude: velocity shear as computed in this work, while in García-Marín et al. (2007) the peak-to-peak velocity amplitude is derived. Col (3): Velocity dispersion: uniformly-weighted mean velocity dispersion as in this work while the nuclear velocity dispersion in García-Marín et al. (2007). Col (4): Half-light radius: it has been derived from the 2MASS K-band images as in this work while it has been derived using HST images (F814W or F160W) in García-Marín et al. (2007). Col (5): Dynamical mass computed using the same criteria described in Sect. 3.4. *The mean values derived in Colina et al. (2005) refer to a selected sample of 8 ULIRG systems.

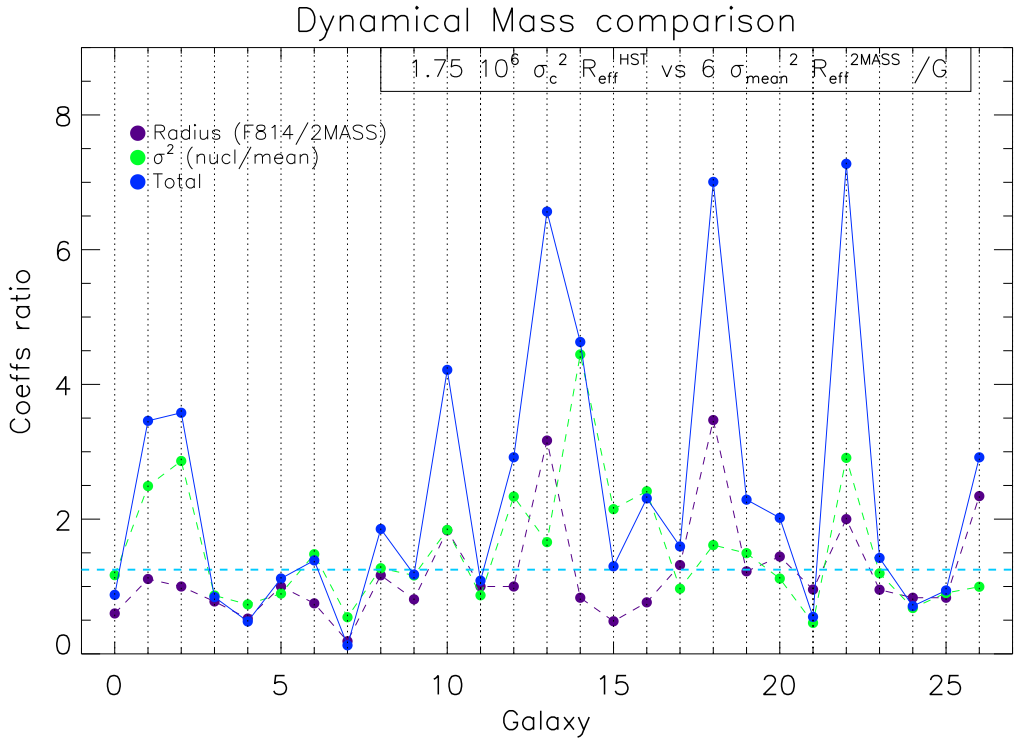

Figure D.2: Comparison between the values used in the two dispersion-dominated formulas: the ratio between the individual parameters are combined in order to derive the total factor (i.e., in blue) should be applied to compare the Colina et al. (2005) formula and Eq. 3.1.

other hand, the subsample analyzed in Colina et al. (2005) shows a lower value of the dynamical mass of the order of 0.4 $\pm$ 0.1 (0.4) $m_{\star}$.

In Fig. D.2 the comparison between the values of the dynamical masses derived following our analysis (i.e., in the dispersion-dominated case) and those derived in their works is shown. The dynamical masses obtained from the analyses of García-Marín et al. (2007) are higher than those derived using the Eq. 3.1 of a (mean) factor of $\sim$ 2. An increment of $\sim$ 20% is due to the constants used in the formulas, while different values of the effective radius and the velocity dispersion further increase the discrepancy. Indeed, only in three cases the ratio between the formula Eq. D.1 and Eq. 3.1 have a discrepancy larger than a factor of 6: in two of them (i.e., IRAS F17208-0014, IRAS F12490-1009), this can be explained as due to a larger R_{eff} in the I-band band while IRAS F14060+2919 shows a quite high σ_c value.